LABEL-FREE FLOW CYTOMETRY USING MULTIPLEX COHERENT ANTI-STOKES RAMAN SCATTERING (MCARS) SPECTROSCOPY

A Thesis
Presented to
The Academic Faculty

by

Charles H. Camp Jr.

In Partial Fulfillment
of the Requirements for the Degree
Doctor of Philosophy in the
School of Electrical and Computer Engineering

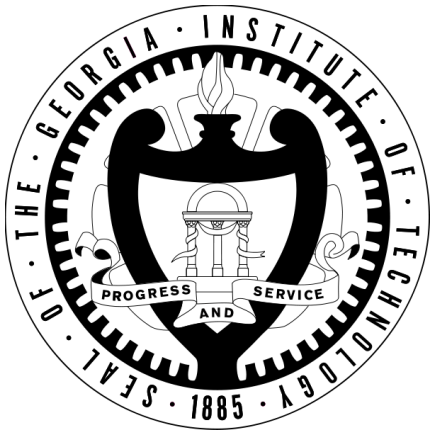

Georgia Institute of Technology
December 2011

LABEL-FREE FLOW CYTOMETRY USING MULTIPLEX COHERENT ANTI-STOKES RAMAN SCATTERING (MCARS) SPECTROSCOPY

Approved by:

Professor Ali Adibi, Advisor
School of Electrical and Computer Engineering
Georgia Institute of Technology

Professor Oliver Brand
School of Electrical and Computer Engineering
Georgia Institute of Technology

Professor John A. Buck
School of Electrical and Computer Engineering
Georgia Institute of Technology

Professor Mostafa A. El-Sayed
School of Chemistry and Biochemistry
Georgia Institute of Technology

Professor Paul L. Voss
School of Electrical and Computer Engineering
Georgia Institute of Technology

Date Approved: 18 August 2011

An expert is a person who has made all the mistakes

that can be made in a very narrow field.

—Niels Bohr (1885-1962)

ACKNOWLEDGEMENTS

First and foremost, I wish to thank my friends and family, who have supported me wholeheartedly through out this long, long ride. Without their support, the many exams, papers, and long nights in the lab would have been unbearably tedious and tiring.

I wish to thank my research advisor, Professor Ali Adibi, for his support and guidance in this endeavor. I am grateful for his unwavering support of my crazy ideas that covered electrical engineering, physics, chemistry, and biology.

I am very grateful to my reading committee for their dedication and guidance during the preparation of this dissertation: Professor John A. Buck, Professor Paul L. Voss, Professor Oliver Brand, and Professor Mostafa A. El-Sayed.

TABLE OF CONTENTS

LIST OF TABLES

LIST OF FIGURES

SUMMARY

Over the last 50 years, flow cytometry has evolved from a modest cell counter into an invaluable analytical tool that measures an ever-expanding variety of phenotypes. Flow cytometers interrogate passing samples with laser light and measure the elastically scattered photons to ascertain information about sample size, granularity, and basic morphology. Obtaining molecular information, however, requires the addition of exogenous fluorescent labels. These labels, although a power tool, have numerous challenges and limitations such as large emission spectra, non-specific binding, available conjugation chemistries, and cellular toxicity, which can alter cellular chemistries . Additionally, these labels may affect the dynamics and thermodynamics of samples such as the lipid bilayer in cell membranes, and the process of conjugating fluorophores and labeling cells can be time consuming; thus, reducing clinical turn-around times and affecting time-sensitive samples . To move beyond fluorescent labels in microscopy, a variety of techniques that probe the intrinsic Raman vibrations within a sample have been developed, such as coherent anti-Stokes Raman scattering (CARS) and Raman microspectroscopy.

In this dissertation, I present the first development of a label-free flow cytometer that measures the elastically scattered photons and probes the intrinsic Raman vibrations of passing samples using multiplex coherent anti-Stokes Raman scattering (MCARS). MCARS, a CARS technique that probes a large region of the Raman spectrum simultaneously, provides rich molecularly-sensitive information. Furthermore, I present its application to sorting polymer microparticles and its use in two example biological applications: monitoring lipid bodies within cultures of *Saccharomyces cerevisiae*, a model yeast with numerous human homologs, and monitoring

the affect of nitrogen starvation on *Phaeodactylum tricornutum*, a diatom, which is being genetically engineered to efficiently produce biofuels.

CHAPTER 1

INTRODUCTION

1.1 Motivation

Flow cytometry is a robust technique for the multiparameter analysis of sample populations with a myriad of uses in biology and medicine: from routine clinical diagnosis of hematological diseases [1–8] to monitoring and investigating marine ecologies, such as toxic algal blooms [9, 10] . Flowing samples are probed at high-speed by one or more lasers, and the scattered photons are measured by multiple detectors. The elastically scattered photons provide information about the morphology and internal "complexity" of the passing samples. To obtain molecularly specific information, however, typically requires the addition of exogenous fluorophores [1, 11–13]. These labels, although a long-standing and powerful tool, have several limitations and challenges, such as nonspecific binding and cytotoxicity, which can alter cellular chemistries and perturb the experimental outcomes [1, 11, 14]. Additionally, the process of conjugating fluorophores and labeling cells can be time consuming; thus, reducing clinical turnaround times and affecting time-sensitive samples (e.g., [15]). Despite these challenges and motivated by the geometric scaling of information, flow cytometers continue to not only rely upon fluorescent labels for molecularly specific information, but also these devices increasingly push the number of labels that can be simultaneously measured. Fluorescent labels, however, emit a broad spectrum of light that challenges the continued expansion of fluorescence-based flow cytometry.

To alleviate the difficulties associated with fluorescent labels, researchers have developed several technologies in microscopy and flow cytometry. Some technologies, such as quantum dots (QDs) and surface-enhanced Raman scattering (SERS) labels,

aim to replace traditional organic fluorophores with labels that operate under different optical mechanisms. QDs are inorganic nanoparticles that are excitable over a significantly broader bandwidth than organic fluorophores, and QDs emit photons within a narrower bandwidth; thus, they can be more densely multiplexed [1, 16, 17]. SERS labels, unlike organic dyes or QDs, emit complex spectra with narrow spectral features that act as spectral bar codes; thus, dense multiplexing is possible, but more sophisticated methods are necessary to spectrally distinguish different labels [18]. An entirely different route to reduce the challenges associated with fluorescent labels is to remove them entirely.

With the growing challenges posed by organic fluorophores and the increasing desire for more information, there is a push for label-free molecularly specific/sensitive techniques—not only in flow cytometry, but also in microscopy. One such technique is Raman spectroscopy in which incident photons inelastically scatter through interactions with sample molecular vibrations [19–22]. As this is a spontaneous process, approximately 1 of every 1,000,000 incident photons experience Raman scattering [22]. The incident photons gain (anti-Stokes scattering) or lose (Stokes scattering) energy equal to the vibrational energy between bonded atoms; thus, providing molecularly specific information about the sample of interest. This technique has a long standing history of detailed molecular analysis in the physical and life sciences ranging from differentiating healthy and diseased lymphocytes [23, 24] to finding defects in semiconductor growths [25, 26]. Recently, this technique was successfully applied to flow cytometry, but it required long integration times due to the weak signal created by the spontaneous Raman process [27]. Coherent anti-Stokes Raman scattering (CARS), on the other hand, is a coherent process that probes the Raman vibrational energies and shows considerable promise as a label-free microscopy technique [28–32]. This technique, unlike traditional spontaneous Raman spectroscopy, only probes a narrow

wavelength region; thus, only single vibrational energies are probed. This, unfortunately, provides limited information, especially in the presence of the so-called non-resonant background (NRB). To practically apply CARS to flow cytometry requires the ability to probe multiple Raman transitions simultaneously. Multiplex CARS (MCARS) and broadband CARS (BCARS) are two CARS techniques that accomplish this task by using broadband sources to probe broad bandwidths of the Raman spectrum. In this dissertation, I present the first implementation and application of MCARS spectroscopy to flow cytometry, which provides a label-free mechanism for probing the Raman energy levels within passing samples at high-speed.

1.2 Scope and Organization

In this dissertation, I describe the development and characterization of the first MCARS flow cytometer. Additionally, several applications of the system are presented. The purpose of this work is to demonstrate the ability of a flow cytometer to analyze samples at high-speed without the use of labeling and to characterize the strengths and limitations of the technique. This dissertation is divided into 7 chapters. Chapter 2 provides the background material on flow cytometry and CARS to prepare the reader with the concepts and context for the original works presented in the remaining chapters. Chapter 3 presents the construction of the MCARS flow cytometer and presents the details of each component system, such as the microfluidic system and the elastically-scattered photons measurement module. Chapter 4 presents the characterization of the individual subsystem components and the performance of the entire MCARS flow cytometer system. Chapter 5 presents the application of label-free flow cytometry to differentiating polymer beads based on size and molecular composition, as well as several biological specimens: *Saccharomyces cerevisiae*, a yeast often used to model higher eukaryotes (including humans), and *Phaeodactylum tricornutum*, a diatom that is important in future bio-energy research

for its ability to produce ethanol and biodiesel. Chapter 7 investigates methods of improving MCARS flow cytometry and future directions of this label-free flow cytometry research. Finally, Chapter 8 summarizes the findings in this dissertations and concludes the work.

CHAPTER 2

BACKGROUND

2.1 Flow Cytometry

Flow cytometry is an invaluable analytical method for the high-throughput analysis of sample populations. Evolving from the Coulter counter, invented in the 1950's, which measured the electrical impedance of passing samples [1, 33], the modern flow cytometer, as developed by Dittrich and Göhde in the 1960's, probes passing samples with one or more laser beams [1, 12]. The elastically scattered photons are measured to ascertain morphological information, and the fluorescent emission from [typically] exogenous fluorophores are measured to obtain molecular information about targeted phenotypes. This system architecture has evolved dramatically over the last half-century to become a workhorse tool in biology and medicine. In clinical use for example, flow cytometers are routinely used to diagnose, monitor, and assess the treatment of a variety of diseases, including the human immunodeficiency virus (HIV), leukemias, and lymphomas [1–8]. In biology, flow cytometry has been applied to monitoring toxic algal blooms, analyzing cell cycle and cellular growth, identifying chromosomal content (e.g., to identify X- and Y-chromosome bearing sperm), monitoring live zebra fish embryos, monitoring microbes in potable water, and for evaluating food and drug safety and efficacy [1, 9, 10].

2.1.1 Flow Cytometer Operation

Flow cytometers are robust instruments for high-throughput analysis of sample populations. Modern flow cytometers are composed of 3 subsystems working in tandem: fluidics, optics, and electronics. A schematic of a flow cytometer is shown in Figure 1. The heart of the fluidics system is the flow cell [see Figure 2(a)]. Within the flow cell,

a sample suspension is fed into and surrounded by a high-speed sheath fluid. The high-speed sheath hydrodynamically focuses the sample stream into a narrow line [see Figure 2(b)]. This focusing of the sample stream aims to ensure that only single samples flow through the optical focal volume. Controlling the relative speed of the sample and sheath streams controls the final width of the sample stream (thus controlling the lateral deviation of the particles within the stream itself) and the speed of the particles flowing through the focal volume.

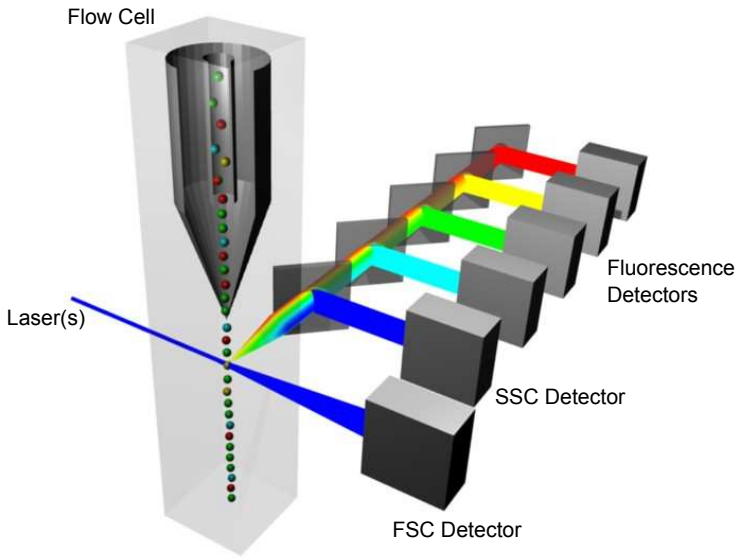

Figure 1: In traditional flow cytometers, a high-velocity sheath stream envelops the sample stream within the flow cell. This hydrodynamically focuses the sample into a single-file line that one or more lasers interrogate. A detector, typically a silicon photodiode, measures the elastically scattered photons in the forward direction (FSC). The strength of the FSC is indicative of sample size. Another detector measures the side-scatter (SSC), which reveals the level of internal complexity within the sample. To measure molecular phenotypes, samples are stained with selective fluorescent labels that are excited by the excitation laser and fluoresce at different wavelengths. A series of dichroic filters and band-pass filters (not shown) isolate specific wavelength regions.

The mechanism of analysis in flow cytometers is the optical interrogation of flowing particles. As the focused particle stream passes through the flow cell, one or more lasers interrogate the stream. Typically, the lasers are focused using cylindrical

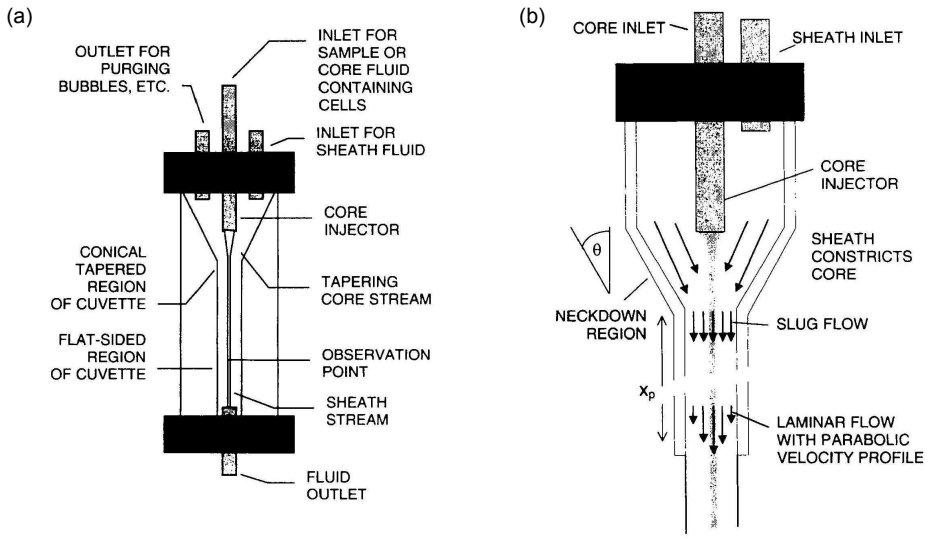

Figure 2: (a) Schematic of typical flow cell. (b) Illustration of flow cell operation. Both images reprinted from [1]. © John Wiley & Sons, Inc.

lenses as to provide an approximate plane-of-light across the entire sample stream. As each sample passes through the focal plane, the elastically scattered photons are recorded in the forward direction (often labeled "forward scatter" [FSC], "small angle scatter", or "forward angle light scatter" [FALS]– in this document, the abbreviation FSC will be used) and in the lateral direction (often labeled "side scatter" [SSC], "large angle scatter", or "right angle light scatter" [RALS]– in this document, the abbreviation SSC will be used). Flow cytometers parameterize sample morphology based on these two measurements with the FSC providing some indication of sample size, and SSC revealing information about the internal complexity (or "granularity") of the sample. Physically, larger particles scatter a predominant amount of incident light in the forward direction. Figure 4(a) is the simulated [normalized] elastic scatter (the S_{11} components of the Mueller scattering matrix) from a polystyrene bead that has a diameter 5 times the incident light wavelength immersed in water. For this large particle, as shown in Figure 4(b), which compares the FSC to SSC, the FSC is significantly larger than the SSC (the FSC is ∼8000 times larger than the SSC). A small particle, on the other hand, scatters light more evenly, as shown in Figure 3(a)

(the S_{11} components of the Mueller scattering matrix), which shows the simulated scattering of a polystyrene bead that has a diameter that is 10% of the wavelength in water. Figure 3(b) shows the relative intensity of the FSC and SSC and reveals that the FSC is only about twice as large as the SSC. For most eukaryotic cells, the cells are relatively large compared to the wavelength of interrogation light (typically, cells are 1 - 20 μm and the incident beam wavelength is 400-670 nm); thus, the outer cell structure does predominantly scatter light in the forward direction. Internal cell structures, such as lipid vacuoles, mitochondria, and granules, are relatively small and contribute to both FSC and SSC. To examine these features for a biological sample, Figure 5 is the scatter plot of SSC versus FSC for a typical lysed blood culture. One can see 3 subpopulations representing lymphocytes, monocytes, and neutrophils (among other granulocytes) [1, 34]. Although measuring the elastically scattered photons provides morphological information that can be used to differentiate these 3 subpopulations, quantifying cell size and internal complexity is extraordinarily challenging as both parameters are extremely sensitive to cell size, shape, surface roughness, and the index of refraction of individual sample components [1]. As an example of this difficulty, a suspension of 9 μm polystyrene (PS) beads and 5 μm poly(methyl methacrylate) (PMMA) beads were measured in a flow cytometer (LSRII, BD Biosciences, Franklin Lakes, NJ). Although both beads are solid particles, they demonstrate pronouncedly different SSC. Additionally, the PMMA beads produce a stronger FSC.

Although FSC and SSC provide a significant amount of sample information, molecularly specific information requires the addition of exogenous fluorophores. These fluorophores are typically composed of a molecularly specific label and a fluorochrome; although, some fluorochromes are reactive or have an intrinsic affinity for particular molecular constituents or intracellular conditions; thus, adding an additional label is unnecessary. Nile Red, for example, is hydrophobic; thus, it is used to stain lipids without the addition of a separate label. In most flow cytometers, the same laser

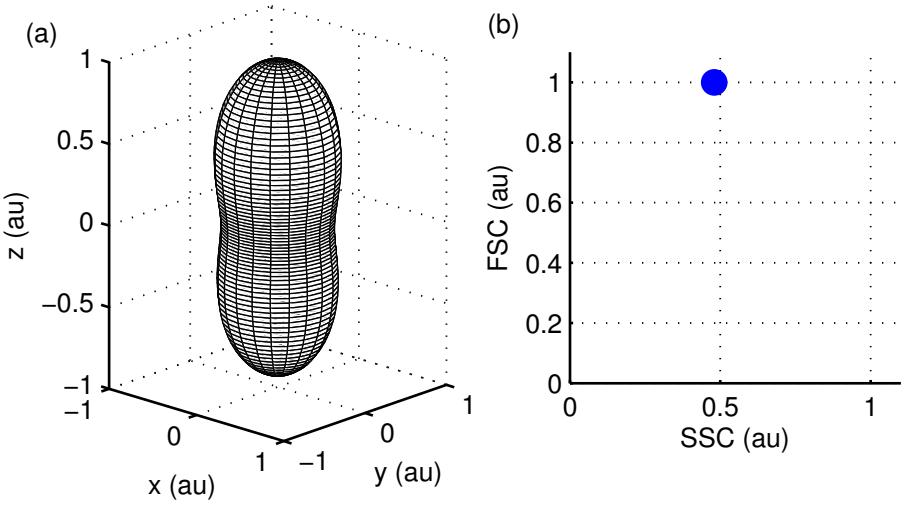

Figure 3: (a) Simulated elastic scatter pattern (normalized S_{11} of the Mueller scatter matrix) of a polystyrene bead with a diameter that is one tenth the incident wavelength. (b) Comparison of the FSC and SSC relative scatter strengths.

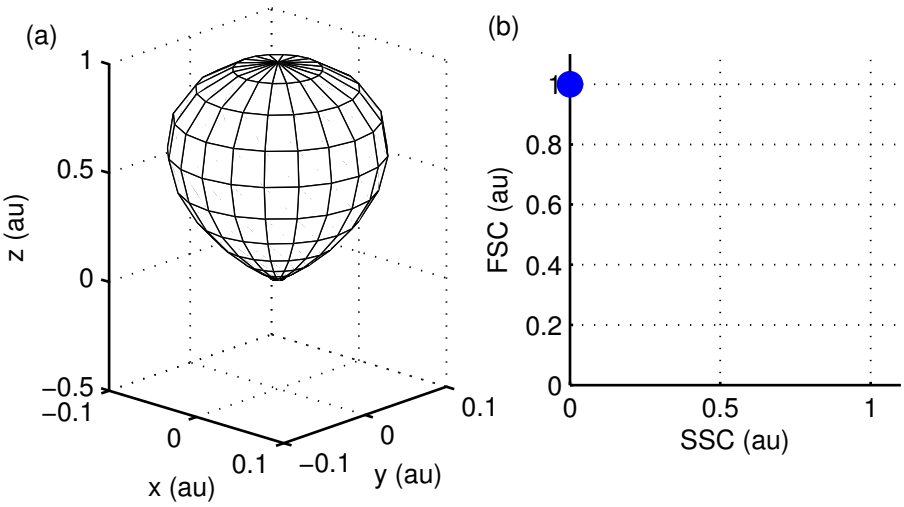

Figure 4: (a) Simulated elastic scatter pattern (normalized S_{11} of the Mueller scatter matrix) of a polystyrene bead that has a diameter that is five times larger than the incident wavelength. (b) Comparison of the of the FSC and SSC relative scatter strengths.

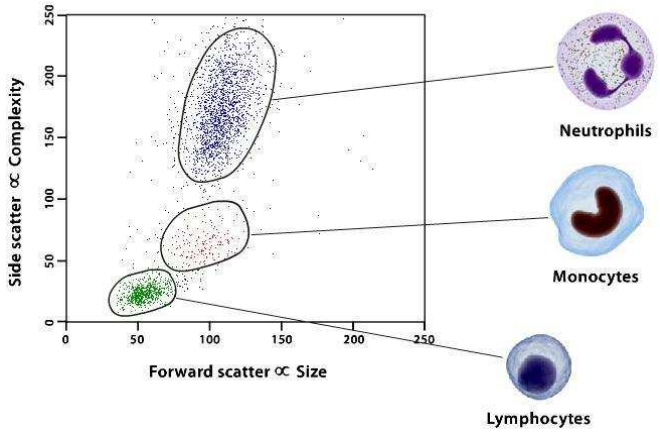

Figure 5: Scatter plot of SSC versus SSC for a typical lysed blood sample. Image obtained from [34]. © Invitrogen by Life Technologies.

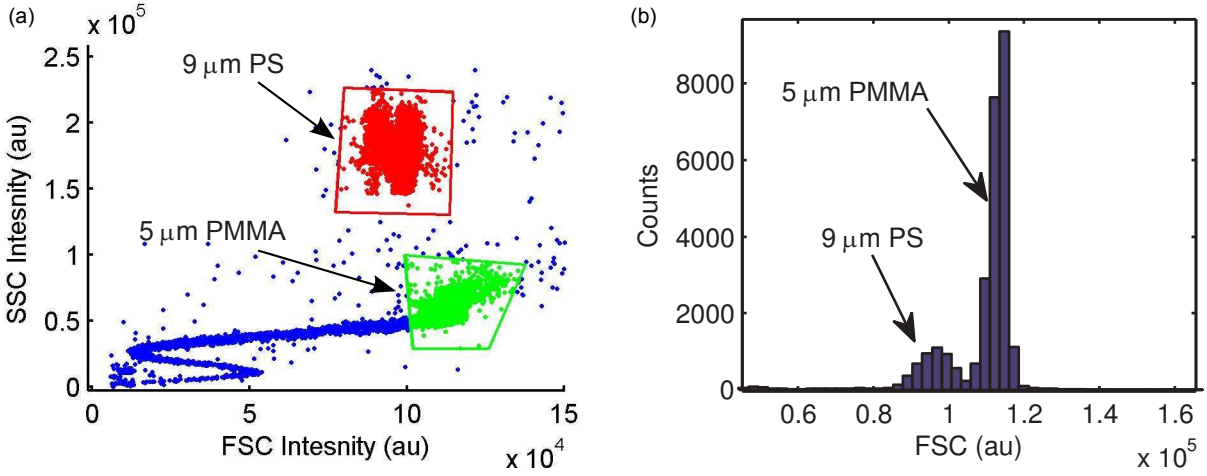

Figure 6: (a) SSC and FSC intensity of a mixture of polystyrene (red) and PMMA beads (green) as analyzed in a commercial flow cytometer. The dominant contribution to the populations are highlighted; thus, the *tail* of the PMMA population is gated out. (b) Histogram of the FSC intensities for the PS and PMMA populations.

used for elastic scatter measurements and additional lasers excite the fluorophores and the resulting fluorescence is collected. The fluorescent emission passes through a series of dichroic filters to isolate different spectral bandwidths, each of which is measured by a detector (typically, a photomultiplier tube [PMT]). Laser sources, fluorophores, and filters must be selected to ensure that each fluorophore is excited and to ensure that the fluorescent emission from each fluorophore is uniquely measurable by one of the PMTs. Example excitation and emission profiles of three commonly used fluorophores are shown in Figure 7.

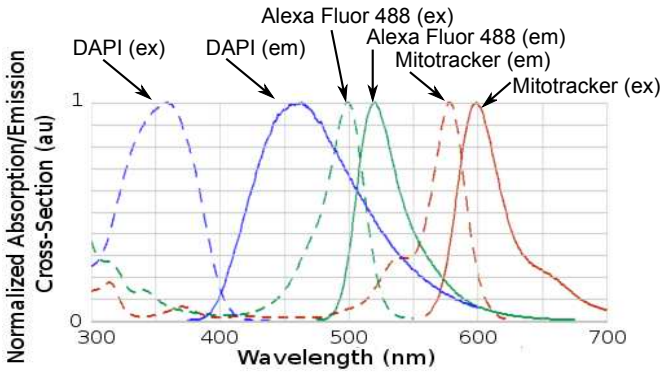

Figure 7: Fluorescent emission (em) and excitation (ex) profiles for 3 common fluorophores: DAPI (blue), Alexa Fluor 488 (green), and Mitotracker (red). Image produced at [35]

The combination of scatter measurement and fluorescent labels has promoted flow cytometers from laboratory curiosity to workhorse tools found across the world in academic, industrial, and clinical settings. Figure 8 shows a list of example parameters and phenotypes that flow cytometers are capable of measuring [1]. Table 1 provides a concise list of technical specifications for 3 commercially available flow cytometers: BD Biosciences LSRII, Accuri C6, and the Union Biometrica COPAS. The BD LSRII is a research-grade flow cytometer capable of up to 10 measurable colors and is the flow cytometer used for sample analysis in this work. The Accuri C6 is a lightweight and compact flow cytometer that represents the state-of-the-art in compact

flow cytometers. Finally, the Union Biometrica COPAS is a flow cytometer specifically designed for the analysis of samples too large for traditional flow cytometers.

Table 1: Specifications of several commercially available flow cytometers.

Parameter	BD LSR II	Accuri C6	Union Biometrica COPAS
Installed Lasers	4	2	2
Wavelengths Choices(nm)	488, 405, 625, 355	488, 640	670, 635, 405, 488, 561, 325, 375
Color Channels	10	4	3
Speed (Events/s)	>20,000	10,000	35
Sample Flow Rate ($\mu L/min$)	60	66	6000
Flow Cell Core Inner Diameter or Size (μm)	430 x 180	200	250-2000
Sample Volume (μL)	100's	50	40000
Focal Volume (μm)	15 x 75	10 x 75	1000 x 1000

2.1.2 Challenges and Current Direction in Flow Cytometry

Flow cytometer technology has greatly expanded over the last half century and is an active area of research. Over the last decade, a large portion of research has focused on increasing the number of simultaneously measurable fluorophores. As the amount of information scales geometrically with the number of color channels, these polychromatic flow cytometers allow diagnoses and analyses not possible with older systems with fewer colors [11]. Fluorescent labels, although a powerful tool, suffer from a number of challenges and limitations:

1. broad emission spectra [1, 11, 14]
2. nonspecific binding [1, 11]
3. photobleaching [16]
4. available conjugation chemistries [11]

PARAMETER	MEASUREMENT METHOD AND PROBE IF USED
Intrinsic Structural Parameters (no probe)	
Cell Size	Electronic (DC) impedance, extinction, small angle light scattering; image analysis
Cell shape	Pulse shape analysis (flow); image analysis
Cytoplasmic granularity	Large angle light scattering, Electronic (AC) impedance
Birefringence (e.g., of blood eosinophil granules)	Polarized light scattering, absorption
Hemoglobin, photosynthetic pigments, porphyrins	Absorption, fluorescence, multiangle light scattering
Intrinsic Functional Parameter (no probe)	
Redox state	Fluorescence (endogenous pyridine and flavin nucleotides)
Extrinsic Structural Parameters (probe required)	
DNA content	Fluorescence (propidium, DAPI, Hoechst dyes)
DNA base ratio	Fluorescence (A-T and G-C preference dyes, e.g., Hoechst33258 and chromomycin A_3)
Nucleic acid sequence	Fluorescence (labeled oligonucleotides)
Chromatin structure	Fluorescence (fluorochromes after DNA denaturation)
RNA content (single and double-stranded)	Fluorescence (acridine orange, pyronin Y)
Total protein	Fluorescence (covalent- or ionic-bonded acid dyes)
Basic protein	Fluorescence (acid dyes at high pH)
Surface/intracellular antigens	Fluorescence; scattering (labeled antibodies)
Surface sugars (lectin binding sites)	Fluorescence (labeled lectins)
Lipids	Fluorescence (Nile red)
Extrinsic Functional Parameters (probe required)	
Surface/intracellular receptors	Fluorescence (labeled ligands)
Surface charge	Fluorescence (labeled polyionic molecules)
Membrane integrity (not always a sign of "viability")	Fluorescence (propidium, fluorescein diacetate [FDA]); absorption or scattering (Trypan blue)
Membrane fusion/turnover	Fluorescence (labeled long chain fatty acid derivatives)
Membrane organization (phospholipids, etc.)	Fluorescence (annexin V, merocyanine 540)
Membrane fluidity or microviscosity	Fluorescence polarization (diphenylhexatriene)
Membrane permeability (dye/drug uptake/efflux)	Fluorescence (anthracyclines, rhodamine 123, cyanines)
Endocytosis	Fluorescence (labeled microbeads or bacteria)
Generation number	Fluorescence (lipophilic or covalent-bonded tracking dyes)
Cytoskeletal organization	Fluorescence (NBD-phallacidin)
Enzyme activity	Fluorescence; absorption (fluorogenic/chromogenic substrates)
Oxidative metabolism	Fluorescence (dichlorofluorescein)
Sulfhydryl groups/glutathione	Fluorescence (bimanes)
DNA synthesis	Fluorescence (anti-BrUdR antibodies, labeled nucleotides)
DNA degradation (as in apoptosis)	Fluorescence (labeled nucleotides)
"Structuredness of cytoplasmic matrix"	Fluorescence (fluorescein diacetate [FDA])
Cytoplasmic/mitochondrial membrane potential	Fluorescence (cyanines, rhodamine 123, oxonols)
"Membrane-bound" Ca^{++}	Fluorescence (chlortetracycline)
Cytoplasmic $[Ca^{++}]$	Fluorescence ratio (indo-1), fluorescence (fluo-3)
Intracellular pH	Fluorescence ratio (BCECF, SNARF-1)
Gene expression	Fluorescence (reporter proteins)

Figure 8: List of measurable parameters and corresponding methods (e.g., labels) in flow cytometry. Reprinted from [1]. © John Wiley & Sons, Inc.

5. cytotoxicity [1, 16]

6. perturbation of local chemistries and thermodynamics [36]

7. time-consumption of the labeling process [15].

Arguable the largest challenge facing organic fluorophores is the broad emission spectrum and the resulting spectral overlap between neighboring color channels. To combat this spectral bleeding, researchers have actively investigated compensation methods [1,11,14]. These mathematical models, implemented in hardware or software, aim to mitigate the effects of spectral overlap. Although these methods may be effective, they bring along their own challenges, limitations, and errors that may skew experimental results [11, 14]. To move away from filter sets and single-channel detectors all together, researchers developed a flow cytometer that uses a detector array spectrometer to capture the full fluorescence spectrum [37]. This instrument demonstrated the ability to detect multiple fluorophores with a good degree of accuracy but at the expense of speed [37].

To circumvent the challenges of using traditional organic fluorophores, various optical methods and labeling technologies have arisen for molecularly-sensitive detection in flow cytometry and microscopy. One such labeling technology is quantum dots (QDs). QDs are inorganic nanoparticles that are excitable with a broader range of wavelengths and emit within a narrower spectral band than traditional organic fluorophores [1, 17]. Although QDs are easier to excite and multiplex, they too have numerous difficulties with cytotoxicity and surface chemistry [16, 17]. To move away from fluorescent dyes all together, a number of research groups have investigated Raman scattering methods to probe the intrinsic Raman vibrational energy levels within a passing sample. These vibrational energy levels provide rich information about the molecular content, thermodynamics, and molecular dynamics of a sample and provide

a mechanism to differentiate samples in a manner that requires no sample preparation. Lau *et al.*, for example, demonstrated a microfluidic cell sorter that successfully separated cells from two leukemia cell lines based on their Raman spectra [27]. Although a powerful tool, in principle, this cell sorter required 120 seconds to acquire the Raman spectrum from each passing cell due to the small spontaneous Raman scattering cross-section; thus, making its use for high-throughput analysis unlikely. Wang *et al.* applied coherent anti-Stokes Raman scattering (CARS) microscopy to monitor passing samples in a microfluidic flow cell and measured up to 100 particles per second [38]. This instrument, however, only probed individual Raman vibrations. Additionally, the problematic nonresonant background (NRB) produced a signal in almost all samples, regardless of whether there existed the Raman vibrational band of interest.

2.2 Coherent Anti-Stokes Raman Scattering

Traditional microscopy techniques, such as bright field, dark field, and differential interference contrast (DIC), observe morphological differences within samples based on their spatial distribution of scattering and absorbing elements. To resolve molecular differences, however, requires imaging samples containing endogenous or exogenous fluorophores. Although fluorescent labels are a powerful and proven technology, extrinsic labels suffer from numerous limitations and challenges, such as cytotoxicity, photobleaching, and nonspecific binding [1, 11, 14]. Additionally, these labels may affect local thermodynamics and chemistries; thus, perturbing experimental outcomes [36]. To circumvent these potential limitations, researchers have developed several microscopy and spectroscopy techniques that probe the intrinsic vibrational energy levels within a molecule. Most notably, infrared microscopy and Raman microspectroscopy (microRaman) have been largely developed, applied to biological samples, and are readily available from commercial vendors [39–44]. Both of these

techniques, however, suffer from several limitations. Infrared microscopy, for example, presents poor spatial resolution due to the infrared sources and high absorption of water [43]. MicroRaman, on the other hand, has high spatial resolution but requires long integration times due to the weak nature of spontaneous Raman and excites sample fluorescence that can completely obscure the Raman spectrum. More recently, researchers (and some commercial vendors) have developed microscopy techniques based on coherent Raman scattering. Techniques such as CARS microscopy [28] and stimulated Raman scattering (SRS) microscopy [45] probe the Raman vibrational energy levels within a molecule, but unlike traditional implementations, these methods coherently excite the sample; thus, generating photons with orders of magnitude higher efficiencies under many biological conditions [32, 46].

Maker and Terhune at the Ford Motor Company [47] first described the CARS process; although, it was not named "CARS" until nearly a decade later [48]. In 1982, Duncan *et al.* were the first to apply CARS to scanning microscopy [49], but it wasn't until 1999 when Zumbusch *et al.* developed a CARS microscope that was fast, sensitive, and relatively simple to integrate with scanning laser systems [28]. Their use of near-infrared (NIR) sources dramatically reduced the NRB and the collinear beam geometry greatly simplified the optical system.

2.2.1 Theoretical Background

CARS is a third-order nonlinear optical process in which a pump and a Stokes photon coherently excite a molecule into a higher Raman vibrational energy level, and a probe photon inelastically scatters off of the excited molecule [see the energy diagram in Figure 9(a)]. Mathematically, CARS is described by the nonlinear wave equation derived from Maxwell's Equations for a currentless and chargeless medium:

$$\nabla \times \nabla \times \widetilde{E}(t,z) = -\frac{n(\omega)^2}{c^2}\frac{\partial^2 \widetilde{E}(t,z)}{\partial t^2} + \frac{1}{\epsilon_0 c^2}\frac{\partial^2 \widetilde{P}^{NL}(t,z)}{\partial t^2}, \tag{1}$$

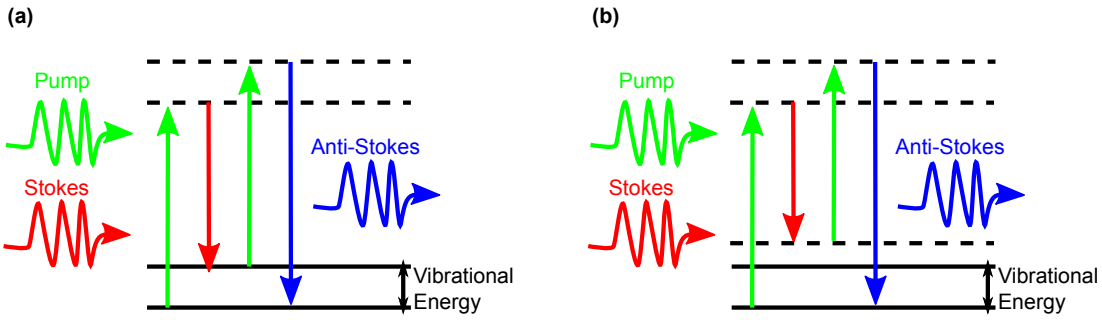

Figure 9: Energy diagram of (a) CARS and (b) the NRB. In (a), a pump and Stokes photon excite the molecule into a higher vibrational energy, and a probe photon inelastically scatters off of the excited mode. In (b), a four-wave mixing (FWM) process produces photons regardless of the existence of vibrational energy levels.

where $\widetilde{E}(t,z)$ is the electric field, $n(\omega)$ is the index of refraction at frequency ω, ϵ_0 is the permittivity of free-space, and $\widetilde{P}^{NL}(t,z)$ is the nonlinear polarization [21,22,50]. A Green's Function can solve this equation for arbitrary nonlinear polarizations [31], but a simple one-dimensional (1D) scalar approximation provides an analytical solution that provides key insights. In the 1D scalar approximation, the electric fields and the nonlinear polarization assume the form:

$$\widetilde{E}(t,z) = \frac{A(z)}{2} e^{-jkz+j\omega t} + c.c. \tag{2}$$

$$\widetilde{P}^{NL}(t,z) = \frac{P^{NL}(z)}{2} e^{j\omega_{as} t} + c.c., \tag{3}$$

where $A(z)$ is the field envelope, $P^{NL}(z)$ is the third-order nonlinear polarization envelope, ω is the optical frequency, k is the z-component of the electric field wave vector, and $c.c.$ denotes the complex conjugate. Specific to the CARS generation process, the electric field in this equation is for the anti-Stokes field and the nonlinear polarization contains the influence of the pump, Stokes, and probe fields. Assuming the slowly varying envelope approximation (SVEA) and applying these assumptions into Eq. (1) simplifies the the nonlinear wave equation:

$$j4k_{as} \frac{\partial A_{as}(z)}{\partial z} = -\frac{\omega_{as}^2}{\epsilon_0 c^2} P^{NL}(z) e^{jk_{as} z}, \tag{4}$$

where $A_{as}(z)$ is the anti-Stokes field envelope and k_{as} is the z-component of the anti-Stokes wave vector ($k_{as} = n\omega_{as}/c$). Additionally, the nonlinear polarization and nonlinear susceptibility are described as:

$$P^{NL}(z) = 6\epsilon_0\chi^{(3)}(\omega_{as};\omega_{p1},-\omega_s,\omega_{p2})\frac{A_{p1}(z)}{2}\frac{A_s^*(z)}{2}\frac{A_{p2}(z)}{2}e^{-j(k_{p1}-k_s+k_{p2})z} \quad (5)$$

$$\chi^{(3)}(\omega_{as};\omega_{p1},-\omega_s,\omega_{p2}) = \chi_{NR}^{(3)} + \chi_R^{(3)} = \chi_{NR}^{(3)} + \sum_k \frac{A_k}{\Omega_k - (\omega_{p1}-\omega_s) - i\Gamma_k}, \quad (6)$$

where $A_{p1}(z)$, $A_s(z)$, and $A_{p2}(z)$ are the pump, Stokes, and probe field envelopes, respectively, with associated wave vector z-components k_{p1}, k_s, and k_{p2} and frequencies ω_{p1}, ω_s, and ω_{p2}. $\chi^{(3)}$ is the third-order nonlinear optical susceptibility [22,29,50,51]. $\chi^{(3)}$ expands into two components: a nonresonant component $\chi_{NR}^{(3)}$ that describes the NRB and a resonant contribution $\chi_R^{(3)}$ that describes the coherent Raman scattering processes. The nonresonant component is assumed to be constant and real, and it describes a four-wave mixing (FWM) process that mimics the CARS process [see Figure 9(b)] [50,51]. A summation of Lorentzian response functions with the k^{th} Raman vibrational contribution described by an amplitude A_k, located at a frequency (energy) Ω_k, and with a half-width Γ_k models the resonant contribution. Inserting Eq. (5) into Eq. (4) yields:

$$j4k_{as}\frac{\partial A_a(z)}{\partial z} = -\frac{3}{4}\frac{\omega_{as}^2}{c^2}\chi^{(3)}(\omega_{as};\omega_{p1},-\omega_s,\omega_{p2})A_{p1}(z)A_s^*(z)A_{p2}(z)e^{-j\Delta kz}, \quad (7)$$

where Δk is the phase matching condition ($\Delta k = k_{p1} - k_s + k_{p2} - k_{as}$). In most practical CARS applications, the Stokes and pump sources are much more intense than the anti-Stokes signal, there is negligible source depletion, and the anti-Stokes signal develops completely within the medium. With these assumptions and through integration over a linear space l, Eq. (7) is solved as

$$A_{as}(l) = \frac{-3\omega_{as}}{16cn(\omega_{as})}\chi^{(3)}(\omega_{as};\omega_{p1},-\omega_s,\omega_{p2})A_{p1}A_s^*A_{p2}\frac{e^{\Delta kl}-1}{\Delta k}. \quad (8)$$

Using the trigonometric identity

$$\frac{1-cos(2x)}{2} = sin^2(x), \quad (9)$$

the anti-Stokes field intensity is

$$I_{as}(l) = 2n(\omega_{as})\sqrt{\frac{\epsilon_0}{\mu_0}}|A_{as}(l)|^2$$
$$\propto \frac{\omega_{as}^2\epsilon_0}{n(\omega_{as})c}\left|\chi^{(3)}(\omega_{as};\omega_{p1},-\omega_s,\omega_{p2})\right|^2 I_{p1}I_sI_{p2}l^2 sinc^2\left(\frac{\Delta kl}{2}\right), \qquad (10)$$

where I_{p1}, I_s, and I_{p2} are the pump, Stokes, and probe field intensities, respectively. Importantly, Eq. (10) expresses that the CARS intensity increases linearly with the pump, Stokes, and probe field intensities. In most CARS microscopy systems, the pump and probe fields are degenerate; thus, the CARS intensity increases quadratically with pump intensity and increases linearly with the Stokes intensity. Additionally, the wavevector mismatch, Δk, when expanded into three-dimensions, is $\Delta\vec{k} = -\vec{k}_{as} + 2\vec{k}_p - \vec{k}_s$ (see Figure 10). As evident from this relationship between the wave vectors, the incident fields spatial orientations need to be controlled to minimize the wave vector mismatch. Although a collinear beam geometry appears to violate the phase matching condition described in Figure 10, tight focusing relaxes this condition [28, 31, 50, 52].

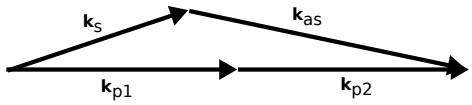

Figure 10: The phase matching condition of the CARS generation process.

Since the reawakening of CARS microscopy research in 1999, the number of journal publications on CARS microscopy has grown from 1 in 1999 to over 350 by 2010 (as analyzed by ISI Web of Science). The areas of research encompass new biological applications and methods for improving molecular sensitivity and specificity. The largest technical challenge for CARS microscopy is the existence of the NRB that is generated by a FWM process [see Figure 9(b)]. Unlike the CARS optical process, which requires the existence of vibrational states at particular energy levels, the NRB can exist regardless of the vibration energy levels, and its intensity can be equal to

or greater than that of the resonant CARS signal. Additionally, the NRB coherently interferes with the resonant CARS signal [as described by the cross terms arising from the square modulus of the $\chi^{(3)}$ in Eq. (10)]; thus, distorting the CARS spectrum from the actual Raman vibrational energy levels. To simulate this effect and to incorporate the pulsed nature of the pump, Stokes, and probe sources, the nonlinear polarization can be described in the frequency domain:

$$P^{(3)}(\omega_{as}) = \int_{-\infty}^{\infty}\int_{-\infty}^{\infty}\int_{-\infty}^{\infty}\frac{3}{8}\epsilon_0\chi^{(3)}(\omega_{as};\omega_{p1},-\omega_s,\omega_{p2})E_{p1}(\omega_{p1})E_s^*(w_s)E_{p2}(\omega_{p2})\times \\ \delta(\omega_{as}-\omega_{p1}-\omega_{p2}+\omega_s)d\omega_{p1}d\omega_s d\omega_{p2}, \tag{11}$$

where ω_{as}, ω_{p1}, ω_s, and ω_{p2} are the anti-Stokes, pump, Stokes, and probe frequencies, respectively, E_{p1}, E_s, E_{p2} are the electric fields of the pump, Stokes, and probe sources in the frequency domain, respectively, and the δ-function ensures conservation of energy (N.B.: this formalism is not derived from the aforementioned scalar approximation, but rather is a new formalism often used for simulating the spectral characteristics of CARS [30, 53]). Furthermore, as is the case in most CARS microscopy systems, the pump and probe sources are degenerate; thus, Eq. (11) simplifies to

$$P^{(3)}(\omega_{as}) = \int_{-\infty}^{\infty}\frac{3}{8}\epsilon_0\chi^{(3)}(\omega_{as};\omega_p,-2\omega_p+\omega_{as},\omega_p)E_p^2(\omega_p)E_s^*(\omega_{as};\omega_p)d\omega_p, \tag{12}$$

where $E_p(\omega_p)$ is the frequency domain representation of the pump/probe field. Figure 11 shows the simulated CARS spectrum generated by a 1 picosecond pump and a supercontinuum Stokes source (a common Stokes source in CARS spectroscopy), approximated by a spectral constant, stimulating a single Raman vibration at 2900 cm^{-1} (A = 1, $\Gamma = 3.3\times10^{11}$ [1.7507 cm^{-1}], $\Omega = 5.4664\times10^{14}$ rad/sec, $\chi_{NR}^{(3)} = 0.5A\Gamma$), which falls within the energy range of CH-stretch vibrations [51, 54]. It should be noted that approximating the supercontinuum by a spectral constant is a common, albeit rough approximation of the Stoke source, as this approximates a Stokes source

that is a single, short pulse; although, actual supercontinua may be composed of several pulses (the actual performance is greatly dependent on numerous parameters such as seed source pulse and spectral characteristics and the fiber itself). Spectral distortions in both peak location and shape are apparent when the NRB is included in the simulation.

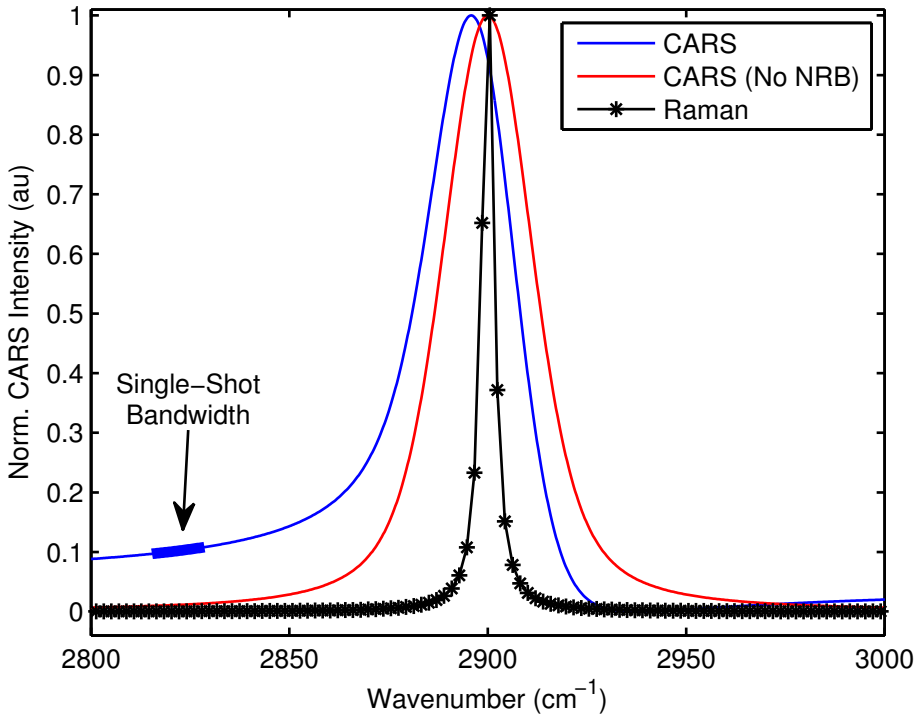

Figure 11: Simulated CARS/MCARS spectrum of a molecule with a single Raman vibrational energy at ∼2900 cm^{-1} (black, stars) with (blue) and without (red) the effect of the NRB. In CARS microscopy and spectroscopy, which are narrowband techniques, the source wavelengths are tuned so that the energy difference between the pump and Stokes corresponds to an anti-Stokes energy of interest. The resultant CARS intensity is recorded at each wavelength (i.e., energy) difference (see the single-shot CARS bandwidth), and the wavelength is scanned across the entire spectrum. MCARS spectroscopy, which probes multiple wavelengths simultaneously, records the entire spectrum at once using a spectrometer.

2.2.2 Spectral Distortions in CARS

Although CARS (and related coherent techniques) are a powerful mechanism of probing the intrinsic Raman vibrational energy levels within a molecule, the acquired

spectra are not simply enhanced Raman spectra as would be acquired with traditional Raman spectrometers. The spontaneous Raman spectrum is related to the third-order nonlinear susceptibility as:

$$I_{Raman}(\omega) \propto \Im\{\chi^{(3)}(\omega)\} \propto \sum_k \frac{A_k \Gamma_k}{(\omega - \Omega_k)^2 + \Gamma_k^2}, \tag{13}$$

where A_k, Γ_k, and Ω_k are the amplitude, half-width, and energy of the k^{th} Raman vibration and ω is the independent variable of energy (frequency) (N.B., $\Im$ is the imaginary component operator) [55]. From this form, one can see that multiple Raman peaks incoherently add together. Additionally, there may exist a background fluorescence excited by the excitation source, which also incoherently adds to the Raman signal. CARS techniques on the other hand produce a spectrum proportional to $|\chi^{(3)}|^2$, which is written as:

$$\begin{aligned} I_{CARS} \propto |\chi^{(3)}|^2 &= |\chi^{(3)}_{NR} + \sum \chi^{(3)}_R(\omega_{as}; \omega_{p1}, -\omega_s, \omega_{p2})|^2 \\ &= |\chi^{(3)}_{NR}|^2 + \sum_{i=1} \left(|\Re\{\chi^{(3)}_i\}|^2 + |\Im\{\chi^{(3)}_i\}|^2 + 2\Re\{\chi^{(3)}_i\}\chi^{(3)}_{NR} \right) \\ &+ \sum_{i=1} \sum_{j>i} 2\Re\{\chi^{(3)}_i\}\Re\{\chi^{(3)}_j\}, \end{aligned} \tag{14}$$

where $\chi^{(3)}_{NR}$ is the third-order nonlinear susceptibility of the nonresonant contribution to the CARS signal, which is assumed to be real and approximately constant over a large spectral range; and $\chi^{(3)}_{i,j}$ is the third-order nonlinear susceptibility of the i^{th} (or j^{th}) component of the resonant contribution to the CARS signal (which can be described further by the form in Eq. 6). In this form, one can see that the Raman peaks coherently add together as well as with the NRB. Additionally, the pulsed excitation sources contribute to the shape of the CARS spectrum as described in Eq. 12; thus, the CARS spectrum is distorted in several ways from the spontaneous Raman spectrum (additionally, coupling and interference between various states can induce further distortion [56]). Figure 12 shows simulated CARS spectra of a single Raman lineshape (A = 1, $\Omega = 5.4664\times10^{14}$ rad/sec [2900 cm^{-1}], $\Gamma = 3.3\times10^{11}$ rad/sec

[1.7507 cm^{-1}], $\chi_{NR}^{(3)} = 0.5A\Gamma$) for various pump pulse widths (the peak power of each simulated source remains constant). One can see that the shortest pulses produce the strongest CARS signal, but the peak is the most distorted from the Raman lineshape and the contrast between the NRB and the resonant signal is the least. The longest pulses, on the other hand, produce the narrowest CARS spectrum with the least spectral distortion, but with the weakest aggregate signal strength. Figure 13 shows the spectral offset for the simulated peak as a function of pump pulse length under different NRB-to-resonant signal ratios ($\chi_{NR}^{(3)}/A\Gamma$) (see [52] for a similar simulated study). Additionally, the bandwidth of the pump source (multiplied by -1) is shown to compare source bandwidth (i.e., resolution) to the spectral offset.

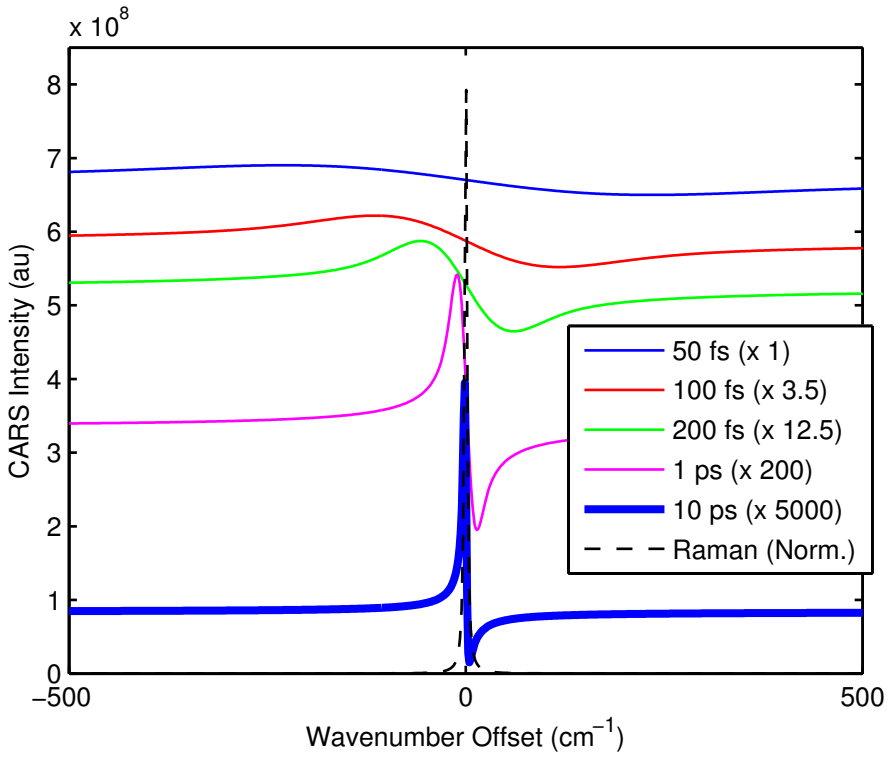

Figure 12: Simulated CARS intensity versus wavenumber offset for a simulated single Raman vibration at 2900 cm^{-1} using excitation pulses of different pump bandwidths (assuming supercontinuum Stokes source) versus a normalized Raman lineshape. The $\chi_R^{(3)}$ was modeled with A = 1, $\Omega = 5.4664 \times 10^{14}$ rad/sec (2900 cm^{-1}), $\Gamma = 3.3 \times 10^{11}$ rad/sec (1.7507 cm^{-1}).

Figure 14 is the simulated CARS (and Raman) spectrum for a molecule with 2

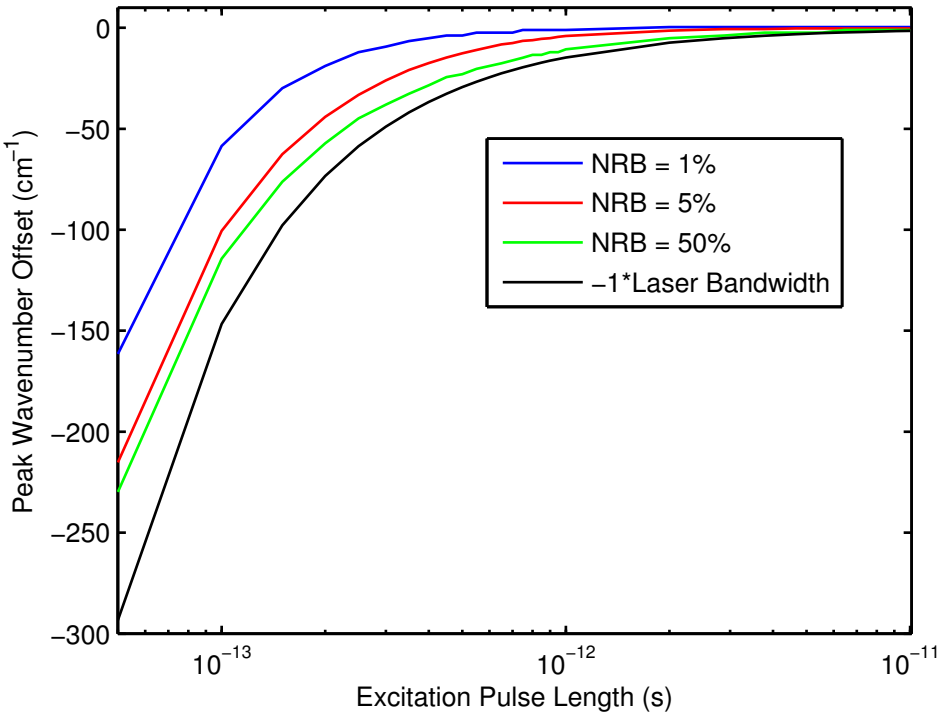

Figure 13: Simulated CARS peak wavenumber offset versus excitation pump pulse length (assuming supercontinuum Stokes source) for a simulated single Raman vibration at 2900 cm^{-1} with varying degrees of NRB strength (i.e., NRB to Raman ratio). For comparison purposes, the bandwidth of the pump pulse for a transform-limited Gaussian pulse versus pulse length is shown (black). The $\chi_R^{(3)}$ was modeled with A = 1, $\Omega = 5.4664 \times 10^{14}$ rad/sec (2900 cm^{-1}), $\Gamma = 3.3 \times 10^{11}$ rad/sec (1.7507 cm^{-1}).

isolated Raman bands at 2860 and 2900 cm^{-1} ($A_1 = A_2 = 1$, $\Omega_1 = 5.4664 \times 10^{14}$ rad/sec [2900 cm^{-1}], $\Omega_2 = 5.3910 \times 10^{14}$ rad/sec [2860 cm^{-1}], $\Gamma_1 = \Gamma_2 = 3.3 \times 10^{11}$ rad/sec [1.7507 cm^{-1}], $\chi_{NR}^{(3)} = 0.5 A_{1,2} \Gamma_{1,2}$). Similar to Figure 11, one can see spectral distortion due to the NRB, but looking at the spectrum in which the NRB is neglected, the effect of interband (i.e., Raman lineshape) interference becomes clear: both peak maxima are distorted from the actual Raman energies (asymmetrically).

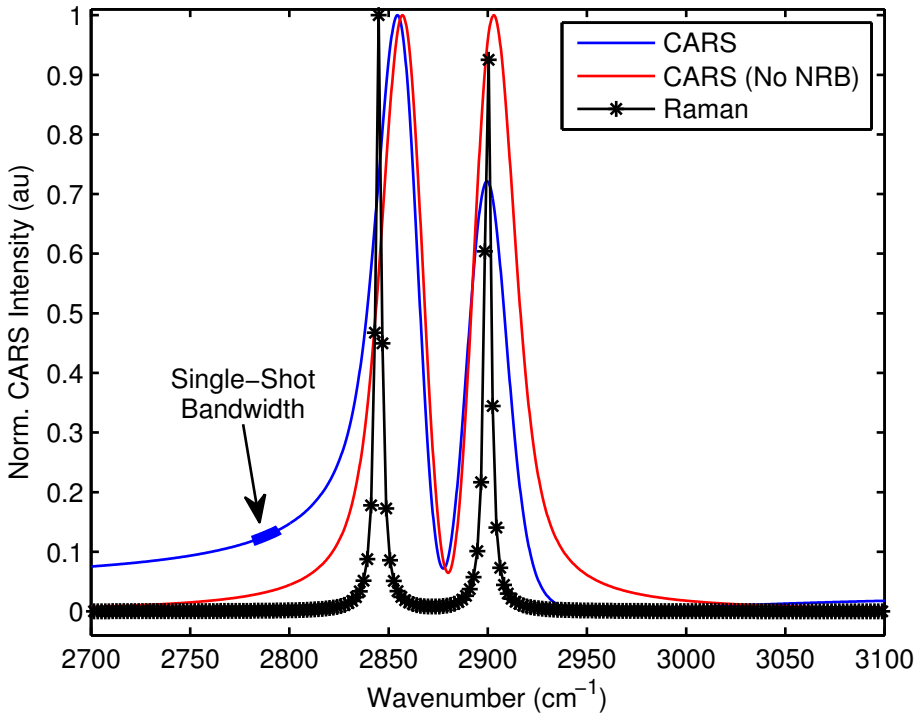

Figure 14: Simulated CARS/MCARS spectrum of a molecule with two Raman bands: one at 2900 cm^{-1} and another at 2860 cm^{-1} (black, stars) with (blue) and without (red) the effect of the NRB. The $\chi_R^{(3)}$ was modeled with $A_1 = A_2 = 1$, $\Omega_1 = 5.4664 \times 10^{14}$ rad/sec (2900 cm^{-1}), $\Omega_2 = 5.3910 \times 10^{14}$ rad/sec (2860 cm^{-1}), $\Gamma_1 = \Gamma_2 = 3.3 \times 10^{11}$ rad/sec (1.7507 cm^{-1}).

2.2.3 CARS Techniques

CARS is a powerful platform for the high-speed, label-free analysis of sample molecules. Over the last several decades, researchers have developed numerous methods for improving the CARS platform. Some of these techniques, such as epi-CARS (ECARS)

[30], polarization CARS (P-CARS) [57], and interferometric CARS (iCARS) [58], were born out of the desire to suppress the NRB in order to more clearly and selectively excite target molecular energies. Techniques such as multiplex CARS (MCARS) [51, 59] and broadband CARS (BCARS) [60] were designed to extend CARS microscopy into a microspectroscopic imaging modality that could probe a broad range of Raman energy levels simultaneously. Additionally, post-processing techniques have developed over the last several years that try to derive the equivalent spontaneous Raman spectrum from the CARS (or MCARS) spectrum; thus, removing the NRB and the associated interference effects.

2.2.3.1 Epi-CARS (ECARS)

Over the last decade, several CARS system architectures have arisen to improve the quality and sensitivity of the CARS signal. The first enhanced CARS architecture was epi-CARS (ECARS) [30, 61, 62]. In the original implementation of CARS microscopy (specifically, called forward-CARS [FCARS]; although, the designation is usually omitted in current publications), the anti-Stokes photons were collected in the forward direction relative to the excitation sources. ECARS, on the other, records the anti-Stokes photons in the backward direction through the same optics used for excitation. Under this system layout, the CARS signal recorded from the background solvent (typically, water) is greatly reduced as most of its anti-Stokes photons propagate in the forward direction. Figure 15 compares the image taken of an NIH 3T3 cell using FCARS and ECARS. One can see significantly higher contrast with the ECARS system geometry. In ECARS, the dominant CARS signal is recorded from small scatterers and from forward-propagating photons that are later scattered backwards (which may arise from reflection from a microscope coverslip, for example, or due to multiple scattering events within a turbid medium) [52]. Although the NRB from the solvent is greatly reduced in ECARS, the resonant CARS signal

is also reduced and the NRB from the Raman scatterer still exists, which maintains the spectral distortions in the recorded spectrum [30].

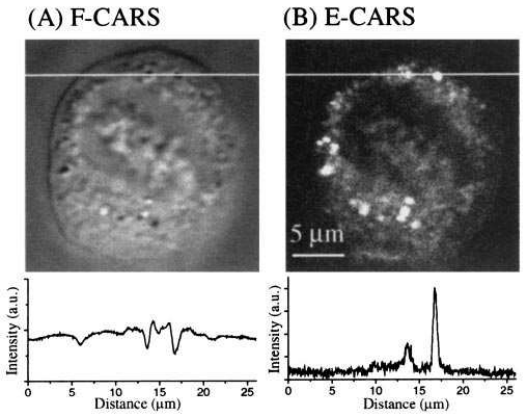

Figure 15: Comparison of the (A) F-CARS and (B) E-CARS images of a NIH 3T3 cell in metaphase and the intensity profiles along a single image row (location denoted by the white line). The sources were tuned to probe the CH stretching vibrational frequency at 2873 cm^{-1}. Reprinted from [62]. © the Biophysical Society.

2.2.3.2 Polarization CARS (P-CARS)

Another early CARS system design was polarization CARS (P-CARS) [57, 63]. In most CARS system (even today), the polarization of the pump and Stokes beams are in parallel, and the anti-Stokes photons are measured with the same polarization. In P-CARS, however, the pump and Stokes beams are linearly polarized at different angles, and a polarizer restricts the polarization of the measured anti-Stokes photons. One can describe the induced polarization of the nonresonant component in the x- and y-direction as:

$$P_x^{NR} = 3\epsilon_0 \chi_{1111}^{NR} E_p^2 E_s^* \cos\phi \tag{15}$$

$$P_y^{NR} = 3\epsilon_0 \chi_{1221}^{NR} E_p^2 E_s^* \sin\phi, \tag{16}$$

$$\tag{17}$$

respectively, where the pump, E_p is polarized along the x-axis, and the Stokes beam, E_s is polarized at an angle ϕ with respect to the x-axis. Assuming χ^{NR} is real, the

induced polarization with respect to the x-axis is polarized at an angle:

$$\alpha = \tan^{-1}\left(\frac{\chi^{NR}_{1221}}{\chi^{NR}_{1111}}\tan\phi\right). \tag{18}$$

Although the nonresonant component is linearly polarized along a particular axis, the resonant component is elliptically polarized due to the complex nature of χ^R. Under these conditions, a polarizer can be placed along the direction perpendicular to the nonresonant polarization, and a background free CARS signal can be recorded [30, 61]. Practically, however, there is a residual background due to birefringence in the system optical train and due the polarization mixing caused by the heavy focusing of the excitation objective lens. And although the contrast between the resonant and nonresonant components of the CARS signal may be greatly enhanced, the strength of the overall CARS signal may be greatly diminished [32]; thus, requiring stronger sources or longer integration times to maintain the same SNR. Figure 16 shows the comparison of CARS and PCARS imaging of polystyrene beads spin-coated onto a glass coverslip and covered with water. One can see that the PCARS images provide a large reduction in the NRB of the aqueous background, but the overall signal strength is noticeably reduced.

2.2.3.3 Multiplex CARS (MCARS)

The traditional implementation of CARS microscopy uses narrowband pump/probe and Stokes sources (typically, picosecond pulse durations) that only excite a narrow range of energies (see Figure 11, which points out the single-shot CARS bandwidth). Although this system architecture is very fast for energy level selective imaging, this technique is very slow for multispectral imaging as tuning the pump and Stokes source over a broad wavelength range is time consuming (most CARS system use a heat-tuned optical parametric oscillator [OPO] to provide one or both excitation sources). An alternative to sweeping the wavelength of the excitation sources is the multiplex CARS (MCARS) technique that uses a combination of broadband sources

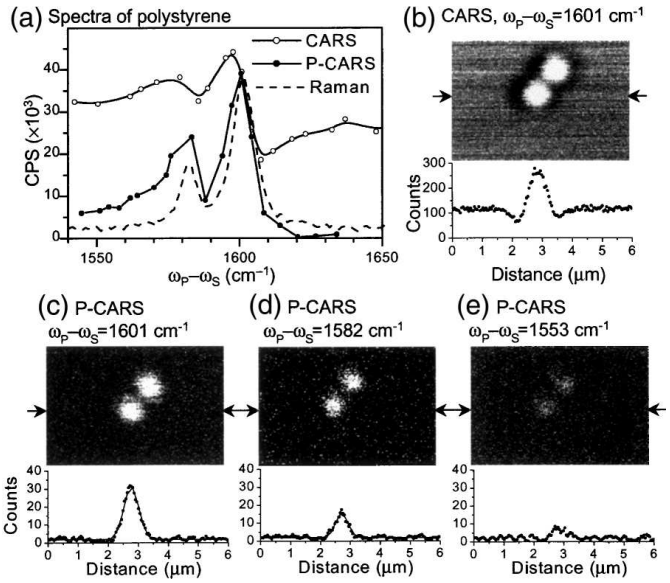

Figure 16: (a) Comparison of CARS, P-CARS (multiplied by a factor of 30), and Raman spectra of polystyrene taken from a 1 μm bead. CARS image of a 1 μm bead with the sources tuned to probe the 1601 cm^{-1} band and the CARS intensity shown for a single row of the image (location denoted by arrows). (c) P-CARS image and line profile of the same beads with the sources tuned to probe the 1601 cm^{-1} band. (d) and (e) P-CARS image and line profile of the same beads with the sources tuned to probe the 1582 cm^{-1} and 1553 cm^{-1} energy levels, respectively. Reprinted from [57]. © Optical Society of America.

to excite numerous Raman transitions simultaneously [see Figure 17(a) for the energy diagram for MCARS] [51,59,64–66]. Additionally, the MCARS system design utilizes a multielement detector, such as a charge-coupled device (CCD) spectrometer to capture full spectra, such as in Figure 11, in a single shot. Figure 18 shows a schematic of a typical MCARS system. Using a similar system, Kano was able to collect the MCARS spectra for HeLa cells with high spatial resolution as shown in Figure 19 [67].

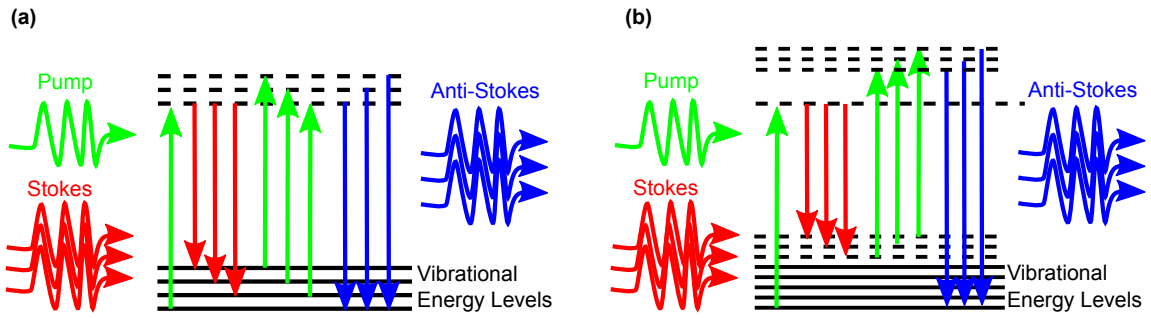

Figure 17: Energy diagram of (a) MCARS and (b) the NRB. In (a), multiple pump and Stokes photons excite the molecule into multiple higher vibrational energies, and probe photons inelastically scatter off of the excited modes. In (b), a FWM process produces photons regardless of the existence of vibrational energy levels.

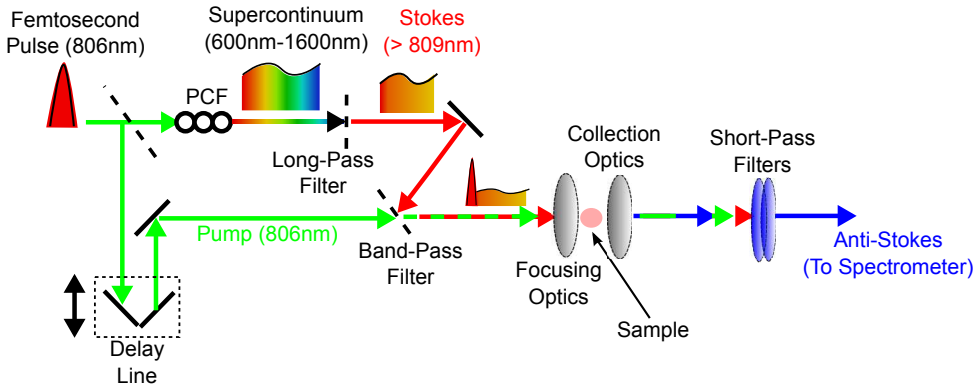

Figure 18: Schematic of a typical MCARS system that utilizes a single femtosecond laser to act as both the pump for the CARS generation process and as a seed source for a length of photonic crystal fiber (PCF) that will generate a supercontinuum for use as a broadband Stokes source. The generated anti-Stokes photons are collected in the forward direction and recorded by a CCD spectrometer.

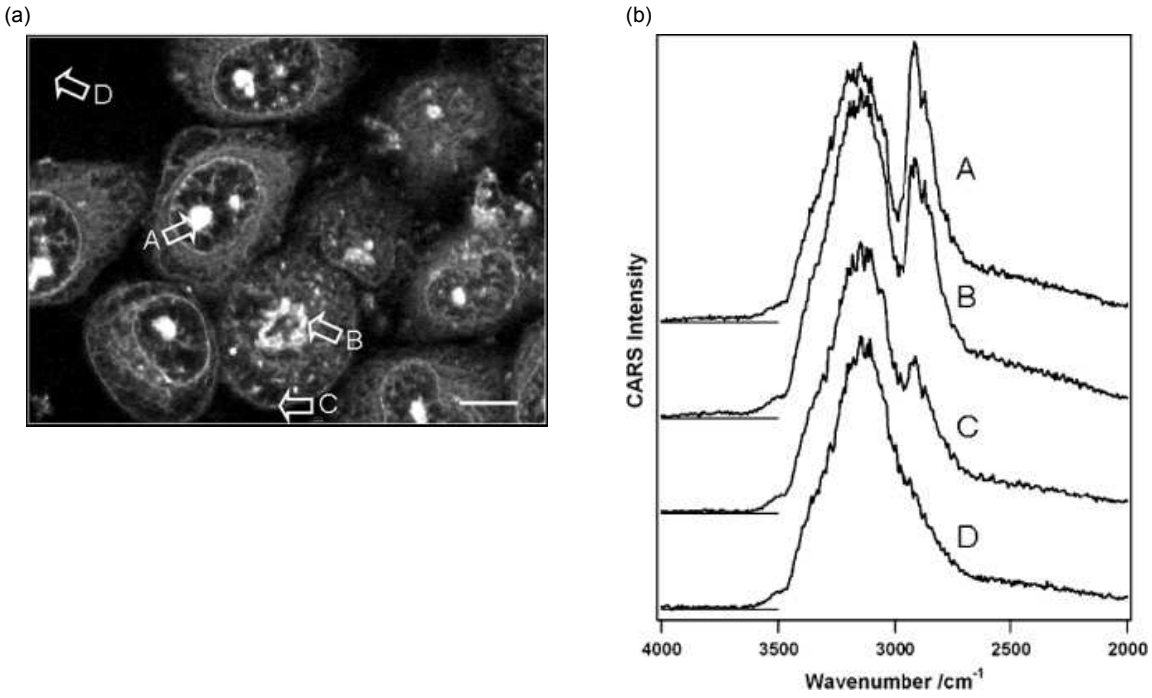

Figure 19: (a) MCARS image of HeLa cells with the pixels depicting the intensity at 2870 cm^{-1} (although a full spectrum is collected at each pixel). (b) MCARS spectra for the points A-D in (a). Reprinted from [67]. © John Wiley & Sons, Ltd..

Although MCARS provides a mechanism for microspectroscopic imaging, there are several technical challenges and limitations of the technique. First and foremost is the continued existence of the NRB. Just as with traditional CARS techniques, the excitation sources generate an NRB that coherently interferes with the anti-Stokes photons; thus, distorting and/or masking the resonant peaks. Additionally, the use of femtosecond sources in MCARS (as opposed to picosecond source in CARS microscopy) exacerbates these distortions and generates a significantly stronger NRB (as described in Section 2.2.2). Additionally, the use of a CCD spectrometer to record the anti-Stokes signal limits the acquisition speeds due to the speed of the charge transfer and analog-to-digital (A/D) circuitry within the CCD camera. Most CCD cameras operate at up to 100 - 200 spectra per second; although, manufacturers are beginning to produce faster cameras capable of several thousand spectra per second (with caveats). Additionally, many implementations of MCARS use a photonic crystal

fiber to generate a supercontinuum Stokes source. Although inexpensive and capable of producing a strong average power over a huge bandwidth, the energy density can be very low relative to CARS systems; thus, longer integration times may be necessary.

2.2.3.4 Interferometric CARS Techniques

Many CARS techniques attempt to reduce the generation of the NRB (e.g., time-resolved CARS [TCARS] [68]) or minimize its detection (e.g., PCARS [57]). Although these techniques work well, they sacrifice resonant signal strength for nonresonant signal suppression. Another method of removing the NRB is through interferometric mixing of the CARS signal with a local oscillator (LO). Some of the first approaches to this technique, called interferometric CARS (iCARS) or heterodyne CARS, were implemented by creating a double-CARS configuration in which two samples were probed simultaneously (in two independent, but identical arms) and the resulting CARS signals were combined with a beam splitter; thus, coherently mixing the two signals with the relative phase delay controlled by adjusting the length of one of the sample arms [69, 70]. In this configuration, the local oscillator arm sample is selected by virtue of having no resonant peaks within the spectral window of interest (e.g., a glass coverslip [69] or deuterated-DMSO [70]). Mathematically, the iCARS output intensity, I_{iCARS} is described as:

$$I_{iCARS} \propto |E_{LO}| + |E_{AS}| + 2E_{LO}E_P^2E_S\times \left[(\chi_{NR}^{(3)} + Re\{\chi_R^{(3)}\})cos\Phi + Im\{\chi_R^{(3)}\}sin\Phi\right], \quad (19)$$

where E_{LO} is the LO electric field, E_{AS} is the anti-Stokes electric field, E_P is the pump electric field (assuming pump and probe are degenerate), E_S is the Stokes electric field, $\chi_R^{(3)}$ and $\chi_{NR}^{(3)}$ are the nonlinear susceptibilities of the CARS process and for the NRB, respectively, and Φ is the phase differences between the CARS field and the LO [69]. By tuning the phase difference between the LO and the CARS field, the entire contribution of the NRB is removed and the CARS signal, which

is proportional to $E_P^2 E_S \chi_R^{(3)}$, is amplified. By selecting the appropriate phase delay between the LO and the CARS signal of interest, this method allows for complete separation of the resonant (Raman) and the nonresonant contributions to the spectra while amplifying the resonant signal [69, 70]. This technique has been applied to both spectroscopy (see Figure 20) and microscopy (see Figure 21). Although these

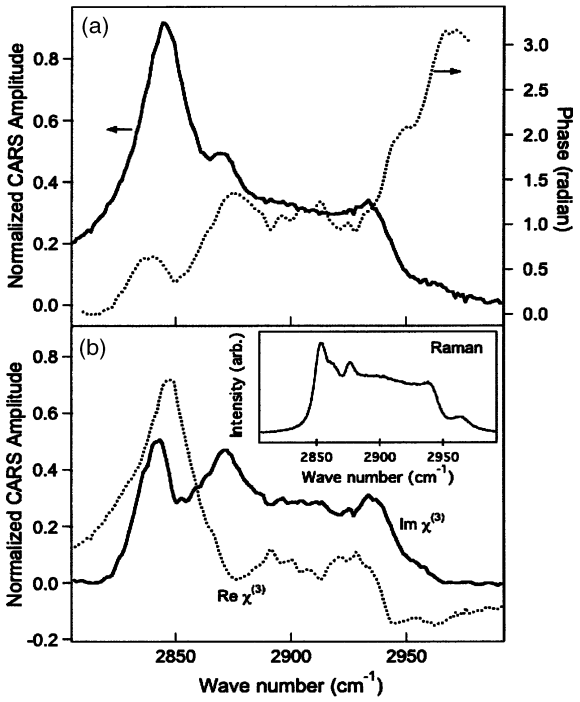

Figure 20: Normalized CARS spectral amplitude and phase of the CH-stretch vibrational band of dodecane. (a) Derived CARS amplitude (solid curve) and phase (dotted curve) from the interference spectrum. (b) The reconstructed real (dotted curve) and imaginary (solid curve) parts of the CARS spectrum. Inset, spontaneous Raman spectrum of dodecane. Reprinted from [69]. © Optical Society of America.

techniques demonstrate the ability to perform iCARS, they do so under a limited operational bandwidth. To apply the strengths of iCARS to a broader range of wavelengths, Kee, *et al.* developed an interferometric scheme built upon an MCARS system [71]. In this system, the LO was generated by producing a CARS signal in the sample with a 100 fs pulse, and the "CARS" signal was generated by using 750 fs pulse. As described in Section 2.2.2, shorter pulses generate a stronger NRB; thus, the 100 fs pulse-generated spectrum contained a significantly stronger NRB to act as

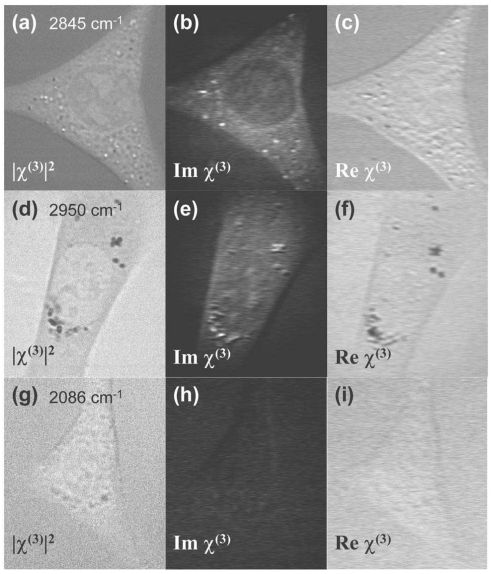

Figure 21: Comparison of heterodyne CARS with noninterferometric CARS imaging of live NIH 3T3 cells. (a) CARS image tuned to 2845 cm^1 and the extracted imaginary (b) and real (c) parts of the CARS signal using iCARS detection. (d) CARS image tuned to 2950 cm^1 and the extracted imaginary (e) and real (f) parts of CARS signal using iCARS detection. (g) CARS image tuned to 2086 cm^1 and the extracted imaginary (h) and real (i) parts of CARS signal using iCARS detection. Reprinted from [70]. © Optical Society of America.

the LO for interferometric detection. Although the LO still contained a noticeable resonant CARS contribution, the authors were capable of reasonably isolating the real and imaginary contributions to the MCARS spectrum [71].

Although the aforementioned systems were capable of demonstrating interferometric detection of anti-Stokes photons, these systems relied on samples to generate a strong LO, which may not always be possible without damaging optical intensities. An alternative approach pursued by a number of researchers relied on generating a coherent LO from the laser source(s) themselves. One method passes the pump and Stokes sources (7 ps pulse lengths) through a PCF prior to coupling into the microscope [72]. Within the PCF, FWM converted a small amount of the pump and Stokes sources into a LO at the same wavelength that the sample to be probed would generate through the CARS process. Another researcher, more simply, used an optical parametric amplifier (OPA) to generate the Stokes source as well as a blue-shifted source that acted as the LO [58]. With the creation of even shorter pulse sources (< 100 fs) that generate broad spectra, some researchers have used a single source and spectrally chopped the source into pump, Stokes, and LO signals [73–76]; although, even with these sources, only a few hundred wavenumbers can be probed simultaneously.

To pursue the possibility of truly broadband interferometric MCARS capable of probing several thousand wavenumbers, I developed the first interferometric MCARS (iMCARS) system [77]. The iMCARS system relies on a single PCF to generate both the Stokes and LO sources [77]. The iMCARS system has the same spectral coverage of wavelength-scanning systems without the added cost and complexity of multiple sources. In comparison to other single-source interferometric CARS systems, iMCARS operates over a larger bandwidth than that afforded by a spectrally divided ultrafast pulse, and iMCARS externally produces the LO; thus, LO production is not a function of the incident light on the sample. Although the iMCARS system

has certain advantages in direct comparison with other interferometric systems, this system also has its own difficulties. As with any system involving PCFs, spectral and intensity fluctuations of the output supercontinuum arise from intensity fluctuations of the seed source. These fluctuations alter pulse lengths, chirp, and spectral coverage; thus, particular care needs to be taken in stabilizing the ultrafast source.

The iMCARS system (shown schematically in Figure 22) uses an angled long-pass filter that spectrally separates the wavelengths above and below 800 nm from the supercontinuum Stokes source. The shorter wavelengths that act as the LO propagate into a delay line that allows control over the temporal overlap between the LO and the pump and Stokes sources (collectively). For initial testing, a compact horizontal microscope was constructed that focuses the pump, Stokes, and LO onto a small cuvette with an achromatic doublet. A 100x long-working distance objective (Mitutoyo, M Plan NIR 100, NA of 0.55) collects the excitation sources, LO, and anti-Stokes photons. From this objective, the beams pass through three short-pass filters as to only pass the collinear CARS and LO signals, and then they are coupled into the CCD spectrometer via a multimode fiber. The lower spectral detection limit of this system is restricted by the filter set to approximately 1400 cm^{-1}, and the upper limit theoretically extends beyond 4000 cm^{-1}.

In the ideal iMCARS system, the LO coherently interferes with the anti-Stokes photons, amplifies the MCARS spectrum, and appropriate filtering in post-processing removes the contributions from the LO. Unfortunately, it proved difficult in experiments to entirely remove the LO from the output spectrum as the interference fringes were very small due to weak coherency between the LO and anti-Stokes photons. Additionally, instability of the PCF source created amplitude and phase instability in the output spectrum. Additionally, chirp in the pump, Stokes, and LO reduced the coherence bandwidth. To compensate for the instability and chirp, the LO was temporally swept and several spectra were collected. Mathematically, this process is

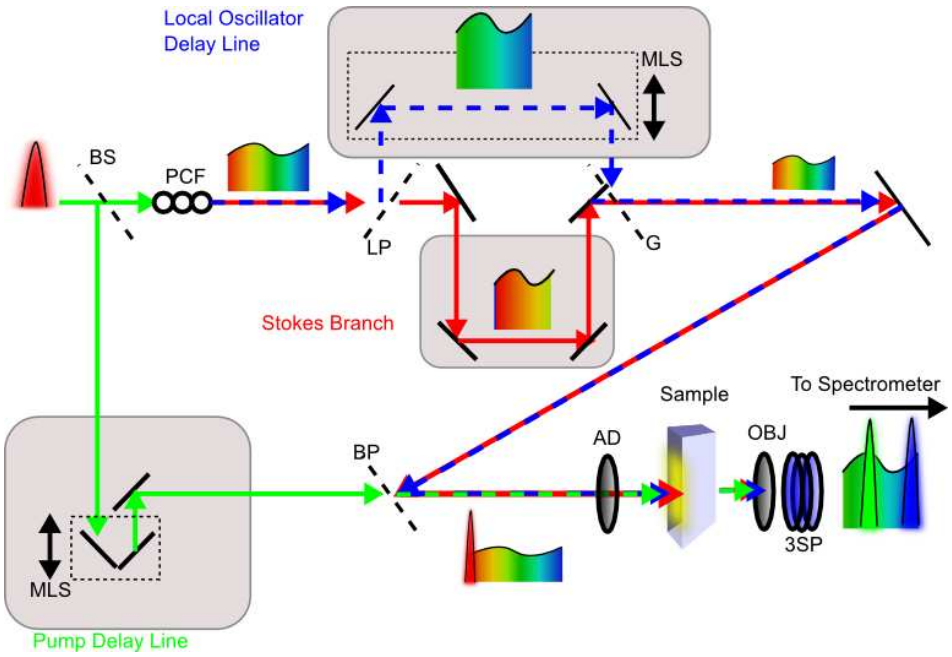

Figure 22: The iMCARS system uses a femtosecond source to seed the PCF for Stokes and LO generation as well as to provide the pump for the CARS process. Two delay lines provide independent temporal control of the pump and LO. BS, beamsplitter; PCF, photonic crystal fiber; LP, long-pass filter; MLS, motorized linear stage; G, optical glass flat; BP, band-pass filter; AD, achromatic doublet; 3SP, 3 short-pass filters; OBJ, objective lens; Spec, CCD spectrometer. From [68].

described as:

$$I_{iMCARS}(\lambda, d) = A(\lambda)^2 + L(\lambda)^2 + 2A(\lambda)L(\lambda)cos\left(\phi(\lambda) + \frac{2\pi}{\lambda}d\right), \tag{20}$$

where I_{iMCARS} is the interference spectral intensity at wavelength λ collected with the LO absolutely temporally displaced by an equivalent length d from the CARS pulse. Additionally, $A(\lambda)$ is the CARS field spectrum, $L(\lambda)$ is the LO field spectrum, and $\phi(\lambda)$ is the intrinsic phase difference between the CARS and LO fields. Assuming the LO is much stronger than the CARS signal, and the LO and CARS pulses are displaced by much greater than the wavelength, the DC terms and LO contribution to the cross-terms can be isolated via low-pass filtering. Collecting several spectra at different temporal displacements between the CARS and the LO pulses, removing the LO contribution, and adding the remaining terms in quadrature reconstructs the CARS spectrum, I_{CARS}:

$$\begin{aligned} I_{CARS}(\lambda) = & \\ & \left|\sum_i 2A(\lambda)cos\left[\phi(\lambda) + \frac{2\pi}{\lambda}(d_i + d_0)\right]cos\left(\frac{2\pi}{\lambda}d_i\right)\right|^2 \\ + & \left|\sum_i 2A(\lambda)cos\left[\phi(\lambda) + \frac{2\pi}{\lambda}(d_i + d_0)\right]sin\left(\frac{2\pi}{\lambda}d_i\right)\right|^2 \\ & \approx N^2|A(\lambda)|^2. \end{aligned} \tag{21}$$

In Eq. (21), N is the number of spectra collected. The absolute temporal delay expressed in equivalent length, d, from Eq. 20 is separated into two terms: d_0, an unknown initial displacement, and d_i, the offset of the LO delay line (as retrieved from the linear stage encoder) for the i^{th} collected spectrum. Additionally, appropriate low-pass filtering (in the Fourier domain) removes the remnant oscillations of the uninterfered MCARS spectrum.

To demonstrate the capability of the system to interferometrically detect multiple

Raman transitions through the C-H stretch region (2800 - 3000 cm^{-1}) simultaneously, a sample of liquid methanol was examined. The delay line swept the LO [see Figure 23(a)] over a delay of 4 fs (35 steps) while the spectrometer recorded interference spectra. Post-processing removed the contribution from the LO [see Figure 23(b)]. As shown in Figure 24, the reconstructed locations of the symmetric (2821 cm^{-1}) and anti-symmetric (2940 cm^{-1}) methyl-stretch bands closely coincide with those found in the MCARS spectrum taken with the same integration time averaged over 35 spectra.

Although the iMCARS system demonstrates a modicum of success with effectively

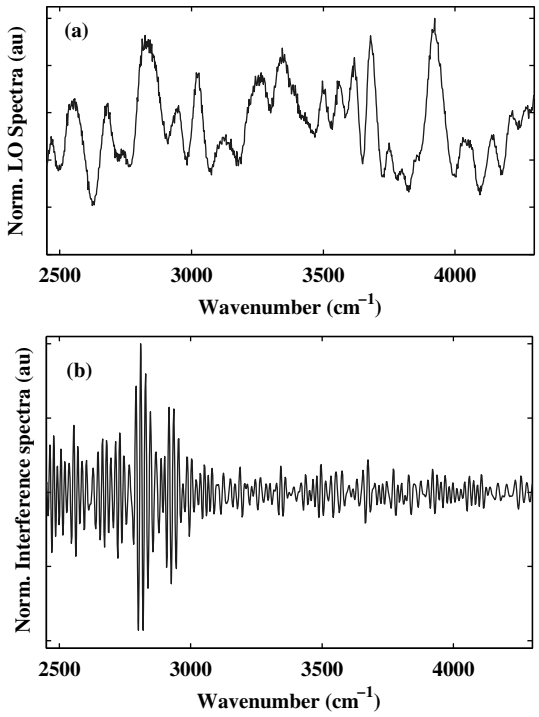

Figure 23: From each collected iMCARS spectrum, low-pass filtering isolates the LO (a). The CARS spectrum is reconstructed from the remaining interference spectrum (b). From [68].

amplifying the CARS signal and removing the NRB, because it requires temporal scanning to reconstruct the MCARS spectrum, it could not realistically be used for high-speed microscopy and flow cytometry.

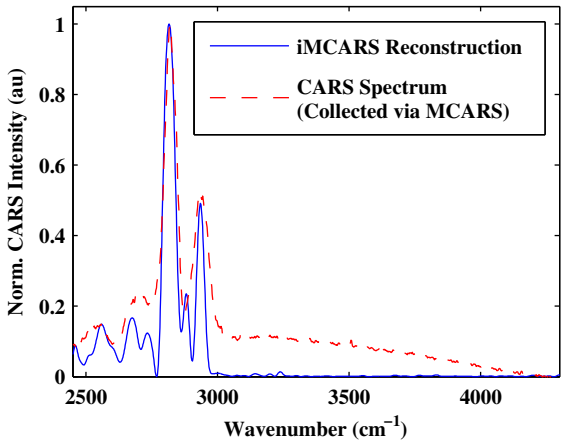

Figure 24: The CARS spectrum (dashed, red) and reconstructed iMCARS spectrum (solid, blue) of methanol normalized to peak intensity. The iMCARS reconstruction closely resembles the CARS spectrum with respect to peak locations and relative intensities with the additional benefit of reduced NRB. From [68].

2.2.3.5 Post Processing Techniques

As described in Eq. (14), the removal of the NRB is not simply a matter of subtraction or division of a nonresonant spectrum. As discussed in the previous subsection, there are physical mechanisms of removing or mitigating the effects of the NRB, but these techniques may be technically challenging, involve costly and complex systems, and they often reduce the strength of the resonant CARS system. An alternative method of removing the NRB is through numerical post-processing methods. As a numerical method, these techniques require no alterations to the optical hardware and are relatively easy to implement (although development, implementation, and processing times may be large). The numerical Raman reconstruction algorithms aim to retrieve the imaginary part of the CARS spectrum as to reconstruct the spontaneous Raman spectrum. In performing this action, these techniques not only diminish or remove the nonresonant contribution to the CARS signal, but also provide a spectrum that is linearly dependent on scatterer concentration (as in the case of Raman spectroscopy) as opposed to the quadratic dependence of CARS. The linear scatterer concentration dependence facilitates the quantitative analysis of samples with the speed and

power of CARS (MCARS) microspectroscopy. The two most popular and prevalent numerical techniques are the maximum entropy method (MEM) reconstruction technique developed by Vartiainen, *et al.* [78–81], and the Kramers-Kronig reconstruction technique developed by Liu, *et al.* [82].

The MEM uses a Fourier series approximation for the CARS (MCARS) lineshape as [79–81]:

$$S_{CARS} = \frac{|\chi^{(3)}_{NR} + \chi^{(3)}_{R}(\omega_{as})|^2}{|\chi^{(3)}_{NR,ref}|^2} \simeq \left| \frac{\beta}{1 + \sum_{k=1}^{M} a_k \exp(-2\pi j k \nu)} \right|^2 = \left| \frac{\beta}{A_M(\nu)} \right|^2, \quad (22)$$

where $\chi^{(3)}_{NR}$ is the NRB that is real and frequency independent, $\chi^{(3)}_{R}(\omega_{as})$ is the resonant contribution to the CARS signal, $\chi^{(3)}_{NR,ref}$ is a normalization term, and ν is a normalized frequency defined as:

$$\nu = \frac{\omega_{as} - \omega_{min}}{\omega_{max} - \omega_{min}}, \quad (23)$$

where ω_{min} and ω_{max} are the minimum and maximum limits of the CARS (MCARS) spectrum. β and $A_M(\nu)$ are found by solving a linear set of equations of the form:

$$\begin{bmatrix} C_0 & C_1^* & \cdots & C_M^* \\ C_1 & C_0 & \cdots & C_{M-1}^* \\ \vdots & \vdots & \ddots & \vdots \\ C_M & C_{M-1} & \cdots & C_0 \end{bmatrix} \begin{bmatrix} 1 \\ a_1 \\ \vdots \\ a_M \end{bmatrix} = \begin{bmatrix} |\beta|^2 \\ 0 \\ \vdots \\ 0 \end{bmatrix}, \quad (24)$$

where the coefficients, C_m, are solved by the Fourier transform of the CARS lineshape at discrete frequency components:

$$C_m = \frac{\sum_{n=1}^{M-1} S(\nu_n) \exp(2\pi j m \nu_n)}{M}. \quad (25)$$

With the arguments for β and $A_M(\nu)$, one can approximate the spectrum through:

$$\chi^{(3)}_{NR} + \chi^{(3)}_{R}(\nu) = \sqrt{S_{CARS}(\nu)} \exp[j\theta(\nu)] \simeq \frac{|\beta| \exp[j\theta(\nu) - j\psi(\nu)]}{A_M(\nu) \exp[-j\psi(\nu)]}, \quad (26)$$

where $\theta(\nu)$ is the phase (to be estimated) of the CARS spectrum, and $\psi(\nu)$ is the so-called maximum entropy phase that is treated as a background phase (i.e., fitting

parameter). Using these relations one approximates the Raman lineshape, $S_{Raman}(\nu)$, as:

$$S_{Raman} \simeq \sqrt{S_{CARS}(\nu)}\sin(\theta). \tag{27}$$

Figure 25 demonstrates the MEM Raman reconstruction of a sample of 1,2-dimyristoyl-sn-glycero-3-phosphocholine (DMPC) small, unilamellar vesicles (SUVs) [80].

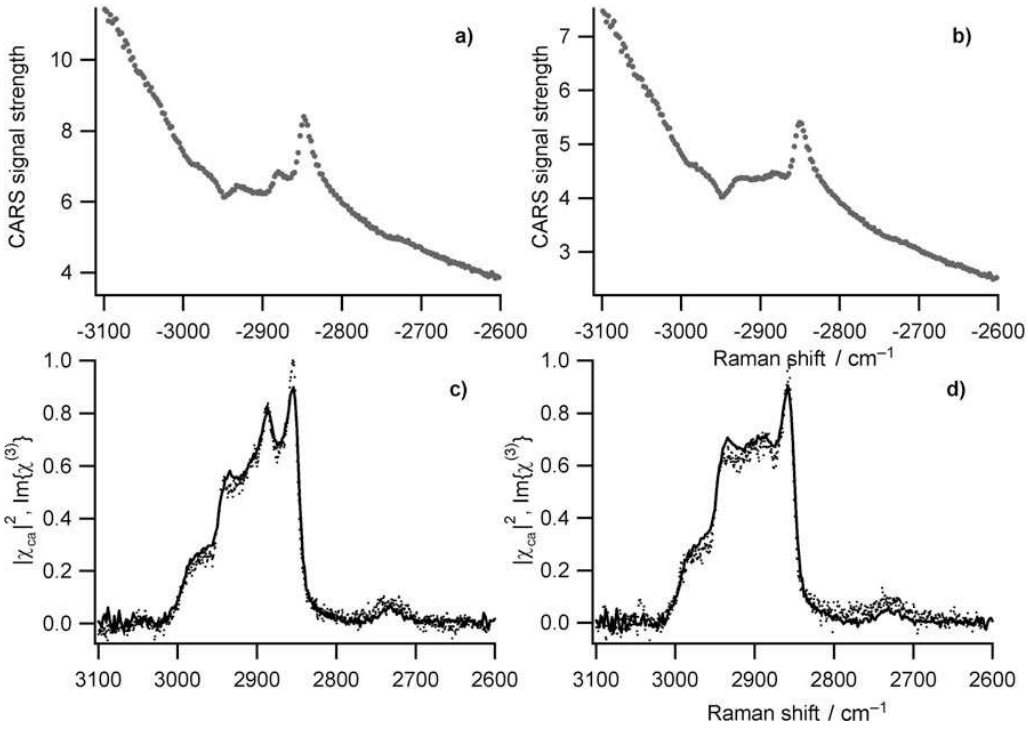

Figure 25: Measured MCARS spectra of a 75 mM DMPC vesicle suspension at 15.8^o C (a) and 30^o C. (c) and (d) are the corresponding reconstructed Raman spectra (solid lines) and the measured Raman spectra (dots) of (a) and (b), respectively. Reprinted from [80]. © Wiley-VCH Verlag GmbH & Co. KGaA, Weinheim

An alternative approach to Raman reconstruction is through a modified Kramers-Kronig (KK) transform [82]. Unlike most applications of the KK relation to nonlinear spectroscopic modalities (such as CARS/MCARS), the modified KK relation relaxes the condition that the impulse response of the system rises like a step-function at t = 0. The relaxation is justified by the fact that in CARS the triggering pulse (i.e., the probe pulse) has a defined bandwidth, the resonant response is complex but the nonresonant contribution is entirely real, and the nonresonant response is not

actually a constant, but rather reflects the convolution of the pump and Stokes pulses (in time) [82]. Under these conditions the phase, $\phi(\omega)$, of the response function, $\chi(\omega)$, using the KK relation is approximated by:

$$\phi(\omega) = -\frac{P}{\pi}\int_{-\infty}^{\infty}\frac{\ln|\chi(\omega'')|}{\omega''-\omega}d\omega'' \simeq 2\Im\left\{\Psi\{\ln|\chi(\omega)\}|\right\} - \frac{\ln|\chi(\omega)|}{2}, \tag{28}$$

where P is the Cauchy principal value and $\Psi\{f(\omega)\}$ is an operator that is defined as (for a generic frequency-dependent function $f(\omega)$):

$$\Psi\{f(\omega)\} = \mathcal{F}\begin{cases}\mathcal{F}^{-1}\{f(\omega)\}, & t \geq 0\\ \mathcal{F}^{-1}\{f_{NR}(\omega)\}, & t < 0,\end{cases} \tag{29}$$

where $f_{NR}(\omega)$ is the nonresonant contribution to the system response (i.e., derived only from $|\chi_{NR}|$). Solving for the system phase, $\phi(\omega)$, one can solve for the imaginary component of $\chi(\omega)$, which is proportional to the spontaneous Raman susceptibility:

$$\chi_{Raman} \propto \Im\{\chi(\omega)\} = |\chi(\omega)|\sin[\phi(\omega)]. \tag{30}$$

Figure 26 demonstrates the extraction of the Raman response from the experimental CARS spectrum of benzonitrile [82].

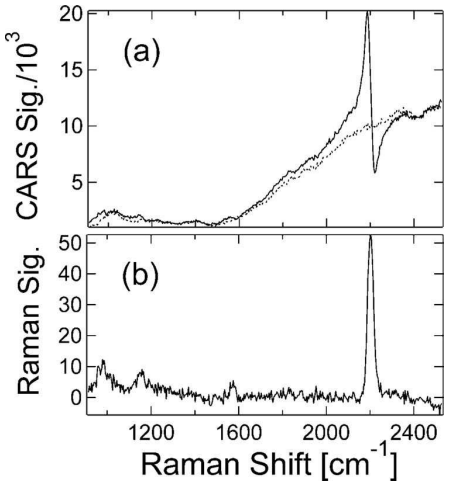

Figure 26: (a) Measured MCARS spectrum of benzonitrile in ethanol at a concentration of 1 M (solid) and a measured NRB (dotted). (b) Raman reconstruction using the KK algorithm. Reprinted from [82]. © Optical Society of America.

CHAPTER 3

SYSTEM DEVELOPMENT OF MULTIPLEX COHERENT ANTI-STOKES RAMAN SCATTERING FOR LABEL-FREE FLOW CYTOMETRY

Flow cytometry systems have relied on elastic scattering measurement and fluorescence detection for over 50 years [1]. The application of MCARS spectroscopy to flow cytometry provides a new paradigm in flow cytometry investigation as it provides the rich molecular information contained within the Raman vibrational energy levels of intrasample molecules. This section presents the design concepts and development of the MCARS flow cytometer. The first section describes the development of the backbone of the system, namely, the MCARS microspectrometer. The second section describes the fluidic subsystem. The third section describes the complete MCARS flow cytometer, and the final section describes the electronics and software that acquire, synchronize, pre-process, and gate the data.

3.1 MCARS Spectroscopy System

The backbone of the label-free MCARS flow cytometer is an MCARS microspectrometer that I originally developed to acquire multispectral, microscopic images (a simplified, 3D schematic of the MCARS system is shown in Figure 27). A complete schematic of the system is shown in Figure 28. In this system, a single femtosecond laser provides the pump for the CARS process and a seed source for a length of PCF that will generate the broadband supercontinuum for use as the Stokes source. Figure 29 shows a picture of the optical train of the MCARS system in which the

femtosecond source is split between the pump and seed sources. The thin beamsplitter (specifically designed for ultrafast sources to minimize dispersion) along with a waveplate provides a mechanism for controlling the power splitting ratio between the pump and seed sources. The pump beam is routed through two lenses forming a telescope that allows for an amount of correction of the beam divergence (although the beam divergence out of the laser is relatively small, the beam width is considerably larger after traversing the system $\sim$2 m path length). The pump beam is then routed through a delay line (constructed from an open retroreflector mounted on a motorized stage that is computer-controlled) that controls the temporal overlap between the pump and Stokes sources. After the delay line, the pump beam is incident upon a narrow bandpass filter that spectrally narrows the pump to a full-width, half-max (FWHM) of < 3 nm (Maxline, Semrock, Inc, Rochester, NY). The seed source is steered by several mirrors towards the PCF fiber (FemtoWHITE 800, NKT Photonics [formerly Crystal Fibre], Birkerød, Denmark). Figure 30 is a picture of the optical train used to steer, control, and couple the seed source into the PCF. A waveplate allows for precise control of the incident polarization as the PCF is a polarization-maintaining fiber; thus, the most efficient supercontinuum generation is formed when the polarization axis of the source and fiber align. A 60x objective lens couples the seed source into the PCF that is mounted on a 3D stage. Through an interplay of nonlinear effects, the $\sim$7.5 nm bandwidth seed source is converted into a supercontinuum that spans over 1000 nm [21, 83, 84]. As shown in Figure 31, the broadband source is coupled from the PCF using a 40x objective lens that is mounted on a linear stage (providing a means to not only fine-tune the output coupling efficiency, but to also control the beam divergence to closely match that of the pump beam). The supercontinuum is long-pass filtered to remove wavelengths below the pump wavelength that would act only to obscure (and to possible interfere with [77]) the anti-Stokes spectrum. The Stokes source is routed by several mirrors

toward the bandpass filter that is used to spectrally narrow the pump source. In this geometry, the bandpass filter acts as a notch filter for the Stokes source (reflective) and as a bandpass filter for the pump. The Stokes source and pump source are spatially aligned as to be collinear after their respective reflection and transmission from/through the bandpass filter. Several more mirrors route the beams into the inverted microscope (a more detailed picture will be presented in Section 3.3). The microscope focuses the incident beams through microscope objective (available magnifications: 10x, 20x, 40x, 60x, and 100x [oil immersion]) onto the sample, which is typically mounted on a microscope coverslip that rests on a home-built piezo stage that provides $\sim$30 nm incremental motion in two dimensions. The output light is collected in the forward direction by an objective lens (selected to match the NA of the focusing objective lens) that collimates the beams and directs them onto a series of short-pass filters (typically, two; although, in earlier development of the system, three were used before a more effective filter set was implemented). These short-pass filters remove the pump and Stokes sources and permit only the anti-Stokes photons to propagate. The anti-Stokes photons are collected by a collimator tip that couples the beam into a multimode fiber (100 - 500 μm core) that is attached to an imaging F number (F/#) matcher (Oriel Imaging F/# Matcher, Newport-Stratford [formerly Oriel Instruments], Stratford, CT) . The F/# matcher matches the NA of the fiber (approximately) to the NA of the spectrograph to improve coupling efficiency. The spectrograph is a dual-turret design that allows for mounting two different gratings (MS-260i, Newport-Stratford, Stratford, CT). Additionally, the turret, through rotation, allows for a user-selectable center wavelength. Also, the user can control the input slit width which affects the effective resolution and the intensity incident on the detector (N.B., typically, the spectrograph, when used with a 600/mm grating, is operated with a 500 μm slit, which maximizes the detected signal while maintaining the spectral resolution afforded by the laser sources). The spectrometer detector is a

1024 x 256 pixel CCD chip (front-illuminated, open electrode) with thermo-electric (TE) cooling down to -80^o C (InstaSpecX, Newport-Stratford, Stratford, CT). The technical specifications for this camera (for both the fast- and slow-A/D circuitry) is shown in Table 2. Table 3 provides the technical specifications of the MCARS microspectrometer system.

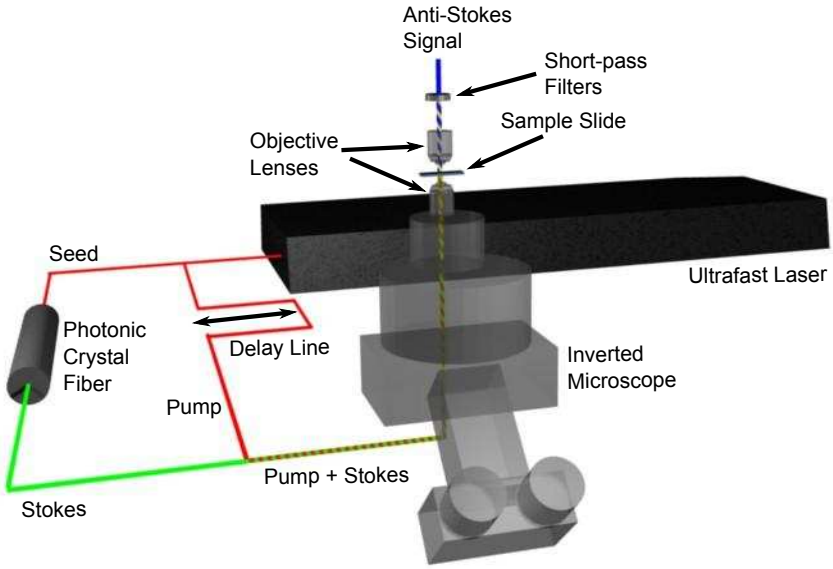

Figure 27: Simplified schematic of the MCARS microspectrometer. A femtosecond laser acts as both the pump for the CARS generation process and as the seed source for a length of PCF that produces the supercontinuum Stokes source. A stack of 3 short-pass filters spectrally separates the anti-Stokes photons from the pump and Stokes beams. A fiber coupler collects the filtered signal, and a multimode fiber transmits the anti-Stokes signal to a CCD-equipped spectrometer (not shown).

One of the first images taken with the MCARS microspectrometer was that of polystyrene (PS) beads mixed with canola oil. A drop was placed on a microscope coverslip, and the sample was raster scanned over an 85 x 85 μm area in ~15 minutes (0.5 s per pixel). A 40x objective focused the excitation sources on the sample, and another 40x objective collected the output beams. The peak anti-Stokes signal at $\sim$ 2850cm^{-1} for the canola oil and the peak at $\sim$ 3030cm^{-1} for PS [see the individual spectra of PS and canola oil in Figure 32(a)] were used to isolate the

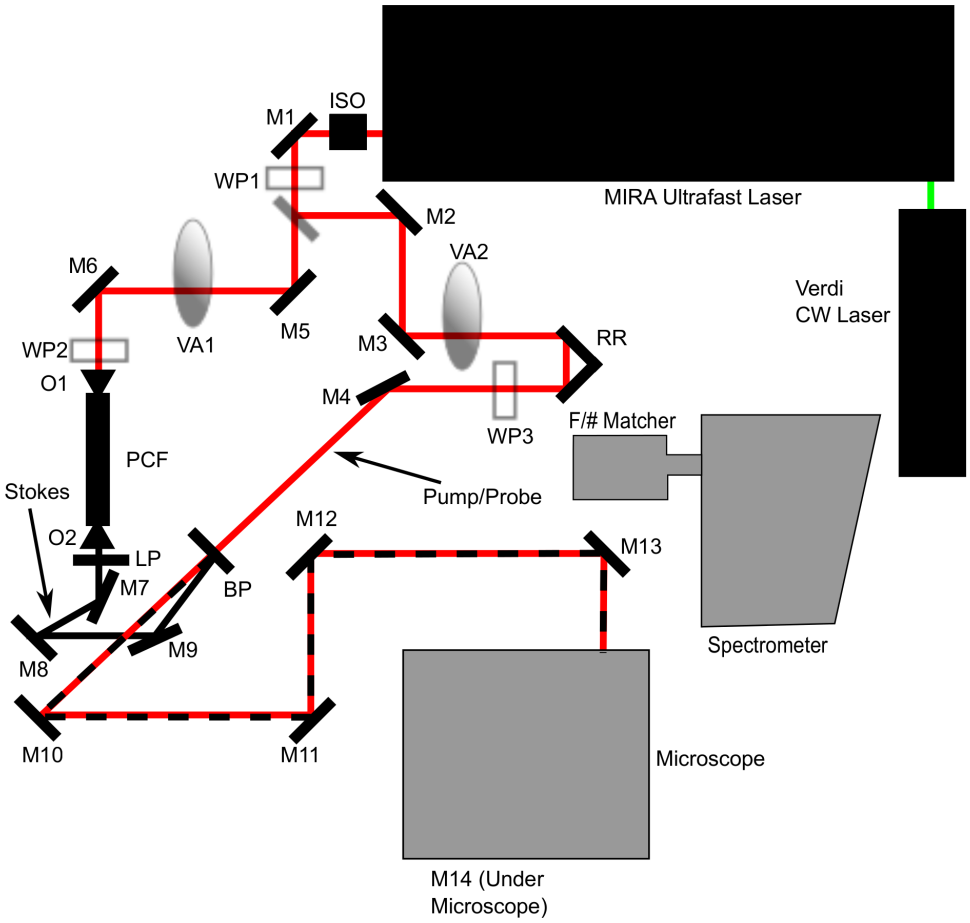

Figure 28: Schematic of the MCARS microspectrometer and flow cytometer optical train. M1-14, mirrors; WP1-3, waveplates; VA1-2, variable attenuators; O1-2, objective lenses; ISO, isolator; PCF, photonic crystal fiber; BP, band-pass filter; LP, long-pass filter; RR, retroreflector. The output light from the microscope is filtered and couples into a multimode fiber (not shown) that connects to the spectrometer through an F/# matcher.

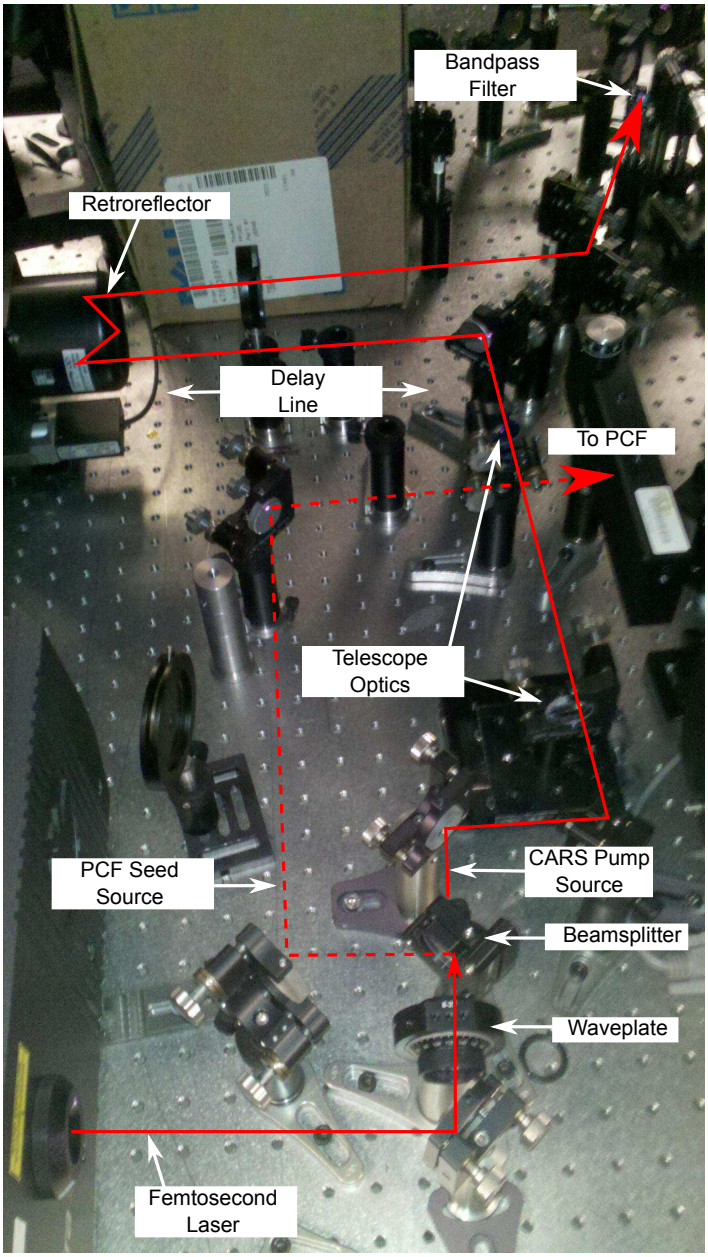

Figure 29: Image of the optical train providing the pump source and the seed to the PCF, which will generate the broadband supercontinuum. The output of the ultrafast laser is split by a 50/50 beamsplitter; thus, providing the seed and pump sources. The pump source is routed through a delay line to enable fine-tuning of the temporal overlap between the pump and Stokes sources. The seed source is directed through a variable attenuator and coupled into the PCF.

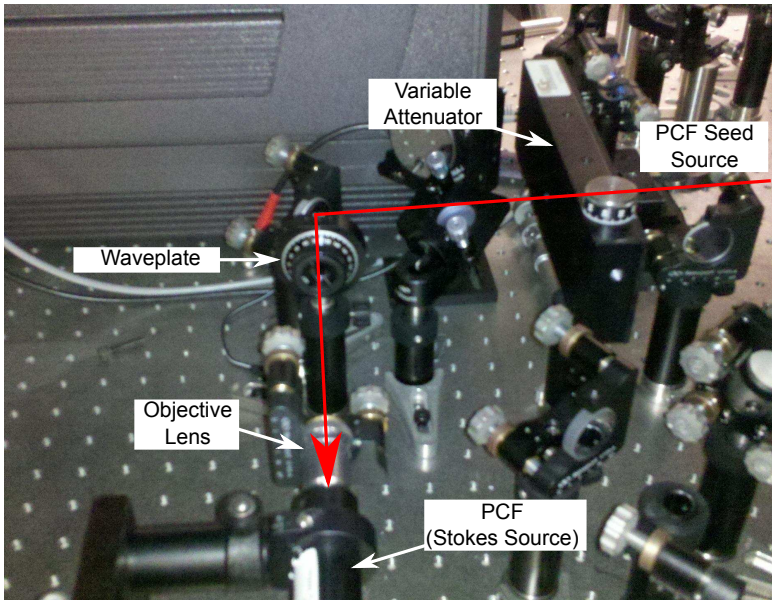

Figure 30: Image of the seed source coupling into the PCF.

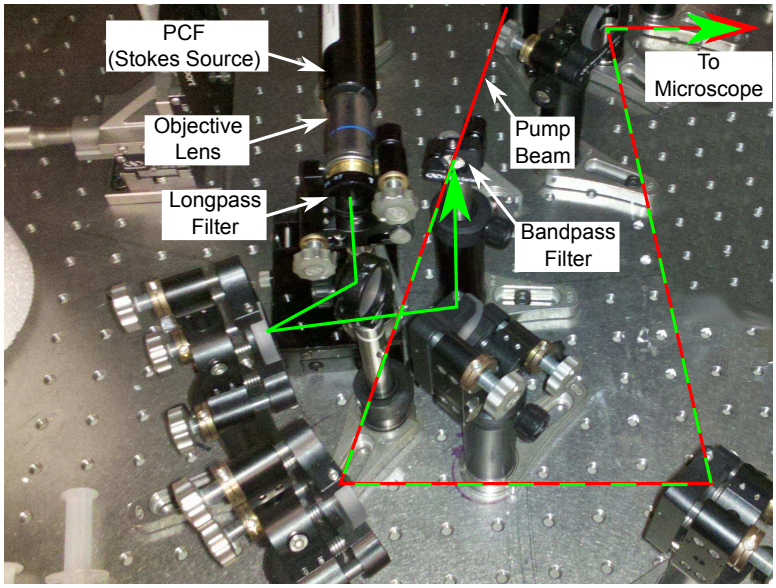

Figure 31: Image of the Stokes source (PCF) output and the recombination of the Stokes and pump sources. The supercontinuum output of the PCF is long-pass filtered, and several mirrors steer the beam onto a narrow bandpass filter. At the bandpass filter, the pump source propagates through and is spectrally narrowed ($<$ 3 nm full-width half-maximum [FWHM]), and the Stokes source, from the opposite direction, is reflected (with the pump-equivalent wavelengths propagating through). The pump and Stokes sources are then routed toward the microscope by several steering mirrors.

Table 2: CCD camera specifications for the MCARS spectrometer system.

Parameter	Value	Units
Wavelength Range	200-1000	nm
Pixel Size	26 x 26	μm
Dark Current (-75^o C)	0.001	e/pixel/s
Read Noise (Slow A/D)	6	e rms
Read Noise (Fast A/D)	24	e rms
Dynamic Range	16	bits
Acquisition Rate (Slow A/D)	54.9	Hz
Acquisition Rate (Fast A/D)	104	Hz
Electronic Gain (selectable)	3, 6, 12	e/count

Table 3: Specification of the MCARS microspectrometer system.

Parameter	Value	Units
MIRA Wavelength	$\sim$806	nm
MIRA Pulse Duration	$<$125	fs
MIRA Pulse Bandwidth	$\sim$8	nm
Stokes Wavelength	850 - 1600	nm
Pump Bandwidth (at sample)	$\sim$3	nm
Pump Power (at sample)	1-50	mW
Stokes Power (at sample)	1-40	mW
Maximum Spectral Record Rate	100	spectra/s
Maximum Sample Stage Range	12.5	mm
Minimum Sample Stage Incremental Motion	$\sim$30	nm
Typical Image Rate (40x40 pixels)	0.5 - 15	min
Single-Shot Bandwidth (grating dependent)	$\sim$84, $\sim$170	nm
Spectrometer Resolution (grating dependent)	$\sim$0.08, $\sim$0.17	nm

contributions from PS and canola oil. Figure 32(b) shows the pseudocolor image of the PS beads (red) in canola oil (blue). As a result of the coloring scheme, pixels that contain contributions from both are purple. Due to refractive effects and destructive interference of the anti-Stokes signal, the areas around the edge of the bead contain no signal [31].

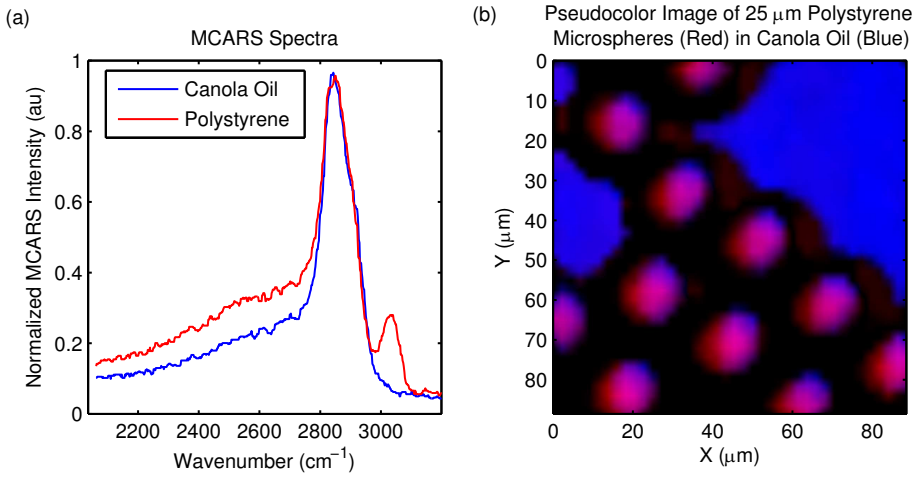

Figure 32: (a) MCARS spectrum of canola oil (blue) and polystyrene (red). (b) Pseudocolor image of 25 μm PS beads mixed with canola oil. Image acquisition required $\sim$15 minutes with a 0.5 s integration time per pixel.

3.2 Microfluidics

The MCARS flow cytometer relies on a glass microfluidic chip (Microfluidic Chip, Translume, Inc., Ann Arbor, MI) to act as the flow cell for sample analysis. The flow cell provides three input ports (300 x 100 μm [width x height]) and a single output port (300 x 100 μm). Each of the input ports are connected to a syringe mounted on a syringe pump (PHD 2000, Harvard Apparatus, Holliston, MA), which allows precise flow control. In this system two ports are used to provide a sheath flow and one port loads the sample suspension. By selecting which ports connect to the sheath syringes and which connects to the sample syringe, the flow characteristics are controllable. To efficiently focus the sample solution into a focused stream, two hydrodynamic methods have been used with this system: hydrodynamic focusing and hydrodynamic herding. Hydrodynamic focusing applies high-speed sheath flows to the two lateral ports of the microfluidic chip, and the sample is pumped into the axial port [see Figure 33(a)]. This mechanism focuses the sample into a small central stream. The force applied by the syringe pump and the ratio of the cross sectional area of the sheath and sample syringes determines the focused stream width and flow speed. Hydrodynamic herding, on the other hand, places the sheath flow on 1 lateral port and on the axial input port. The remaining lateral port receives the sample flow [see Figure 33(b)]. This focusing method forces the samples to flow along the side wall; thus, minimizing lateral deviation of the sample stream due to perturbations (e.g., pulsation) in the sheath and sample flow characteristics [85–87]. Due to the direct contact of the sample with the glass sidewall, however, the samples may adhere to the glass.

In commercial flow cytometers, the sample and sheath flows are independently controllable, but in the developed flow cytometer, a single syringe pump is used; thus, the flow characteristics are controlled by selecting different sized syringes for the sample and sheath flows. To calculate the flow characteristic of the flow channel, I

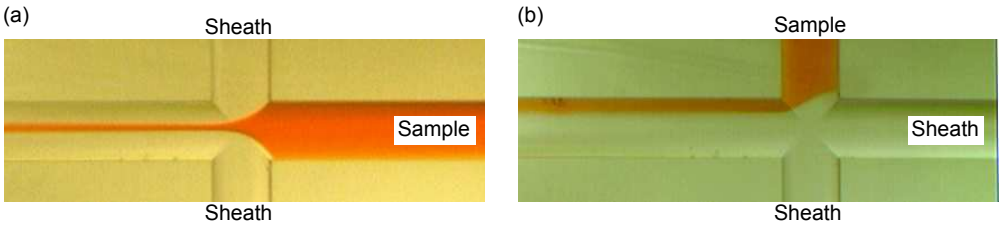

Figure 33: Images of red dye flowing through a glass flow cell. (a) Demonstrates hydrodynamic focusing in which syringes pump the sheath fluid through both lateral ports and the sample through the axial input port. (b) Demonstrates hydrodynamic herding in which the syringe pump pumps the sheath fluid through one lateral port and the axial input port and the sample through the other lateral port.

applied the mathematical formulation of [88] to the flow chip geometry (see Figure 34). Specifically, one begins with the principle of mass conservation, which in this context states that the total amount of fluid entering the system must equal the total amount of fluid leaving the system:

$$Q_o = Q_i + 2Q_s = \overline{v_o} \times w_o \times h, \tag{31}$$

where Q_o, Q_i, and Q_s are the output, sample input, and [individual] sheath input volumetric flow rates; $\overline{v_o}$ is the average stream-wise velocity of the output; and w_o and h are the width and height of the output channel, respectively. Additionally, the amount of sample flow entering the system is the same as the amount of fluid exiting through the focused stream:

$$Q_i = \overline{v_f} \times w_f \times h, \tag{32}$$

where $\overline{v_f}$ is the average velocity of the focused stream at the output, and w_f is the width of the focused sample stream. From these equations, the ratio of the focused stream width, w_f, to the output stream width, w_o, is

$$\frac{w_f}{w_o} = \frac{Q_i}{\gamma(Q_i + 2Q_s)}, \tag{33}$$

where a new parameter γ has arisen and is defined as the ratio of the average stream-wise velocity of the focused stream to the average stream-wise velocity of the output

channel:

$$\gamma \triangleq \frac{\overline{v_f}}{\overline{v_o}}. \tag{34}$$

For systems under laminar flow (i.e., low Reynolds number) with incompressible, Newtonian fluids, the fluid motion is governed by the Navier-Stokes Equation as:

$$\frac{\partial^2 u}{\partial x^2} + \frac{\partial^2 u}{\partial y^2} = \frac{1}{\mu}\frac{dp}{dz} = C, \tag{35}$$

where u is the stream-wise velocity, μ is the viscosity, p is the pressure, and C is a constant. For a rectangular channel, this can be solved as:

$$\begin{aligned} u(x,y) =& \frac{4h^2}{\mu\pi^3}\left(-\frac{dp}{dz}\right)\sum_{n=0}^{\infty}(-1)^n\left\{1 - \frac{cosh[(2n+1)\pi x/h]}{cosh[(2n+1)\pi w_o/2h]}\right\}\times \\ & \frac{cos[(2n+1)\pi y/h]}{(2n+1)^3} \end{aligned} \tag{36}$$

and integrating over the depth dimension provides the average stream-wise flow within the output channel:

$$\begin{aligned} \overline{u}(x) =& \frac{1}{h}\int_{-h/2}^{h/2} u(x,y)dy = \frac{8h^2}{\mu\pi^4}\left(-\frac{dp}{dz}\right)\sum_{n=0}^{\infty}\frac{1}{(2n+1)^4}\times \\ & \left\{1 - \frac{cosh[(2n+1)\pi x/h]}{cosh[(2n+1)\pi w_0/2h]}\right\}. \end{aligned} \tag{37}$$

Provided that the flow is symmetric across the lateral axis of the flow channel and

$$\overline{v_*} = \frac{2}{w_*}\int_0^{w_*/2}\overline{u}(x)dx, \tag{38}$$

where v_* can be v_f or v_o (integrating over the appropriate width), one can rewrite Eq. 18 as:

$$2\int_0^{w_f/2}\overline{u}(x)dx = \int_{-w_o/2}^{w_o/2}\overline{u}(x)dx\frac{Q_i}{Q_i+2Q_s} = \int_{-w_o/2}^{w_o/2}\overline{u}(x)dx\frac{r_i^2}{r_i^2+2r_s^2}, \tag{39}$$

where r_i and r_s are the radii of the syringes used for the sample and sheath flows, respectively. Solving for the left- and right-hand sides simultaneously provides the focused flow width, w_f, which can be used to find the focus flow velocity, v_f, [using

Eq. (17)] and γ [using Eq. (18)]. The simulated [normalized] stream-wise velocity for the glass channel is shown in Figure 35. One can see that the flow for this channel geometry is not the parabolic shape found in larger flow cells [see, for example, Figure 2(b)].

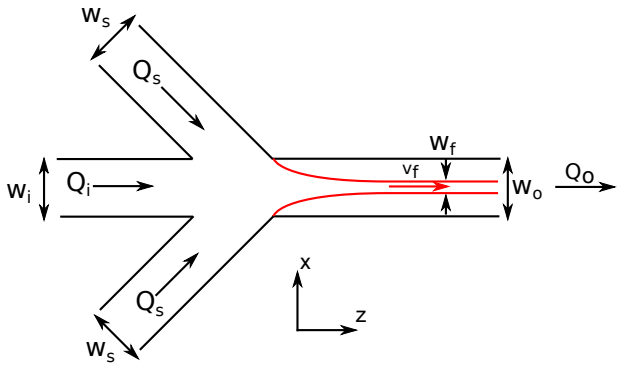

Figure 34: Schematic of flow channel with flow dynamic parameters identified. Q_i, Q_s, and Q_o are the volumetric flow rate for the sample input, sheath inputs, and output, respectively. w_i, w_s, and w_o are the channel widths of the sample input, sheath inputs, and outputs, respectively. w_f is the width of the focused stream. v_f is the stream-wise flow velocity of the focused stream. Not shown: h is the channel height and v_o is the stream-wise velocity of the output channel. Imaged based on Figure 1 in [88].

To better understand the MCARS flow cytometer fluidic system performance, one can apply the previous mathematical model to the developed system. Table 4 presents the flow system parameters for the simulation (N.B., sample injection rates are limited to practical flow rates: the system can inject over 30 mL/min with large diameter syringes). Figure 36 simulates the sample and sheath (total) width versus the diameter of the sample injection syringe (fixed sheath syringe diameter 12.45 mm, which was the largest syringe available that easily fits within the syringe pump). Figure 37 is the flow velocity versus sample volumetric flow rate for the 4 available sample syringe sizes. One can see that as the sample syringe diameter decreases, the velocity of the flow increases to maintain a given flow rate. In selecting the appropriate size syringe, one needs to account for sample velocity and flow rate as the velocity will determine the sample transit time; thus, affecting the strength of the recorded signal.

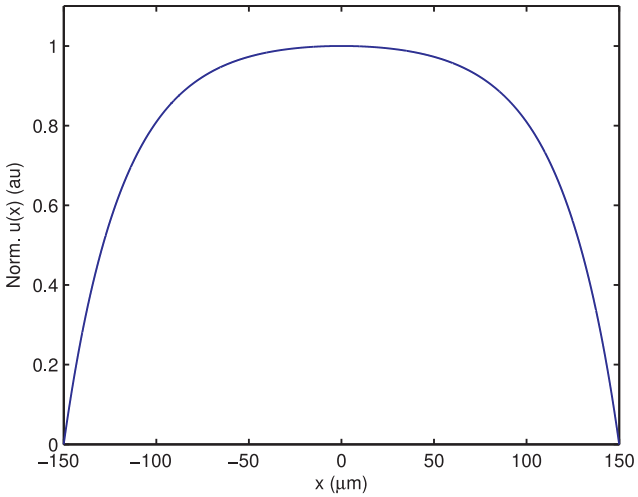

Figure 35: Normalized stream-wise flow velocity within the flow chip. The flow channel is 300 μm wide and 100 μm deep; thus, the velocity profile is not parabolic, such as found in much larger flow cells, and the flow profile is not homogeneous across the chip as it would be if the chip was significantly shallower.

Table 4: Specifications of the developed MCARS flow cytometer fluidic subsystem.

Parameter	Value	Units
Sheath Syringe Volume	6	mL
Sample Syringe Volume	0.1, 0.25, 0.5, or 1.0	mL
Sheath Syringe Diameter	12.45	mm
Sample Syringe Diameter	1.46, 2.3, 3.26, 4.61	mm
Sample Injection Rate	0.0001 - 0.001	mL/min
Channel Widths	300	μm
Channel Depths	100	μm

Additionally, one will need to account for the sample concentration as small diameter syringes will generate fast moving samples that are spaced far apart. For example, Figure 38 shows the number of particles per second flowing through the flow cell for a sample of 5 μm particles at a concentration of $10^7/mL$ as a function of [sample stream] volumetric flow rate. One needs to consider, however, that the flow cytometer will only be able to analyze a single stream of particles. For example, if a 1 mL sample syringe is used, the sample stream will be nearly 20 μm wide; thus, approximately, 1 of every 4 particles, on average, will be probed. Experimentally, I have monitored flowing particles under these conditions, and the particles flow through the flow cell in lanes– neighboring particles force other particles into neighboring lanes; thus, a 20 μm sample stream performs to a good degree like 4 individual sample streams. Without any lateral flow (such as can be caused by obstructions), the particles flow at the same lateral location across the flow cell for the length of the chip; thus, the approximation seems reasonable. Figure 39 shows the number of particles flowing through the focal region of the flow cytometer as a function of sample volumetric flow rate and includes the penalty associated with sample streams wider than the hypothetical 5 μm particle (concentration of $10^7/mL$). In this figure, one can see that for the smallest syringes the measurable particles per second matches the ideal case of all particles propagate through the focal volume. For larger syringes, however, the effect of the sample stream width being significantly larger than the 5 μm particles is pronounced. To compensate for this effect, the sample concentration can be adjusted.

The CCD camera attached to the spectrograph (InstaSpecX, Newport-Stratford, Stratford, CT) typically operates at 100 Hz. To operate at maximum efficiency, one particle should pass through the focal volume every 10 ms. The optimal sample concentration versus volumetric flow rate are shown in Figure 40, which is also a function of sample syringe size. Finally, as the velocity of flowing particles is a function of the sample syringe size, Figure 41 demonstrates the effect of the SNR of

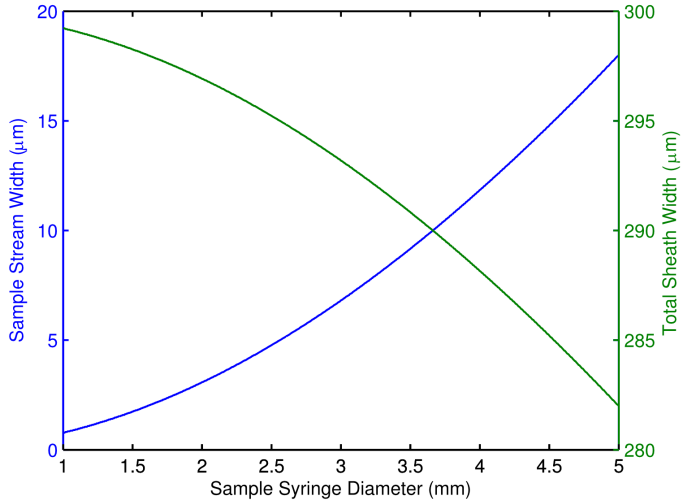

Figure 36: Simulated sample stream (left axis) and sheath stream (right axis) width as a function of sample syringe diameter with the sheath syringes fixed with a 12.45 mm diameter.

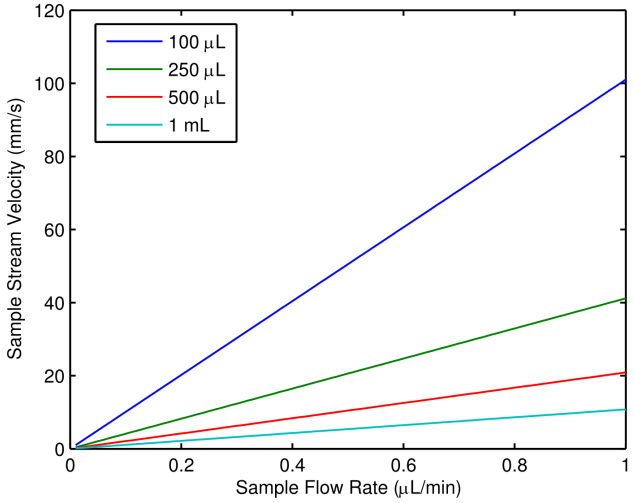

Figure 37: Sample stream as a function of sample syringe volumetric flow rate for four different sample syringe volumes. As the syringe volume (i.e., diameter) increases, the sample stream velocity slows resultant of the increase in the sample stream width as shown in Figure36.

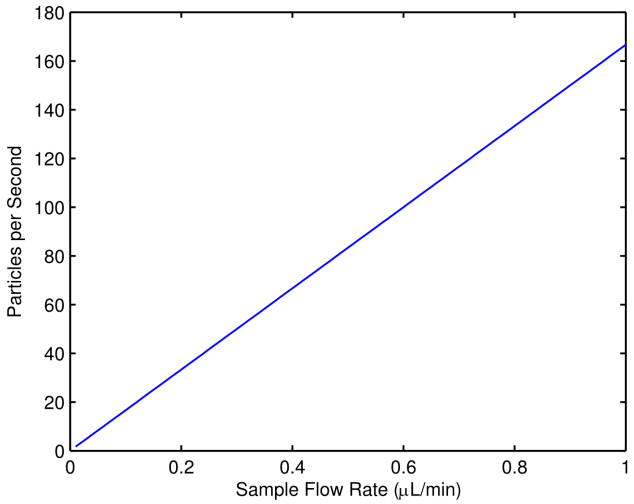

Figure 38: The number of particles per second flowing through the flow cell as a function of sample volumetric flow rate for a hypothetical 5 μm particle sample suspension with a concentration of $10^7/mL$.

the recorded MCARS spectrum versus volumetric flow rate for the 4 different syringe sizes. Based on the previous figures, one may conclude that the 100 or 250 μL sample syringes are the optimal selection for efficiently injecting the sample, but Figure 41 shows that the largest syringe also has the advantage in that it moves the largest volume at the slowest velocity; thus, the SNR is the highest. Also, at low volumetric flow rates (typically below 0.1 $\mu L/min$), the samples may stick and aggregate along the input port. Additionally, the smallest syringes may suffer from backflow as their small injection rates are very sensitive to pulsation (i.e., sheath and syringe flow perturbations) of the syringe pump. To balance out the advantages of single-stream flow offered by the smallest syringes, and the stability and velocity profile of the larger syringes, I have adopted the 250 and 500 μL syringes (older research uses the 1 mL sample syringe) in standard operating procedures.

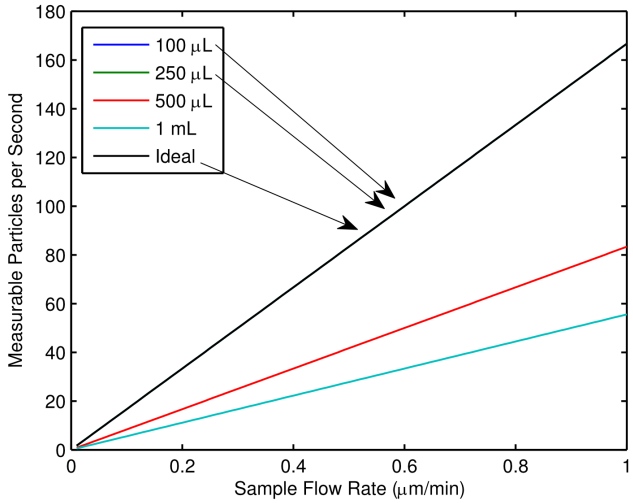

Figure 39: The number of particles per second flowing through the flow cell focal region as a function of sample volumetric flow rate for a variety of sample syringe sizes for a hypothetical 5 μm particle sample suspension with a concentration of $10^7/mL$. As larger diameter sample syringes produce a larger sample stream, the number of particles per second flowing through the focal volume is reduced from those flowing through the entire flow cell.

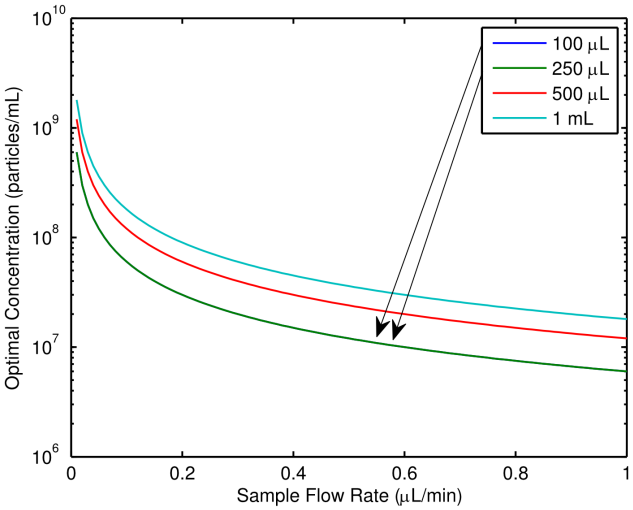

Figure 40: The optimal concentration of the sample suspension as a function of sample volumetric flow rate in order to have 100 particles flow through the focal region per second.

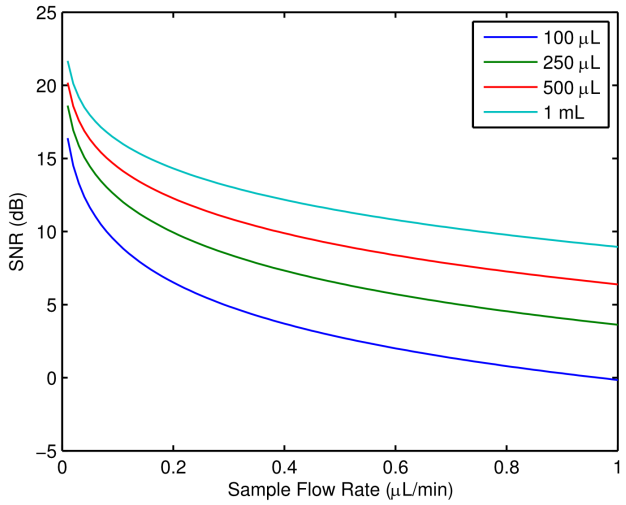

Figure 41: The measurable SNR of a hypothetical particle as a function of sample syringe volumetric flow rate. As the syringe diameter decreases, *ceteris paribus*, the SNR decreases due to the sample velocity increasing (see Figure 37), which reduces the sample transit time.

3.3 MCARS Flow Cytometer System

The MCARS flow cytometer was constructed upon the MCARS microspectrometer platform as described in Section 3.1. Figure 42 shows a schematic of the label-free flow cytometer system. Unlike the traditional MCARS system, the MCARS flow cytometer collects not only anti-Stokes photons, but also records the elastically scattered photons in the forward and lateral directions. Figure 43 shows a picture of the cytometer system including the coupling of the incident beams into the microscope, the excitation and collection optics, and the elastic scatter measurements detectors. The incident beams are focused onto a microfluidic chip (see Figure 44), and a module collects the anti-Stokes photons and residual pump and Stokes beams in the forward direction with a 50x long-working distance objective and separates the light with a dichroic beam splitter (DMLP900, Thorlabs, Newton, NJ) (N.B.: the published implementation of this system uses a 10x long-working distance objective). Ideally, the collection objective would match the NA of the excitation optics, but the fluidic ports present a space limitation. A silicon detector measures the sample FSC (PDA36A, Thorlabs, Newton, NJ) of the transmitted longer wavelengths. In this configuration, the FSC signal strength is inversely proportional to the scatter strength. Additionally, another amplified silicon detector is placed near the chip, laterally from the flow direction, to record the SSC. A high-speed data acquisition board (DAQ) (NI-DAQ 6366, National Instruments, Austin, TX) collects the signal from both silicon detectors, and a LabView VI processes the data (N.B.: in the published implementations of this system, the elastic scatter was measured only in the forward or lateral direction using a NI-DAQ 6251 DAQ board, which did not provide for simultaneous sampling over multiple channels [85–87]). Within the optical module, the shorter wavelengths that reflect off of the dichroic mirror propagate through two short-pass filters, which only transmit the anti-Stokes photons. A fiber-coupled collimator tip collects the anti-Stokes photons and transmits them to a spectrograph (MS-280i,

Newport Stratford, Inc., Stratford, CT) equipped with a CCD camera (InstaSpecX, Newport-Stratford., Stratford, CT). The signal from the CCD camera transmits to a computer (Dell OPTIPLEX 755, 2.66 Ghz Intel Core 2 Duo CPU, 3.25 GB RAM) and records in LabView. The technical specifications of the MCARS flow cytometer are presented in Table 5.

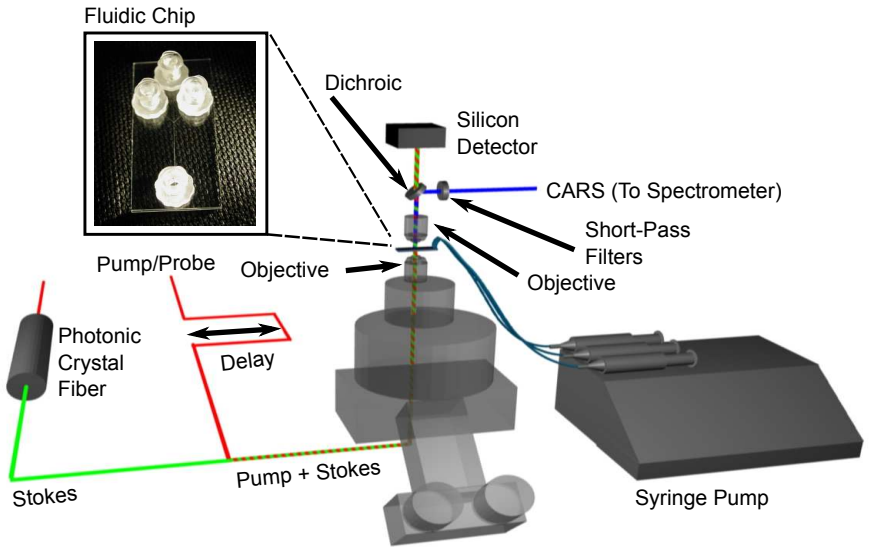

Figure 42: Schematic of label-free flow cytometer that uses MCARS to obtain molecularly specific information. A femtosecond laser acts as both the pump for the CARS generation process and as the seed source for a length of PCF that produces the supercontinuum "Stokes" source. An amplified silicon detector measures the elastically scattered photons in the forward direction. Another amplified silicon detector, positioned close to the fluidic chip measures side-scattered photons (SSC) (not shown).

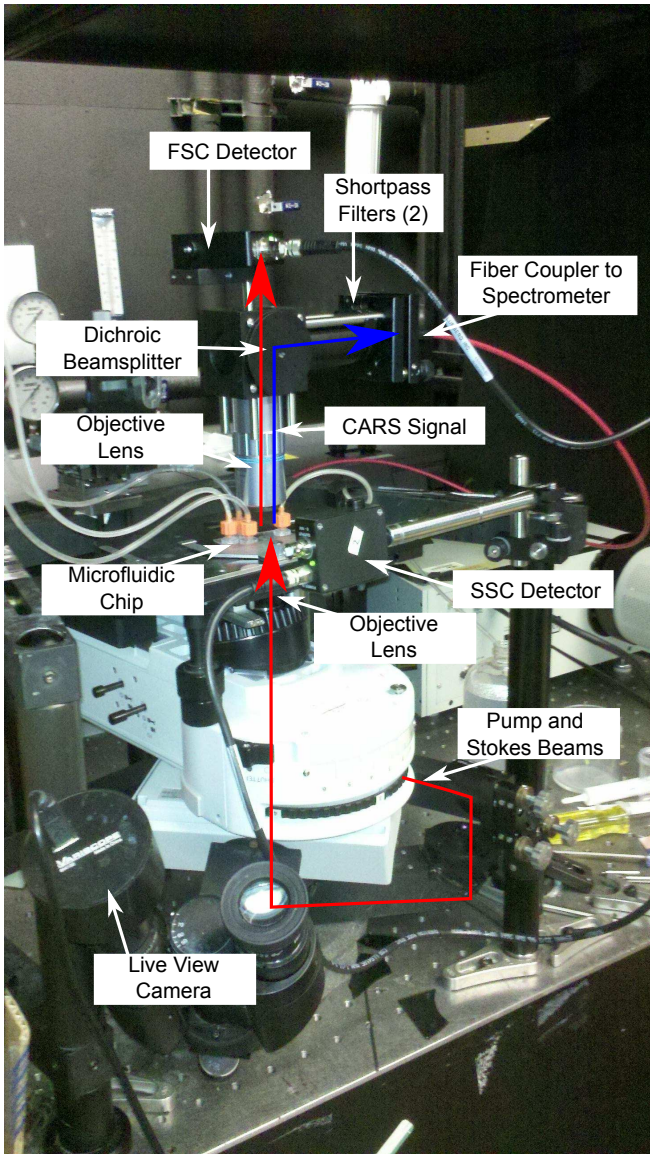

Figure 43: Image of label-free flow cytometer. The pump and Stokes sources are coupled into the inverted microscope through a periscope and then focused onto the microfluidic chip from below. Elastically scattered photons at an oblique angle (SSC) are recorded by an amplified silicon detector. A long-working distance objective lens collects the CARS signal and the transmitted pump and Stokes beams (elastically scattered photons in the forward direction [FSC]). The objective lens collimates which are spectrally separated by a dichroic beamsplitter that transmits longer wavelengths (> 900 nm). These transmitted photons are collected onto an amplified silicon detector to measure FSC. The shorter wavelengths are further filtered by two short-pass filters, and the remaining anti-Stokes photons (CARS) are coupled into the collimator-tipped fiber that carries them to a spectrometer.

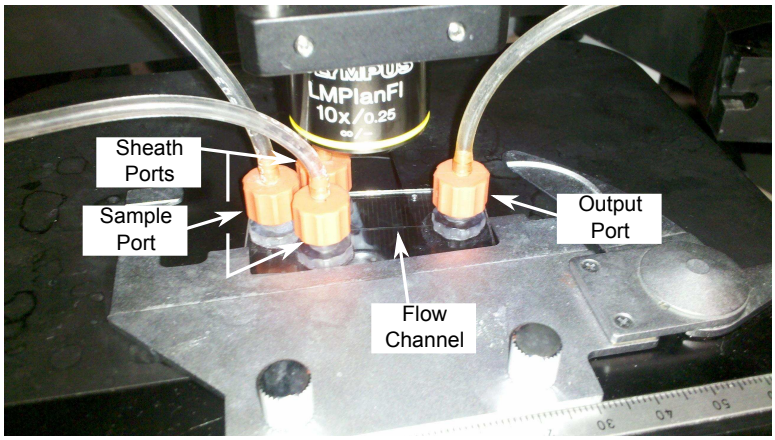

Figure 44: Close-up image of the microfluidic chip. Three input ports provide two sheath flow streams and a sample input. The output port is connected through tubing to a waste vessel.

Table 5: Specifications of the MCARS flow cytometer system.

Parameter	Value	Units
Ultrafast Source Wavelength	∼806	nm
Ultrafast Source Pulse Duration	<125	fs
Ultrafast Source Pulse Bandwidth	∼8	nm
Stokes Wavelength	850 - 1600	nm
Pump Bandwidth (at sample)	∼3	nm
Pump Power (at sample)	1-50	mW
Stokes Power (at sample)	1-40	mW
Maximum Spectral Record Rate	100	spectra/sec
Typical Spectral Record Rate	50	spectra/sec
Maximum Sample Stream Flow Rate	>200	$\mu L/min$
Typical Sample Stream Flow Rate	0.2 - 1	$\mu L/min$

3.4 Electronics and Software

Successful collection of MCARS flow cytometry data involves synchronization and acquisition from several electronic devices. Additionally, the software that operates the system needs to properly co-register spectral and scatter measurements to properly apply gates and to store data at high-speed. Figure 45 is a flowchart of system operation. When the software begins (written in LabView with MATLAB plug-in components), the CCD camera, the DAQ master clock, and the analog input channels are initialized. For the CCD camera, this step sets the cooling temperature (-70^o C), the analog-to-digital (A/D) gain (typically, high gain) and speed (high-speed), the integration time, the region of interest of the 2D CCD chip (1024 x 256 pixels), and the acquisition mode (external triggering on a rising edge). The master clock, which is based on a 80 MHz counter, creates a 100 Hz square wave that will trigger the CCD camera and the analog input channels acquisitions. The analog input channels, which will record the elastic scatter detector voltages, record data at up to 1,000 kHz (user-selectable; typically ∼10-100 kHz) when triggered. Next, the CCD camera is given a start command, followed by the analog input channels. Finally, the master clock is initiated after the other 2 channels to ensure that acquisition begins on the first clock pulse. The first two acquisitions of the system are the background FSC, background SSC, and background MCARS spectrum. These background measurements will be used by the software gates to compare future acquisitions.

Next, the system moves into normal acquisition mode. The LabView software now specifies that each channel will only operate in 1 second intervals. Due to on-board memory of the DAQ and the data transfer rates, it was found that the most efficient data acquisition occurs when multiple spectral and elastic scatter measurements are captured and then the data is collected by the computer. For example, collecting an individual spectrum at 100 Hz and recording the elastic scatter profiles at 10 kHz, allows the system to operate at only 30 Hz due to the latency between storing

the data in computer memory and restarting the DAQ and CCD acquisition. On the other hand, collecting the data for 100 cycles before transferring data to the computer, permits system speed at nearly 93 Hz (with the maximum possible being 100 Hz). During typical system operation, 100 spectra are collected, 10,000-1,000,000 elastic scatter measurements (per scatter channel) are registered into 100 scatter profiles (i.e., each MCARS spectrum is co-registered with an FSC and an SSC scatter measurement), and the data is passed along to software gates. The software gates provide the user with a variety of options to independently evaluate the scatter and spectral measurements. For example, the scatter gate can be set to only accept cycles in which the SSC scatter voltage passes above 5 V (0 V baseline) and the FSC voltage must drop below 5 V (10V baseline), and the spectral gate can be set to accept only spectra with a peak with a given strength in a particular spectral region. Additionally, the user can select how the spectral data is pre-gate processed. For example, the background can be subtracted from the MCARS spectra, the MCARS spectra can be normalized to the background spectra (such as in [85–87]), or the KK reconstruction algorithm can be applied before the gates are evaluated (most recently the typical pre-processing method). If a spectrum or elastic scatter measurement do not pass a respective gate, the background buffer for the elastic scatter and/or spectral measurements is updated with the mean between the new spectrum and the previously recorded background spectrum. If, however, an acquisition passes all gates, the MCARS and elastic scatter arrays are updated with these recording, and the background buffer is recorded into the background array for storage. The motivation for constantly updating the background arrays (as opposed to relying on the first two acquisitions that initialized the background arrays) is to account for spectral and baseline fluctuations in the MCARS measurements and elastic scatter measurement, respectively. This is especially important with the use of a PCF for the Stokes source, as the output can fluctuate noticeably (not necessarily significantly)

over a matter of minutes. As this software operates in 100 acquisition bursts, the described gate evaluation and array updating occur for the 100 samples in parallel. After the number of passed gates exceeds a user-defined value, the data arrays are saved to disk.

To characterize the synchronization of the acquisition system, I placed an augmented chopper wheel in the incident beam path leading into the microscope. The area of the chopper wheel where the incident beams pass was taped except for a single slit. This allowed the wheel to be rotated at speed of 100 - 900 Hz with a pulse of light being created at approximately 3 - 30 Hz with pulse widths of 4.4 - 0.56 ms. The CCD recorded a small spectral segment of the incident Stokes beam that bled through the filter set at 775 nm (during MCARS measurement, this bleed-through is spectrally separated from the region of interest; thus, it does not interfere with measurements). For example, I recorded the spectrum and FSC scatter measurement (baseline fluctuations) for the chopper rotating at 473 Hz (pulse repetition rate $\sim$15.9 Hz, pulse width $\sim$1.1 ms). Figure 46 shows the scatter plot of MCARS maximum intensity versus elastic scatter maximum intensity for 3000 acquisitions. One can see the low state acquisitions (i.e., incident beams blocked), and the high-state acquisitions. There are also two clusters in which the MCARS and elastic scatter measured opposite polarities (i.e., one signal read high and the other low) that result from the CCD and elastic scatter becoming unsynchronized. Proper synchronization and gating the system to only capture high-state elastic scatter produces the scatter plot in Figure 47. In this plot, one can see that the majority of the signal occurs when both channels measure a high signal. There is still, however, a significant portion of the MCARS spectral maximum that is not near the maximum value. The spread of spectral maxima is a side-effect of using a CCD camera and its method of capturing light, recording data, and clearing the CCD chip in preparation for the next record cycle. A

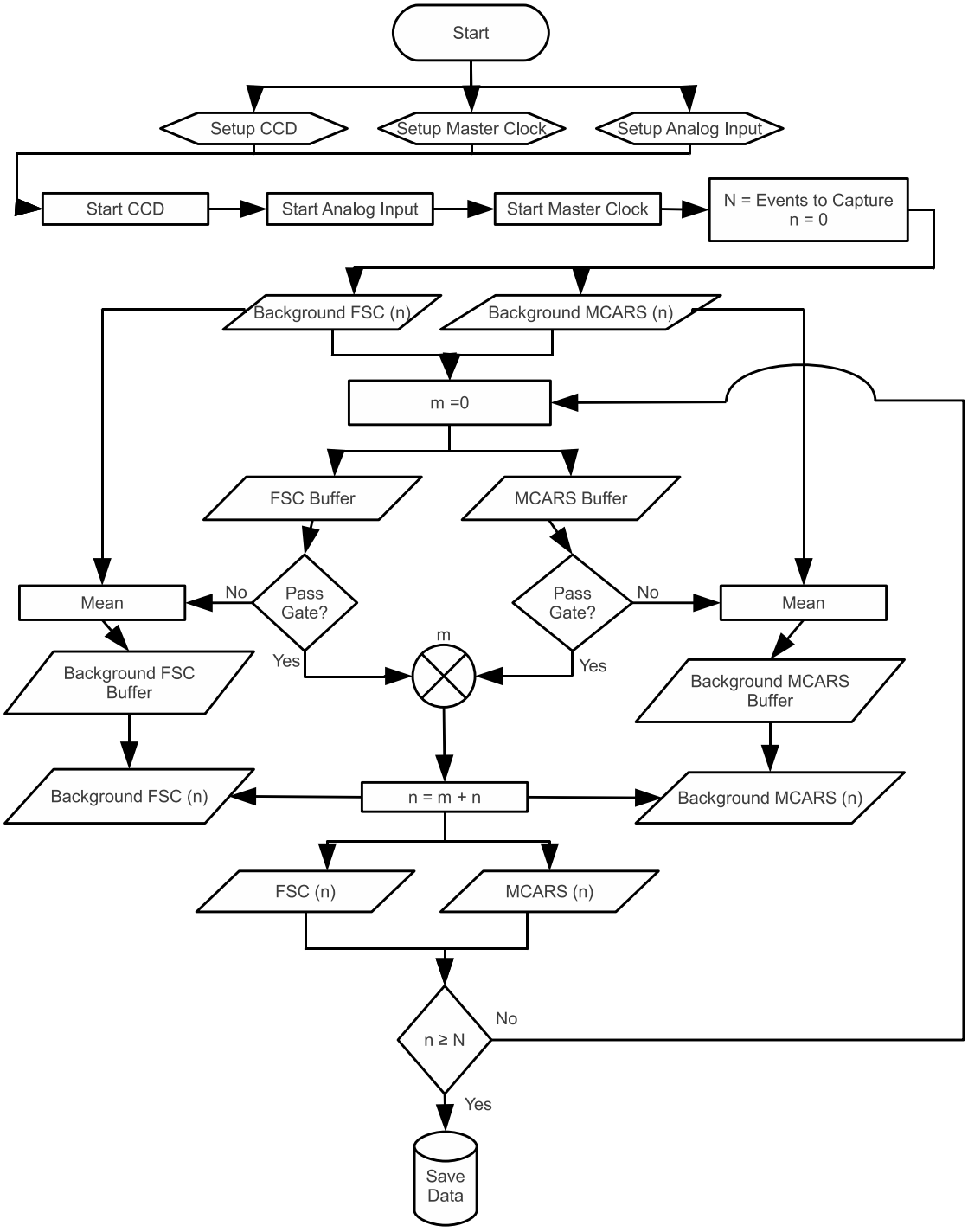

Figure 45: System flowchart for MCARS flow cytometer.

2D CCD chip is composed of rows and columns of individual elements that have electrical connections to neighboring elements (the exact wiring is camera-dependent). In the developed system, the chip operates in full vertical binning mode; thus, after each acquisition, the electrical charge from each column (each column represents a unique spectral range) is collected into a single bin of a shift register, and once all the columns have been loaded into the separate bins of a shift register, the signal is forwarded onto the analog-to-digital (A/D) subsystem of the CCD for quantification (see Figure 48). In order to vertically shift the charges down the shift register, the charge of each element is incrementally shifted down one row at a given rate ($\sim$30 μs per row). The uppermost row(s) is deactivated and cleaned during which this element(s) will not accept any new charge. The lower rows, however, are still able to accept new charges. In a system, such as the one described in this thesis that operates without a shutter, the lower rows are able to accept new charges not only from rows above, but also from those created by new incident photons. Although the CCD chip has an integration time of 1 ms, the time in which it captures photons is closer to 8.5 ms. Additionally, as more CCD elements are deactivated and cleaned, the effective area of the CCD decreases. The elastic scatter measurement, however, continuously records into the DAQ memory; thus, there is no sensitivity penalty [see Figure49(a)]. Looking at the maximum MCARS signal versus the position within the 10 ms cycle that the signal arrived, as shown in Figure 49(b), demonstrates the aforementioned affect. This measurement shows that the CCD chip records data most efficiently between the trigger (time 0) and approximately 6 ms. From around 6-8.5 ms, the CCD records photons at a rapidly reducing efficiency. Based on this measurement, the recorded MCARS spectrum could be amplitude corrected to account for the reduced efficiency; although, this may introduce additional noise and errors. After 8.5 ms, the CCD is completely inactive. Figure 50 shows the MCARS maximum intensity as a function of elastic scatter measurement with MCARS spectral gating (the MCARS

intensity must meet a threshold) and elastic scatter gating to only record when light passes through the chopper slit. Additionally, the recorded spectrum of the CCD has been corrected based on the time in which the light was recorded.

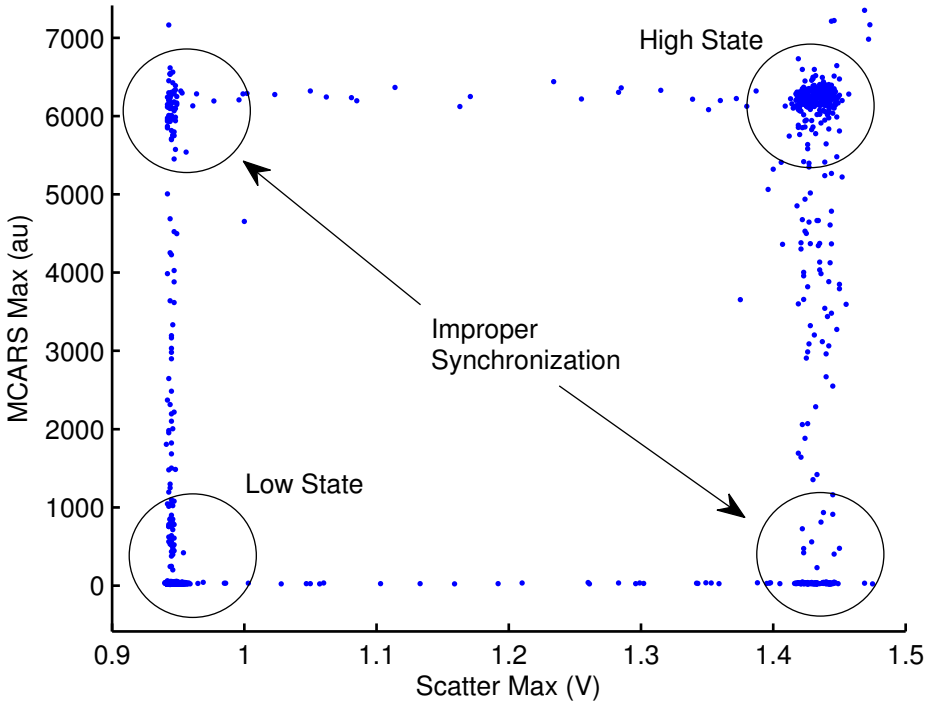

Figure 46: The maximum spectral intensity versus the maximum scatter voltage when using an augmented chopper wheel to pulse the incident source beam coupled into the microscope. The chopper wheel is rotated at approximately 473 Hz, producing ∼1.1 ms pulses at ∼15.9 Hz repetition rate. Although the system properly records scatter and spectra for the high state (beams passing the chopper wheel) and the low state (beams blocked), improper gating and synchronization between the CCD and elastic scatter measurement DAQ produce data in which one detector measures a low state and the other a high state (and vice versa).

The electronics and software subsystem of the MCARS flow cytometer allows for acquisition of sample spectra and elastic scatter measurements at over 100 Hz with full software processing and gating at over 90 Hz. The software system, beyond data handling, allows the user great flexibility in how to analyze, pre-process, and gate data. Figure 51 shows the graphical user interface of the "Flotonics" software package during operation. The sample under test in the screenshot is a mixture of

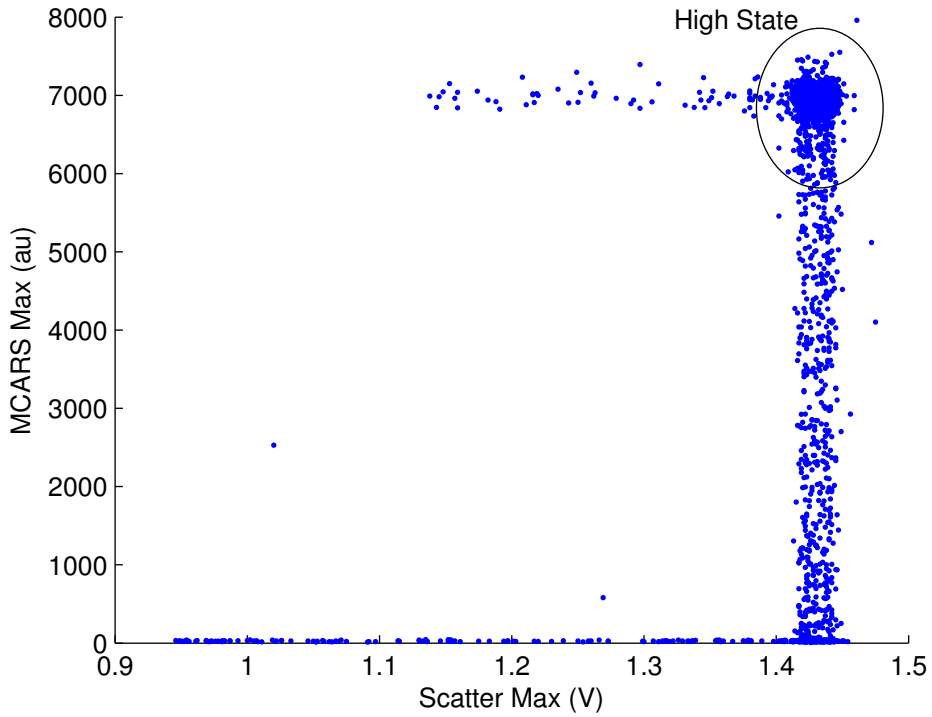

Figure 47: The maximum spectral intensity versus the maximum scatter voltage when using an augmented chopper wheel to pulse the incident source beam coupled into the microscope. The chopper wheel is rotated at approximately 473 Hz, producing ∼1.1 ms pulses at ∼15.9 Hz repetition rate. The system is gating to only capture high states and the detectors are synchronized. The data that deviated from the expected high state is resultant of the CCD capturing photons outside of the ideal recording window of approximately 6 ms.

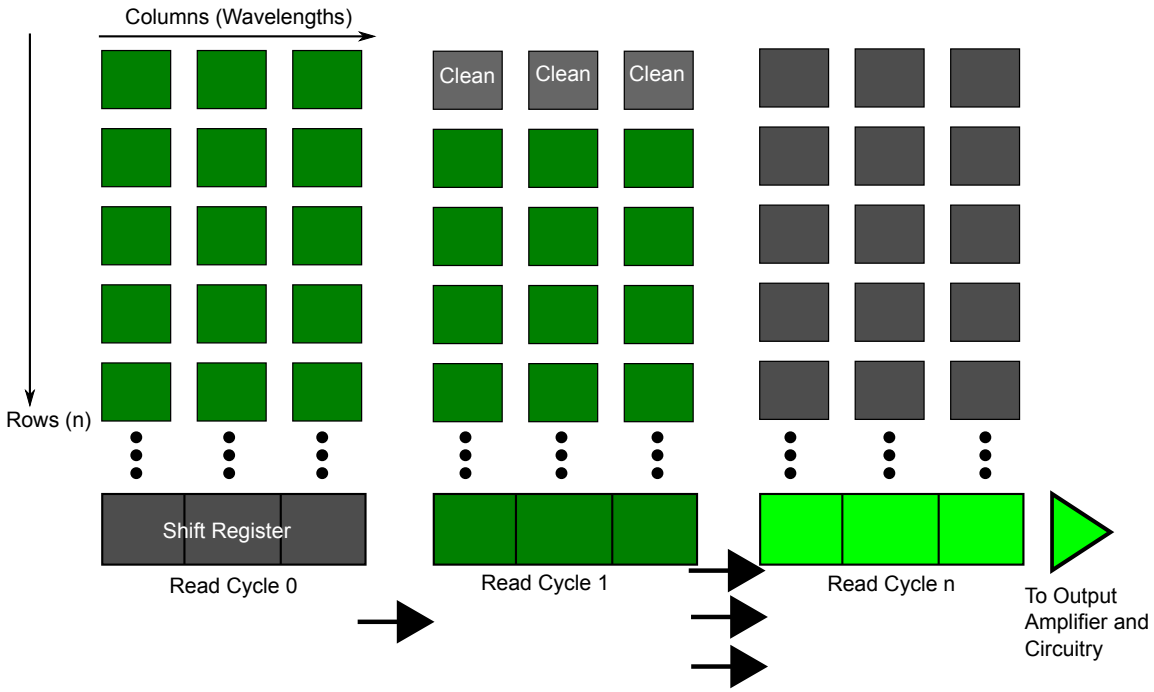

Figure 48: Schematic depicting the operation of a 2D CCD array in full vertical binning mode. In the recording phase, photons generate charges within each element of the chip. During the read cycle, the charge from each row is shifted downward by one row at a time into a shift register. The uppermost row is deactivated (i.e., cannot store new charges) and cleaned (i.e., remnant charges are removed), but the remaining CCD elements are able to receive charges not only from upper rows shifting their charges downward, but also from new incident photons. During the read cycle, the CCD camera continues to record photons but with increasingly diminished capacity and efficiency. After all the charges have been collected in the shift register, the charges are forwarded to analog amplification circuitry and A/D circuitry for counting and transmission to the computer.

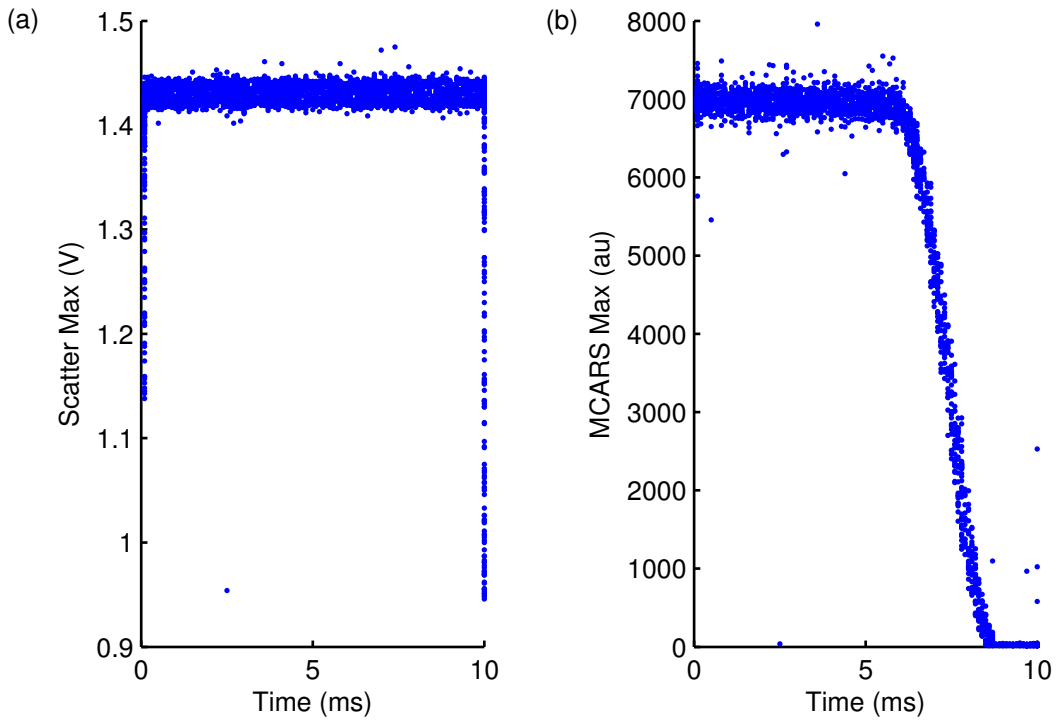

Figure 49: (a) The maximum scatter voltage versus the clock time within a single acquisition in which. (b) The maximum spectral intensity versus clock time within a single acquisition. As the DAQ continuously captures voltages at 10 kHz, the recorded scatter voltage is not effected by the time during the acquisition it arrived (excluding the first and last temporal bin, which are affected by triggering jitter). The CCD, however, most faithfully records spectra during the first [approximate] 60 ms of the acquisition window. After the first 60 ms, the CCD camera begins to collect and quantify charges and begins deactivating rows of the CCD chip.

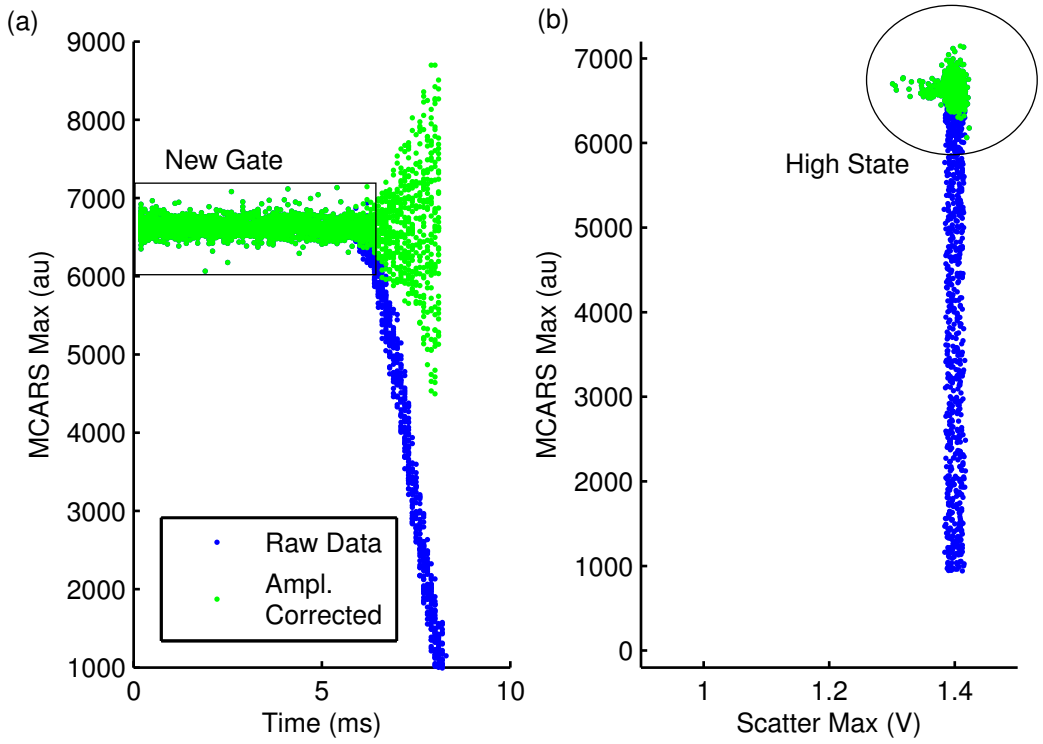

Figure 50: (a) The maximum spectral intensity versus clock time within a single acquisition. The raw data (blue) depicts the reduced CCD efficiency as photons arrive after the first ∼6 ms of the acquisition. Amplitude correct (green) can be performed on data to account for the reduced efficiency, and a new gate can be placed on the corrected data to remove the amplified noise from the amplitude correction algorithm. (b) The maximum spectral intensity as a function of the maximum scatter voltage. With proper gating, the high state (i.e., beams pass through the chopper wheel) is successfully captured. The raw data (blue) reveals the spectral fluctuation, but with proper gating and amplitude correction presented in (a), the high state subpopulation is significantly tighter.

PS beads. One can see the windows showing real-time FSC and SSC waveforms, the Raman reconstruction (KK algorithm) of the samples that passed the gates, the current background MCARS spectrum, a scatter plot of the SSC versus FSC, and pertinent system information such as sample passage rate, net acquisition rate, and remaining time. Additionally, the software allows the user to customize the data pre-processing (e.g., KK reconstruction algorithm), gating of all channels independently, the speed and operation of the elastic scatter module (and monitor the real-time speed of the subsystem) as well as all adjustable parameters for the MCARS spectrometer.

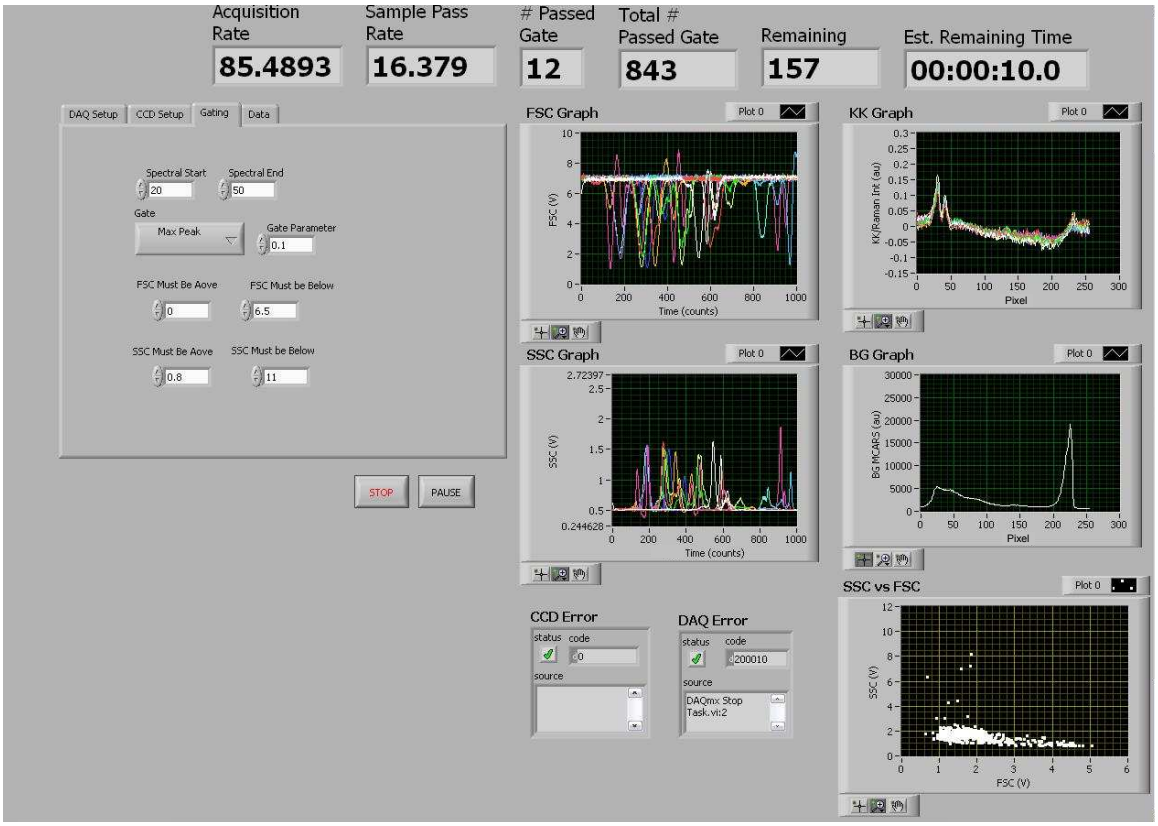

Figure 51: Screenshot of software during operation. The sample under test in the screenshot is a mixture of PS beads. One can see the windows showing real-time FSC and SSC waveforms, the Raman reconstruction (KK algorithm) of the samples that passed the gates, the current background MCARS spectrum, a scatter plot of the SSC versus FSC, and pertinent system information such as sample passage rate, net acquisition rate, and remaining time.

The developed MCARS flow cytometry software and electronics subsystem provides a powerful and flexible platform for the acquisition and analysis of MCARS flow cytometric data. Its development not only represents a software development feat in complex multi-instrument synchronization, but also a challenging design effort in data and memory management and event handling. Future enhancements, such as coding all or parts of the software in compiled languages, such as C, could provide further speed enhancements. Additionally, upgrading the computer hardware (currently, a Dell OPTIPLEX 755, 2.66 Ghz Intel Core 2 Duo CPU, 3.25 GB RAM) could improve the performance as larger acquisition segments could be processed (the 3.25 GB memory limit of the 32-bit operating system limits the most efficient spectral block size to $\sim$100 per second). Finally, upgrading the CCD camera would provide a dramatic improvement in performance as the current system is limited to a maximum speed of 100 Hz based on the data transfer rates of the CCD electronics.

CHAPTER 4

SYSTEM CHARACTERIZATION

In this chapter, I will characterize the MCARS spectroscopy subsystem, the elastic scatter measurement platform, and the performance of the complete system. In the first section, I will demonstrate that the MCARS spectroscopy subsystem is both stable and with the help of the KK reconstruction algorithm, able to properly probe the Raman vibrational band structure of sample molecules with high resolution and SNR. In the second subsection, I will present the characterization of the elastic scatter platform. It will be demonstrated that the elastic scatter measurements can be used to separate sample subpopulations based on FSC and SSC intensities, and under certain conditions, can be used to size particles. Additionally, the effect of sample flow rate will be experimentally demonstrated and the implications discussed. In the final subsection, I will characterize the SNR of the MCARS flow cytometer and discuss many of the technical points to consider when analyzing samples of various composition and size.

4.1 MCARS Spectroscopy

4.1.1 Stability

The MCARS spectroscopy subsystem is the backbone of the MCARS flow cytometer from which it derives its sensitivity and resolution. Unlike CARS microscopy systems that typically rely on a combination of lasers and/or parametric devices that are fixed to particular wavelengths, most MCARS system rely on a single femtosecond laser and a PCF to produce the pump and Stokes sources, respectively. Although the PCF provides an efficient and inexpensive means to produce a supercontinuum source, they are highly sensitive to seed source power and wavelength fluctuations

and input beam alignment. To demonstrate the stability of the MCARS system, the MCARS spectrum of objective oil was recorded every 1 second for 20 minutes. This period of time was determined to represent the longest likely time to analyze a sample in the flow cytometry system. Additionally, the spectrometer settings were adjusted to represent the typical setting used during flow cytometry experiments: high-speed A/D, high electronic gain, 1 ms integration time (which is the longest integration time in which the spectrometer will operate at 100 Hz), and the CCD camera binned full-vertically and by 4 pixels horizontally (spectrally). Also, the excitation beams were attenuated with a variable attenuator to demonstrate realistic MCARS amplitudes for flowing particles. The test was performed under realistic conditions (i.e., far from ideal) and contain contributions from the environment, such as vibrations due to nearby construction, building infrastructure, air currents, and laboratory equipment; although, the entire system resides on a floating table, which greatly reduces these effects. The Raman spectrum of the objective oil, which was used as the sample for this test, is shown in Figure 52. The spectrum was collected on a Thermo Nicolet MicroRaman system. Figure 53(a) shows the time stack spectra from the developed MCARS system and Figure 53(b) shows the mean (black), maximum (blue), and minimum (red) spectrum obtained over the 20 minute period. Within the MCARS system bandwidth, one can see three peaks at $\sim$2850 cm^{-1} ("peak 1"), $\sim$1580 cm^{-1} ("peak 2"), and at $\sim$1450 cm^{-1} ("peak 3"). Peak 1 likely corresponds to the combination of peaks at 2855 cm^{-1}, 2924 cm^{-1}, and 3063 cm^{-1} in Figure 52. These peaks are closely spaced with regard to their FWHM and the weaker peaks at 2855 nearly blends into the larger peak even when using Raman spectroscopy. Additionally, the quadratic dependence of CARS on molecular concentration indicates that the larger peaks will become substantially larger than the weakest peak at 3063 cm^{-1}, which in combination with the spectral distortions described in Chapter 2 and the spectral resolution afforded by the femtosecond pump source and the spectrometer binning,

inhibit the ability to isolate these three peaks. Peak 2 corresponds with the Raman peak at 1605 cm^{-1} and peak 3 with the Raman peak at 1445 cm^{-1}. Figure 54(a)-(c) shows the intensity fluctuation over the 20 minute recording period of peaks 1, 2, and 3 respectively. One can see that the peak fluctuations of peak 1 and peak 3 are approximately ±2% from the mean and peak 2 is approximately ±1.5%. Figure 54(d)-(f) show the corresponding peak location fluctuations as a function of time. Peak 1 appears to fluctuate the most heavily ($\pm 8.5 cm^{-1}$ from the mean); although, examination of Figure 53(b) shows that this peak is nearly flat between two pixels; thus, these fluctuations are overstated. Additionally, in this wavelength range, the spectral separation between neighboring CCD pixels is ∼17 cm^{-1}; thus, these fluctuations are between just two pixels. Peak 2 demonstrates the fewest fluctuations. Peak 3 demonstrates the most fluctuations ($\pm 17 cm^{-1}$ [±1 pixel]), which results from the relatively broad, flat spectral shape.

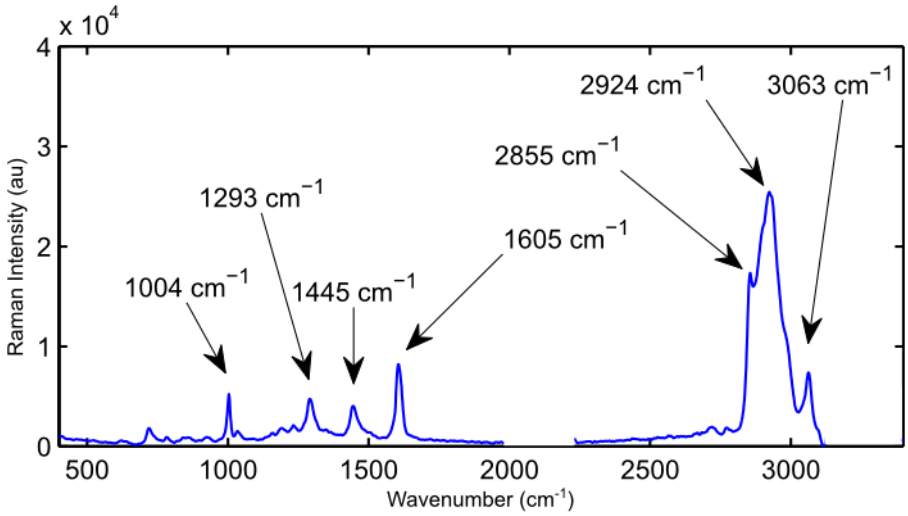

Figure 52: Raman spectrum of objective oil collected on a Thermo Nicolet Micro-Raman microspectrometer system.

Without data processing, this system demonstrates, typically, better than ±1 CCD pixel resolution. Recently, the KK reconstruction algorithm was integrated into the MCARS flow cytometer software for data pre-processing; thus, one needs to

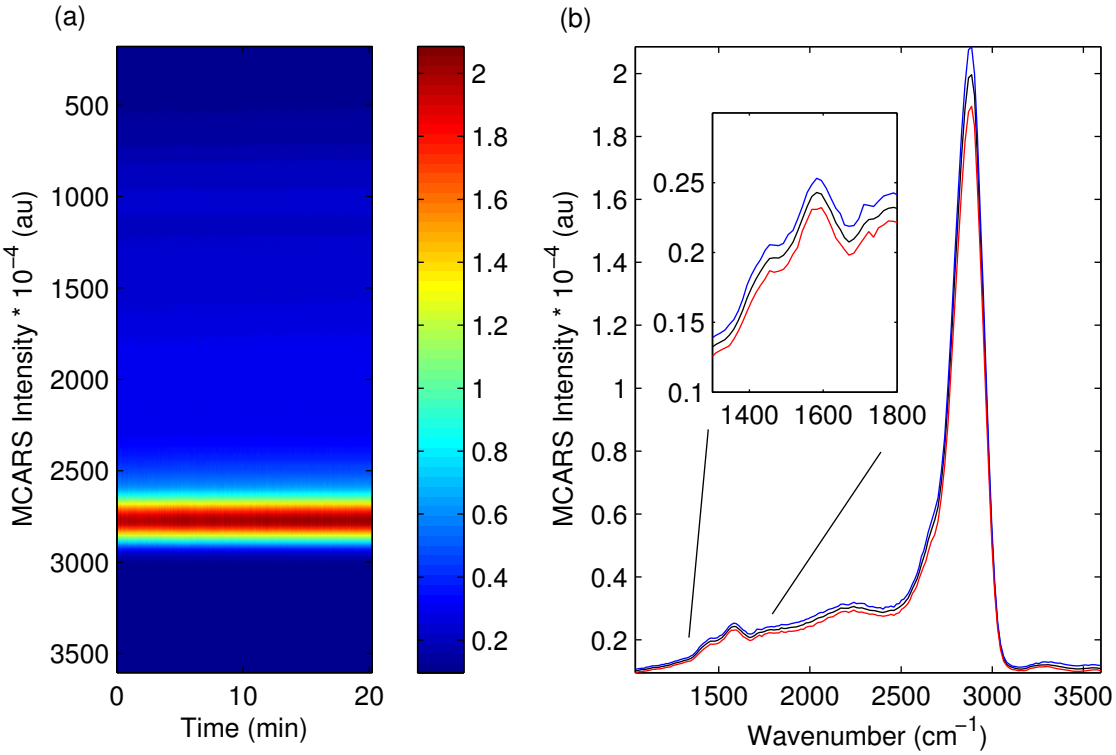

Figure 53: (a) Time stack image of the MCARS spectra for a sample of objective oil. Each spectra was collected with a 1 ms integration time with a 1 second delay between images over a 20 minute period. (b) The mean (black), max (blue), and minimum (blue) spectral features recorded over the 20 minute period. The peak at $\sim$2850 cm^{-1} will be referenced as "peak 1", the peak at $\sim$1580 cm^{-1} will be referenced as "peak 2", and the peak at $\sim$1450 cm^{-1} will be referenced as "peak 3".

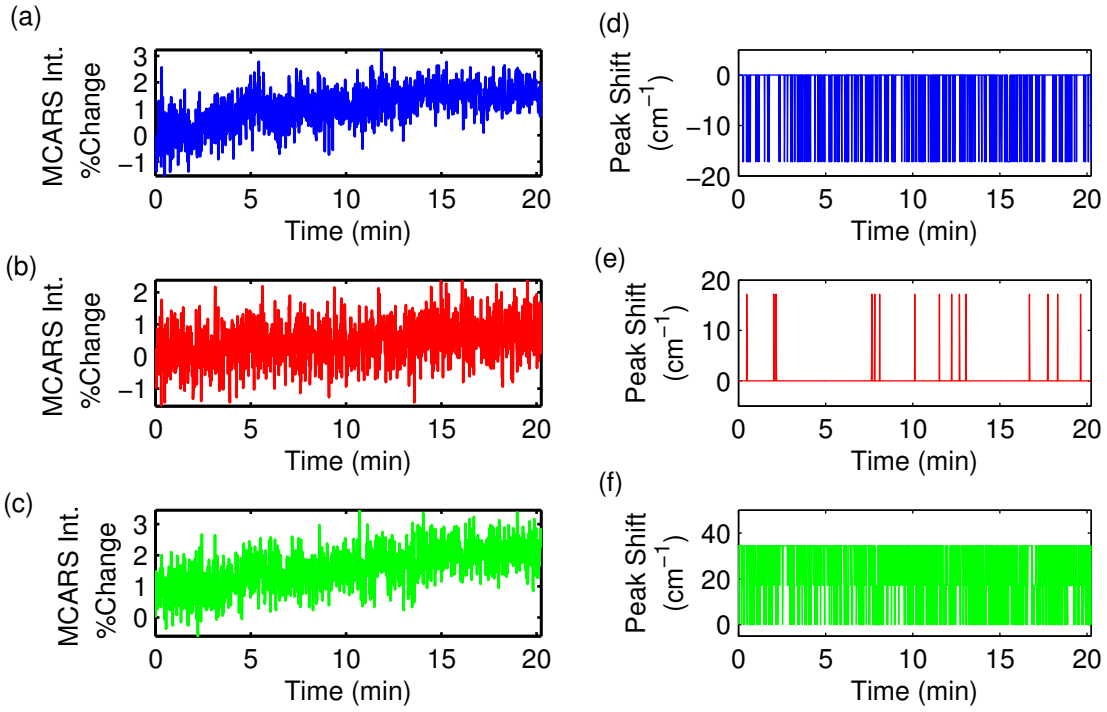

Figure 54: (a)-(c) The percentage change in the peak intensity height for the first (blue), second (red), and third (green) peaks, respectively. (d)-(f) The spectral shift of the first (blue), second (red), and third (green) peaks, respectively. A change of 1 spectral bin (pixel on the CCD) is equal to ∼12 - 17 (cm^{-1}) (the wavenumber spacing is not constant across the entire spectrum).

investigate the stability of the Raman reconstructed data as well. Using the previously recorded raw data and the spectrum of water collected at the beginning of the 20 minute test to approximate the nonresonant background, the KK-reconstructed spectra were generated. Figure 55(a) and (b) shows the time stack spectra and the mean (black), maximum (blue), and minimum (red) spectra, respectively. In the reconstructed spectra, peak 1, 2, and 3 have shifted to 2887, 1604, and 1449 cm^{-1}, respectively, which closely aligns with the experimentally recorded Raman peak locations. Figure 56(a)-(c) shows the intensity fluctuation over the 20 minute recording period of peaks 1, 2, and 3 respectively. Compared to the raw data, the intensity fluctuation of peak 1 has remained approximately the same, but the relative intensity fluctuations of peak 3 has increased slightly. More importantly, however, the spectral locations fluctuations of peak 1 and 3 (see Figure 56(a) and (c)) have dramatically reduced with the location of peak 1 being constant and peak 3 only shifting ± 1 pixel 0.4% of the samples. Peak 2, on the other hand, has degraded in both intensity fluctuations and spectral location. The root cause of this degradation is from phase errors in the KK reconstruction. These errors arise from the use of a single background image with a low SNR (see Figure 57). Collecting the MCARS spectrum of water with higher power incident beams would greatly improve the reconstruction. Additionally, as described in Chapter 3, the background spectrum is constantly updated during cytometer operation; thus, one can expect a significantly improved reconstruction with smaller fluctuations (as will be demonstrated later in this chapter and through out the text).

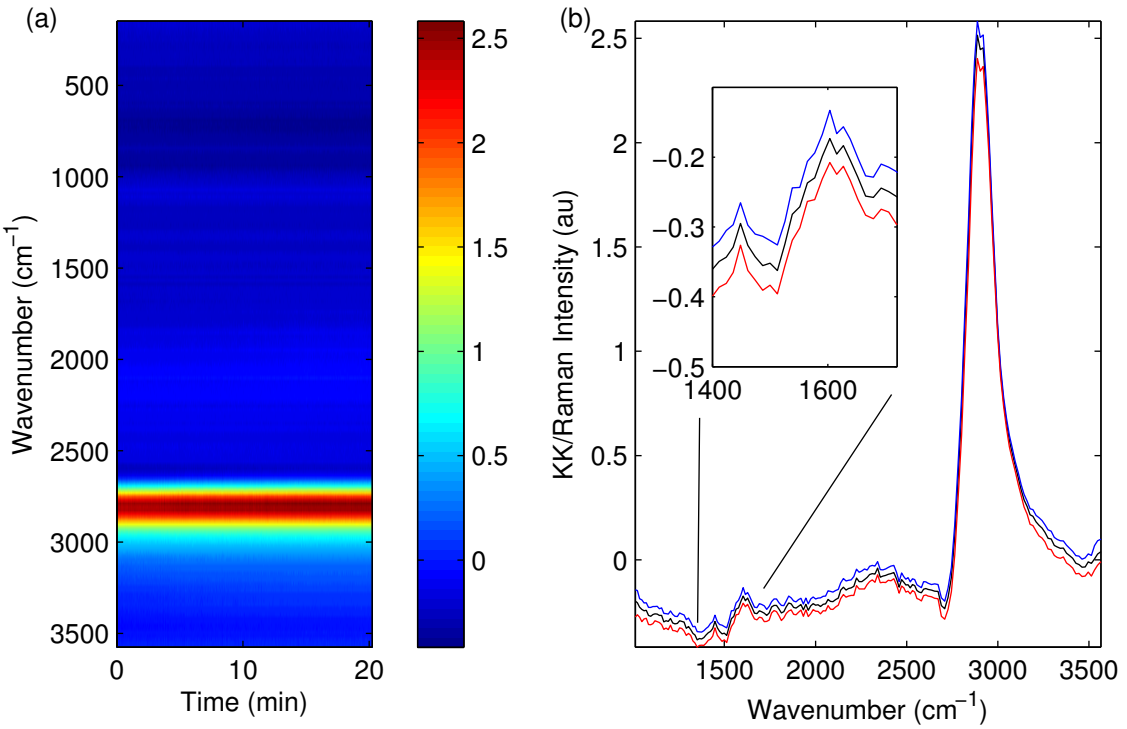

Figure 55: (a) Time stack image of the KK Raman (KK/Raman) reconstruction from the MCARS spectra for a sample of objective oil. Each spectra was collected with a 1 ms integration time with a 1 second delay between images over a 20 minute period. (b) The mean (black), max (blue), and minimum (blue) spectral features recorded over the 20 minute period. The peak at ∼2887 cm^{-1} corresponds to "peak 1" in Figure 53 as the peaks at ∼1604 cm^{-1} and ∼1449 cm^{-1} correspond to peaks 2 and 3, respectively.

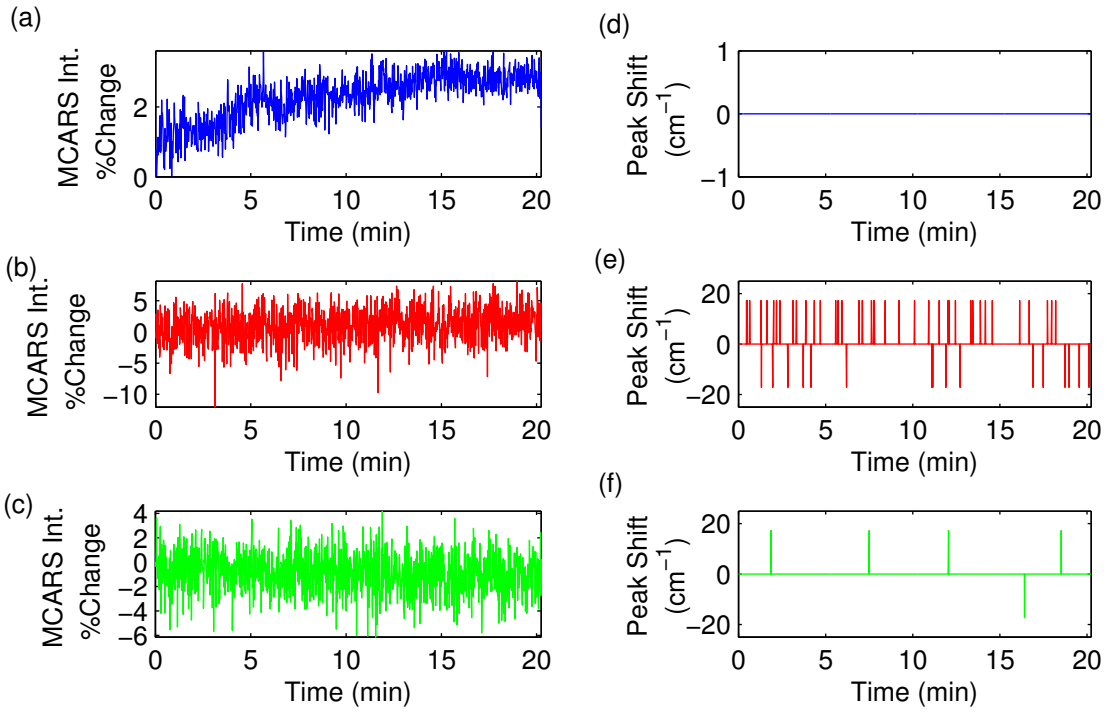

Figure 56: (a)-(c) The percentage change in the peak intensity height for the first (blue), second (red), and third (green) peaks, respectively. (d)-(f) The spectral shift of the first (blue), second (red), and third (green) peaks, respectively. A change of 1 spectral bin (pixel on the CCD) is equal to $\sim$12 - 17 (cm^{-1}) (the wavenumber spacing is not constant across the entire spectrum).

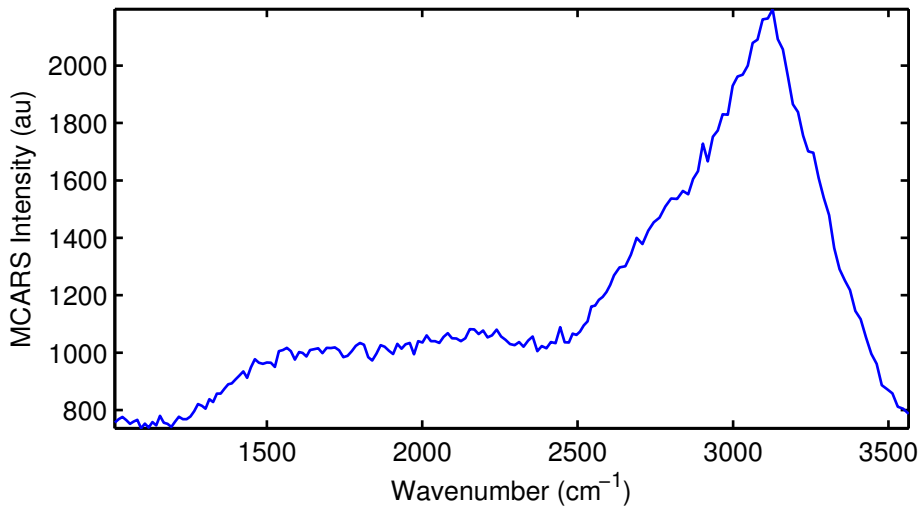

Figure 57: MCARS spectrum of water used to approximate the nonresonant background for the KK reconstruction algorithm.

4.1.2 Sensitivity

The sensitivity of MCARS spectrometers is a function of several factors including spectrometer sensitivity and sample molecular concentration. Additional sample specific considerations such as the relative intensity of the resonant and nonresonant contributions to the CARS signal also affect the sensitivity of the CARS/MCARS system. The SNR of a CCD detector may be described as:

$$SNR_{CCD} = \frac{M\Phi\eta t}{\sqrt{M\Phi\eta t + MDt + N_r^2}}, \tag{40}$$

where M is the number of binned pixels, Φ is the incident photon flux (photons/pixel/s), η is the quantum efficiency (wavelength dependent), t is the integration time, D is the dark current (e/pixel/s), and N_r is the read noise (e rms/pixel). Previously, I have analyzed the SNR of the CCD spectrometer for a sample of PS and PMMA beads, and I compared the SNR of the CCD detector under different A/D speed settings with those of other available CCD spectrometers (Table 6 presents the specifications of the simulated CCD cameras) and a PMT [gain: 10^6, anode radiate sensitivity: $8x10^4$, noise figure (F): 1.3, and anode dark current: 1 nA] as shown in Figure 58 [85]. In this figure, the solid portions of the lines represent the available integration times for each detector, and the dashed lines represent a theoretical continuation of these lines if the electronics allowed these speeds *ceteris peribus*. One can see that the CCD detectors are theoretically more sensitive than the PMT with integration times below 100 μs– this of course being a major drawback of CCD detectors is that they currently cannot operate at these speeds. Looking at the currently implemented detector, one can see that the low-speed A/D would have a significant SNR advantage over the high-speed A/D due to the reduced read noise by a factor of 4, but at operable speeds, there is little distinction between the two. As the system is going to be primarily used within the flow cytometer, speed is a large consideration; thus, the high-speed A/D is the typical setting with a 1 ms integration time.

Table 6: Specifications used to simulate SNR versus integration time of various CCD detectors (see Fig. 6): Newport InstaSpec X (low- and high-speed A/D settings) (Newport Stratford, Inc., Stratford, CT), Andor DU970N-BV (Andor Technology plc, Belfast, Ireland) , Princeton Instruments/Acton (PI/Acton) PIXIS:100F (Princeton Instruments, Trenton, NJ). These performance specifications are typical numbers and do not necessarily represent optimized settings, but rather typical values [89–91].

	InstaSpec, Slow A/D	InstaSpec, Fast A/D	Andor	PI/Acton
Binned Pixels	256	256	200	100
Readout Speed	100 kHz	2 MHz	2.5 MHz	2 MHz
Dark Current (e/p/s)	0.001	0.001	0.006	0.002
Read Noise (e/p/s)	6	24	8	12
Spectral Rate (/sec)	35	185	602	450

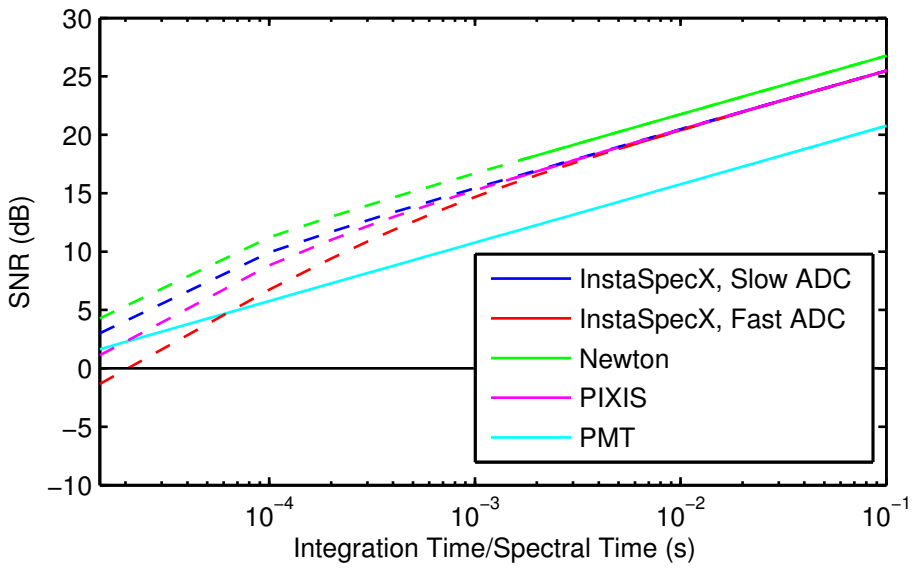

Figure 58: SNR of a variety of detectors: Newport InstaSpec X (low- and high-speed A/D settings [denoted ADC]), Andor DU970N-BV, PI/Acton PIXIS:100F, and a generic PMT. The solid-line portion of each plot represents currently available speeds. The dashed-portion of each plot is the calculated SNR if there were no hardware restrictions on the integration time. The black horizontal line denotes where SNR = 0 dB. Reprinted from [85]. © Optical Society of America.

Another consideration of the CCD sensitivity is the pixel binning. As described in Eq. 40, pixel binning can improve the SNR by tying neighboring pixels together; thus, increasing the number of photons collected per pixel group. The trade-off from binning is spectral resolution. To optimize and characterize the effects of pixel binning, I measured the MCARS spectrum from a sample of objective oil as a function of integration time and binning (N.B., the CCD chip is always full-vertically binned; thus, binning in this context implies along the horizontal/spectral axis). It should be noted that in this context, integration times refers to the time between spectral acquistions to best approximate the full window of time for which the CCD can accept charge. For example, as discussed in Section 3.4, a 1 ms integration time results in an operating speed of 100 Hz; thus, for this characterization, I would denote the integration time as 10 ms. The speed of spectral acquisitions was measured through the "Logic Out" electrode of the CCD camera on an oscilloscope. The "Logic Out" electrode generates a TTL signal that is in the high state during acquisitions. For no pixel binning, the spectrum was measured for integration times longer than 100 ms. For the scenarios when pixel binning was used, however, the integration time was limited by detector saturation; thus, for 8x binning, one could only integrate up to 13.8 ms. Figure 59 shows the recorded SNR of the dominant CH-stretch peak ($\sim$2859 cm^{-1}) and the theoretical SNR calculation. One can see that for no binning, the SNR calculation closely follows the experimentally measured data. The 4x binning scenario experimentally demonstrates an SNR enhancement of 1-3 dB over not binning, but the theoretical calculations indicate that the improvement should be larger. The disparity between the theoretical calculations and experimental data results from the fact that the individual MCARS spectral features contain a limited bandwidth, but the theoretical calculation assumes that the photon flux is constant over all pixels. This is to say that after the spectral coverage of the binned pixels becomes larger than the width of the MCARS line shapes, there is only a reduction

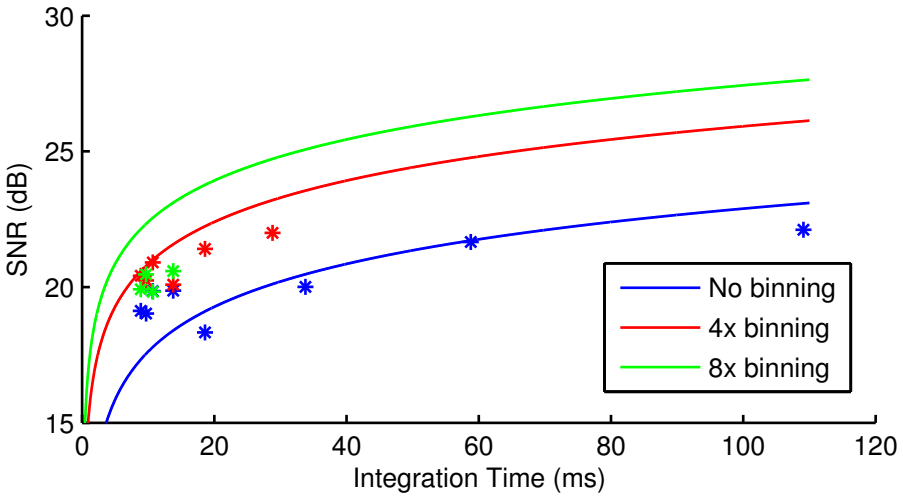

Figure 59: Experimentally measured (stars) and theoretically calculated (solid lines) SNR as a function of integration time for the 2879 cm^{-1} (CH-stretch) peak of a sample of objective oil for no [spectral] CCD binning (blue), 4x binning (red), and 8x binning (green). As the binning increases, the deviation between the theoretical calculations and experimental measurements increases due to the finite bandwidth of the CH-stretch peak. One can see that the SNR increase between 4x and 8x binning is minimal (and the spectral resolution is decreased by a factor of 2); thus, I have selected 4x binning for experimental use in the system to balance spectral resolution and SNR.

in resolution and an increase in noise. This is demonstrated for the 8x binning case in which the SNR is not greatly different from the 4x binning case and the difference between the experimental results and the experimental calculation has expanded. From these results, I find that 4x binning provides the best balance of resolution and sensitivity at high speed. Figure 60 shows the SNR as a function of integration time for the three dominant peaks of the MCARS spectrum. As shown in this figure, even the relatively weak peaks demonstrate an SNR above 10 dB at minimum integration times.

Beyond system considerations, sample composition also plays a critical role in determining the MCARS response. As described in Chapter 2, the Raman response is linearly proportional to the concentration of molecular scatterers, but the CARS response is quadratically proportional; thus, the CARS signal is significantly stronger

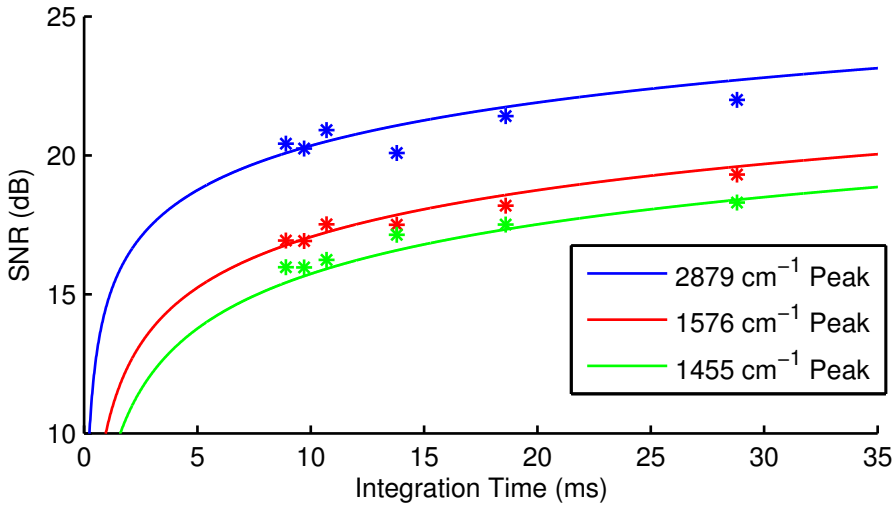

Figure 60: Experimentally measured (stars) and theoretically calculated (solid lines) SNR as a function of integration time for the 2879 cm^{-1} (blue), 1576 cm^{-1} (red), and 1455 cm^{-1} (green) peaks of a sample of objective oil (4x binning).

for dense scatterers. To characterize the sensitivity of the MCARS spectrometer to scatterer concentration, I analyzed two sample that represent relative extremes: methanol as a representative small molecule, and canola oil that is representative of the dense lipid scatterers found within cells. To characterize the system sensitivity to each sample, several aliquots with various levels of dilution were prepared. The MCARS spectra were recorded under flow cytometric conditions: high-speed A/D, high gain, 4x pixel binning, and a 1 ms integration time (100 Hz). Additionally, the MCARS spectra were processed with the KK reconstruction algorithm to remove the effects of the NRB and to better linearize the intensity as a function of concentration. For each experiment spectral features were selected and their KK reconstructed intensity recorded for each concentration. The sensitivity was quantified by constructing a linear regression from these points and finding where this regression fell below the background level. The results of these experiments represent the only quantitative sensitivity results for an MCARS microspectrometer.

The first experiment analyzed the system sensitivity to methanol. Methanol is a small hydrocarbon representative of small molecule analytes that are miscible in

aqueous media. For this experiment, the diluent was water, which primarily generates NRB and has no actual overlapping Raman features with methanol. Figure 61(a) shows the MCARS spectra of methanol (red) and water (blue). Figure 61(b) shows the KK reconstructed spectra of methanol with the MCARS spectra of water used to approximate the NRB. Although the NRB can be approximated in other fashions, such as by measuring the MCARS spectra of glass– a commonly employed method, using water, because it is the diluent, simplifies the sensitivity measurement as the KK-reconstructed spectra contain only the contributions from the methanol. The spectral feature from methanol used to monitor the sensitivity is the $\sim 2950 cm^{-1}$ CH-stretch peak. I analyzed several aliquots of the methanol-water blend ranging from 20% methanol to 1%. Figure 62 shows the spectral peak ratios as a function of methanol concentration. Additionally, the figure plots a linear regression of the data points and the measured background due to noise, which serves as the baseline. From this figure, one can observe that the system is sensitive down to approximately 0.97% methanol, which equates with a molar concentration of 242 mM (the density was measured to be $\sim$ 0.79 g/mL, and the molecular weight is 32.04 g/mol [a well-characterized standard value]). A 1% solution of methanol was measured and the spectral peak strength is approximately at the same level as the noise. With a ~ 1 μm^3 focal volume, this is approximately 1.46×10^8 molecules.

The second experiment analyzed the system sensitivity to canola oil. Canola oil is a vegetable oil that has a lipid content of almost exclusively triacylglycerides (TAGs) [92], which are the dominant storage lipids in many organism cells (e.g., *S. cerevisiae*) [93, 94]. TAGS are not a single type of lipid, but rather a family of lipids composed of an ester derived from glycerol and three fatty acids (the exact combination of fatty acids specifies the exact type of TAG). Canola oil is predominantly composed of TAGs derived from three unsaturated fatty acids: oleic acid (48%), linoleic acid (32%), and linolenic acid (9.3%); although, at least 7 other fatty

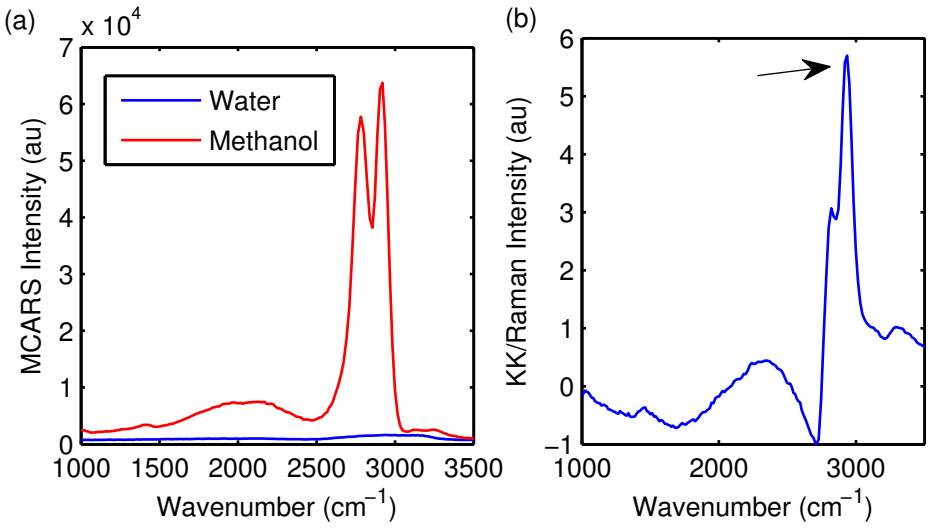

Figure 61: (a) The MCARS spectra of methanol (red) and water (blue). (b) The KK reconstructed spectra of methanol with the MCARS spectra of water used to approximate the NRB. For analysis, I selected the $2950cm^{-1}$ peak (arrow).

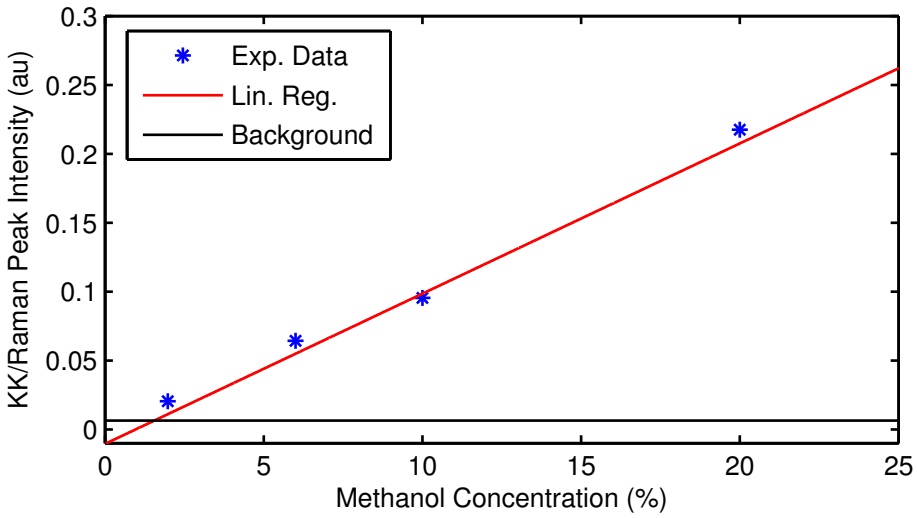

Figure 62: Plot of the KK reconstructed peak at $\sim 2950.1cm^{-1}$ as a function of analyte concentration (experimentally measured data: blue stars, linear regression: red, background noise level: black). One can see the minimal methanol concentration is $\sim 0.97\%$, which corresponds to a molar concentration of ~ 242 mM.

acids contribute [92]. The predominant saturated fatty acid is palmitic acid (7%). Relevant to the expected MCARS spectrum, one expects to see a peak around 1600-1650 cm^{-1}, which is created by the C=C bond stretching. In order to quantify the sensitivity of the system to the analyte, I needed to find a solvent that could dissolve all of the sample constituents. Alcohols, such as methanol, are used frequently in the energy industry to selectively dissolve certain canola oil constituents (canola oil is a prime candidate for the production of biodiesel). I found that acetone was able to completely dissolve the canola oil without any noticeable traces of the analyte. To qualify the strength of the sample-of-interest, two points from within the spectra were selected and compared their relative intensities. One of the points corresponds to a local maximum of the analyte, and the other point a local maximum for the solvent. The NRB was approximated by the MCARS spectrum from a glass coverslip– a common sample used for this purpose). Using acetone, however, presents its own challenges for use as a solvent as its dominant Raman band overlaps with the dominant Raman band of canola oil (as shown in Figure 63), acetone has a strong Raman band at 2935 cm^{-1}, which overlaps with the 2887 cm^{-1} peak of canola oil. A somewhat better option is monitoring the peak at 1639 cm^{-1} of canola oil (C=C stretch) and the 1692 cm^{-1} peak for acetone (C=O stretch). Although these peaks do overlap, the spectral separation provides the necessary contrast. Figure 64 shows the spectral peak ratios as a function of methanol concentration. Additionally, the figure plots a linear regression of the data points and the ratio of these spectral locations for Acetone. From this figure, one can see that the system is sensitive down to approximately 4.61% canola oil, which equates with a molar concentration of 40 mM (the density was measured to be 0.771 g/mL, and the molecular weight is assumed to be 876.6339 g/mol [92]). With a $\sim$1 μm^3 focal volume, this is approximately 2.44×10^7 molecules. In many circumstances, lipids do no dissolve within cells, but rather form solid organelles [95–97]. Under this assumption, a spherical lipid inclusion would need

a diameter of at least 0.44 μm. It should be noted that using the smaller peak at 1639 cm^{-1} demonstrates the sensitivity of the system to that peak. Detecting the larger peak at 2935 cm^{-1} would demonstrate increased sensitivity. For methanol, the sensitivity degradation between monitoring of its smaller peak at 1461 cm^{-1} and the dominant peak is a factor of ∼25. This appears to be the same as the ratio between the dominant CH-stretch peak and the smaller CH_3-deformation peak, which was measured to be ∼25. As the ratio of the dominant CH-stretch peak and the C=C stretch peak is not as large (∼10), one expects an actual improvement in sensitivity measuring the CH-stretch peak at 2935cm^{-1} of around a factor of 10. With this improvement, the sensitivity would be ∼4 mM, which would reduce the measurable diameter for a spherical inclusion to ∼44 nm.

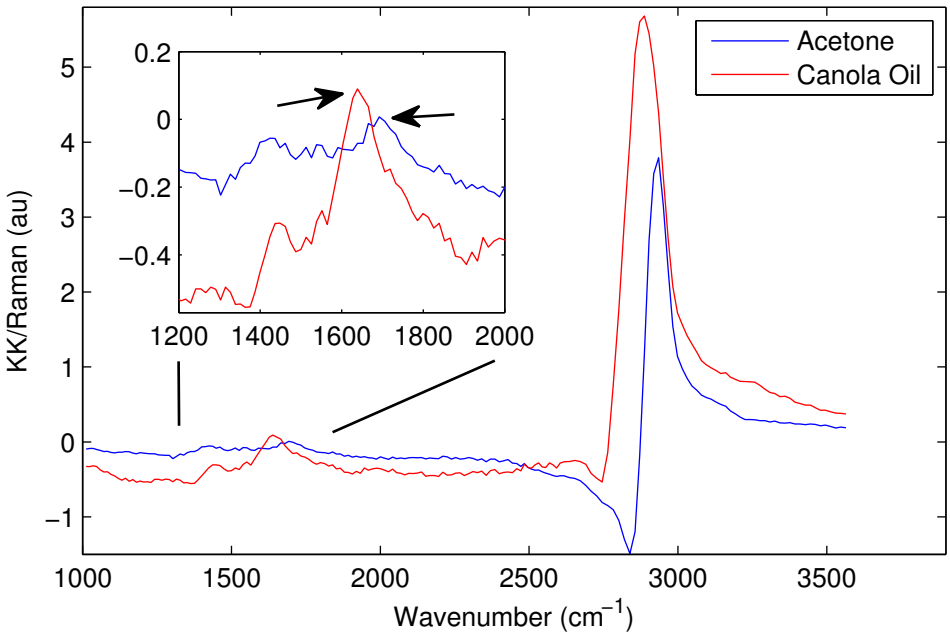

Figure 63: The KK reconstructed spectra of acetone (blue) and canola oil (red). For analysis, I selected two spectral points (arrows) corresponding to spectral maxima of the analyte and the solvent: the 1639 cm^{-1} C=C stretch peak of canola oil and the 1692 cm^{-1} C=O stretch peak of acetone.

In this subsection, I characterized the sensitivity of the MCARS spectroscopy

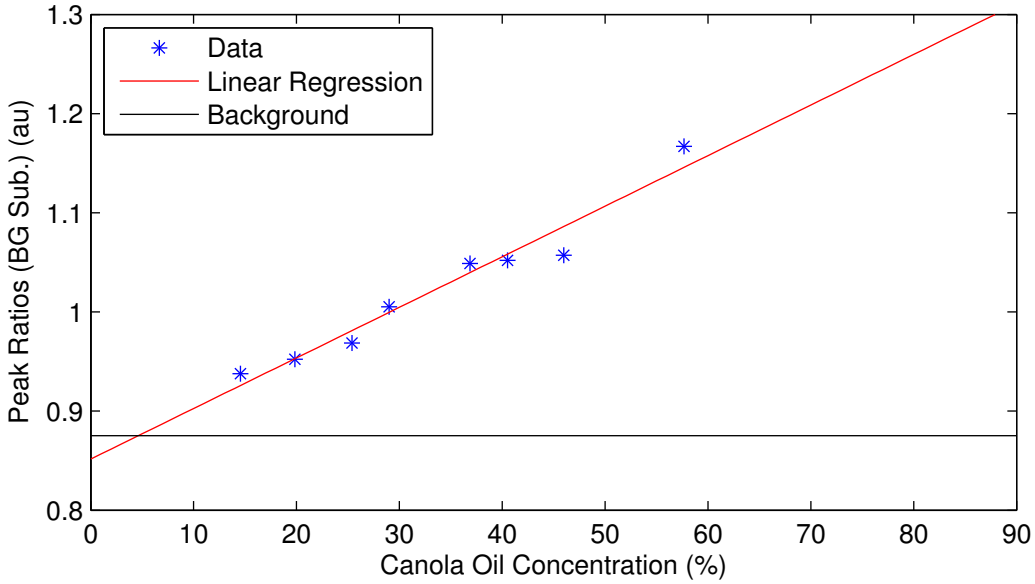

Figure 64: Plot of the KK reconstructed peak ratios between the 1639 cm^{-1} peak of canola oil and the 1692 cm^{-1} peak of acetone as a function of analyte concentration (experimentally measured data: blue stars, linear regression: red). The ratio of these peaks for the pure solvent is shown in black to identify the minimal levels of detection. One can see the minimal canola oil concentration is $\sim$4.61%, which corresponds to a molar concentration of 40 mM.

subsystem based on sample composition and detector performance. I presented evidence that this system is sensitive down to at least 40 mM (possibly below 4 mM) for Canola Oil and ∼242 mM for methanol, representative large and small molecules, respectively. For TAG lipid bodies, I estimate that the system can detect inclusions with a diameter of ∼0.44 μm using the C=C stretch band; although, I believe using the CH-stretch band presents sensitivities to bodies of ∼40 nm. Additionally, I presented the CCD spectrometer performance characteristics under a variety of conditions. I conclude that the CCD spectrometer best performs at high-speed with a 4x pixel binning as to maximize the signal collection, minimize the noise, and to maintain spectral resolution. Additionally, for strong signals, as is often the case for lipids, the CCD spectrometer speed is limited by electronics hardware data transfer rates and not by system sensitivity. This characterization indicates that MCARS flow cytometry, *ceteris peribus*, could operate at speeds considerably faster than the 100 Hz afforded by the current CCD hardware; although, for small molecules, concentrations would need to be considerable.

4.1.3 Characterization of Fluorescent Labels Effect on MCARS Flow Cytometry

Coherent Raman techniques such as CARS and MCARS are powerful techniques for the label-free analysis of sample constituents. Although MCARS is typically limited by the available sources to 100's of μM to mM concentrations, CARS microscopy systems have demonstrated improved sensitivity by a factor of $\sim$50 [98]. Even with these enhanced sensitivities, fluorescent labeling technology is undeniably strong for low concentration molecular analysis. Immunofluorescent techniques, for example, are capable of detecting a few hundred surface receptors [1] (although for intracellular analysis, the cell must be fixed as the antibody cannot cross the cell membrane). With the specificity of antibodies, and the sensitivity of fluorescent techniques, immunofluorescent technology is not likely to be superseded by label-free techniques anytime soon. As such, I wish to analyze the unique concept of using MCARS flow cytometry in conjunction with fluorescence detection flow cytometry. To this end, I investigated the spectral response to fluorophores. Specifically, I analyzed the MCARS spectra emanating from 4 different (and very commonly analyzed) fluorochromes: 5-carboxytetramethylrhodamine (5-TAMRA), sulforhodamine 101 (SR101), fluorescein, and nile blue. Figure 65 shows the absorption (a) and emission (b) profiles of these four fluorochromes (data collected from [99]). It should be noted that these emission and absorption profiles are for the fluorochromes dissolved in a particular solvent (see caption). In all experiments, fluorochromes were suspended in DMSO, which (approximately) does not contribute to the pH of the suspension; thus, it may be assumed that the pH is $\sim$7 for all samples. Additionally, these experiments represent only the fluorophore response under MCARS excitation conditions; thus, the fluorescent samples are not pumped with any signal other than the pump and Stokes sources, as well as the anti-Stokes photons generated from the CARS process. In many commercial flow cytometers, the excitation sources are focused individually

along the sample flow path– not collinearly, as to provide a mechanism to isolate the fluorescent emission from each laser source. In a combined MCARS and fluorescent flow cytometerm similar isolation techniques would be necessary to prevent the pumped fluorescent signal from interfering with the MCARS spectrum.

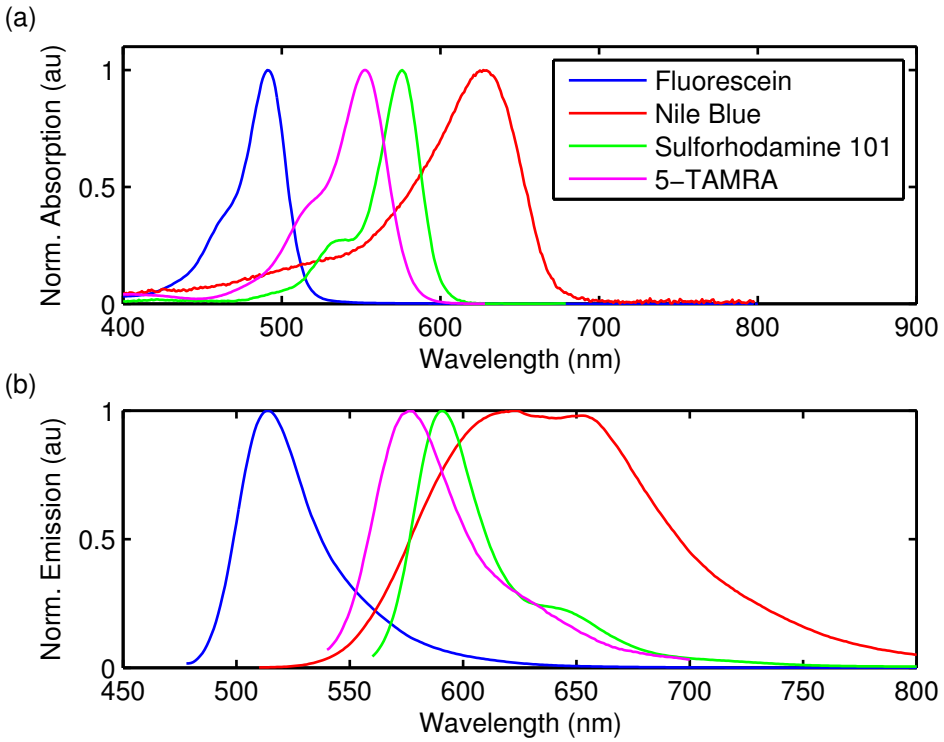

Figure 65: (a) The absorption profile of fluorescein [blue, solvent: tris(hydroxymethyl)aminomethane) (THAM), pH:9], Nile Blue (red, solvent: ethanol), 5-carboxytetramethylrhodamine (5-TAMRA) (green, solvent: methanol), sulforhodamine 101, and nile blue [99].

SR101 is often used as a reactive dye that ionically binds to proteins [1]. In this test, I analyzed a 1 mM sample of SR101 diluted in DMSO (R-14792, Molecular Probes, Eugene, OR). Figure 66(a) shows the MCARS spectra of SR101 and DMSO recorded under typical flow cytometric conditions. Additionally, Figure 66(b) shows the KK-reconstructed spectrum using the signal from DMSO to approximate the NRB. One can see no noticeable spectral features through the 1000-3200 cm^{-1} region. One can detect, however, absorption of the primary peak at $\sim 2900 cm^{-1}$ of DMSO,

and there exists slight fluorescent emission in the wavelength region as indicated by the CH-stretch peak reduction but a rise in neighboring spectral regions. Additionally, there exists a stronger fluorescent emission, as shown in Figure 67, at around 622 nm, which overlaps with the $\sim$3600 cm^{-1} of the Raman spectrum. As this sample is 1 mM, and most application of SR101 use at least a 100 fold decrease in this concentration, it is safe to assume that SR101 could be applied to samples of interest for MCARS analysis without any significant influence.

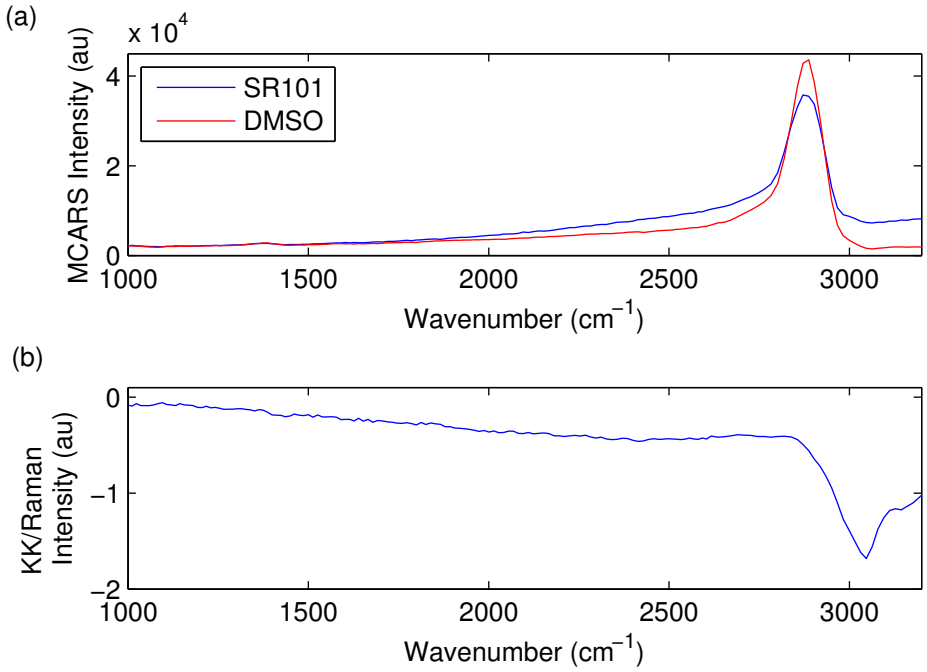

Figure 66: (a) MCARS spectra of SR101 (blue) and DMSO (red). The CH-stretch peak is slightly reduced in the SR101 solution and there is slight fluorescent emission. (b) KK reconstructed spectrum of SR101 using the MCARS spectrum of DMSO as the NRB estimation. There exist no noticeable Raman spectral features other than a reduction in the CH-stretch peak intensity.

Nile blue perchlorate is a positively charged phenoxazone that is used for lipid staining (specifically, acidic lipid staining) [1, 100–102]. The spectral absorption and emission maxima of nile blue in water is $\sim$627 and 663 nm, respectively [100]. Figure 68 shows the recorded MCARS spectra of a solution of Nile Blue in DMSO at a variety of concentrations (relative to a 1 mM stock solution [R-14792, Molecular

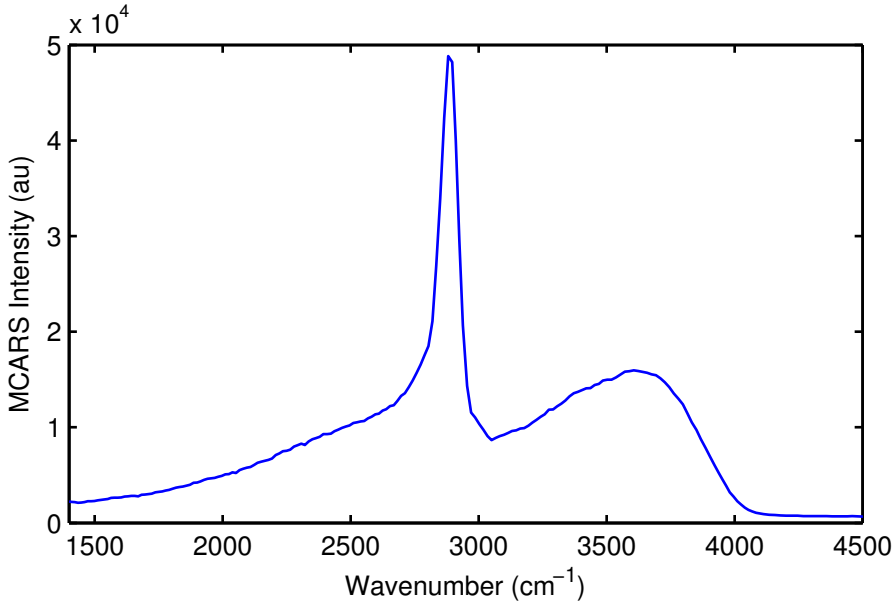

Figure 67: MCARS spectrum of SR101 1 mM solution with the spectrometer observing the spectral region corresponding to Raman energies of $\sim$1500-4500cm^{-1}. The SR101 solution generates a fluorescent signal centered at $\sim$3600cm^{-1}, which corresponds to 622 nm. This signal is spectrally removed from most Raman bands; thus, its practical influence in MCARS spectroscopy is limited.

Probes, Eugene, OR]). Interestingly, one notices that Nile Blue absorbs a significant portion of the spectrum between $\sim$2000 - 3200cm^{-1} at high concentrations and there exists no noticeable MCARS component from the nile blue itself. Figure 69 demonstrates the reduction in the intensity of the CH-stretch band from DMSO at $\sim$2930cm^{-1} as a function of nile blue concentration. I have fit an exponential decay (following the Beer-Lambert Law) profile to the data and found that the MCARS spectrum is completely absorbed around an $\sim$80% concentration ($\sim$800 μM). On the other end of the spectrum, I find no noticeable reduction in the CH-stretch peak intensity with nile blue concentrations below $\sim$0.05% (50 μM); although, with increased pump and Stokes power the effect could increase as stronger absorption energy would arise. With sensitivities this low, one needs to carefully consider the use of nile blue staining prior to MCARS analysis. Although in DMSO, the absorptive property was limited to >2000 cm^{-1}, nile blue is very sensitive to the pH of its environment;

thus, the absorption band could shift dramatically [100].

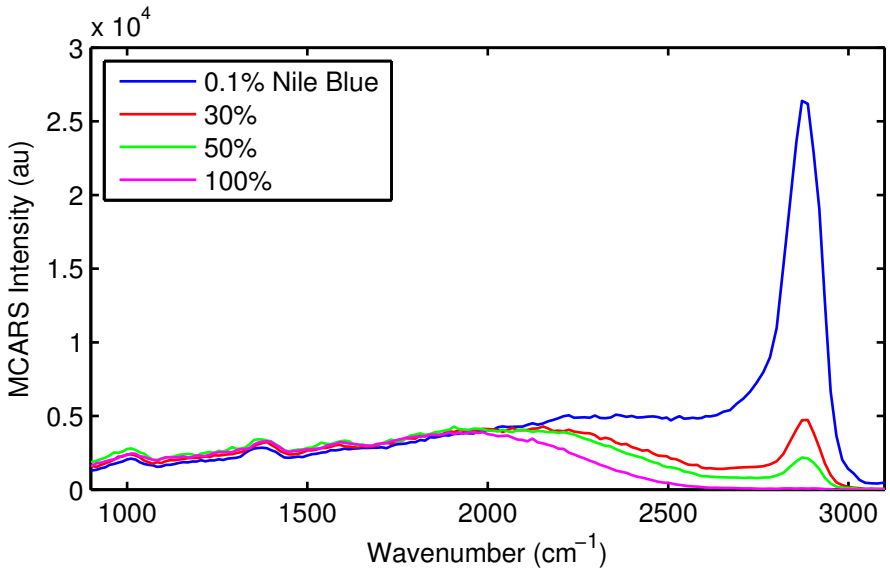

Figure 68: MCARS spectra of a solution of Nile Blue in DMSO at a variety of concentrations (relative to a 1 mM stock solution).

Fluorescein is one of the most common fluorophores (as well as its derivatives, such as fluorescein isothiocyanate [FITC]) [1]. The maximum absorption and emission wavelengths of fluorescein are approximately 491 and 514 nm, respectively (although, there is also a strong absorption band below 300 nm as well). I analyzed a sample of 1 mM fluorescein and observed no noticeable spectral features in the MCARS spectrum (see Figure 70. Under illumination from a halogen lamp, there was slight fluorescent noticeable outside of the Raman spectral window ($<$ 600 nm, corresponding to $>$ 4200 cm^{-1} within the Raman viewable window). Observing these results, fluorescein appears to be an ideal candidate for use with MCARS flow cytometry as the absorption and emission bands are well below the MCARS spectral window. Additionally, many of the most common flow cytometry fluorochromes are derived from fluorescein, such as fluorescein isothiocyanate (FITC); thus, further promoting this cooperative use of MCARS and fluorescein-derived fluorochromes.

5-TAMRA (also known as TMRh or TMR) is a common fluorochrome for DNA studies due to the ease of covalently attaching it to DNA [103, 104]. 5-TAMRA

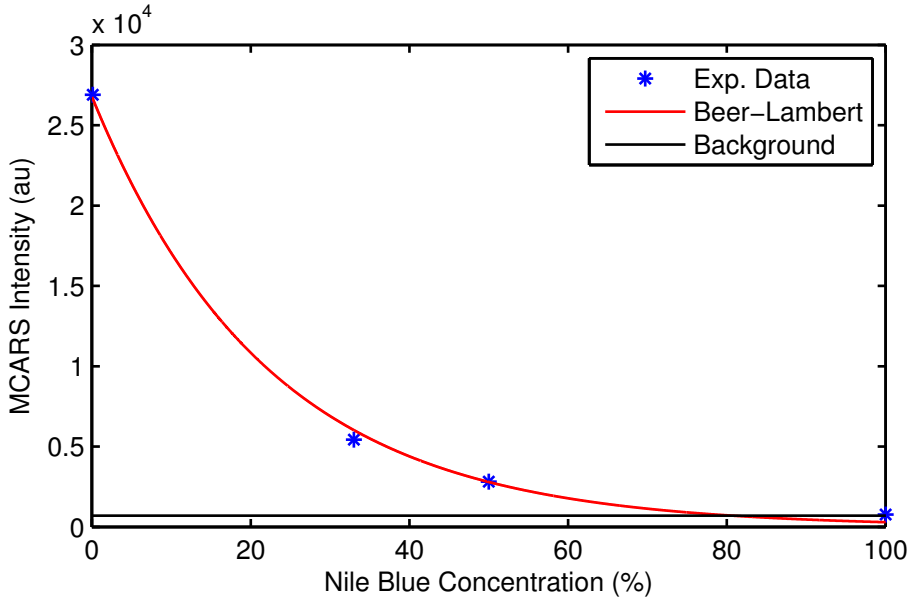

Figure 69: Measured MCARS peak intensity (blue, stars) for a solution of nile blue in DMSO at various concentrations (relative to a 1 mM stock solution). An exponential decay profile is fit to the data representing the absorption of photons as described by the Beer-Lambert Law (red). The lowest detectable signal is identified by the background signal level (black).

has absorption and emission maxima at approximately 553 and 576 nm, respectively (at pH 7) [99]. I analyzed a sample of 1 mM 5-TAMRA under flow cytometric conditions and observed no noticeable spectral peaks, as shown in Figure 71. The peak intensity of DMSO was reduced by approximately 4% and the background (either due to NRB or fluorescence) rose by $> 65\%$ above $3000cm^{-1}$. Additionally, there was a slight increase of the background below $\sim 2775cm^{-1}$ by $\sim 8\%$. To observe the spectral features that may arise from higher excitation powers, the pump and Stokes powers were increased to their maximum ($\sim$40 mW Stokes, 50 mW pump), as shown in Figure 72 (often the pump and Stokes intensities are reduced to prevent photodamage to certain, susceptible samples and/or to prevent CCD saturation, such as seen in the figure). In this figure, there are no noticeable Raman-related features from the fluorochrome; although, there is a noticeable increase in the background. Below $2775cm^{-1}$ the background increased by $\sim 8\%$ and up to $\sim 65\%$ beyond $3000cm^{-1}$.

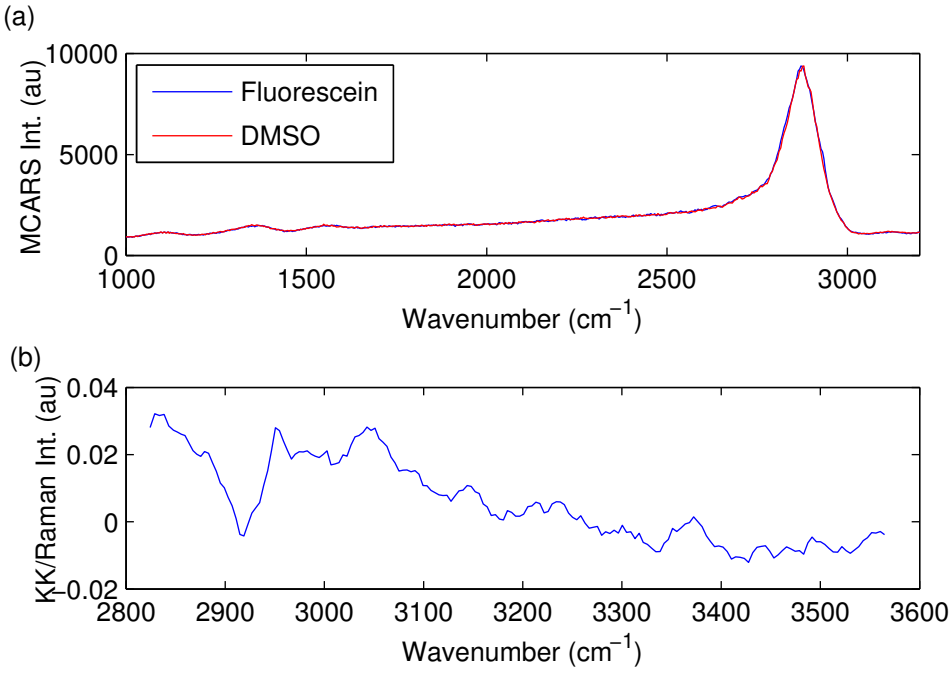

Figure 70: (a) MCARS spectra of fluorescein (blue) and DMSO (red). The MCARS spectra are virtually identical; thus, there appears to be no contribution from the 1 mM solution of fluorescein in DMSO. (b) KK reconstructed spectrum of fluorescein using the MCARS spectrum of DMSO as the NRB estimation. There exist no noticeable Raman spectral features other than a reduction in the CH-stretch peak intensity above the KK reconstruction noise.

With this apparent linear rise in background level with the strength of the MCARS spectral intensity, the fluorescence from 5-TAMRA at practical concentrations (< 100 μM) (as pumped from the CARS process) would likely not compete with the MCARS spectrum. As such, 5-TAMRA appears to be a compatible label for use with MCARS.

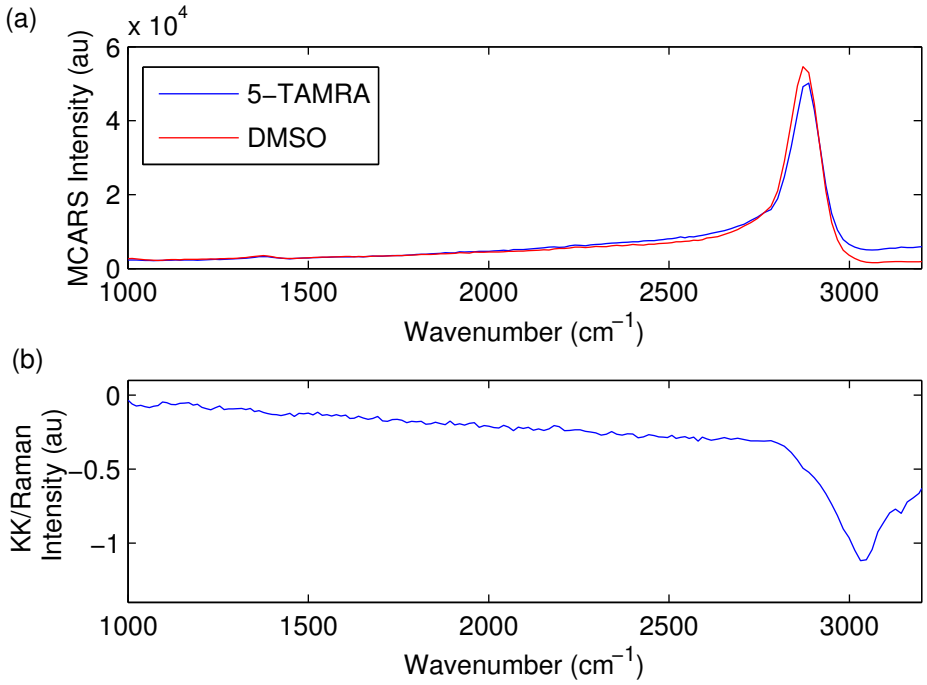

Figure 71: (a) MCARS spectra of 5-TAMRA (blue) and DMSO (red). The CH-stretch peak is slightly reduced in the 5-TAMRA solution and there is slight fluorescent emission. (b) KK reconstructed spectrum of 5-TAMRA using the MCARS spectrum of DMSO as the NRB estimation. There exist no noticeable Raman spectral features other than a reduction in the CH-stretch peak intensity.

The addition of MCARS spectroscopic information has the potential to revolutionize flow cytometry by dramatically expanding the measurable molecular information without the further addition of fluorescent labels. This addition of MCARS spectroscopy, though, does not preclude the use of fluorescent labeling technology, which has dramatically evolved over the last century. In flow cytometry, for example, immunofluorescent techniques are capable of highlighting and targeting individual

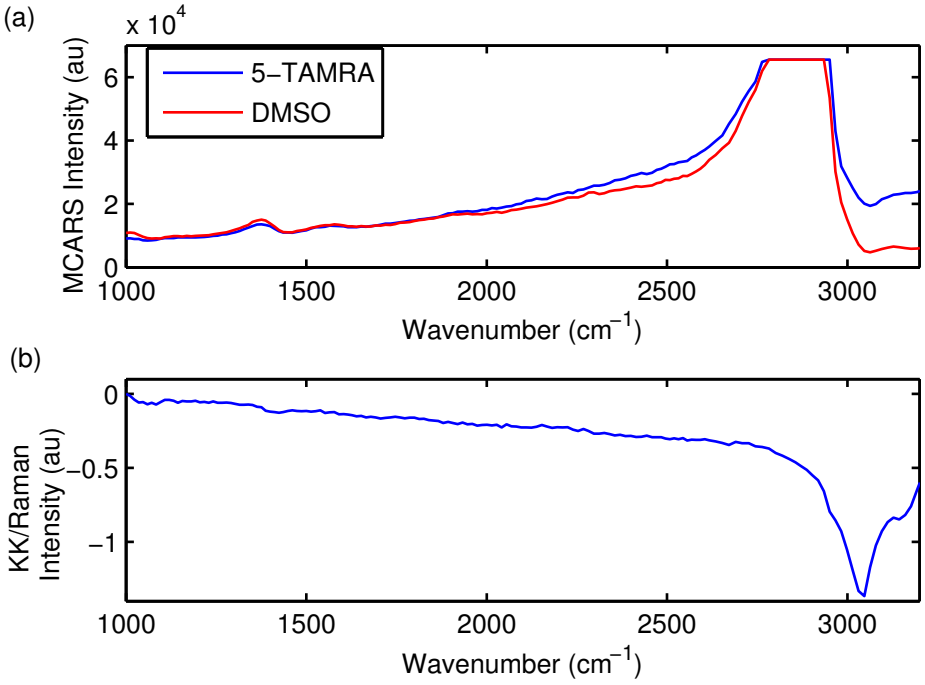

Figure 72: (a) MCARS spectra of 5-TAMRA (blue) and DMSO (red) with maximum excitation powers. The CH-stretch peak is slightly reduced in the 5-TAMRA solution and there is slight fluorescent emission. (b) KK reconstructed spectrum of 5-TAMRA using the MCARS spectrum of DMSO as the NRB estimation. There exist no noticeable Raman spectral features other than a reduction in the CH-stretch peak intensity.

surface antigens. This level of molecular specificity and sensitivity is not yet available with MCARS spectroscopy; therefore, to extract the most molecular information in MCARS flow cytometry, will likely require the continued use of some fluorescent labels.

4.2 Elastic Scatter Platform

Elastic scatter measurements are used in flow cytometry to provide rough morphological information. In cellular analyses, FSC measurements provide qualitative information about cell size, and the SSC measurements provide insights into the internal granularity. Deriving quantitative information, however, is a much more difficult task as FSC and SSC are both affected by a number of factors including sample size, shape, surface roughness, and index of refraction (of each cellular components). With this in mind, I will characterize the performance of the elastic scatter module of the developed label-free flow cytometer and identify occasions in which quantitative analysis may be achievable. To characterize the system, I will use polymer microspheres that are often used as model cells.

The first analysis of the elastic scatter platform analyzes the effect of sample flow rate on elastic scatter measurement. For this analysis, a suspension of polystyrene beads with a $6\mu m$ diameter (Duke Standards 4206A, Thermo Scientific, Waltham, MA) were injected into the flow cell with a 500 μL syringe and were analyzed at various sample flow rates. At each flow rate, the FSC and SSC elastic scatter measurements were recorded at 100 kHz. Figure 73 shows a recorded FSC and SSC waveform for a flowing polymer bead. This figure labels many of the measurable parameters that will be referenced through out this work. Figure 74 is a scatter plot showing the measured SSC width (N.B., FSC width is the same as SSC width for these solid particles) with respect to FSC. The sample flow rate was varied from 0.3 $\mu L/min$ (6.266 mm/s) to 1.2 $\mu L/min$ (25.07 mm/s). As shown in this figure, the FSC remains the same regardless of flow rate, which is expected with the morphology of the particles remaining the same through out the test. Although the FSC remains constant, the SSC width decreases with increasing flow rate. Additionally, one can see that the spread of the SSC width increases with decreasing sample flow rate. This is not only due to the increasing elastic scatter resolution with flow rate reduction,

but also the effects of optical force, friction between the particles and the bottom of the flow channel (at slower speeds, the dense polymer spheres roll along the bottom of the channel [as opposed to biological cells that tend to flow mid-channel]), and the decay of the hydrodynamic focusing. Figure 75(a) compares the experimentally measured mean SSC width (error bars show the standard deviation) with the theoretically calculated values as a function of sample flow rate. One can see that the experimental data agrees well with the theoretical calculations, demonstrating the inverse proportionality between SSC width and the sample stream flow rate (and velocity). Figure 75(b) shows the experimental and theoretical results for the same experiment over a larger range of flow rates: from 1.2 $\mu L/min$ (25.07 mm/s) to 4 $\mu L/min$ (83.55 mm/s). One can see the expected reduction of the SSC width and the continued reduction of the standard deviation.

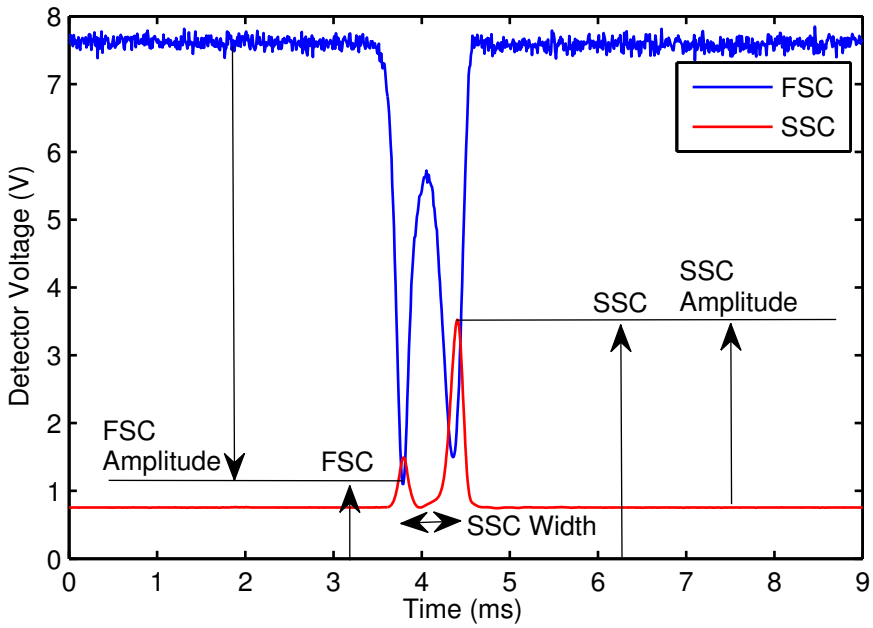

Figure 73: FSC (blue) and SSC (red) waveform recorded from two amplified silicon detectors. Arrows and labels identify various measurable parameters, such as FSC and SSC, FSC and SSC amplitude, and FSC and SSC (width) (N.B.: in this example SSC and FSC widths are the same; thus, the labeling of FSC width was neglected for pictorial clarity).

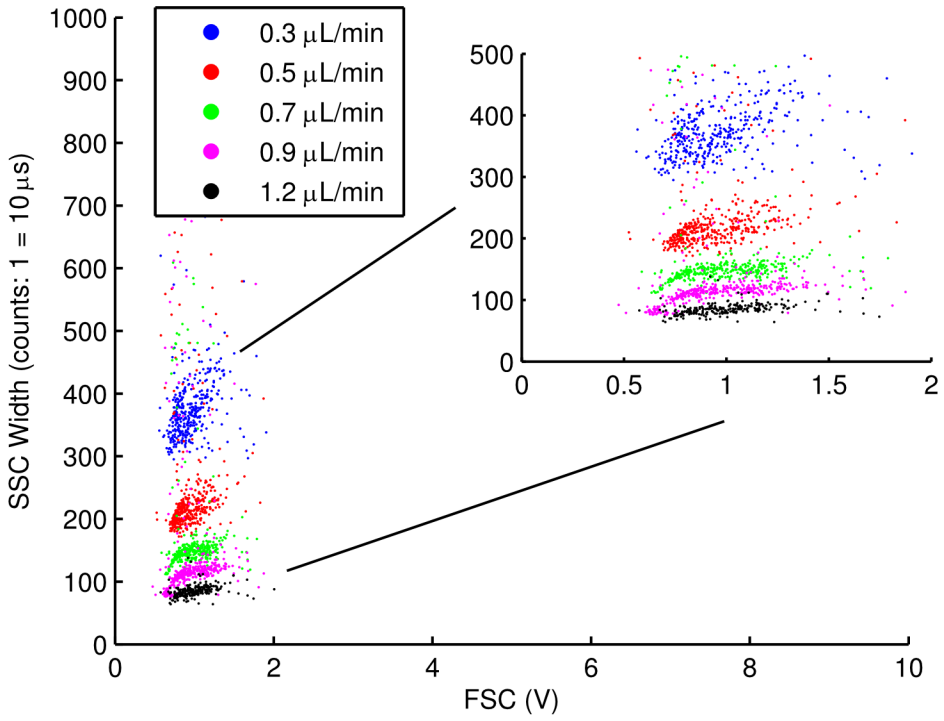

Figure 74: Experimental measurement of SSC width versus FSC for a polystyrene bead suspension (6 μm diameter) fed into the flow cell at different volumetric rates. Inset, close-up view of the measurement. As the volumetric flow rate of the sample increases, the measured SSC width decreases.

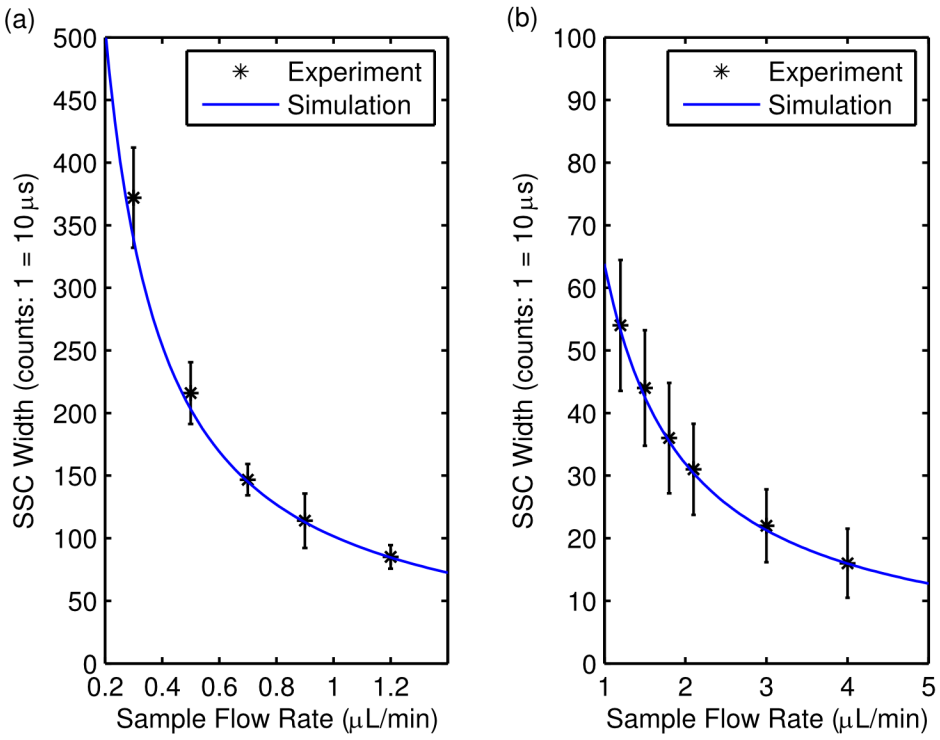

Figure 75: (a) SSC width versus sample flow rate for a 6 μm polystyrene bead as measured experimentally (black stars with error bars denoting one standard deviation) and calculated theoretically (blue) over the range of 0.2 - 1.4 $\mu L/min$. (b) (a) SSC width versus sample flow rate for a 6 μm polystyrene bead as measured experimentally (black stars with error bars denoting one standard deviation) and calculated theoretically (blue) over the range of 1 - 5 $\mu L/min$.

Although not directly related to the elastic scatter measurements, Figure 76 shows the MCARS spectral SNR as a function of flow rate for the analysis presented in Figure 75(a) (N.B., the data has been centered so that the SNR at 0.3 $\mu L/min$ is 0). In this figure, the experimental data and the theoretical calculations closely overlap. Additionally, one sees that the SNR data more closely follows theory than the elastic scatter data in Figure 75, which is due to the fact that the particles are much larger than the focal volume; thus, with small deviations in space, the focal spot is still completely within the solid particle. The elastic scatter, on the other hand, is probed by a much larger cone of light– not just the focal volume; thus, the sensitivity is heightened.

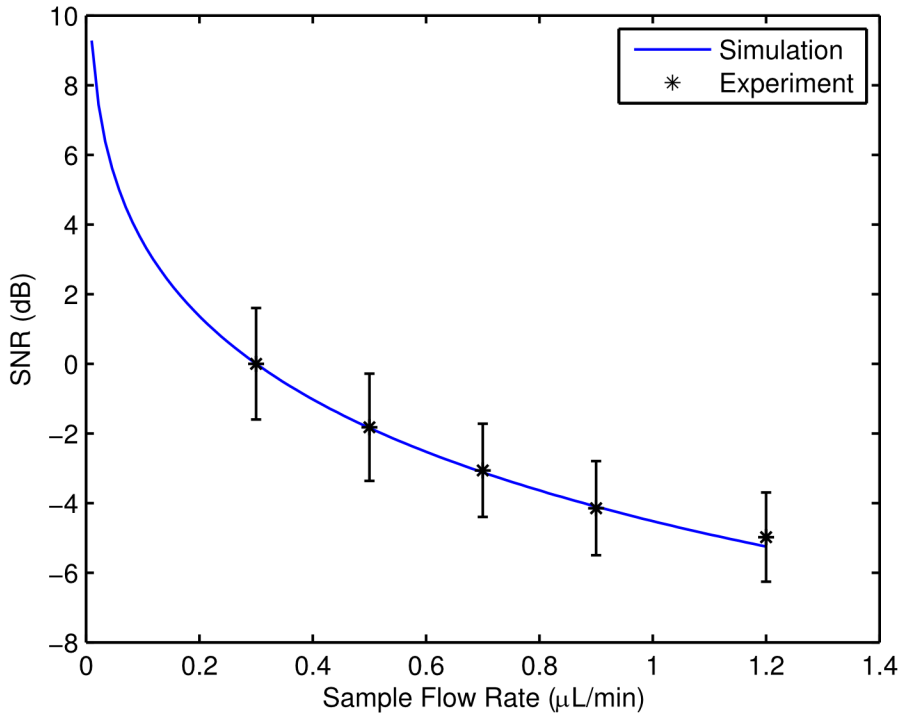

Figure 76: Experimentally measured (black stars with error bars denoting one standard deviation) and simulated (blue) SNR of the CH-stretch band of 6 μm polystyrene beads as a function of sample volumetric flow rate. The SNR is relative to the actual SNR at a flow rate of 0.3 $\mu L/min$.

Elastic scatter measurements provide a level of information about the size and

internal complexity about the samples of interest. Although elastic scatter, especially FSC, is related to the size of the sample, the relation is not linear and is convoluted by other factors such as the indices of refraction (for every component of the sample) [1]. For example, calibrating a flow cytometer with polystyrene beads, will not help in exactly sizing a biological sample, such as cells. As this characterization experiment, however, uses the same beads throughout, the system can be calibrated to obtain quantitative size measurements. Figure 77 presents the calculated diameters of the flowing particles as a function of flow rate, with (a) covering a range of 0.3 - 1.2 $\mu L/min$, and (b) covering 1.2 - 4 $\mu L/min$. Prior to the experiment, the system was calibrated with the same 6 μm beads flowing at 0.12 $\mu L/min$. In general, the sizing information has a smaller standard deviation at slower speeds as each temporal unit in the elastic scatter measurements corresponds to a smaller and smaller fraction of the size of the particle. At speeds below 0.7 $\mu L/min$, however, one can see the aforementioned combination of optical forces, cell-surface friction, and the reduction in the hydrodynamic focusing effect resulting in an over-estimate in the particle size (i.e., the particle is traveling slower than expected). At higher speeds, as shown in Figure 77, the mean diameter estimate is more stable, but the standard deviation increases with the flow rate increase (as each temporal bin corresponds to a larger fraction of the particle size).

To further characterize the sizing capabilities of the MCARS flow cytometer, I analyzed a suspensions of 6, 7, and 8 μm diameter beads back-to-back with no system alterations between samples. The particles were injected into the flow cytometer at 0.7 $\mu m/min$ ($\sim$14.62 mm/s). Figure 79(a) shows the SSC amplitude as a function of FSC amplitude for the suspension. One can see that each sample size creates a well defined subpopulation. If the particles are sized based on system calibration with a separate suspension of 6 μm diameter beads, as shown in Figure 79(b), one can see that the sizes are underestimated for beads other than the 6 μm sample.

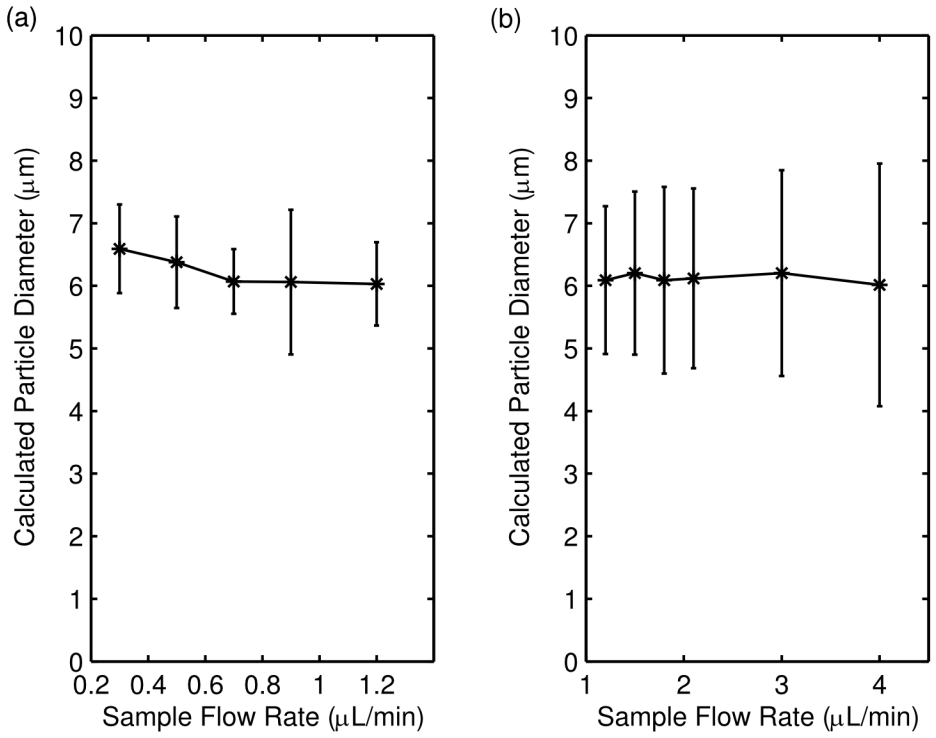

Figure 77: (a) Calculated diameter as a function of flow rate for 6 μm polystyrene beads corresponding to the experimental data shown in Figure 75(a) with the errorbars indicating one standard deviation. One can see that as the sample stream slows, the effects of optical trapping and surface friction become more pronounced; thus, slowing the particles and increasing the calculated diameter. (b) Calculated diameter as a function of flow rate for the experimental data shown in Figure 75(b) with the errorbars indicating one standard deviation. One can see that as the sample stream flow rate increases, the mean calculated diameter remains nearly correct, but the error increases due to the limited temporal resolution of the elastic scatter measurement.

If, however, the system is calibrated without the assumption that each time pixel, as recorded by the elastic scatter platform, is a constant value of time, improved sizing is obtained as shown in Figure 80(a). In this figure, I have also included a 9 μm diameter PS particle (not used for calibration). To calibrate the system in this manner, three suspensions of particles (6, 7, and 8 μm diameters) were analyzed, and a linear function was fitted to the measured SSC width as a function of particle size. For comparison, I calibrated the system sizing based on FSC amplitude and compared the sizing data for 6, 7, 8, and 9 μm PS beads as shown in Figure 80(b). Using FSC amplitude presents much more reliable information and more isolation between histogram peaks. To qualify the difference between the FSC amplitude-based sizing and the elastic scatter width characterization, I simulated the elastic scatter generation (normalized intensity of the scattered field) for an 8 μm particle flowing in the +x-direction as a function of y-offset as shown in Figure 78(a) and (b). One can see that with slight deviations from the focus, the width between elastic scatter peaks can be dramatically affected, whereas the FSC is the same for y-offsets less than $\sim$3 μm (i.e., 75% of the diameter). From these results, the traditional rule that FSC is a truly poor indicator of size appears to be relaxed for a focused beam flow cytometer. For comparison, I ran the 6, 7, 8, and 9 μm PS particles through a commercial flow cytometer. Figure 81(a) shows the SSC amplitude versus FSC amplitude. One notices that as size increases from 6 to 8 μm diameters, the FSC increases, but interestingly at 9 μm, the FSC drops again. Repeated tests demonstrated the same features. Similar to the calibration of the FSC amplitude with the MCARS flow cytometer, I calibrated the commercial flow cytometer FSC strength as a function of size for the 6, 7, and 8 μm particles. Figure 81(b) shows the normalized histogram of sizing information. Additionally, I performed the same sizing analysis using the FSC-width (FSC-W) (i.e., time-of-flight) measurement with the commercial flow cytometer as shown in Figure 82(a) and (b). Although the FSC-W should indicate particle diameter based

on the width of the FSC signal, one can see that the sizing is even less accurate that using FSC amplitude (often, FSC-W is used in biological analysis to gate out aggregated samples). In comparison, the MCARS flow cytometer sizing based on FSC amplitude is more indicative of cell size than that taken with the commercial flow cytometer due to the focused excitation beams (focused beam flow cytometry is sometimes referred to as "slit-scanning"), which is known under certain conditions to provide enhanced morphological analysis [105, 106]).

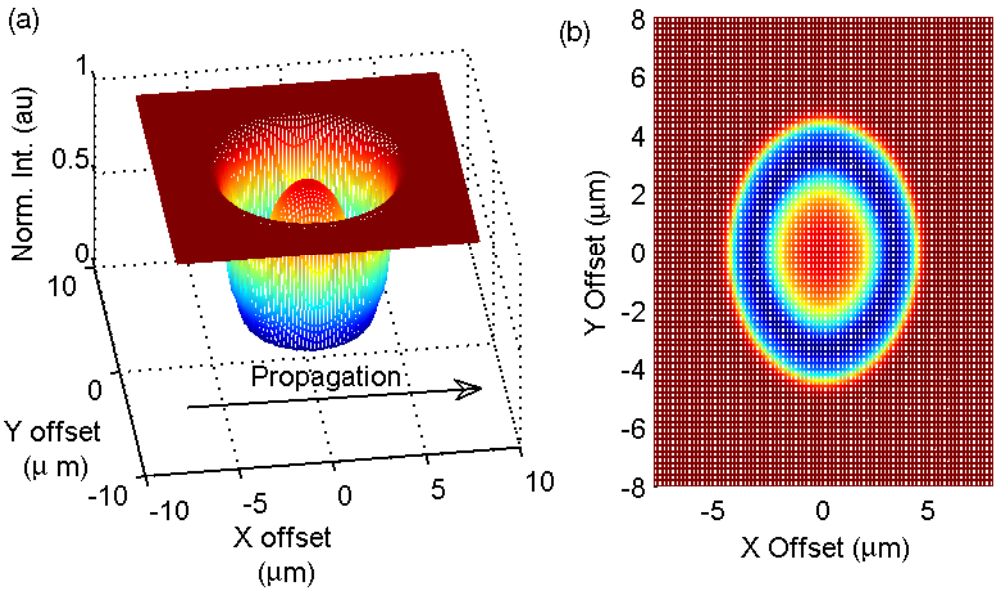

Figure 78: (a) Normalized scatter field intensity as a function of x-offset and y-offset for an 8 μm diameter particle. The elastic scatter waveform (FSC) is determined by following a fixed y-offset as a function of x-offset, as the x-offset is the simulated direction of propagation. (b) Intensity map of the elastic scatter (FSC) as a function of x-offset and y-offset. This plot is the same as (a) viewed from above.

As previously mentioned, numerous parameters beyond particle size affect the strength of the elastic scatter measurements. To demonstrate these effects, I analyzed a suspension of 6 μm PS beads and 5 μm PMMA beads with a commercial flow cytometer as well as with the label-free flow cytometer. Figure 83(a) and (b) shows the scatter plots of SSC versus FSC taken on the commercial system and the label-free flow cytometer, respectively. One can see that with the commercial flow cytometer

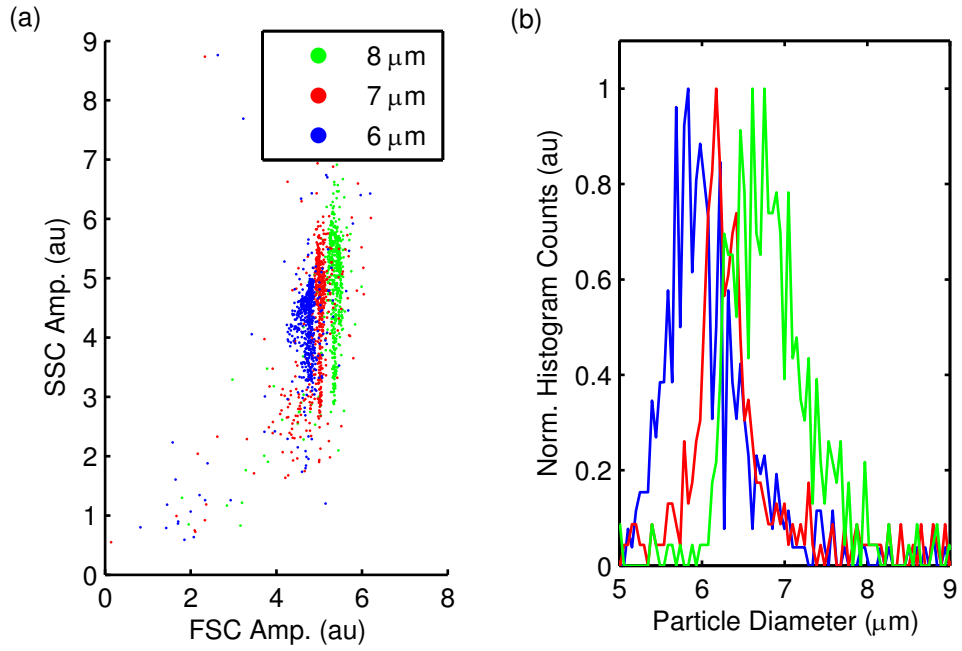

Figure 79: (a) Scatter plot of SSC amplitude versus FSC amplitude for 6, 7, and 8 μm PS beads recorded with the MCARS flow cytometer. (b) Histogram of calculated particle size based on SSC width calculations.

the FSC of the PMMA is significantly larger than for the PS beads even though the PMMA bead is smaller. With the MCARS flow cytometer, however, the FSC is smaller for the PMMA bead. Using the same calibration as previously described (i.e., calibrating based on the FSC amplitude for 6, 7, and 8 μm PS beads), I calculated the particle diameters based on FSC strength as shown in Figure 84(a) and (b). One can see that, again, the MCARS flow cytometer is more accurate for characterizing particle size than the commercial flow cytometer.

Although the MCARS flow cytometer has demonstrated the ability to analyze flowing particles and produce approximate particle size based on time-of-flight measurements (SSC width or FSC width) and FSC amplitude. The demonstrated particle analyses thus far have focused on cell-sized polymer beads. When analyzing small particles, however, another optical effect may affect certain analysis parameters: optical trapping forces [27, 107]. Figure 85 shows representative FSC waveforms for 1.6 μm particles at different flow rates (N.B., these particles are sold as 1.6 μm particles,

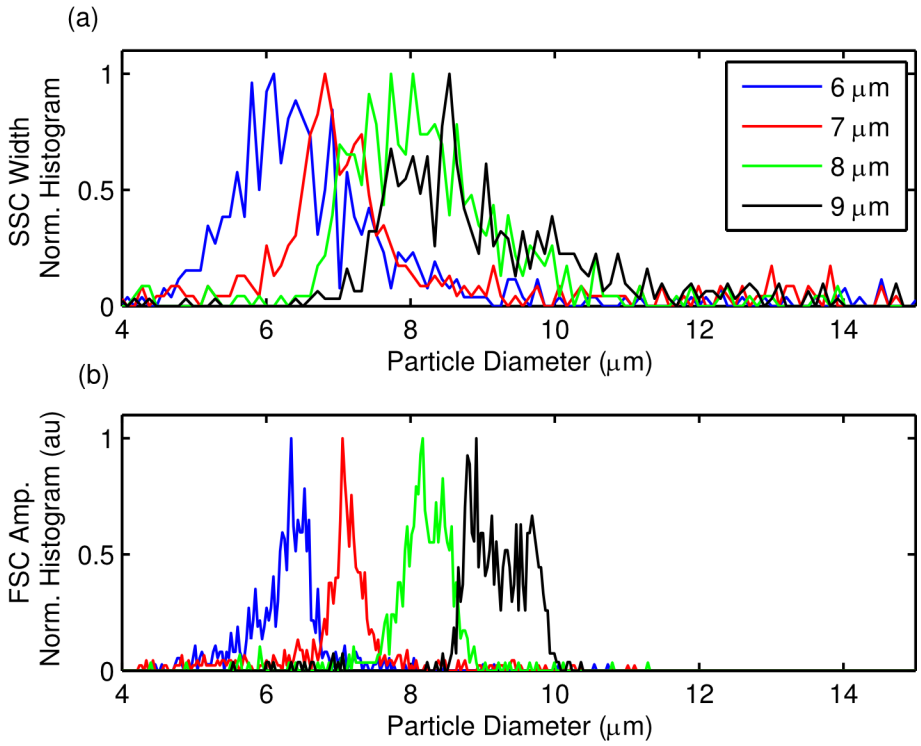

Figure 80: (a) Histograms of calculated particle size based on SSC width calculations for 6, 7, 8, and 9 μm PS beads. (b) Histograms of calculated particle sizes based on FSC amplitude measurements. The system was calibrated in both (a) and (b) using measurements for the 6, 7, and 8 μm diameter particles.

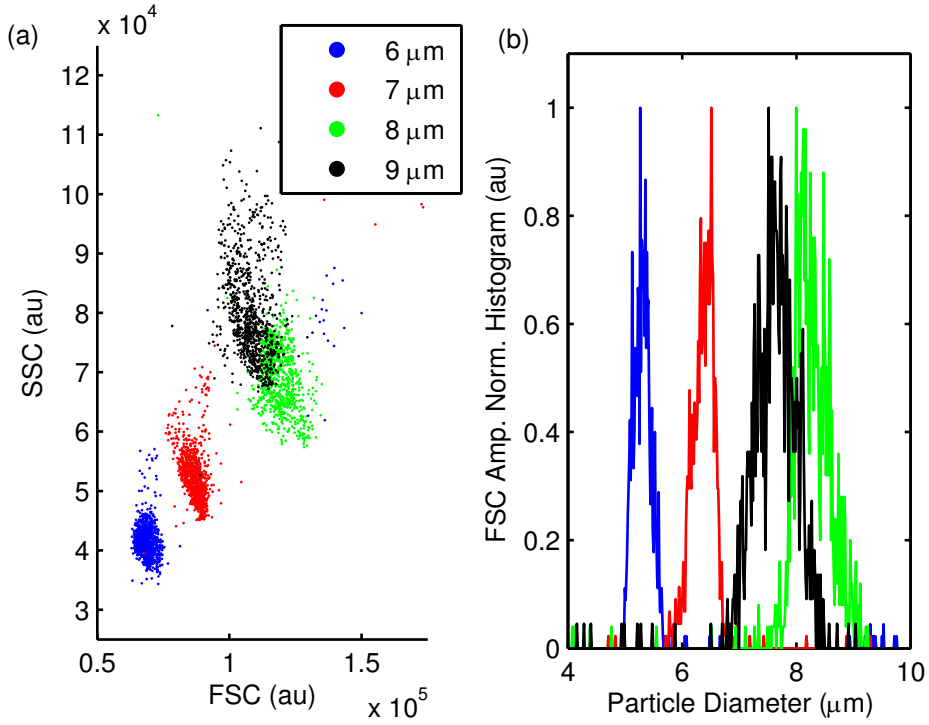

Figure 81: (a) Scatter plot of SSC amplitude versus FSC amplitude for 6, 7, 8, and 9 μm PS beads recorded with a commercial flow cytometer. (b) Histogram of calculated particle size based on FSC amplitude. The system was calibrated using measurements for the 6, 7, and 8 μm diameter particles.

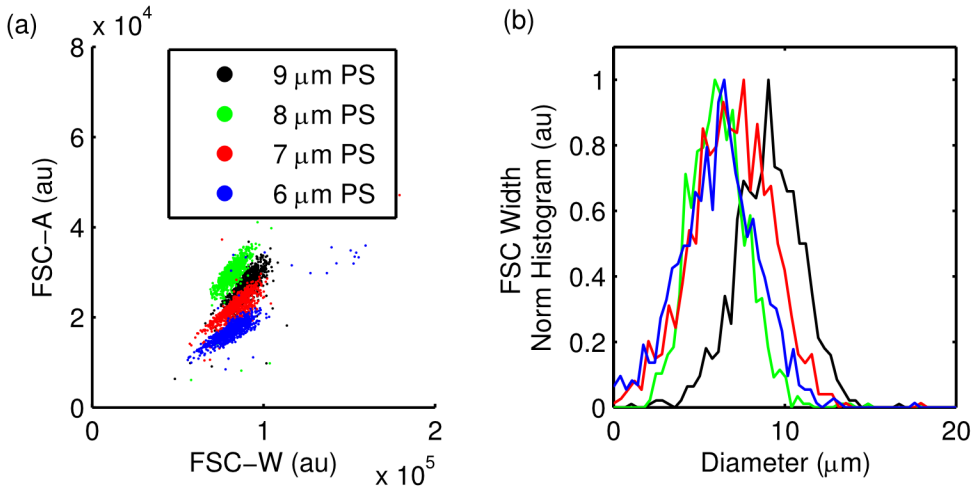

Figure 82: (a) Scatter plot of FSC width (FSC-W) as a function of FSC amplitude (FSC-A) (typically, FSC-A is synonymous with FSC). (b) Histogram of particle size based on the system calibration of 6, 7, and 9 μm PS beads.

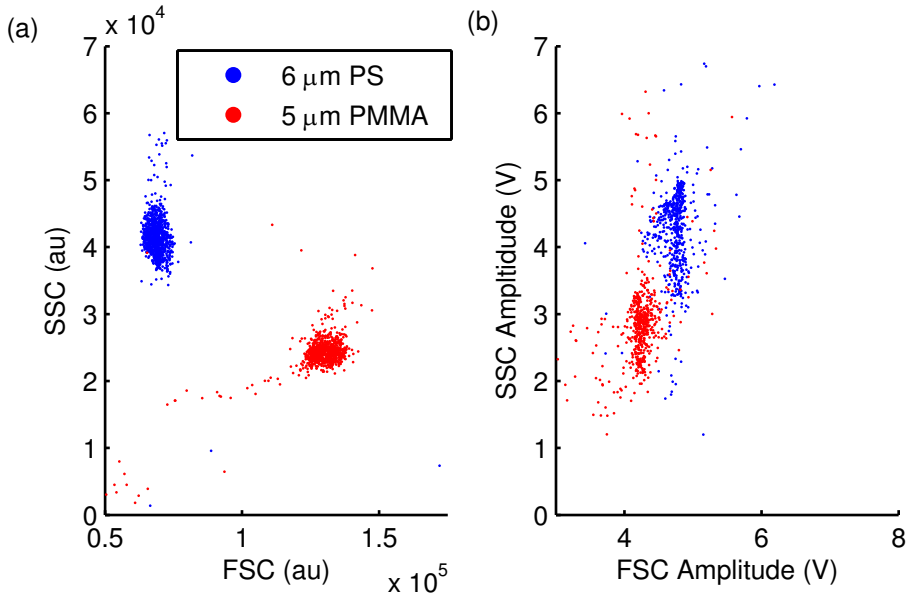

Figure 83: Scatter plots of SSC versus FSC taken on the commercial system (a) and the label-free flow cytometer (b).

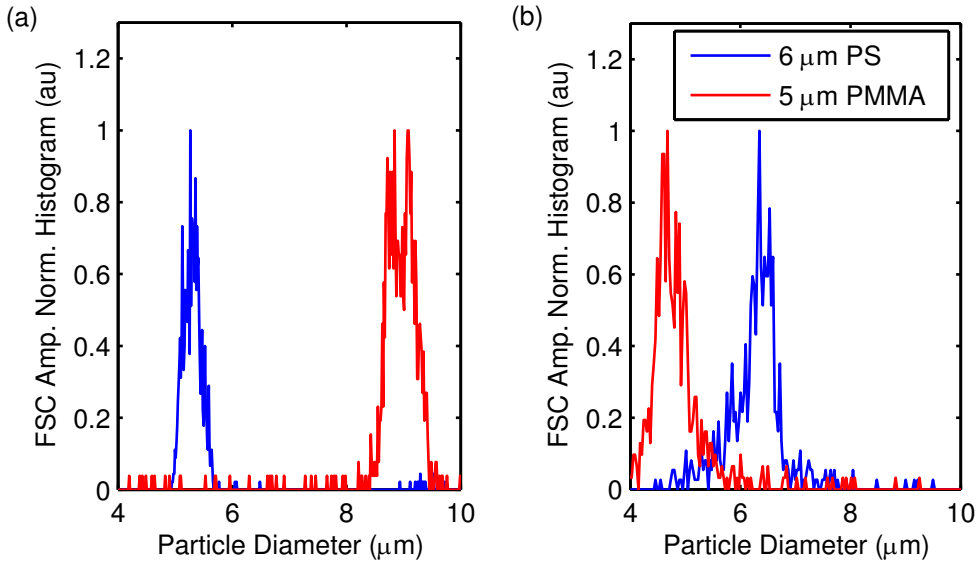

Figure 84: Histograms of calculated particle sizes based on FSC amplitude measurements for the commercial flow cytometer (a) and the MCARS flow cytometer (b).

but the actual size is 1.587 μm). The FSC amplitude is nearly the same at all velocities (3.5 V, which corresponds to $\sim$1.9μm), but the FSC and SSC waveforms form a single peak with an elongated tail for speeds below $\sim$20.89 mm/s with the current system settings (increasing or decreasing the pump and Stokes power will increase or decrease this velocity, respectively). Under these conditions, the previous description of FSC width and SSC width are no longer valid, and FSC amplitude is the only parameter to calibrate the particle size.

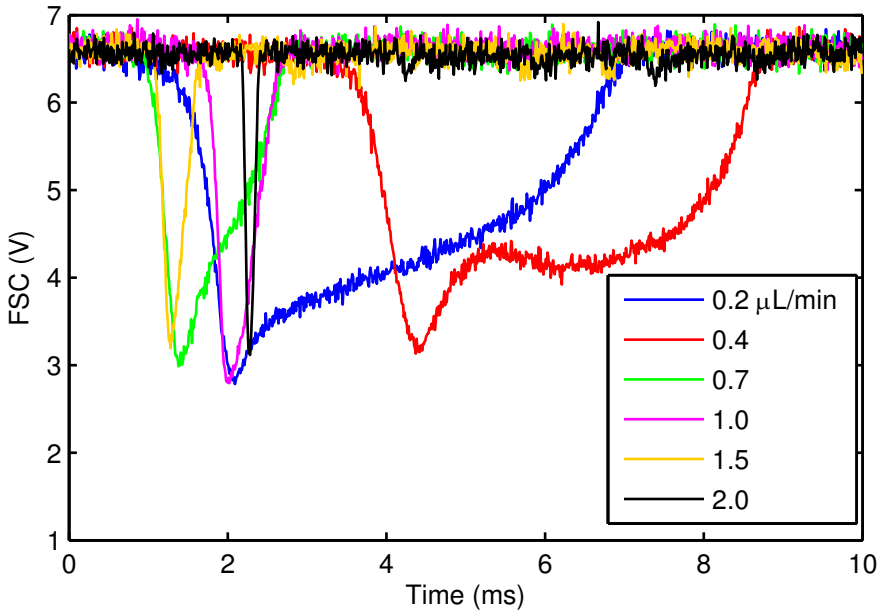

Figure 85: FSC waveforms of 1.6μm PS beads flowing at 0.2 (blue), 0.4 (red), 0.7 (green), 1.0 (magenta), 1.5 (orange), and 2.0 (black) $\mu L/min$.

In this section, I demonstrated the effect of flow rate on scatter measurement performance. Additionally, I demonstrated particle sizing based on SSC/FSC width and FSC amplitude for a variety of particle sizes and different compositions. It was demonstrated that under current operating conditions, FSC amplitude is the most accurate method of calculating sample size. Additionally, I demonstrated that the MCARS flow cytometer focused-beam geometry improves particle sizing capabilities over traditional flow cytometry when properly calibrated.

4.3 MCARS Flow Cytometer

Although most of the characteristics of the MCARS label-free flow cytometer are derived from the previously described performance of the elastic scatter platform and the MCARS microspectrometer subsystem, under flow cytometric operation, the SNR is both a function of the strength of the scatterer and of the strength of the background. The developed MCARS flow cytometer uses a shutterless spectrometer to record the MCARS spectra; thus, photons are collected regardless of whether a particle is present. Additionally, the spectrometer operates at a constant acquisition rate (typically, 100 spectra/s); thus, spectra are recorded over a fixed window. To model these conditions, I will describe the SNR of the MCARS flow cytometer as:

$$SNR = \frac{\phi_s \eta M t_s}{\sqrt{[\phi_s t_s + \phi_{BG}(T - t_s)]\eta M + DMT + N_r^2}}, \tag{41}$$

where t_s is the sample transit time; T is integration time; ϕ_s and ϕ_{BG} are the photon flux of the CARS process and the aqueous background, respectively; and η, M, D, and N_r are the CCD quantum efficiency, pixel binning, dark current, and read noise, respectively. It should be noted that the actual model incorporates the pulsed nature of the laser sources. The ultrafast laser in the system generates ∼125 fs (which are dispersed to ∼322 fs after spectral filtering) at a repetition rate of 86 MHz. At this repetition rate, the pulses are separated by ∼12 ns. The relaxation time for the typical Raman transition is less than 1 ps; thus, the recorded MCARS spectrum is an average of the anti-Stokes photons generated over the number of excitation pulses within the integration window (e.g., over 1 ms there are 86,000 excitation pulses). Under these conditions and with relatively long integration times relative to the 12 ns pulse separation, it is entirely unnecessary to account for the pulsed nature of the sources. Figure 86(a) plots the SNR as a function of flow rate (500 μm sample syringe) for four different ratios of sample and aqueous background photon fluxes. For example, the CH-stretch peak of neat methanol (discussed in Section

4.1) is approximately 80 times larger than the response of the aqueous background at 2930 cm^{-1} (due to the NRB). Canola oil is greater than 120 times larger. The solid line represent the model presented in Eq. 41, and the dashed lines represent the ideal scenario in which the spectrometer only records photons during the transit time of the particle. Figure 86(b) plots the difference in the SNR between the realistic SNR and the ideal SNR (ΔSNR) for each of the photonic flux ratios. One can see that at smaller flow rates, the ΔSNR approaches 0. This intuitively makes sense as the portion of time in which the spectrometer records any signal from the aqueous background approaches 0. Additionally, one can see that for strong scatterers (relative to the aqueous background), the SNR loss is significantly less than for weak scatterers. This effect is amplified as the flow rate increases. In practical terms, this effect more greatly influences the sensitivity of the MCARS flow cytometer to weak scatterers, such as the dilute molecules within cells. For large, strong scatterers, such as lipid vacuoles, this effect is relatively small (less than 5 dB, even at high flow rates).

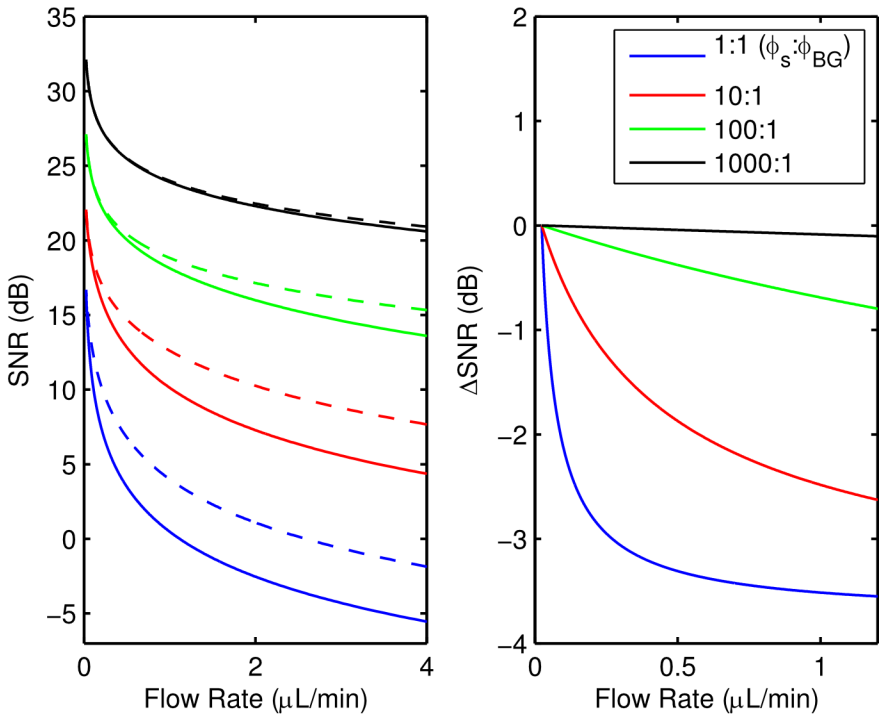

Figure 86: (a) SNR versus sample flow rate (500 μL sample syringe) under different ratios of the photon flux of the sample (ϕ_s) to background photons from the water (ϕ_{BG}). Solid lines are calculated using Eq. 41 that incorporates the photons collected during each spectral acquisition from the sample and the background. Dashed lines demonstrate the ideal scenario in which the spectrometer is triggered to record only during the presence of a sample and a shutter is used to prevent photon accumulation when no particles are present. (b) Plot demonstrating the difference (ΔSNR) between the ideal SNR and the SNR of the shutterless, untriggered spectrometer.

CHAPTER 5

APPLICATIONS OF LABEL-FREE FLOW CYTOMETRY

MCARS flow cytometry offers the first label-free mechanism to optically analyze the molecular content of flowing particles at high-speed. During the development of the system, I analyzed several different systems ranging from polymer bead assays to a variety of species and strains of yeasts. In the first section, I will describe the application of label-free flow cytometry to the analysis of polymer beads, which are often used as model systems, calibration standards, and for bead assays in flow cytometry. In the second section, I will describe the analysis of the diatom *Phaeodactylum tricornutum* a diatom that is fluorescent even under NIR excitation; thus, making its analysis with traditional Raman spectroscopy and flow cytometry challenging. In the final section, I will describe examinations of various strains and cultures of *Saccharomyces cerevisiae*, a yeast often used as a model system for higher eukaryotic organisms, including humans.

5.1 Analysis of Polymer Beads

Polymer beads are a tool often used in microscopy and flow cytometry as model systems, bead assays, and calibration standards. One of the first proof-of-principle demonstrations of MCARS flow cytometry analyzed a suspension of 5 μm PS and 5 μm PMMA beads [85]. This test injected the beads slowly ($\sim$185 $\mu m/s$ [as measured]) into a glass microfluidic chip (50 μm width, 20 μm depth), and the fluidic chip inputs were organized to induce hydrodynamic herding along the side wall. With this integration time and the additional data transfer time, the CCD spectrometer captured each particle with approximately 3 spectra. The MCARS spectra were recorded at 100 Hz, and no gating was applied; thus, all spectra (water and beads)

were recorded. Figure 87(a) shows a typical time-stack that captures the MCARS spectra of PS, PMMA, and the broad spectrum of water. Figure 87(b) and (c) shows the individual spectra (smoothed with a 7^{th}-order Savitzky-Golay filter) of PMMA and PS, respectively.

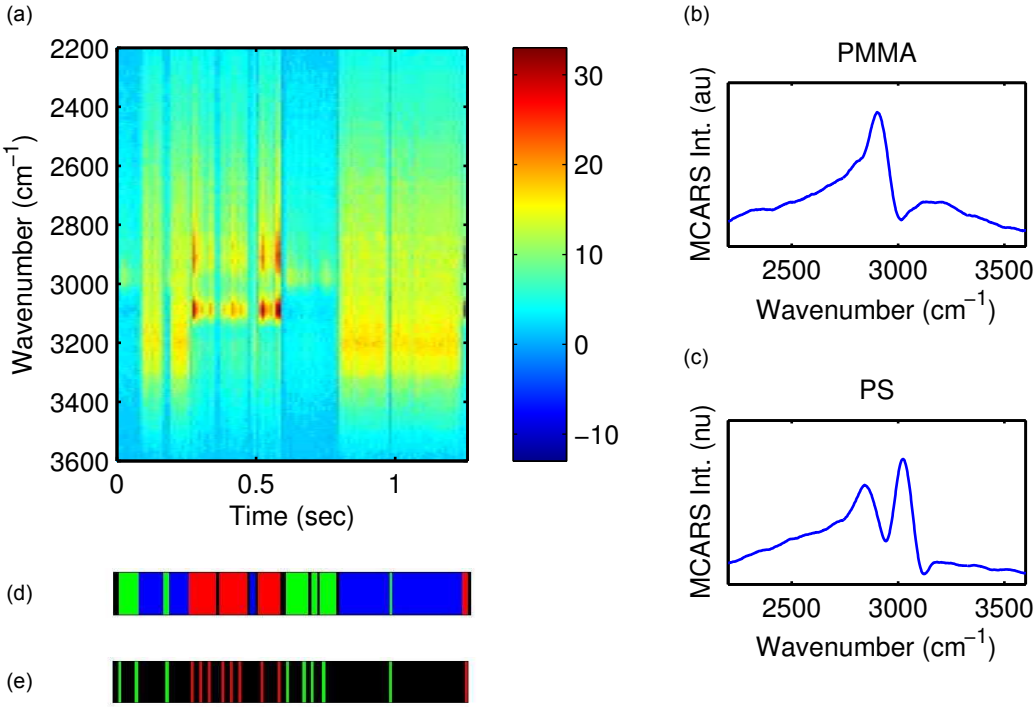

Figure 87: (a) Time-stack MCARS spectra of polystyrene and PMMA beads flowing at approximately 185 $\mu m/s$. The pump and Stokes source powers were approximately 38 and 8 mW, respectively. Example MCARS spectrum of (b) PMMA and (c) PS taken from this time-stack, respectively. (d) Classification of spectra using PCA: green = PMMA, red = PS, blue = water, black = signal below minimum. (e) Particle centers determined by local maxima of spectral intensities. Figure adapted from [85].

To classify the spectra in real-time, a principle component analysis (PCA) tool was developed in MATLAB. PCA is an eigenvalue technique that reduces the number of independent variables by combining variables of high variance that are correlated (in this case spectral features) into eigenvectors (principle components) [108]. This operation condenses a large number of correlated variables into a few independent variables. For application to MCARS flow cytometry, this technique is valuable as

it requires no training sets and is computationally fast. Figure 88 shows the principle components of the spectra recorded in Figure 87(a). Figure 87(d) shows the classification of the particles versus time. Because the beads were purposely propagated slowly through the flow cell resulting in approximately 3 spectra per bead, the spectral intensities were analyzed to find the maximum intensity that approximately corresponded to the bead centers. Figure 87(e) isolates the individual bead centers.

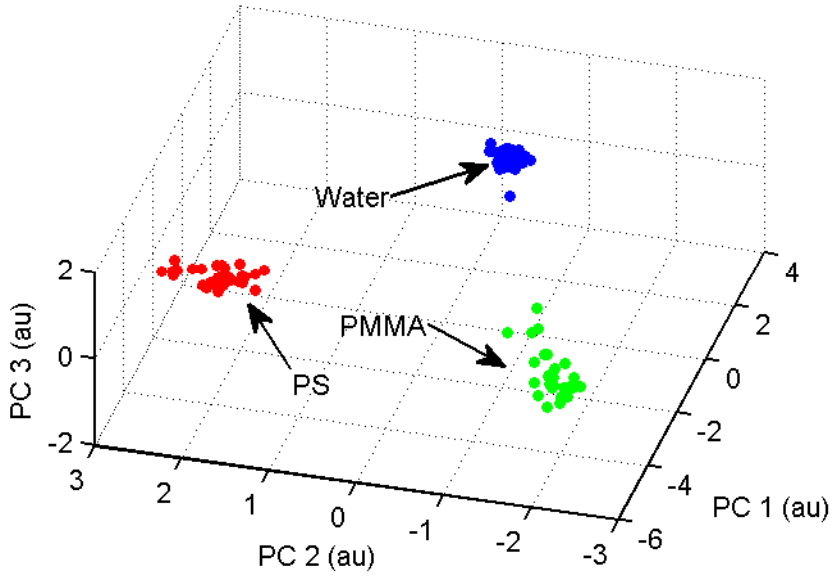

Figure 88: PCA Analysis of spectra in Figure 87(a). The PCA tool, developed in MATLAB, isolates the spectral differences between the samples and allows for easy clustering.

Since this first demonstration of MCARS flow cytometry, the label-free flow cytometer system has greatly evolved with improved optics, fluidics, and electronics. The current system can record flowing polymer beads at speeds greater than 10 mm/s with approximately the same SNR as presented in [85]. Additionally, the newest iteration of the MCARS flow cytometer records MCARS spectra spanning nearly 2000 cm^{-1}, which provides not just the relevant molecular information in the methyl-stretch region but also into the "finger print" region of the Raman vibrational energy levels, which is more unique to each molecule. Additionally, the elastic scatter

measurements provides a new complex layer of information to asses the morphological features of flowing samples.

To demonstrate the application of the MCARS flow cytometer to isolating polymer beads (such as would be necessary in a bead assay), I analyzed a suspension of 9, 8, 7, 6, and 1.6 μm PS beads and 5 μm PMMA beads. The suspension was fed into the flow cell with a 500 μL syringe and injected at a flow rate of 0.7 $\mu L/min$ ($\sim$14.62 mm/s). The MCARS spectra were recorded at 100 Hz, and the FSC and SSC recorded at 100 kHz. The software gating was set to only record spectra for particles that had an elastic scatter profile (FSC and SSC) over the baseline voltage (below a threshold for FSC) and a KK-reconstruction above a given threshold. Figure 89 is a scatter plot of the SSC amplitude as a function of FSC amplitude for the suspension. One can clearly see that each particle size creates a defined subpopulation as the FSC amplitude varies with particle size (more clearly with the focused-beam architecture than with traditional flow cytometers as discussed in Section 4.2). The subpopulations were defined and the color coding applied using a variety of parameters such as FSC amplitude, SSC amplitude, maximum spectral wavenumber (to separate PS and PMMA), and maximum spectral peak. For example, Figure 90 demonstrates the isolation of the 1.6 μm beads from particles with similar FSC amplitude value based on KK-reconstructed spectra maximum peak intensity. With the subpopulations defined, the KK-reconstructed spectra for the six particles are shown in Figure 91 (mean spectra collected during the experiment). As expected, the intensity of the spectrum diminishes as the particle size decreases. Additionally, one can clearly identify spectral peak down to $\sim 1000 cm^{-1}$.

Beyond isolating the individual subpopulations, I also characterized the sizes of the flowing particles. I calibrated the system prior to the analysis of the suspension with suspension of 6, 7, and 8 μm particles (as described in Section 4.2). Figure 92(a)

shows the histogram of the sizing data for the raw data collected for the entire suspension. Figure 92(b) shows the histogram of the sizing data for the subpopulations identified by various spectral and elastic scatter metrics. One can see relatively accurate sizing for the cell-sized particles (these particles are also close to and encompass the size of the calibration standards). For the smallest particles in this suspension, the calibration underestimates the size. For comparison, I analyzed the same beads used in this experiment on a commercial flow cytometer (each bead size was analyzed separately, but no system alterations were performed) as shown in Figure 93(a). The commercial flow cytometer records increasing FSC amplitudes as the particle sizes increase until the 9 μm particle, which has an unexpectedly low FSC amplitude. Additionally, the PMMA beads demonstrate a significantly higher FSC amplitude than expected (based on just size), which is stronger than that from 8 and 9 μm PS beads. Using the calibration method for FSC amplitude described in Section 4.2, I calculated the sizes for the different particles as shown in Figure 93(b). One can clearly see relatively accurate sizing data for the particles nearest the calibration standards and for the 1.6 μm beads. For the 9 μm particles and the PMMA beads, the sizing information is off by $\sim$9% and $\sim$28%, respectively. By contrast the MCARS flow cytometer is within 2% for the 9 μm PS beads and within 4.5 % for the PMMA beads. A summary of the sizing measurements for the MCARS flow cytometer and the commercial flow cytometer is presented in Table 7. In general, the FSC amplitude measurements collected from the MCARS flow cytometer generate size measurements within 5% of the actual particle size– three of the samples are within 1%. The obvious exception is for the smallest particle in which the limited sample set, optical trapping that can perturb the measurement, and the small particle size that leads to large fluctuations possible due to lateral and vertical deviations from the focal volume generated significant error. In comparison with the commercial flow cytometer, the MCARS flow cytometer produces more accurate data for all samples excluding the

1.6 μm PS bead (the commercial flow cytometer has a more accurate mode size, but the system records multiple subpopulations of these beads) and the 8 μm PS bead (in which they are tied).

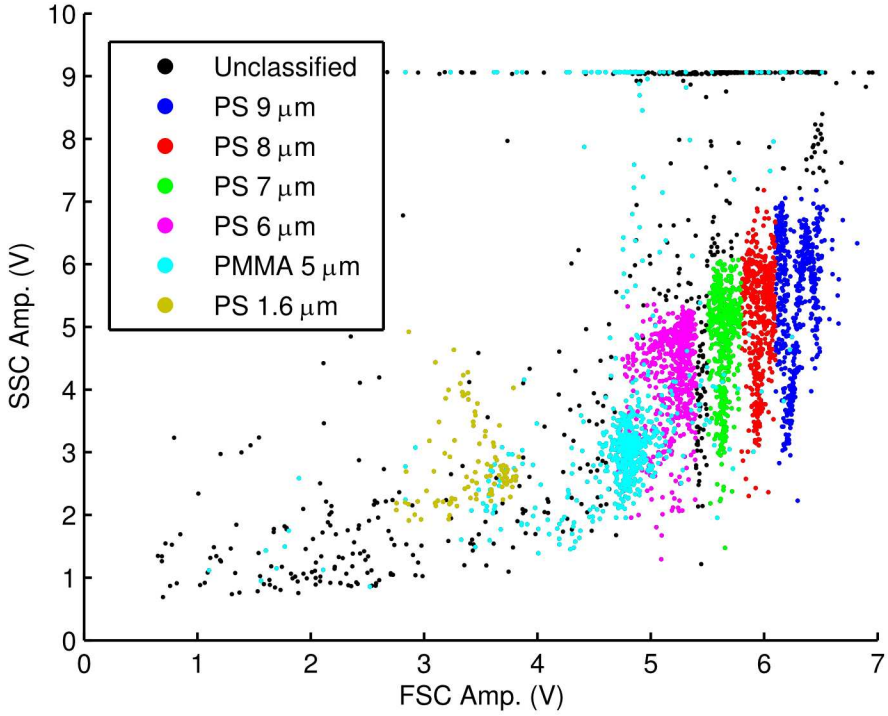

Figure 89: Scatter plot of SSC amplitude versus FSC amplitude for a suspension of 9 (blue), 8 (red), 7 (green), 6 (magenta), and 1.6 (yellow) μm diameter PS beads and 5 μm PMMA beads (cyan). The color coding was assigned based on parameters such as FSC, SSC, maximum MCARS spectral peak number, and maximum MCARS spectral peak intensity. Unassigned beads are colored black.

Beyond solid polymer beads, I also analyzed a suspension of "pink" PS beads (6 μm diameter) (FP-6058-2 , Spherotech Inc., Lake Forest, IL), and nile red PS beads (10.2 μm) (FP-10056-2, Spherotech Inc., Lake Forest, IL), along with nonfluorescent PS beads (6 μm diameter) (4206A, Duke Scientific, Waltham, MA) for comparison. These fluorescent beads are fabricated by polymerizing the fluorochrome in styrene around a PS core or by staining a PS bead. The KK reconstructed spectra are shown in Figure 94. In the presence of the strong CARS response of PS or from the limited concentration of the dye molecules within the focal volume, the signal generated from

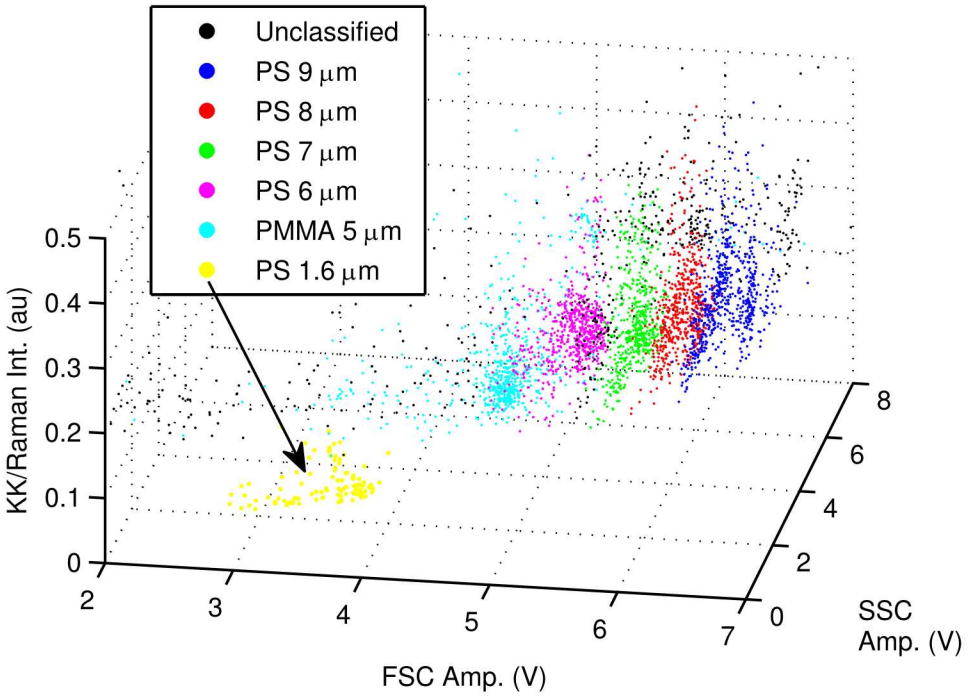

Figure 90: Scatter plot of KK-reconstructed maximum spectral intensity as a function of FSC amplitude and SSC amplitude for a suspension of 9 (blue), 8 (red), 7 (green), 6 (magenta), and 1.6 (yellow) μm diameter PS beads and 5 μm PMMA beads (cyan). The color coding was assigned based on parameters such as FSC, SSC, maximum MCARS spectral peak number, and maximum MCARS spectral peak intensity. Unassigned beads are colored black.

Table 7: Table of polymer bead sizes (listed size and actual size [if supplied by manufacturer]) and the calculated sizes (and standard deviation, σ) using the MCARS flow cytometer and a commercial flow cytometer. Calibration was performed with a sample of 6, 7, and 8 μm PS beads (as described in Section 4.2).

Particle/Actual (μm)	MCARS FC Size (μ)	Error (%)	FC Size (μm)	Error (%)
9/8.956	8.65	-1.74	7.52	-8.72
8/7.979	8.00	0	8.00	0
7/6.982	7.02	0.27	6.51	-3.50
6/6.007	5.97	-0.31	5.27	6.54
5	4.58	-4.38	8.84	27.75
1.6/1.587	0.78	-34.09	1.75	4.88

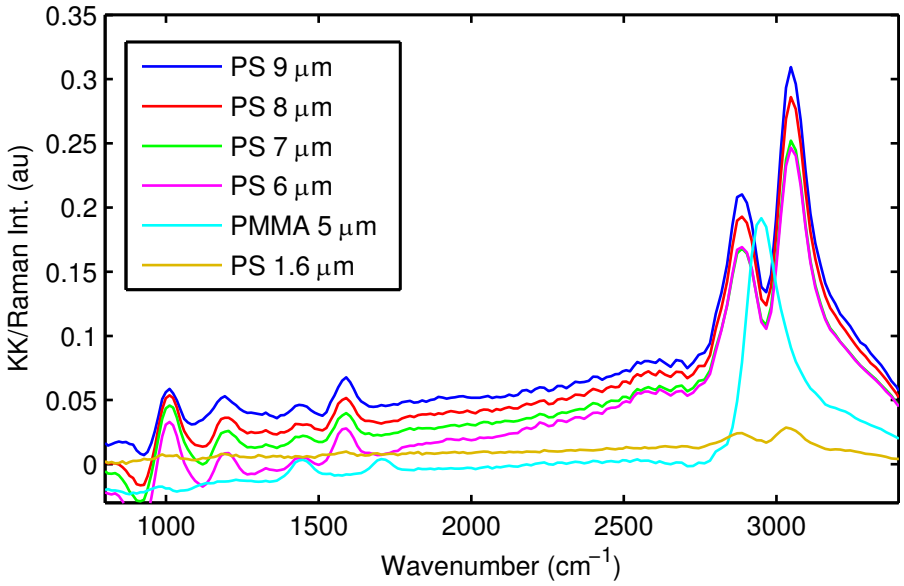

Figure 91: KK-reconstructed spectral for a suspension of 9 (blue), 8 (red), 7 (green), 6 (magenta), and 1.6 (yellow) μm diameter PS beads and 5 μm PMMA beads (cyan).

both beads did not show appreciable difference from a solid PS bead.

In this section, I demonstrated the capability of the MCARS flow cytometer to analyze suspensions of polymer beads with different size and composition. Additionally, sizing approximations based on the FSC amplitude demonstrated improved performance compared with FSC amplitude measurements taken with a commercial flow cytometer. Additionally, the MCARS flow cytometer was able to distinguish PS and PMMA beads based on molecular composition. Using an even larger variety of beads with differing sizes and compositions (e.g., nylon and silica), this system provides a label-free mechanism to distinguish particles with potential use for bead assays.

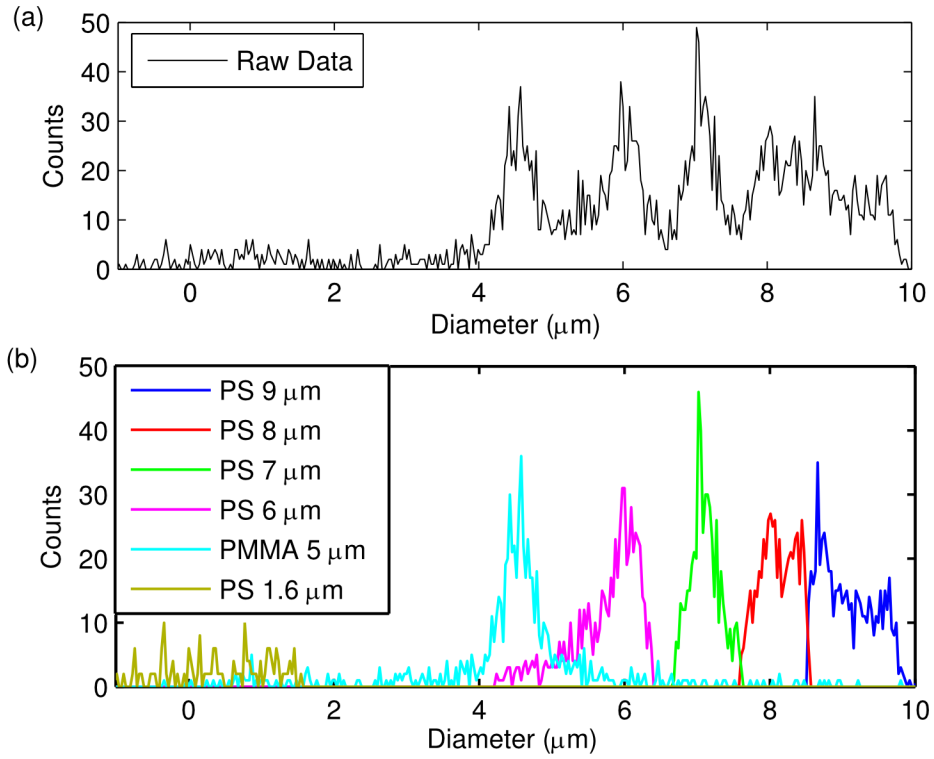

Figure 92: (a) Histogram of sizing information based on FSC amplitude for all data collected. The system was calibrated with a separate suspension of 6, 7, and 8 μm PS beads (the same calibration used in Section 4.2). (b) Histogram of sizing information based on FSC amplitude for a suspension of 9 (blue), 8 (red), 7 (green), 6 (magenta), and 1.6 (yellow) μm diameter PS beads and 5 μm PMMA beads (cyan).

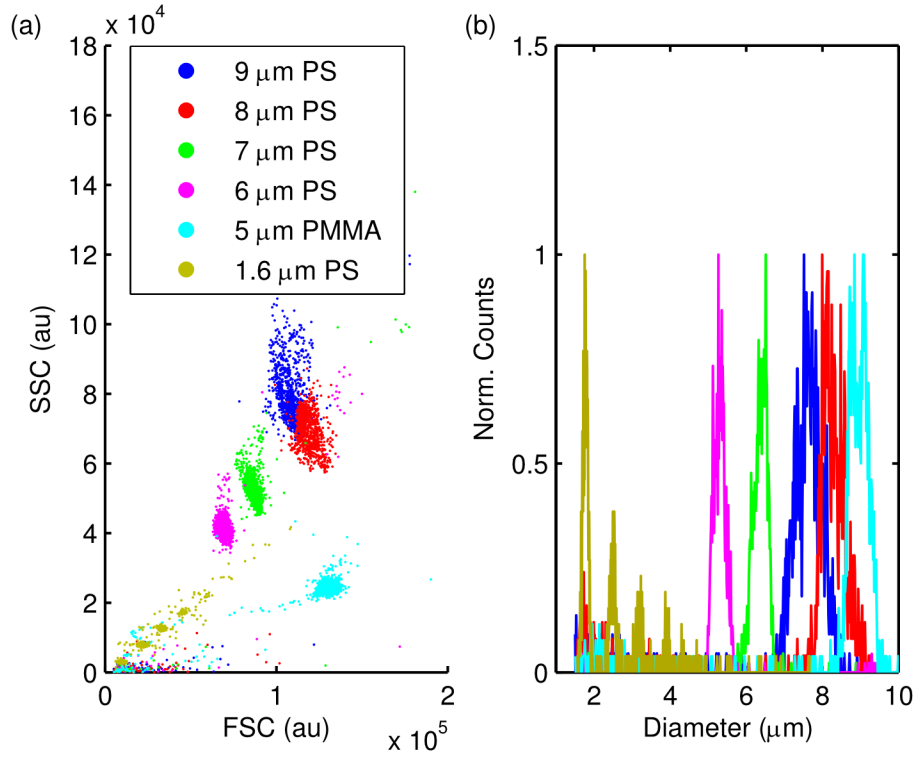

Figure 93: (a) Scatter plot of SSC as a function of FSC for suspensions of 9 (blue), 8 (red), 7 (green), 6 (magenta), and 1.6 (yellow) μm diameter PS beads and 5 μm PMMA beads (cyan). (b) Normalized histogram of calculated particle sizes based on the calibration method described in Section 4.2.

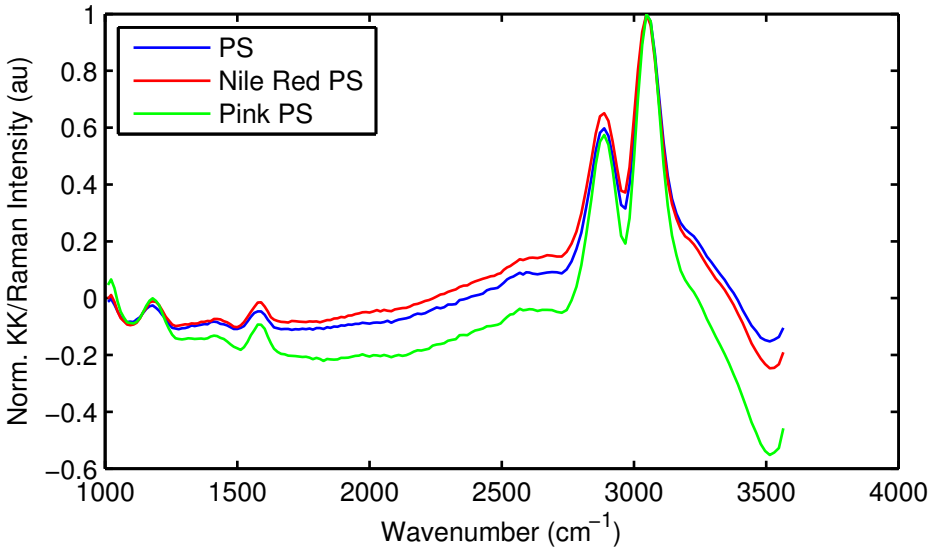

Figure 94: KK reconstructed spectra of 6 μm diameter nonfluorescent polystyrene (blue), 6 μm "pink" PS beads, and 10.2 μm PS beads with nile red

5.2 Phaeodactylum tricornutum

Algae are potentially an excellent vehicle for bio-fuel production [109–112]. Currently, bioethanol is primarily produced from corn and sugar cane; however, algae are also a particularly adept microorganism as they are capable of storing up to 50% of their biomass in the form of high energy compounds, such as neutral triacylglycerides (TAGs) [109]. Additionally, algae have many advantages over traditional land plants such as they can be grown on non-arable lands in saline or salt water, and they can be harvested year round.

One particular algae of interest in the diatom *Phaeodactylum tricornutum*. This pennate diatom has the unique feature that it is not encased in an amorphous silica frustule; thus, for growth these diatoms do not require silicic acid, which is beneficial for large scale growth. Additionally, the genetic sequence of these algae is known and many pathways of genetic manipulation are well understood [113,114]. These diatoms represent a challenge to analyze as many varieties of diatoms brightly fluoresce (even under near-infrared [NIR] excitation). This fluorescence can obscure measurements taken with flow cytometers (see Figure 95) and microRaman spectrometers (see Figure 96).

For this research, I applied the system to two cultures of diatoms in order to observe differences between cultures based on their nitrogen health. Diatoms grown in low nitrate conditions (150 $\mu M\ KNO_3$) are expected to generate large amounts of storage lipid vesicles, and diatoms grown under high nitrate conditions (1.5 mM KNO_3) should not produce storage lipids in any large amount. Figure 97 is a fluorescence microscopy image of Nile Red stained diatoms under high (a) and low (b) nitrate conditions. In Figure 97(a), one can observe the lack of any noticeable lipid vesicles (which would show as bright yellow orbs) but rather a pronounced chloroplast (large orange organelle). In Figure 97(b), on the other hand, one can clearly discern several storage lipid vesicles.

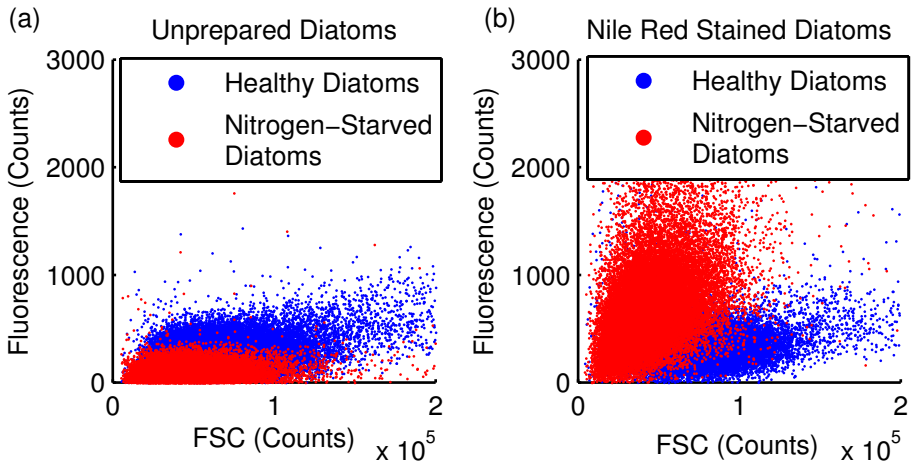

Figure 95: (a) Scatter plot of fluorescence versus FSC for healthy diatoms (blue) and nitrogen-starved diatoms (red) that are unprepared. (b) Scatter plot of fluorescence versus FSC for healthy diatoms (blue) and nitrogen-starved diatoms (red) that are stained with a Nile Red, a hydrophobic fluorophore that aggregates near lipids.

In this experiment, the diatoms were injected into the system at 0.2 $\mu L/min$ ($\sim$2.153 mm/s) with a 1 mL syringe. The MCARS spectra were recorded at 100 Hz, and the FSC was recorded at 10 kHz. In this experiment, I acquired data for 1000 cells from each culture. Figure 98 shows the histogram of recorded FSC amplitude. In this histogram, one can vaguely see that the healthy diatoms produce, on average, a slightly larger FSC amplitude than the nitrogen starved diatoms. Analysis of the raw data reveals that the healthy diatoms average FSC amplitude is $\sim$9% larger than for the nitrogen starved. This qualitatively agrees with flow cytometric analysis that shows a larger FSC for healthy diatoms (see Figure 95).

Figure 99 is a scatter plot showing the peak MCARS amplitude as a function of MCARS peak wavenumber. The results clearly separate the populations of the diatoms grown under high nitrogen (healthy) from those with reduced nitrogen. The healthy diatoms form two subpopulations: one with a dominant peak $\sim$2200 cm^{-1} (referenced as subpopulation 2), and another subpopulation centered around 2850 cm^{-1} (referenced as subpopulation 1). Further analysis shows spectral shifts of the

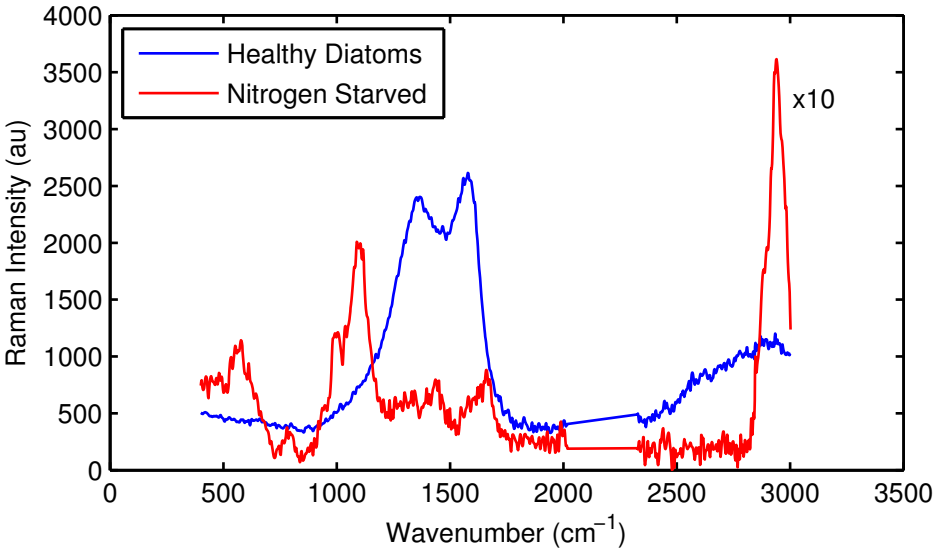

Figure 96: Raman spectra (collected on a microRaman system) of the diatom *P. tricornutum* grown under adequate (blue) and low nitrogen levels (red) (N.B., the spectrum from the low nitrogen growth culture is multiplied by a factor of 100 for graphical clarity). Due to the expansion of the chloroplast organelle, which contains numerous lipids and fatty acids, such as chlorophyll a, the spectrum obtains from the nitrogen healthy diatom demonstrates a tremendous fluorescence that obscures the Raman spectrum. The chloroplast of the nitrogen-starved diatom is much reduced in size and content; additionally, under low nitrogen conditions, algae generate a large amount (over 20-50% of their mass) of storage lipid vacuoles; thus, a spectrum is recoverable.

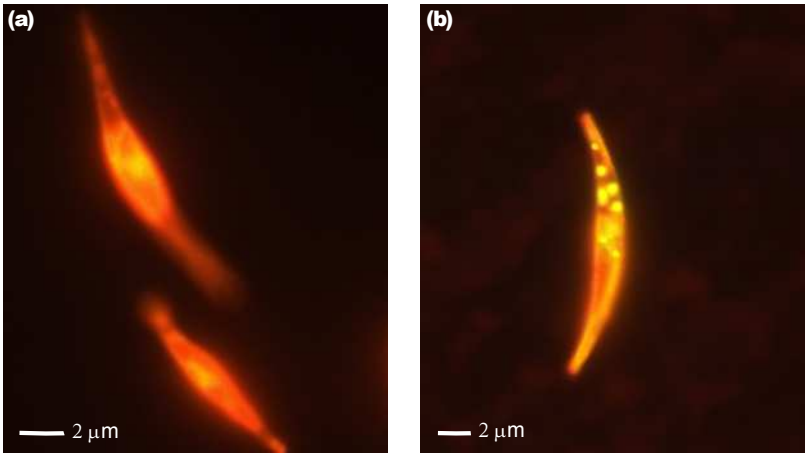

Figure 97: (a) Fluorescence micrograph of healthy algae grown under nominal nitrogen conditions. The large orange structure is the chloroplast. (b) Fluorescence micrograph of algae starved of nitrogen during growth. The yellow spheres are lipid droplets that have formed during growth.

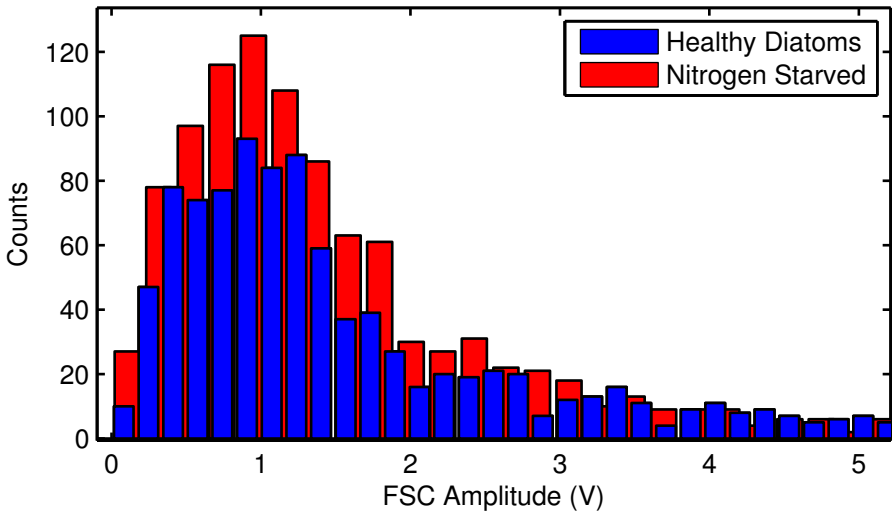

Figure 98: Histogram of the healthy (blue) and nitrogen-limited (red) FSC amplitude.

dominant methyl-stretch region peaks depending on the nutritional state (see Figure 99, inset, for representative spectra of the individual diatoms as taken from the same data set). These results may indicate an expansion of the size and density of the chloroplast, which is full of lipid-rich pigments, such as chlorophyll a, and a reduction of the triglycerides found within the storage lipids under nitrogen-starved conditions. Interestingly, the healthy diatoms exhibit large spectral features within the Raman "silent region" ($\sim$2000 - 2600 cm^{-1}) that may be due to NIR excitation enhancement that chlorophyll a and beta-carotene are known to possess [115, 116]. Figure 100 shows the mean KK-reconstructed Raman spectra for the healthy culture subpopulations and the nitrogen starved population. Subpopulation 1 and the nitrogen starved spectra are similar with a dominant CH-stretch peak around 2930 cm^{-1}. Subpopulation 1 also presents a strong peak at $\sim$1528 cm^{-1}, which may correspond to the C-C vibration within chlorophyll a [116]. The nitrogen starved population, contains a similar peak but at 1520 cm^{-1}, which may be generated from the C=C vibrational band of beta-carotene, whose relative strength over the bands of chlorophyll a is indicative of a nitrogen starved algal population [116].

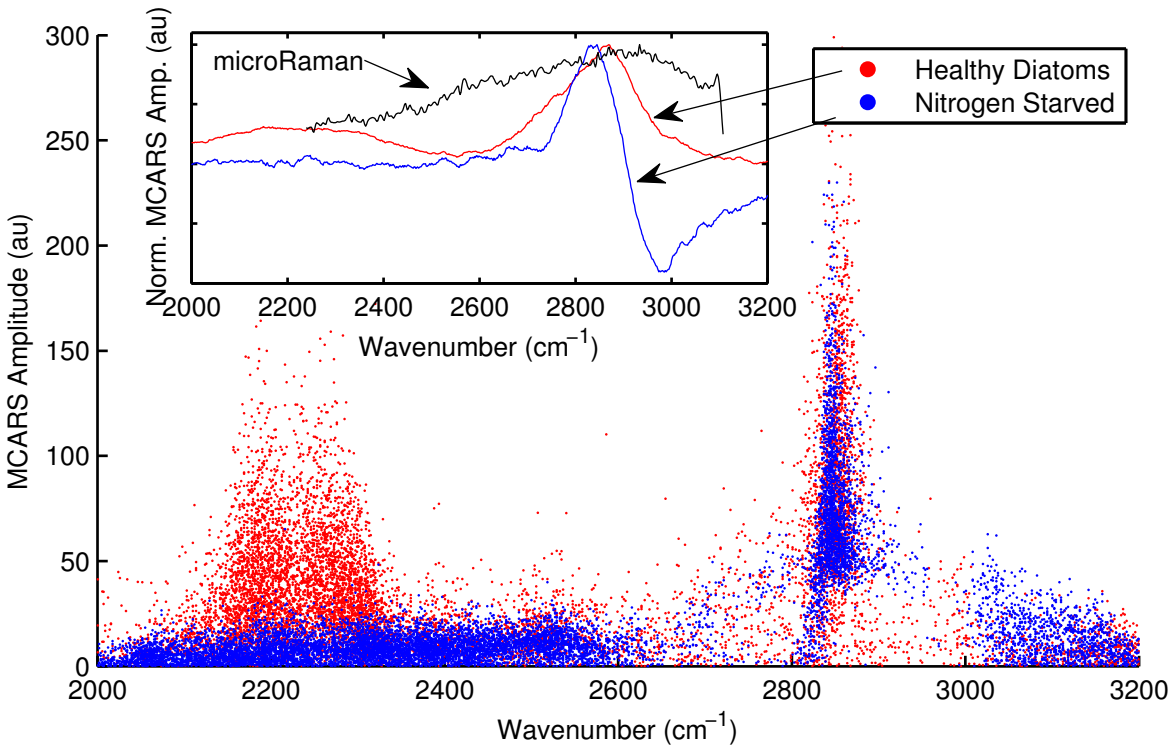

Figure 99: Scatter plot of MCARS peak amplitudes versus spectral location for healthy (red) and nitrogen starved (blue) diatoms. Inset, spectrum of an individual healthy diatom (red), a nitrogen starved diatom (blue), and the spectrum of a healthy diatom collected under a commercial microRaman spectrometer. The microRaman spectrum shows that the healthy diatom produces a tremendous amount of fluorescence that completely obscures the Raman bands.

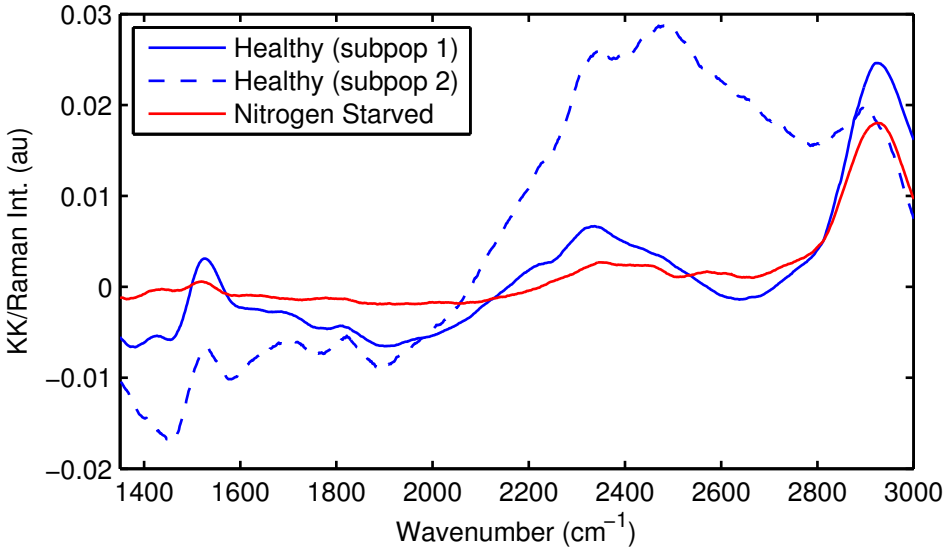

Figure 100: KK-reconstructed Raman spectra for the health culture subpopulations (blue solid and blue dashed) and the nitrogen starved population (red). Subpopulation 1 and the nitrogen starved spectra are similar with a dominant CH-stretch peak around $2930cm^{-1}$. Subpopulation 1 also presents a strong peak at $\sim 1528cm^{-1}$, which may correspond to the C-C vibration within chlorophyll a. The nitrogen starved population, contains a similar peak but at $1520cm^{-1}$, which may be generated from the C=C vibrational band of beta-carotene, whose relative strength over the bands of chlorophyll a is indicative of a nitrogen starved algal population.

In this experiment, I targeted two cultures of the diatom *P. tricornutum* with the desire to quickly inspect the MCARS (and KK-reconstructed) spectra and to observe the spectral differences between the two. Under these growth conditions (i.e., nitrogen control), it may be possible to ascertain the TAG content indirectly by observing the strength of the MCARS or KK reconstructed spectra within the silent region as the dominant contributor to this is assumed to be from chlorophyll a. Quantitative analysis, however, is more difficult due to the contribution of the NIR excitation. Additionally, under different growth conditions, the coupling between chlorophyll a production and nitrate supply may have a different relation. An alternative route to monitor the TAG production in diatoms is through monitoring other bands over a larger spectral bandwidth. Heraud, *et al.*, for example, showed a statistical difference in the $1157cm^{-1}$ beta-carotene CH-deformation and the $1325cm^{-1}$ chlorophyll a CH-deformation band intensities depending on nitrogen availability to the chlorophyte algae *Dunaliella tertiolecta* [116]. Their results, however, demonstrate a stronger ability to differentiate cells rather than to quantify TAG composition. With improved spectral bandwidth (N.B., the current MCARS system is now capable of monitoring down to $\sim 1000cm^{-1}$) and improved excitation sources (for improved spectral resolution and SNR), the ability to better quantify the lipid content within these diatoms is promising.

5.3 Saccharomyces cerevisiae

Yeasts are unicellular fungi that are used for a broad range of purposes ranging from biofuel production [117] to modeling human diseases [94]. These tiny organisms have been used for thousands of years (sometimes unknowingly) for such purposes as leavening bread and fermentation. In biological research, yeasts are often used as model organisms with a variety of benefits such as their ease of genetic manipulation and fast growth cycle. In my research, specifically, I predominantly work with the budding yeast *Saccharomyces cerevisiae*. *S. cerevisiae* is a particularly important yeast for biological research as it was the first eukaryote to have its entire genome sequenced and it contains many homologs to higher eukaryotic organisms, including humans [118]. One particular homolog is the triacylglyceride lypolysis pathway [93, 94]. Understanding the physiology behind this pathway and other related pathways is of great importance as the metabolism of lipids is connected to many diseases and undesirable conditions such as obesity, diabetes, atherosclerosis, and lysosomal storage disorders (LSDs) (e.g., Tay-Sachs disease and Gaucher disease) [96, 97, 119, 120].

For the first analysis of *S. cerevisae*, I analyzed the morphological and chemical composition (primarily lipid-rich organelles) of intrapopulation cells [87]. I prepared a liquid culture of yeast from a dry stock (Fleischmann's ActiveDry Yeast, ACH Food Companies, Inc., Cordova, TN). The liquid culture was prepared with filtered water at $\sim 40^o$ C and was provided dextrose as the primary carbon nutrient ($\sim$50% w/w). For analysis, a sample of the culture was removed and diluted to a concentration of approximately 2×10^7 cells/mL. Prior to injection into the flow cell, the sub-suspension was sonicated for several minutes and then filtered with a 35 μm mesh membrane. The cells were injected into the system with a 1 mL syringe at 4 $\mu L/min$ ($\sim$4.3 mm/s). The MCARS spectra of the flowing cells were recorded at 100 Hz and the FSC recorded at 10 kHz. The gating was performed in software and triggered from

changes to the FSC. Figure 101(a) is a density scatter plot of the maximum versus the minimum FSC for 7685 cells (the intensity represents the density of data points, with blue areas demonstrating low density, and red areas describing high density). The baseline FSC (i.e., no particles are present) is ∼6 V. One can clearly see two subpopulations: one with a substantial voltage above the baseline, and one predominantly below. Figure 101(b) represents two individual elastic scatter measurements taken from each region that typify the aforementioned effect. The exact shape of the FSC waveform is dependent on the refractive and diffractive effects due to the cell size, shape, and internal complexity and structure. Additionally, the high NA excitation objective creates a large cone of light that probes the cell over a large volume; thus, the transit time recorded in the elastic scatter measurement may be elongated from the actual transit time through the focal volume (∼2 - 4 ms). The subpopulation with the larger maximum FSC likely contains cells with internal scatterers (such as lipid vacuoles) that provide a mechanism for constructive interference between the incident beam and the scattered photons, whereas the lower maximum FSC population contains fewer scatterers; thus, the incident beams are only slightly refracted due to the near index matching between the cytoplasm and the aqueous sample flow [121]. Figure 102(a) shows the mean MCARS spectra (normalized to the spectrum of water) for the two subpopulations described in 101(a). One can see that the high maximum FSC population exhibits strong spectral peaks at 1411, 1624, and 2867 cm^{-1}. Because of the coherent mixing between the NRB and the resonant CARS signal, MCARS spectral peaks are typically distorted from their spontaneous Raman counterparts. To counteract these effects, I applied a Kramers-Kronig transform technique for spectral reconstruction using the raw MCARS spectrum of the yeast as the signal and the spectrum of the aqueous background as the estimated NRB [82]. Figure 102(b) shows the mean reconstructed spectra for the two yeast subpopulations and a Raman

spectrum collected from a lipid-rich yeast collected on a commercial microRaman system. For the high-maximum FSC subpopulation, 4 peaks are resolved at 1318, 1442, 1662, and 2935 cm^{-1} that correspond closely with those found in the spontaneous Raman spectrum at 1328 cm^{-1}, 1442 cm^{-1} (CH_2-deformation), 1652 cm^{-1} (amide I), and 2930 cm^{-1}(CH-stretch). The low FSC subpopulation resolves only a single clear peak around 2935 cm^{-1} and two broad, weak peaks around 1582 cm^{-1} and 1430 cm^{-1}. Based on this analysis, one can see that, indeed, the high-FSC population contains more prominent lipid-rich internal scatterers than the low-FSC population. In this yeast culture, ∼71% of the cells measured exhibited a prominent CH-stretch peak associated with the lipid-rich organelles within the cells [95]. This agrees closely with the measurement performed with a commercial flow cytometer using Nile Red lipophilic stain (∼72%).

In another experiment, I compared cultures of *S. cerevisiae* under different nutritional conditions. In this experiment, I used a pre-prepared liquid cultures of *Saccharomyces cerevisiae* (Yeast Strain 1056, Wyeast Laboratories, Columbia River Gorge, OR). The liquid culture ($\sim 8\times10^8 cells/mL$) was subdivided into two subcultures, and one subculture was given a liquid nutrient (wort base) containing essential nutrients, such as amino acids, nitrogen sources, and sugars, to activate the yeasts metabolism. The cultures were incubated for approximately 3.5 hours and then analyzed. For each analysis, the subculture was diluted to a concentration $\sim 4 \times 10^7$ (which approximately coincides with the optimal concentration described in Figure 40). Each aliquot was injected into the flow cell with a 500 μL syringe at 0.2 $\mu L/min$. Each recording analyzed 1,000 cells (repeat collections performed for all cells). The system was gated so that the FSC and SSC crossed above the baseline voltages, and the KK-reconstructed signal of each cell had to contain a spectral peak above the noise level. Figure 103(a) and (c) plots density scatter plots (the intensity represents the density of data points, with blue areas demonstrating low density, and red areas describing

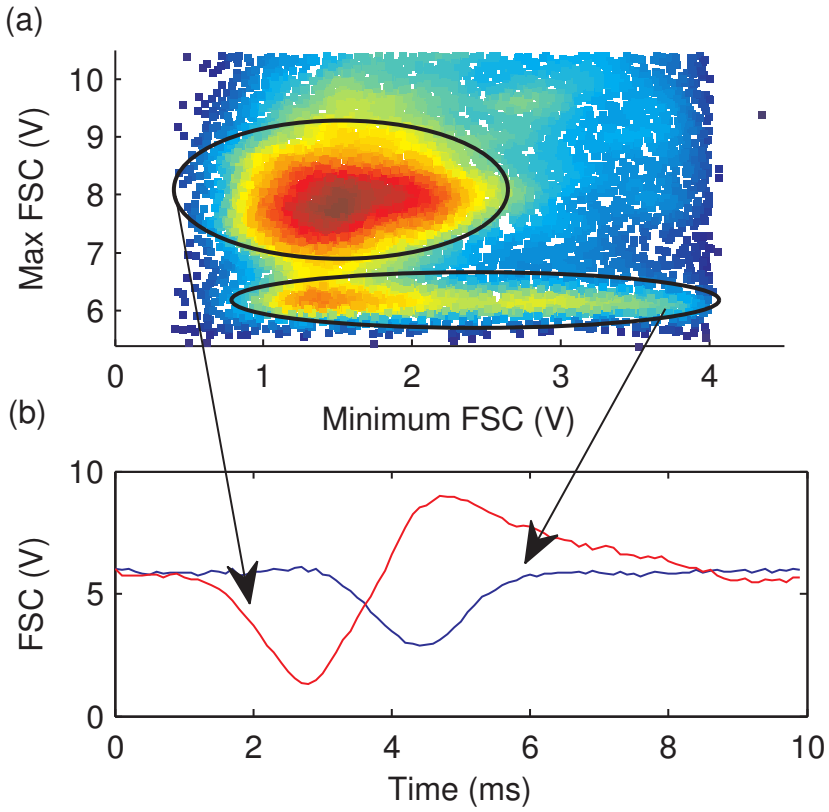

Figure 101: (a) Density scatter plot of maximum FSC voltage versus minimum FSC voltage for *S. cerevisiae*. (b) shows two representative time-traces of FSC from within the two subpopulations in (a). Image reprinted from [87]. © Optical Society of America.

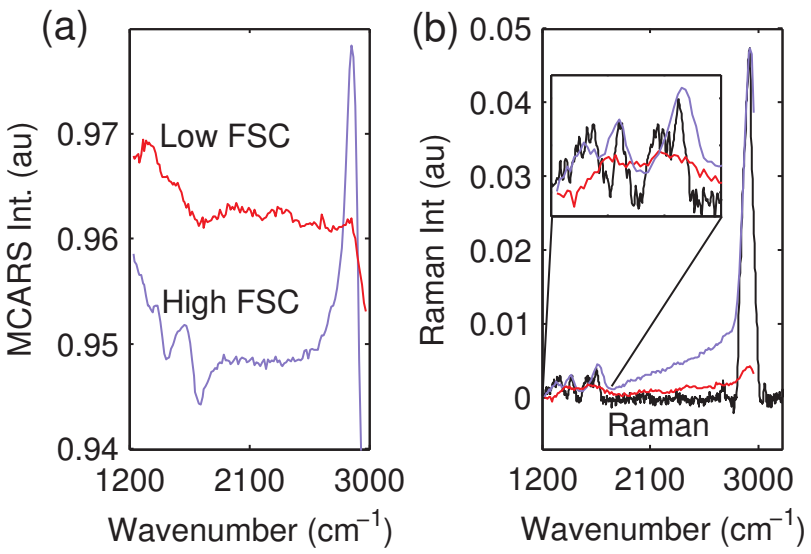

Figure 102: (a) Mean MCARS spectrum of the subpopulations of yeast in 101(a) with high (blue) and low (red) maximum FSC. Corresponding reconstructed Raman spectrum compared to the spontaneous Raman spectrum of a lipid-rich yeast (black). Image reprinted from [87]. © Optical Society of America.

high density) of the SSC amplitude as a function of FSC amplitude of the unfed and fed cultures of strain 1056, respectively. Additionally, Figure 103(b) and (d) shows the density scatter plots of the maximum KK-reconstructed peak intensity (the CH-stretch peak at $\sim$2930 cm^{-1}) as a function of FSC amplitude. The KK-reconstructed spectra of the fed and unfed yeast cultures and the corresponding Raman spectrum collected on a confocal Raman microscope are shown in Figure 104. In this figure, one can see that many of the Raman bands overlap between the spontaneous Raman spectrum and those collected with the MCARS flow cytometer. Additionally, these bands are all similar with those previously presented for the single yeast culture. As a side note, over the course of analyzing many different cultures of yeast, it has become apparent that bread yeasts (such as Fleischmann's ActiveDry previously presented) demonstrate a markedly higher level of lipid content than yeasts selectively bread for brewing (such as Wyeast Strain 1056 and several other strains analyzed [e.g., Wyeast strain 2308]). For comparison, the flow cytometric data is presented in Figure 105.

Comparing the elastic scatter collected with the MCARS flow cytometer and the commercial flow cytometer presents slight differences. The SSC of both techniques approximately follows the same trend of the FSC; although the FSC is elongated for the unfed case. Molecularly, one sees that the unfed yeasts demonstrate an enhanced level of lipid contributions. Unlike traditional flow cytometry, however, the MCARS flow cytometer highlights cells with smaller FSC generating a larger MCARS (KK-reconstructed) response. This may result from the focused beam architecture of the MCARS flow cytometer: with larger cells, the lipid bodies are able to spread out over a larger volume. Within smaller yeasts, however, the lipid bodies are confined to a smaller area. With a focused-beam geometry that scans a subregion of the cell, there is a heightened probability of scanning one or more lipid inclusions. Figure 106 is a micrograph collected on a confocal microscope of nile red stained yeast cells. In this figure, one can see that the lipid body content is approximately the same between the two cells, but the smaller cell confines these lipid bodies. It should be noted that the intensity of the fluorescence from the lipid droplets is a function of the larger cell passing on much of the nile red stain to its offspring, the smaller cell. Although the MCARS flow cytometer highlights the lipid content of cells with a smaller FSC, it does demonstrate an overall increase in the total lipid content of the unfed cell population.

In this section, I demonstrated the analysis of the yeast *Saccharomyces cerevisiae*. This particular yeast is a model organism with many human homologs. In the presented experiments, the MCARS flow cytometer analyzed morphological features and the content of lipid-rich organelles. Future research could utilize knock-out yeasts to gain further incite into lipid metabolic pathways. Although lipid research is of vital importance, future system improvements to MCARS flow cytometry, such as enhanced laser sources and improved detection speed, could further improve the use of MCARS flow cytometry to further molecular analyses.

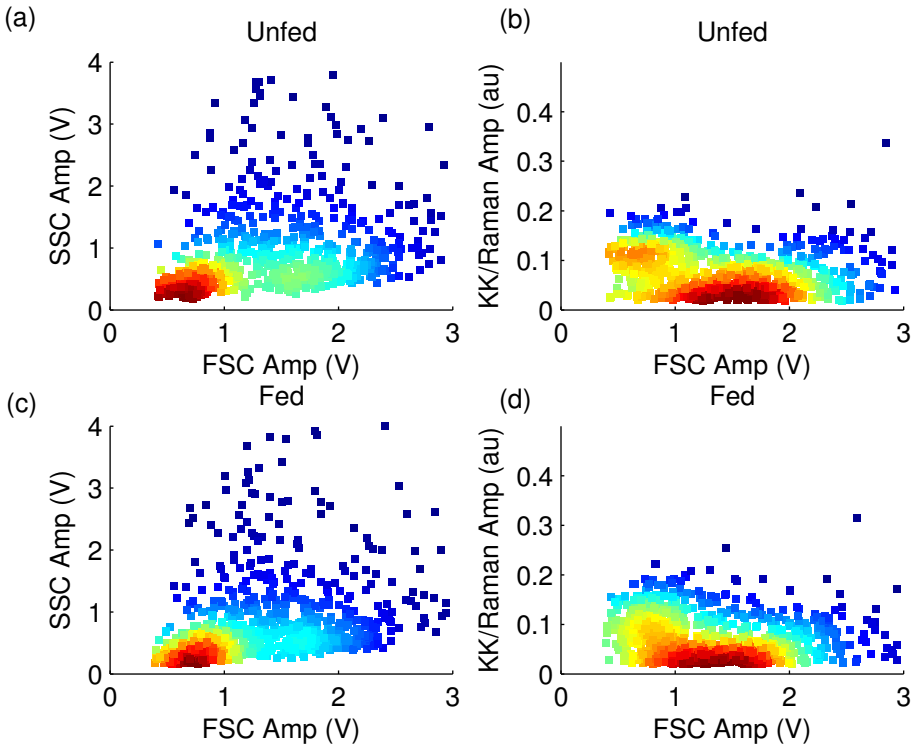

Figure 103: (a) SSC amplitude as a function of FSC amplitude for the unfed culture of *S. cerevisaie* (Wyeast strain 1056). (b) KK-reconstructed peak intensity of the CH-stretch peak at $\sim 2930 cm^{-1}$ for the unfed culture. (c) SSC amplitude as a function of FSC amplitude for the fed culture of *S. cerevisaie*. (d) KK-reconstructed peak intensity of the CH-stretch peak at $\sim 2930 cm^{-1}$ for the unfed culture.

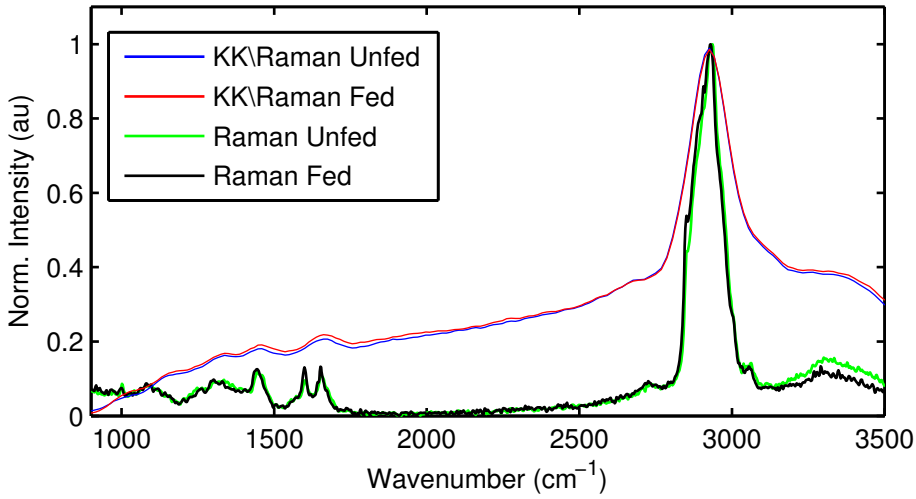

Figure 104: Normalized KK-reconstructed spectra of the unfed (blue) and fed (red) yeasts in comparison with the spontaneous Raman spectra of the unfed (green) and fed (black) yeasts.

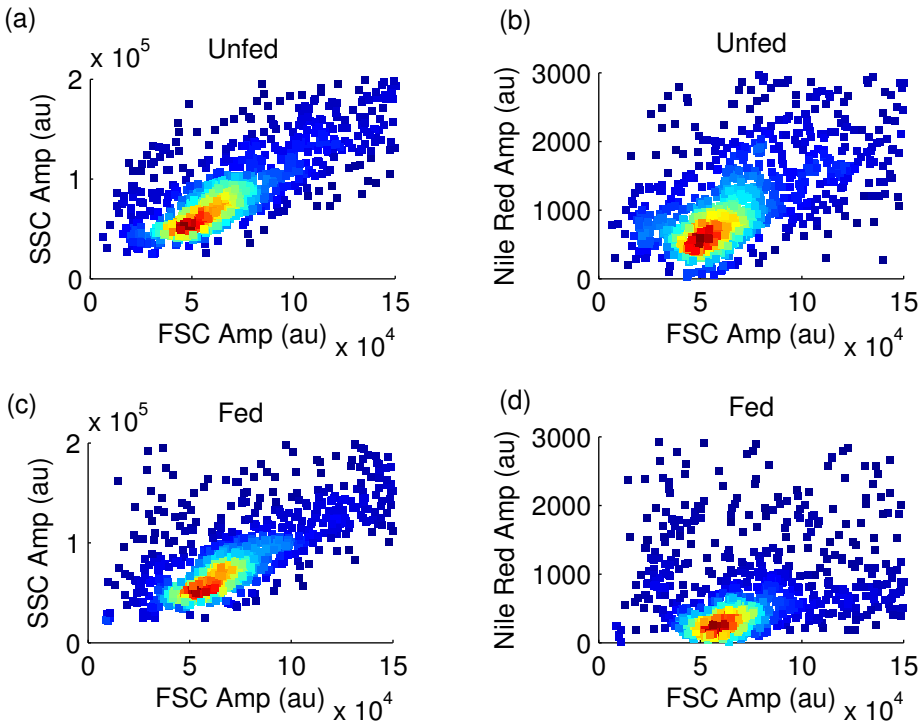

Figure 105: (a) SSC amplitude as a function of FSC amplitude for the unfed culture of *S. cerevisaie* (Wyeast strain 1056). (b) Fluorescence intensity as a function of FSC for the unfed culture. (c) SSC amplitude as a function of FSC amplitude for the fed culture. (d) Fluorescence intensity as a function of FSC for the fed culture.

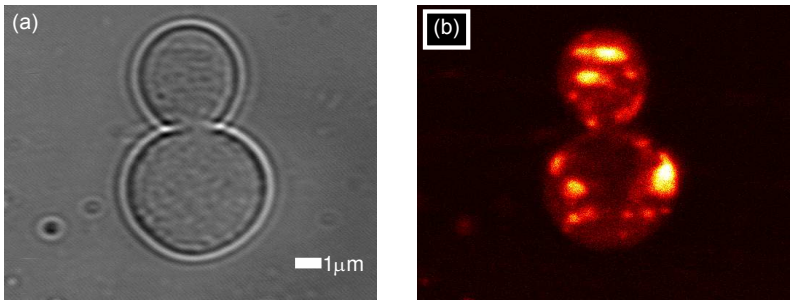

Figure 106: (a) DIC image of two S. cereviae cells collected with a confocal microscope. (b) Confocal microscopy image of the fluorescence from within the same cells stained with Nile Red.

In this chapter, I demonstrated a variety of applications for MCARS flow cytometry such as polymer bead analysis and the analysis of the biological samples *P. tricornutum* and *S. cerevisae*. These example highlight many of the strengths of MCARS flow cytometry, such as improved sizing of polymer beads based on FSC amplitude, and the ability to analyze lipid content without the necessity of exogenous labels. This chapter also served to demonstrate that although MCARS flow cytometry has developed rapidly, there are still numerous areas of improvement to further the technique. The next chapter discusses many system enhancements and future applications of MCARS flow cytometry to even further promote this technique as a powerful analytical tool.

CHAPTER 6

IMPROVING MCARS FLOW CYTOMETRY AND FUTURE DIRECTIONS

MCARS flow cytometry is a developing area of research that combines the label-free abilities of coherent Raman spectroscopies with the high-speed, single-cell analysis capabilities of flow cytometry. Throughout the previous chapters, the MCARS flow cytometry platforms demonstrated numerous applicability to a range of samples. These demonstrations represent not only a milestone in coherent Raman development, but also a starting point for further system enhancements to truly create a more versatile tool. In this chapter, I will present several opportunities for system enhancement as well as several potential new applications.

6.1 Improving Label-Free Flow Cytometry

6.1.1 PCF for Enhanced Stokes Source Energy Density

MCARS spectroscopy is a powerful tool for the label-free analysis of sample molecular composition. These systems, unlike CARS microscopy systems, utilize broadband sources to probe a wide Raman spectral region; thus, providing dense multiplex information in a single acquisition. MCARS systems, in their typical architecture, employ a single laser to act as the pump source and to seed a length of PCF for the generation of a broadband Stokes source to probe beyond 3000 cm^{-1} [60, 64, 122–127]. The microstructured interior of these fibers create tight optical confinement that results in huge local field intensities. This mechanism allows even modest pump powers to experience strong nonlinear interactions. Through an interplay of soliton formation,

decay, and collapse; Raman scattering; FWM; and a variety of other linear and nonlinear, coherent and incoherent effects, a narrowband pump evolves into a "white light" source spanning over 1000 nm [83, 84, 128]. Unfortunately, these supercontinuum sources compromise spectral breadth for energy density. This reduced energy density in the Stokes source requires additional energy in the pump source to increase the intensity of the anti-Stokes photons, which may induce photodamage [46, 129]. In order to more efficiently generate anti-Stokes photons and to reduce the risk of sample damage, new PCF sources need to be investigated and selected (or designed if necessary) to generate a broad supercontinuum (∼250 nm with a ∼800 nm pump/seed) that is also energy dense.

Over the last decade, the commercial availability of PCFs has expanded as these fibers are useful for inducing large nonlinear effects with modest incident optical powers. For MCARS spectroscopy, this availability of PCFs opens the doors to improved Stokes sources which may reduce the gap between CARS and MCARS sensitivities. CARS microscopy systems, typically, utilize a picosecond laser and an OPO to generate the Stokes and pump sources, respectively. For example, the system described in [123] uses a 1064 nm, 7 ps Nd:Vanadate laser to act as the Stokes source and to pump and OPO that provides a 5 ps tunable pump source between 780-930 nm (both sources operate at 76 MHz repetition rate). The average power of each incident source on the sample is 50 mW. The Stokes source bandwidth is ∼0.14 nm (2.1 cm^{-1}), and the pump source bandwidth is ∼0.33 nm (2.93 cm^{-1}); thus, the power density is ∼357 mW/nm (24 mW/cm^{-1}) and 151.5 mW/nm (17 mW/cm^{-1}) for the pump and Stokes sources, respectively. Under these conditions, nearly all of the optical power is focused within, for example, a 1 cm^{-1} wide Raman band. The developed MCARS system, on the other hand, uses a 806 nm, ∼125 fs source to act as the pump (after spectral filtering the source pulse duration is ∼322 fs) and to seed a length of PCF. Incident on the sample, the pump is ∼50 mW and the Stokes source is ∼10-40 mW spanning 850

- 1600 nm. The power density of the pump is ∼16.9 mW/nm (1.1 mW/cm^{-1}) and the Stokes source (at 40 mW) 0.053 mW/nm (0.006 mW/cm^{-1}). As the intensity of the anti-Stokes photons is quadratically proportional to the intensity of the pump and linearly proportional to the intensity of the Stokes,this leads to orders of magnitude higher intensity of anti-Stokes photons (experimentally, approximately 3-4 orders of magnitude including detector sensitivities). To improve MCARS sensitivities, it is, therefore, imperative to improve the excitation sources. Beyond stronger, more stable pump sources, the supercontinuum source requires extensive improvement to provide the levels of power necessary to provide high-quality spectra.

To [qualitatively] describe the creation of the supercontinuum in a PCF as to better optimize the future selection of the PCF for Stoke source generation, I created a frequency-domain simulation tool in MATLAB that simulates the generation of the supercontinuum along the length of fiber (all fibers simulated to be 12 cm long). The simulation tool was developed in MATLAB and uses a 5^{th} order Runge-Kutta method to solve for the generalized nonlinear Schrödinger's Equation (NLSE) in the frequency-domain at each spatial step [130, 131]. The effects included in this simulation are dispersion, stimulated Raman scattering, self steepening, and self-phase modulation (SPM) [21,22,128,132]. Figure 107 shows the spectral (a) and temporal (b) evolution of a 10 kW peak power, 50 fs incident pulse (hyperbolic secant), centered at 835 nm (the dispersion terms [up to 10^{th} order] are given in Table 8 [128]). This fiber closely resembles the performance of many fibers used for supercontinuum generation with a zero-dispersion wavelength at 780 nm. In this simulation, ∼36% (17.59 mW) of the incident power falls within the range of interest for Raman (0 - 3100cm^{-1}). Within this region, only about 0.033% (16 μW) falls within the CH-stretch energy region (2800-3000cm^{-1}). Increasing the pump peak power to 20 kW decreases the percentage of the incident power coupled into the wavelength region of interest to 31.3% but increases the total power in this region to 30.58 mW (the power coupled

into the CH-stretch energy region is 1.27 mW) (see Figure 108). Increasing the peak pump power even higher to 30 kW, reduces the coupling power even further to 23.3% (34.2 mW), and the CH-stretch coupled power reduces to 0.675% (0.989 mW); thus, increasing the incident power increases the total output power coupled to Raman spectral region, but decreases the coupling efficiency.

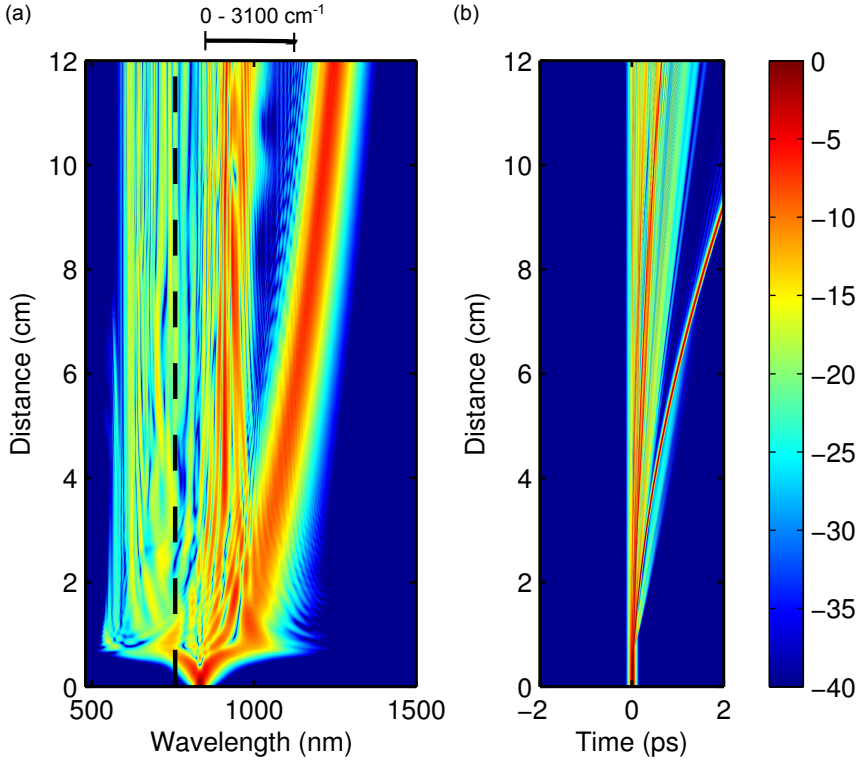

Figure 107: (a) Simulated spectral evolution of an 835 nm, 50 fs seed pulse within a PCF. The dashed lines indicate the zero-dispersion wavelengths. (b) Simulated temporal evolution of the seed pulse propagating through the PCF.

An alternative solution to forming a continuum that lies within the spectral region of interest may be provided by PCFs with two closely spaced zero-dispersion wavelengths [133]. By pumping these PCFs within the anomalous dispersion regime, higher-order soliton formation and decay occur, but the normal dispersion region of the fiber spectrum lying just to the red side of the anomalous region confines the soliton formation over a small spectral region. In turn, this produces a supercontinuum over a narrower region [128, 133]. To simulate a fiber with two closely spaced

Table 8: Dispersion terms (at 835 nm) for the simulated PCF with a zero dispersion wavelength at ∼780 nm [128].

Coefficient	Value	Units
β_2	-11.830	ps^2/km
β_3	8.1038×10^{-2}	ps^3/km
β_4	9.5205×10^{-5}	ps^4/km
β_5	2.0737×10^{-7}	ps^5/km
β_6	5.3943×10^{-10}	ps^6/km
β_7	1.3486×10^{-12}	ps^7/km
β_8	2.5495×10^{-15}	ps^8/km
β_9	3.0524×10^{-18}	ps^9/km
β_{10}	1.7140×10^{-21}	ps^{10}/km

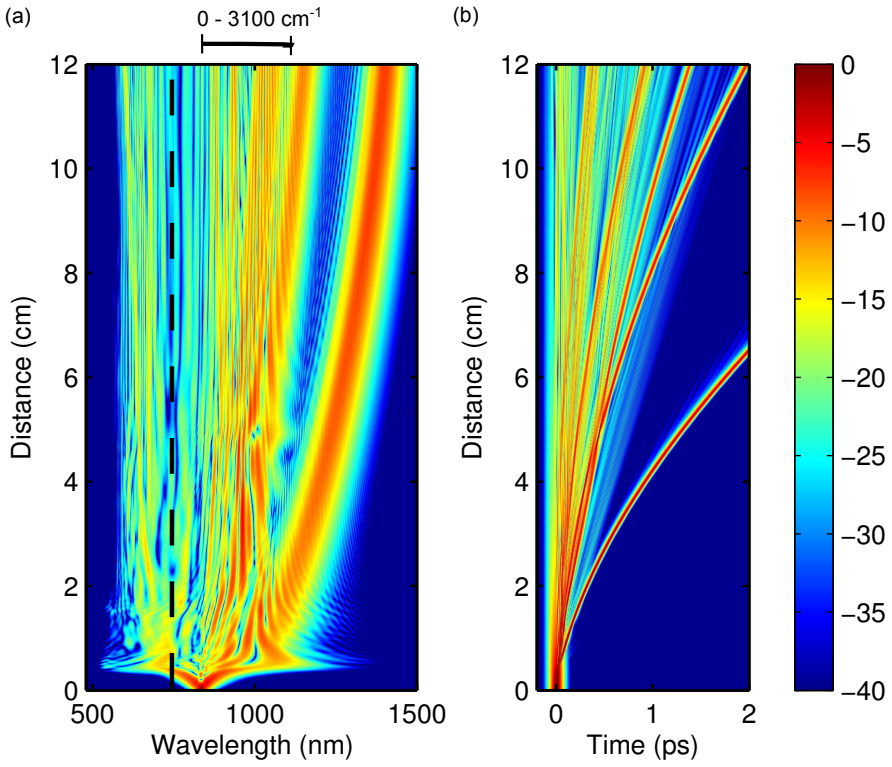

Figure 108: (a) Simulated spectral evolution of an 835 nm, 50 fs seed pulse within a PCF. The dashed lines indicate the zero-dispersion wavelengths. (b) Simulated temporal evolution of the seed pulse propagating through the PCF.

zero dispersion wavelengths, I approximated up to the β_7 dispersion term based on the β_2 diagram presented in [133] (this particular fiber was developed for MCARS: FemtoWhite-CARS, NKT Photonics, Birkerød, Denmark). The β_2 and dispersion diagrams for the simulated fiber are presented in Figure 109(a) and (b), respectively. Table 9 provides up to the 7^{th}-order dispersion term for the simulated fiber. Figure 110 shows the spectral (a) and temporal (b) evolution of a 10 kW peak power, 50 fs incident pulse (hyperbolic secant), centered at 835 nm within the simulated fiber. One can see obvious spectral differences in comparison to Figure 107 such as the breadth of the supercontinuum is greatly diminished, and the intensity of the spectrum is primarily flat in the region of wavelengths longer than the pump. For this simulated fiber, 47.5% (23.2 mW) of the optical power at the beginning of the PCF is converted into wavelengths within the Raman region. Additionally, 0.26% (0.122 mW) of the optical power falls within the CH-stretch Raman energy region– approximately an order of magnitude more power than with the fiber presented in Figure 107. In the previously presented fiber with a single zero-dispersion wavelength, there existed a prominent spectral feature around $1300 cm^{-1}$. Increasing the incident power, as shown in Figure 108 to the PCF would only push that prominent band further away from the pump (and further outside of the Raman energy region of interest). This dual zero-dispersion wavelength fiber, on the other hand, produces a much broader prominent spectral region centered at ∼1000 nm and increasing the incident power will only have a modest impact on this wavelength– as will adjusting the pump wavelength. To demonstrate these effects and to simulate a more-optimized source for MCARS, I simulated the same fiber with the center wavelength at 806 nm (i.e., the center wavelength of the current MCARS system) and a seed source peak power of 30 kW (∼1.7 nJ, ∼147 mW) as shown in Figure 111 (the dispersion terms up to the 7^{th}-order are presented in Table 10). Again, one can see the generated spectrum is relatively flat and is centered around 1100 cm^{-1}. In this simulation,

32.2% (46 mW) of the incident power was converted into wavelengths within the Raman region of interest. Additionally, 5.8% (8.5 mW) of the incident power was converted into wavelengths falling within the CH-stretch energy region. Compared to the single-zero-dispersion wavelength fiber, this simulated fiber provides over 500 times the output power within the CH-stretch region and a factor of 2.67 improvement over the entire Raman region of interest.

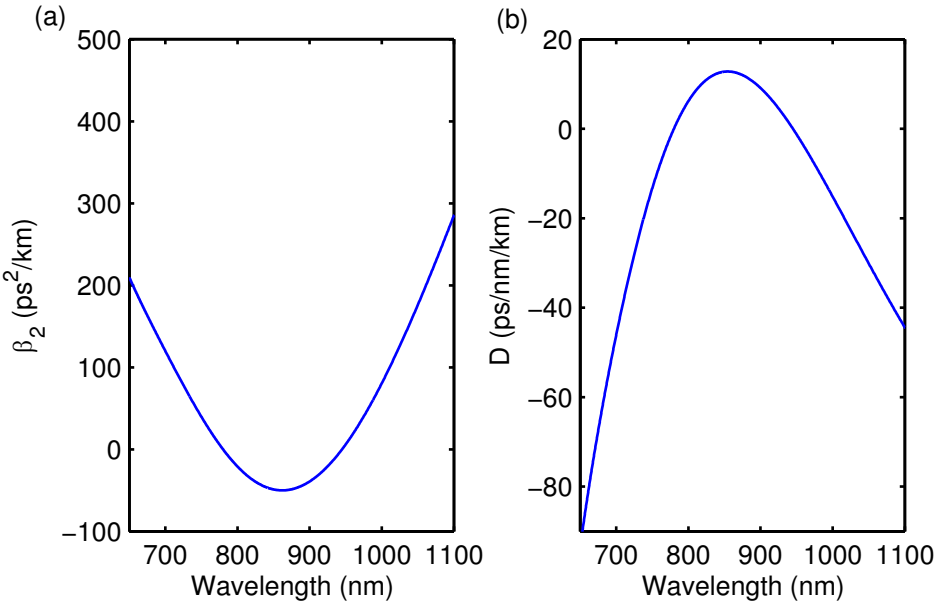

Figure 109: (a) Simulated β_2 dispersion term for a commercially available PCF with two closely-spaced zero-dispersion wavelengths. (b) Simulated dispersion, D.

Table 9: Dispersion terms (at 835 nm) for a simulated PCF with two closely-spaced zero dispersion wavelengths at ∼775 and 945 nm [133].

Coefficient	Value	Units
β_2	-4.4401	ps^2/km
β_3	3.06461×10^{-2}	ps^3/km
β_4	5.7867×10^{-4}	ps^4/km
β_5	-2.6111×10^{-6}	ps^5/km
β_6	2.0297×10^{-9}	ps^6/km
β_7	4.9453×10^{-11}	ps^7/km

Although the sensitivity of MCARS has traditionally been diminished by the low

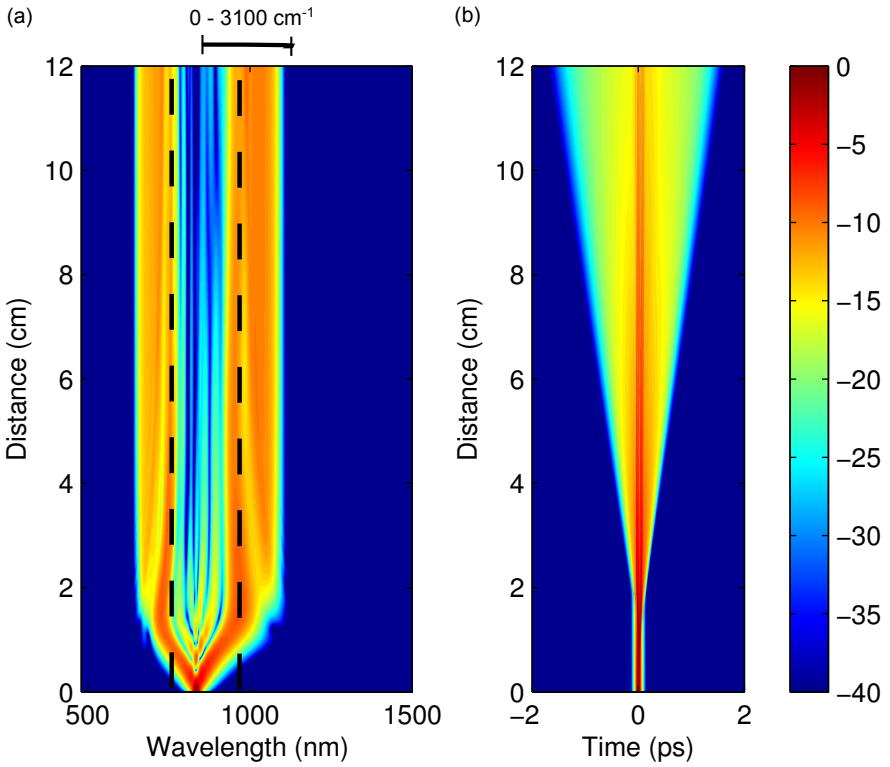

Figure 110: (a) Simulated spectral evolution of an 835 nm, 50 fs seed pulse within a PCF. The dashed lines indicate the zero-dispersion wavelengths. (b) Simulated temporal evolution of the seed pulse propagating through the PCF.

Table 10: Dispersion terms (at 806 nm) for a simulated PCF with two closely-spaced zero dispersion wavelengths at ∼775 and 945 nm [133].

Coefficient	Value	Units
β_2	-2.6181	ps^2/km
β_3	5.7631×10^{-2}	ps^3/km
β_4	4.1780×10^{-4}	ps^4/km
β_5	-2.6342×10^{-6}	ps^5/km
β_6	1.3176×10^{-9}	ps^6/km
β_7	4.9453×10^{-11}	ps^7/km

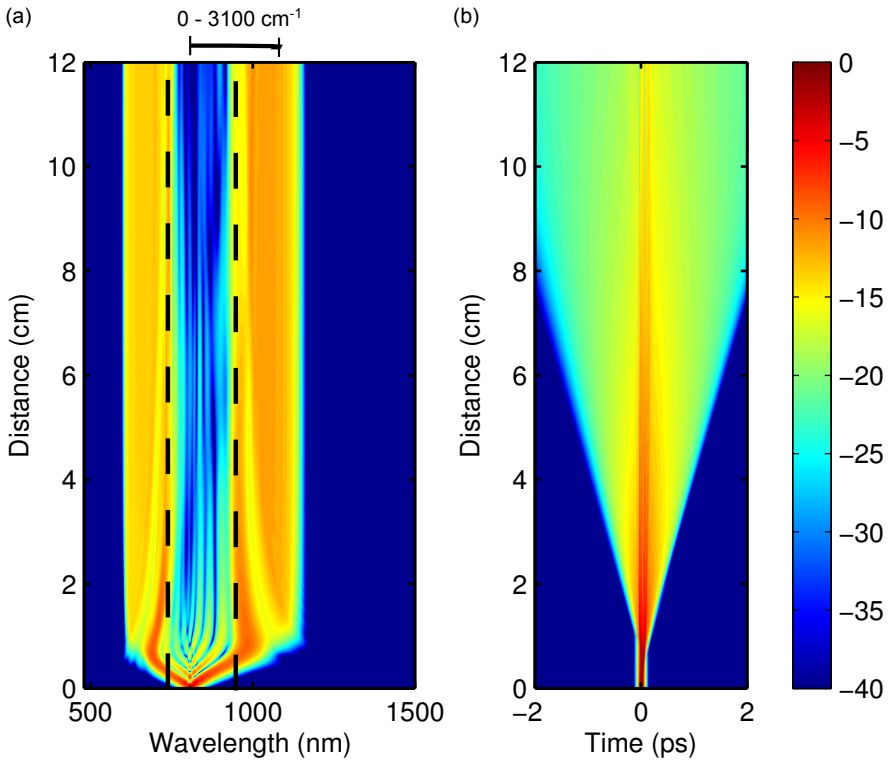

Figure 111: (a) Simulated spectral evolution of an 806 nm, 50 fs seed pulse within a PCF. The dashed lines indicate the zero-dispersion wavelengths. (b) Simulated temporal evolution of the seed pulse propagating through the PCF.

energy densities of the supercontinuum Stokes source and the optical damage threshold that prevents increasing the pump source intensity *ad infinitum*, the emerging varieties of commercially available PCFs offer hope. For MCARS applications, the arrival of PCFs with two closely spaced zero-dispersion wavelengths coincidentally falling near the Raman energy range of interest appear to be a promising ally in promoting MCARS spectroscopy to CARS microscopy sensitivities. Additionally, improving the pump and Stoke source open up numerous other system enhancements, such as having the ability to spectrally filter the pump beam and still maintain large powers, and the possibility of using high-speed, multi-element detectors, such as CMOS cameras. Clearly, it is of vital important to improve the laser sources for use in MCARS spectroscopy.

6.1.2 Multimodal Flow Cytometry

Label-free flow cytometry using MCARS provides a new paradigm in flow cytometric analysis. Although this new technique offers the possibility of molecular analysis without labels, current source and detector limitations place constraints on the molecular sensitivity of analysis. For analysis of large molecule, moderate concentration analytes, such as intracellular proteins, it is likely that source and detector improvements will overcome these limitations as CARS microscopy has demonstrated sensitivity levels capable of observing these cellular constituents. For small molecules and low concentration molecules, such as intracellular glucose and cell surface receptors, the challenge is considerable and another solution may prove more immediately practical: multimodal flow cytometry that combines fluorescence detection and MCARS spectroscopy.

As discussed in Chapter 4, the sensitivity of MCARS flow cytometry to dilute solutions of fluorochromes (and fluorophores) is limited. From this perspective, there is no limitation to using both fluorophores and MCARS flow cytometry. Additionally, many fluorophores are excited and emit in spectral regions below the anti-Stokes photon wavelengths for the demonstrated system. In order to enhance the operation of MCARS flow cytometry, multimodal flow cytometry utilizes both MCARS spectroscopy and fluorophore detection to create a system that relies on minimal fluorescent markers for sample analysis, but offers the flexibility to analyze a broad range of analytes and phenotypes. For example, Figure 112(a) and (b) shows the absorption and emissions spectra of seven common fluorophores that have emission profiles outside of the spectral window used for MCARS spectroscopy. Additionally, as fluorophore concentrations are usually in the micromolar concentration (or less), the spectra of the Raman profiles of these fluorophores are unlikely to interfere with the MCARS spectra of the molecular constituents of the sample of interest.

In order to fully realize the potential of multimodal flow cytometry, I envision

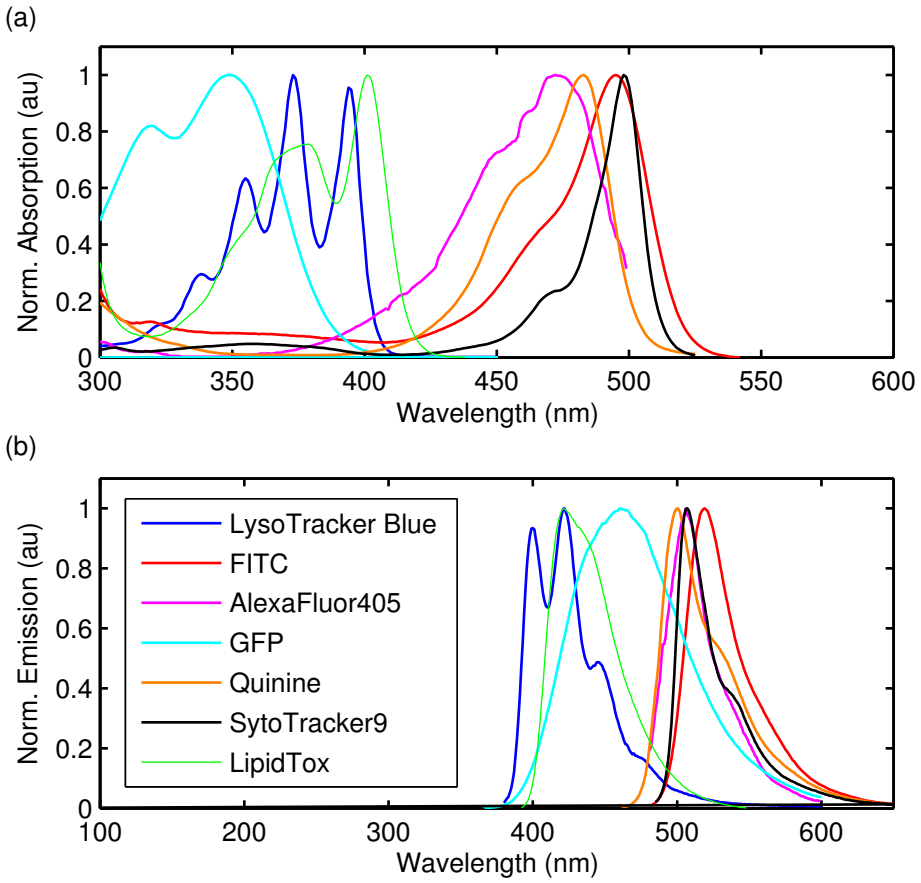

Figure 112: (a) Absorption and (b) emission profiles of several common fluorochromes/fluorophores. By properly selecting fluorophores that do not absorb or emit within the same spectral region as the MCARS signal, multimodality may be possible.

a compact spectrometer capable of simultaneously analyzing the fluorescent and MCARS spectra in a single box. Figure 113 presents a schematic of a high-speed, dual channel spectrometer. This spectrometer uses multianode PMTs as multielement detectors. Multianode PMTs are PMTs in which the anode is electrically and optically segmented to act as a multichannel detector. Currently, the largest multianode PMTs (linear array) contain 32 channels (e.g., the Hamamatsu H7260 series, Hamamatsu Photonics K. K., Iwata City, Japan). Two of these PMT modules could be placed side-by-side to expand the detection bandwidth and resolution (with fine-tuning available with grating selection and distance between the detector and grating) for both the fluorescent and MCARS detection. In order to collect the signals from each anode of each detector, one could use a a multichannel integrating DAQ such as the PhotoniQ IQSP582 (Vertilon, Wastford, MA). These specialized DAQ systems are designed to record up to 64 channels at up to 250 kHz, simultaneously.

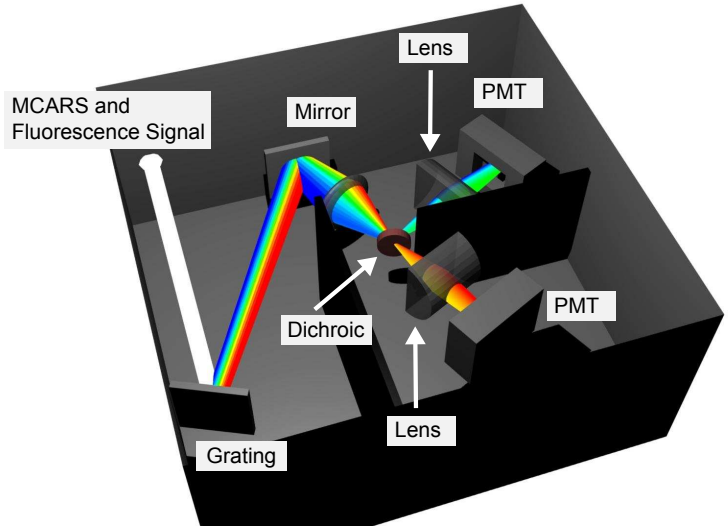

Figure 113: Schematic of a multimodal flow cytometer spectrometer capable of recording both fluorescence intensity (and/or spectra) and MCARS spectra. This system is envisioned with multi-anode PMTs (although other high-speed detectors are possible) to facilitate high-speed measurements.

With the speed and sensitivity afforded by multianode PMTs, and the flexibility, selectivity, and sensitivity provided through fluorescent labeling (or other labeling

technologies), the multimodal flow cytometer could provide a generalized tool capable of analyzing the Raman spectra of passing sample at high-speed while monitoring targeted phenotypes with fluorescent probes.

6.1.3 Stimulated Raman Scattering (SRS) Flow Cytometry

In this work, I have presented the first label-free flow cytometer that utilizes a non-linear optical process to probe molecular composition. Although CARS/MCARS is a powerful technique for label-free optical analysis, other optical mechanisms could provide additional performance and sensitivity. One technique, in particular, that shows promise is stimulated Raman scattering (SRS), which has recently demonstrated even higher sensitivity than CARS microscopy [45]. SRS is similar to CARS in that Raman molecular vibrations are excited, but unlike CARS, the detection is not of the anti-Stokes photons, but rather observation of the absorption of the pump or Stokes source. The sensitivity of SRS is greatly improved over CARS techniques due to the nonexistence of a background signal (although cross-phase modulation and sample absorption can perturb the experimental measurements). The lack of a background signal provides superior sensitivity to CARS (over four orders of magnitude [45]), and the lack of the NRB also generates SRS spectra that are not distorted from the spontaneous Raman spectra. Figure 114(A) and (B) provides the energy diagram and the input and output spectra gathered from SRS, respectively. Figure 114(C) demonstrates the use of high-speed Stokes source modulation, in order to induce a high-speed modulation in the output signal that can be used in conjunction with lock-in detection to isolate the SRS signal from other sources of signal fluctuation. Figure 114(D) presents a schematic of an SRS microscope, and (E) demonstrates the sensitivity of the SRS microscope described in [45] to $50\mu M$ of retinol solution. Finally, Figure 114(F) demonstrates the difference between a collected SRS and CARS spectrum (the CARS spectrum was collected by sweeping the excitation source wavelengths; thus, it is not an MCARS spectrum), and (G) demonstrates the similarity between the spontaneous Raman spectrum and the SRS spectrum of retinol in the CH-stretch Raman energy region.

Although SRS provides higher sensitivity than CARS, current implementations of

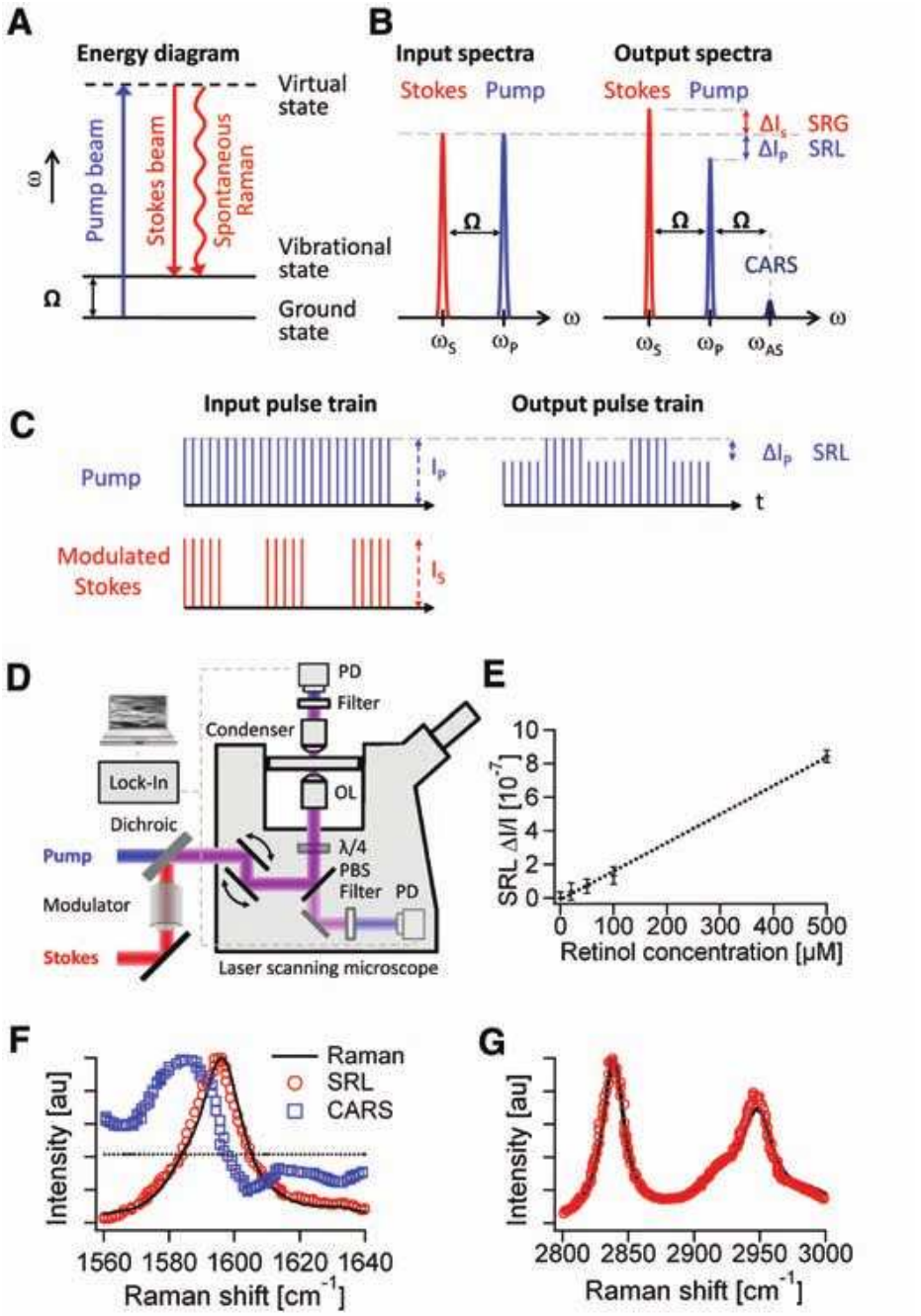

Figure 114: (A) Energy diagram of stimulated Raman scattering (SRS). (B) Through the SRS optical mechanism, pump photons are absorbed (stimulated Raman loss [SRL]) and Stokes photons are generated (stimulated Raman gain [SRG]). (C) For the detection of SRL, the Stokes beam is modulated. Measuring the pump beam and the imparted modulations, allows for recovery of the SRL intensity. (D) Schematic of an SRL microscope with lock-in detection. (E) The measured SRL of retinol as a function of concentration demonstrating the linear dependence of the SRL signal on concentration. The demonstrated sensitivity limit is 50 μM. (F) The recorded SRL spectrum (red), CARS spectrum (blue), and spontaneous Raman spectrum (black) of retinol in methanol around 1595 cm^{-1}. (G) The SRL spectrum (red) and spontaneous Raman spectrum (black) of neat methanol.

SRS require wavelength scanning to provide multispectral information (a broadband implementation of SRS was demonstrated, but was only capable of probing single vibrational energy levels per acquisition [134]). Additionally, CCD detectors do not offer lock-in detection capabilities. Two alternatives to CCD cameras, however, are multianode PMTs and photodiode arrays. The Heliotis C2 Camera (Heliotis AG, Root Längenbold, Switzerland), for example, contains a 144x90 pixel photodiode array that natively provides the hardware to simultaneously demodule each channel at up to 300 kHz. Using this camera on the output of a spectrograph, one could monitor the spectral gain bands within the supercontinuum of the supercontinuum source. Alternatively, one could use the output of a PCF as a broadband pump source (in conjunction with a relatively narrowband Stokes source) and monitor the absorption bands within the supercontinuum.

SRS is a relatively new technique for the label-free microscopic analysis of biological samples. Although much development is required to implement multiplex (broadband) SRS, the sensitivity rewards could be tremendous. Additionally, the developed technique would not only serve as a subsystem for label-free cytometry, but could also greatly impacts label-free microspectroscopy.

6.2 Future Applications

Throughout this thesis, I have presented several demonstrations of the application of label-free flow cytometry to biological specimens and pertinent assay techniques. These demonstrations serve to illuminate the applicability of MCARS flow cytometry to a range of samples, but there are numerous other possibilities for biological and chemical analysis as well as in clinical use. Additionally, with improvements in excitation sources and detector speeds, these possibilities will further increase. Two specific example applications for label-free flow cytometry are for real-time blood analysis for surgical patients and for real-time monitoring of water quality.

Cardiopulmonary bypass is a surgical technique used extensively during open-heart surgery. During this procedure, the operation of the heart is taken over by a series of mechanical pumps and machines (such as oxygenators, which infuse passing blood with oxygen). Currently, real-time monitoring of blood gas and white blood cell activity is limited; thus, decisions making for such procedures as blood transfusion rates and coagulant addition are made with only limited information at hand [135–137]. Additionally, even the efficacy of point-of-care techniques, as opposed to laboratory testing, are called into question [138]. MCARS flow cytometry, on the other hand, could actively monitor the state of red blood cells (such as the oxygenation [139], white blood cell activation (see Figure 115 for an MCARS image of a lysed blood cell taken with the developed MCARS microspectrometer), and platelet function, and the system could be directly connected to the bypass fluidic system.

Ensuring the quality of waterways and potable water is vitally important across the globe. In numerous countries, clean, safe water is a luxury not a guarantee. Additionally, in light of environmental disasters and the threat of terrorism, monitoring municipal water supplies and recreational areas has found a new importance. Monitoring the quality of water, however, is a time-consuming task that often relies on a myriad of assays to determine the chemical and microbial content of water.

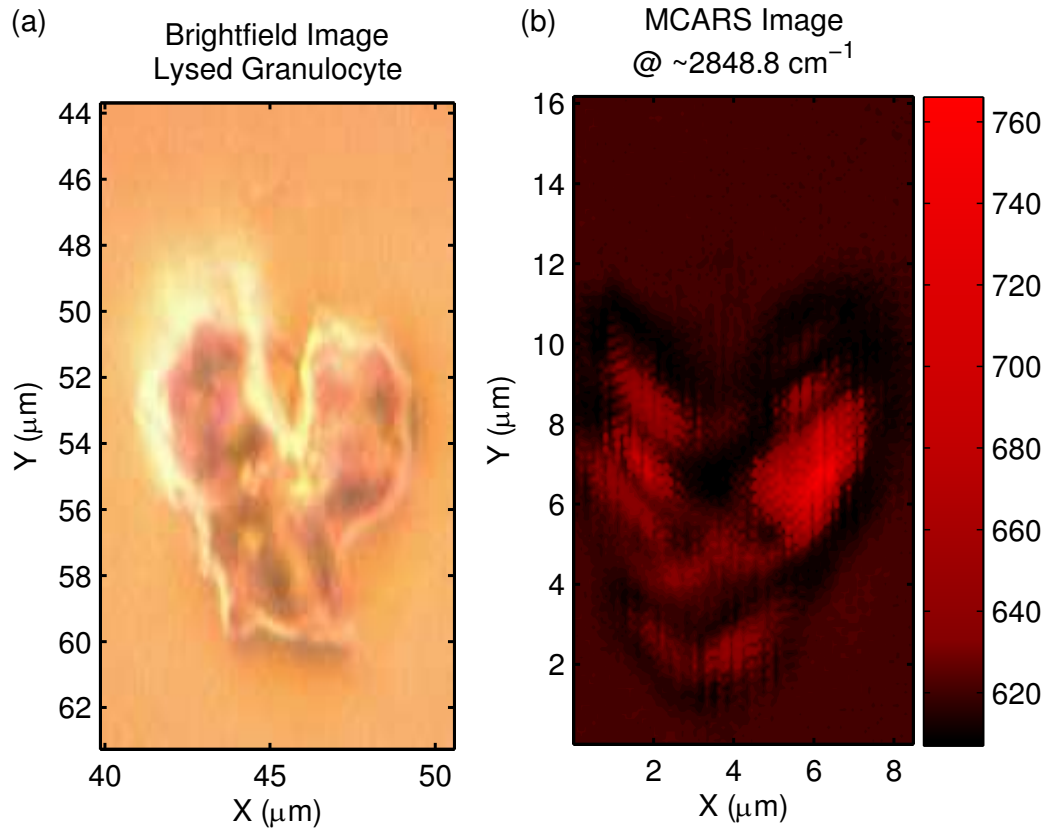

Figure 115: (a) Bright field micrograph of a lysed granulocyte. (b) MCARS microspectrograph of the same lysed granulocyte at $\sim 2848.8 cm^{-1}$.

Many microbial assays rely on analyzing culture growth of microbes found in the sample [140–142]. These tests often require several hours to a few days to quantify the analysis. Additionally, direct testing of the water by traditional flow cytometers is laborious as it would require the constant addition of fluorescent labels [141], it would be slow as incubation of the cells with the fluorescent labels require minutes to hours, and the focal volume is huge compared to bacteria; thus, their direct observation is challenging [1]. MCARS flow cytometry, on the other hand, uses a focused beam architecture ("slit-scanning" [105, 106]); thus, it may provide better resolution and sensitivity to microbes, and it removes the necessity of fluorophores; therefore, eliminating the cost and time-consumption necessary for the analysis [1, 121].

CHAPTER 7

CONCLUSION

In this research, the main focus has been on the development and implementation of the first label-free flow cytometer using MCARS spectroscopy. The first course of action was the development and characterization of the MCARS microspectrometer subsystem. The developed system demonstrated high-speed acquisition of sample spectra and was applied to a number of biologically relevant specimens to demonstrate molecular sensitivity and the feasibility of identifying different compounds based on their MCARS spectrum. Additionally, the first implementation of interferometric MCARS (iMCARS) was developed and the feasibility of its use investigated. Further MCARS investigation included quantitative analysis of the sensitivity of the system to demonstrative model chemicals. Although this research focused on the elimination of fluorescent labels, these labels offer a level of sensitivity for small and rare molecules (such as surface proteins) that MCARS is currently unable to detect. To leverage the strength of these labels without eliminating the possibility of MCARS analysis, the sensitivity of MCARS to fluorescent markers (using several common fluorochromes) was investigated, and it was determined that certain fluorescent probes and MCARS can coexist in the same system without interference.

The next step in the development of the MCARS flow cytometer was the integration and characterization of the fluidics and elastic scatter measurement platforms along with the MCARS spectroscopic subsystem. Modeling of the flow performance in the microfluidic chip provided practical performance limitations and parameters of

the fluidics subsystem. Combining MCARS spectroscopy and elastic scatter measurement of flowing samples offers dense multiparameter information about the morphology and composition of the sample. Through extensive experimental characterization and modeling of elastic scatter within samples demonstrated the sensitivity of the elastic scatter platform to the size and composition of the flowing sample, and along with understanding of the fluid dynamics within the flow cell, offered the ability to qualitatively and (under certain conditions) quantitatively extract morphological information about the flowing particles at high-speed. Finally, the sensitivity of the MCARS spectrometer subsystem was compared with the sensitivity of an MCARS microspectrometer in view of the fact that spectra are collected constantly, regardless of whether a sample is present. This investigation demonstrated that under current operating conditions, the sensitivity is minimally affected by the use of flowing samples, but as integration times reduce and flow rates increase, certain considerations and further system development might be necessary to maintain high molecular sensitivity.

To demonstrate the applicability of the system to biological analyses, several example samples were explored. The first biologically-relevant tool was the analysis of assay beads. Bead assays are a powerful tool for the analysis of samples that are difficult to directly analyze. The MCARS flow cytometer demonstrated the ability to identify polymer beads of differing size and composition. Performance strengths, such as its improved sizing capabilities, and limitations were also addressed. The next samples were cultures of the diatom *Phaeodactylum tricornutum*. Although their native fluorescence, even under NIR excitation, can prevent the use of Raman microspectroscopy, the MCARS flow cytometer was capable of recording unique MCARS spectra for each diatom at high-speed. Using this system, information about the health of the diatom as related to its nitrogen source availability was demonstrated. The

final biological samples analyzed were several cultures of yeast. Yeasts are a powerful model organism that contains many homologs to higher eukaryotic organisms–including humans. The MCARS flow cytometer demonstrated a high-level of sensitivity to the intracellular lipid organelles and provided the first MCARS spectra for this organism extending into the "fingerprint" region of the Raman spectrum.

MCARS flow cytometry provides a powerful platform for the analysis of molecular composition of flowing samples. As the first demonstration of label-free flow cytometry using nonlinear optical methods, this system opens up new paradigms in cytometric analysis and avenues of research and development in biology, chemistry, and medicine. Additionally, this system offers the possibility of integration into commercial flow cytometers as it is compatible with traditional assay techniques. Finally, the characterization and demonstration of a label-free flow cytometer offers a testbed for other nonlinear optical techniques to be applied to flow cytometric analysis. Techniques, such as SRS, could be developed and implemented and even possibly replace MCARS as the tool of choice for label-free flow cytometry.

A brief summary of the main contributions of this work:

- I demonstrated the first use of a photonic crystal fiber for the generation of a supercontinuum Stokes source and a broadband local oscillator for use in interferometric MCARS.
- I developed and characterized the first label-free flow cytometer that utilizes a nonlinear optical process to analyze molecular constituents of flowing samples over a broad spectral range.
- I demonstrated the fastest MCARS spectral acquisition rate (100 Hz) and the fastest MCARS acquisition rate capable of probing into the "fingerprint" region of the Raman spectrum with high sensitivity.

- I presented the first quantitative analysis of MCARS sensitivity to molecular concentration.
- I presented the first analysis of yeast cells beyond the CH-stretch Raman energy region.
- I presented the first MCARS and MCARS flow cytometric analysis of algal samples.

REFERENCES

[1] H. M. Shapiro, *Practical Flow Cytometry* (Wiley-Liss, New York, 2003), 4th ed.

[2] J. Juco, J. T. Holden, K. P. Mann, L. G. Kelley, and S. Li, "Immunophenotypic analysis of anaplastic large cell lymphoma by flow cytometry," Am. J. Clin. Pathol. **119**, 205–212 (2003).

[3] R. C. Braylan, A. Orfao, M. J. Borowitz, and B. H. Davis, "Optimal number of reagents required to evaluate hematolymphoid neoplasias: Results of an international consensus meeting," Cytometry **46**, 23–27 (2001).

[4] B. L. Wood, M. Arroz, D. Barnett, J. DiGiuseppe, B. Greig, S. J. Kussick, T. Oldaker, M. Shenkin, and E. S. an d P. Wallace, "2006 Bethesda International Consensus recommendations on the immunophenotypic analysis of hematolymphoid neoplasia by flow cytometry: Optimal reagents and reporting for the flow cytometric diagnosis of hematopoietic neoplasia," Cytometry B **72**, S14–S22 (2007).

[5] L. M. Coetzee, S. S. Tay, D. Lawrie, G. Janossy, and D. K. Glencross, "From research tool to routine test: CD38 monitoring in HIV patients." Cytometry B Clin. Cytom. **76**, 375–384 (2009).

[6] B. H. Davis, J. Holden, M. Bene, M. Borowitz, R. Braylan, D. Cornfield, W. Gorczyca, R. Lee, R. Maiese, A. Orfao, D. Wells, B. Wood, and M. Stetler-Stevenson, "2006 Bethesda International Consensus recommendations on the flow cytometric immunophenotypic analysis of hematolymphoid neoplasia: Medical indications," Cytometry B **72**, S5–S13 (2007).

[7] K. Bauer, R. Duque, and T. V. Shankey, *Clinical Flow Cytometry: Principles and Applications* (Williams and Wilkins, Baltimore, 1993).

[8] J. Careym, J. McCoy, and D. Keren, *Flow Cytometry in Clinical Diagnosis* (American Society for Clinical Pathology, Chicago, 2007), 4th ed.

[9] H. A. Bowers, A. Brutemark, W. F. Carvalho, , and E. Graneli, "Combining flow cytometry and real-time PCR methodology to demonstrate consumption by *Prymnesium parvum*," J . Am. Water Resources Assn. **46**, 133–143 (2010).

[10] S. Jacquet, M. Heldal, D. Iglesias-Rodriguez, A. Larsen, W. Wilson, and G. Bratbak, "Flow cytometric analysis of an *Emiliana huxleyi* terminated by viral infection," Aquat. Microb. Ecol. **27**, 111–124 (2002).

[11] N. Baumgarth and M. Roederer, "A practical approach to multicolor flow cytometry for immunophenotyping," J. Immuno. Meth. **243**, 77–97 (2000).

[12] M. G. Macey, *Principles of flow cytometry*, Flow Cytometry: Principles and Applications (Humana, Totowa, New Jersey, 2007).

[13] D. A. McCarthy, *Fluorochromes and fluorescence*, Flow Cytometry: Principles and Applications (Humana, Totowa, New Jersey, 2007).

[14] M. Roederer, "Spectral compensation for flow cytometry: visualization artifacts, limitations, and caveats," Cytometry **45**, 194–205 (2001).

[15] A. D. Michelson, "Flow cytometry: a clinical test of platelet function ," Blood **87**, 4925–4936 (1996).

[16] U. Resch-Genger, M. Grabolle, S. Cavaliere-Jaricot, R. Nitschke, and T. Nann, "Quantum dots versus organic dyes as fluorescent labels." Nature Methods **5**, 763–775 (2008).

[17] P. K. Chattopadhyay, D. A. Price, T. F. Harper, M. R. Betts, J. Yu, E. Gostick, S. P. Perfetto, P. Goepfert, R. A. Koup, S. C. De Rosa, M. P. Bruchez, and M. Roederer, "Quantum dot semiconductor nanocrystals for immunophenotyping by polychromatic flow cytometry." Nature Medicine **12**, 972–977 (2006).

[18] D. A. Watson, L. O. Brown, D. F. Gaskill, M. Naivar, S. W. Graves, S. K. Doorn, and J. P. Nolan, "A flow cytometer for the measurement of Raman spectra." Cytometry A **73**, 119–128 (2008).

[19] N. B. Colthup, L. H. Daly, and S. E. Wiberley, *Introduction to Infrared and Raman Spectroscopy* (Academic, Boston, 1992), 3rd ed.

[20] D. A. Long, *Raman Spectroscopy* (McGraw-Hill, New York, 1977).

[21] G. P. Agrawal, *Nonlinear Fiber Optics* (Academic, San Diego, 2001), 3rd ed.

[22] R. W. Boyd, *Nonlinear Optics* (Academic, San Diego, 2003), 2nd ed.

[23] J. W. Chan, D. S. Taylor, T. Zwerdling, S. M. Lane, K. Ihara, and T. Huser, "Micro-Raman spectroscopy detects individual neoplastic and normal hematopoietic cells." Biophys. J. **90**, 648–656 (2006).

[24] J. W. Chan, D. S. Taylor, S. M. Lane, T. Zwerdling, J. Tuscano, and T. Huser, "Nondestructive identification of individual leukemia cells by laser trapping Raman spectroscopy." Anal. Chem. **80**, 2180–2187 (2008).

[25] H. Siegle, A. Kaschner, A. Hoffmann, I. Broser, C. Thomsen, S. Einfeldt, , and D. Hommel, "Raman scattering from defects in GaN: The question of vibrational or electronic scattering mechanism," Phys. Rev. B **58**, 13619–13626 (1998).

[26] S. Nakashima, "Raman imaging of semiconductor materials: characterization of static and dynamic properties," J. Phys. Condens. Matter **16**, S25–S37 (2004).

[27] A. Y. Lau, L. P. Lee, and J. W. Chan, "An integrated optofluidic platform for Raman-activated cell sorting." Lab Chip **8**, 1116–1120 (2008).

[28] A. Zumbusch, G. R. Holtom, and X. S. Xie, "Three-dimensional vibrational imaging by coherent anti-Stokes Raman scattering," Phys. Rev. Lett. **82**, 4142–4145 (1999).

[29] S. Mukamel, *Principles of Nonlinear Optical Spectroscopy* (Oxford, New York, 1995).

[30] J. X. Cheng, A. Volkmer, L. D. Book, and X. S. Xie, "An epi-detected coherent anti-Stokes Raman scattering (E-CARS) microscope with high spectral resolution and high sensitivity," J. Phys. Chem. **105**, 1277–1280 (2001).

[31] J. X. Cheng, A. Volkmer, and X. S. Xie, "Theoretical and experimental characterization of coherent anti-Stokes Raman scattering microscopy," J. Opt. Soc. Am. B **19**, 1363–1375 (2002).

[32] C. L. Evans and X. S. Xie, "Coherent anti-Stokes Raman scattering microscopy: chemical imaging for biology and medicine," Annu. Rev. Anal. Chem. **1**, 883–909 (2008).

[33] W. H. Coulter, "High speed automatic blood cell counter and analyzer," Proceedings of the National Electronics Conference **12**, 1034–1040 (1956).

[34] I. by Life Technologies, "Introduction to Flow Cytometry," `http://probes.invitrogen.com/resources/education/tutorials/4Intro\_Flow/player.html` .

[35] Invitrogen by Life Technologies, "Fluorescence SpectraViewer," `http://www.invitrogen.com/site/us/en/home/support/Research-Tools/Fluorescence-SpectraViewer.html` (2011).

[36] M. Hao and F. R. Maxfield, "Analyzing microdomains in biological membranes using fluorescence techniques," J. Fluorescence **11**, 287 – 295 (2001).

[37] G. Goddard, J. C. Martin, M. Naivar, P. M. Goodwin, S. W. Graves, R. Habbersett, J. P. Nolan, and J. H. Jett, "Single particle high resolution spectral analysis flow cytometry," Cytometry A **69A**, 842–851 (2006).

[38] H. W. Wang, N. Bao, T. T. Le, C. Lu, and J. X. Cheng, "Microfluidic CARS cytometry," Opt. Express **16**, 5782–5789 (2008).

[39] K. Maquelin, C. Kirschner, L.-P. Choo-Smith, N. A. Ngo-Thi, T. van Vreeswijk, M. Stmmler, H. P. Endtz, H. A. Bruining, D. Naumann, and G. J. Puppels, "Prospective study of the performance of vibrational spectroscopies for rapid

identification of bacterial and fungal pathogens recovered from blood cultures." J. Clin. Microbiol. **41**, 324–9 (2003).

[40] D. F. M. Willemse-Erix, M. J. Scholtes-Timmerman, J.-W. Jachtenberg, W. B. van Leeuwen, D. Horst-Kreft, T. C. Bakker Schut, R. H. Deurenberg, G. J. Puppels, A. van Belkum, M. C. Vos, and K. Maquelin, "Optical fingerprinting in bacterial epidemiology: Raman spectroscopy as a real-time typing method." J. Clin. Microbiol. **47**, 652–9 (2009).

[41] A. Bosch, A. Min, C. Vescina, J. Degrossi, B. Gatti, P. Montanaro, M. Messina, M. Franco, C. Vay, J. Schmitt, D. Naumann, and O. Yantorno, "Fourier transform infrared spectroscopy for rapid identification of nonfermenting gram-negative bacteria isolated from sputum samples from cystic fibrosis patients." J. Clin. Microbiol. **46**, 2535–46 (2008).

[42] D. J. M. Mouwen, M. J. B. M. Weijtens, R. Capita, C. Alonso-Calleja, and M. Prieto, "Discrimination of enterobacterial repetitive intergenic consensus PCR types of Campylobacter coli and Campylobacter jejuni by Fourier transform infrared spectroscopy." Appl. Environ. Microbiol. **71**, 4318–24 (2005).

[43] M. Jackson, M. G. Sowa, and H. H. Mantsch, "Infrared spectroscopy: a new frontier in medicine." Biophys. Chem. **68**, 109–25 (1997).

[44] D. L. Wetzel, "MICROSPECTROSCOPY:Imaging Molecular Chemistry with Infrared Microscopy," Science **285**, 1224 (1999).

[45] C. W. Freudiger, W. Min, B. G. Saar, S. Lu, G. R. Holtom, C. He, J. C. Tsai, J. X. Kang, and X. S. Xie, "Label-free biomedical imaging with high sensitivity by stimulated Raman scattering microscopy." Science **322**, 1857–61 (2008).

[46] M. Cui, B. R. Bachler, and J. P. Ogilvie, "Comparing coherent and spontaneous Raman scattering under biological imaging conditions," Optics Letters **34**, 773 (2009).

[47] P. Maker and R. Terhune, "Study of Optical Effects Due to an Induced Polarization Third Order in the Electric Field Strength," Phys. Rev. **137**, A801–A818 (1965).

[48] R. F. Begley, A. B. Harvey, and R. L. Byer, "Coherent anti-Stokes Raman spectroscopy," Appl. Phys. Lett. **25**, 387–390 (1974).

[49] M. D. Duncan, J. Reintjes, and T. J. Manuccia, "Scanning coherent anti-Stokes Raman microscope," Optics Letters **7**, 350 (1982).

[50] E. O. Potma and X. S. Xie, "Theory of Spontaneous and Coherent Raman Scattering," in "Handbook of Biomedical Nonlinear Optical Microscopy," , B. R. Masters and P. T. C. So, eds. (Oxford University, New York, 2008), pp. 164–185.

[51] J.-x. Cheng, A. Volkmer, L. D. Book, and X. S. Xie, "Multiplex Coherent Anti-Stokes Raman Scattering Microspectroscopy and Study of Lipid Vesicles," J. Phys. Chem. B **106**, 8493–8498 (2002).

[52] J.-X. Cheng and X. S. Xie, "Coherent Anti-Stokes Raman Scattering Microscopy: Instrumentation, Theory, and Applications," J. Phys. Chem. B **108**, 827–840 (2004).

[53] M. Marrocco, "A quantitative approach to evaluate the problem of coherence of spectral components of the third-order susceptibility generating coherent anti-Stokes Raman signals," J. Raman Spectrosc. **38**, 452–459 (2007).

[54] I. W. Levin, *Advances in Infrared and Raman Spectroscopy* (Wiley Heyden, New York, 1984), vol. 11, pp. 1–48.

[55] R. Hellwarth, "Third-order optical susceptibilities of liquids and solids," Progress in Quantum Electronics **5**, 1 (1979).

[56] M. Balkanski, K. Jain, R. Beserman, and M. Jouanne, "Theory of interference distortion of Raman scattering line shapes in semiconductors," Physical Review B **12**, 4328 (1975).

[57] J. X. Cheng, L. D. Book, and X. S. Xie, "Polarization coherent anti-Stokes Raman scattering microscopy," Opt. Lett. **17**, 1341–1343 (2001).

[58] D. L. Marks, C. Vinegoni, J. S. Bredfeldt, and S. A. Boppart, "Interferometric differentiation between resonant coherent anti-Stokes Raman scattering and nonresonant four-wave-mixing processes," Appl. Phys. Lett. **85**, 5787–5789 (2004).

[59] G. W. H. Wurpel, J. M. Schins, and M. Müller, "Chemical specificity in three-dimensional imaging with multiplex coherent anti-Stokes Raman scattering microscopy," Opt. Lett. **27**, 1093–1095 (2002).

[60] S. H. Parekh, Y. J. Lee, K. A. Aamer, and M. T. Cicerone, "Label-free cellular imaging by broadband coherent anti-Stokes Raman scattering microscopy." Biophys. J. **99**, 2695–2704 (2010).

[61] A. Volkmer, J. X. Cheng, and X. S. Xie, "Vibrational imaging with high sensitivity via epidetected coherent anti-Stokes Raman scattering microscopy," Phys. Rev. Lett. **87**, 023901 (2001).

[62] J. CHENG, Y. JIA, G. ZHENG, and X. XIE, "Laser-Scanning Coherent Anti-Stokes Raman Scattering Microscopy and Applications to Cell Biology," Biophysical Journal **83**, 502 (2002).

[63] J.-L. Oudar, R. W. Smith, and Y. R. Shen, "Polarization-sensitive coherent anti-Stokes Raman spectroscopy," Applied Physics Letters **34**, 758 (1979).

[64] H. N. Paulsen, K. M. Hilligsøe, J. Thøgersen, S. R. Keiding, and J. J. Larsen, "Coherent anti-Stokes Raman scattering microscopy with a photonic crystal fiber based light source," Opt. Lett. **28**, 1123–1125 (2003).

[65] C. Otto, A. Voroshilov, S. G. Kruglik, and J. Greve, "Vibrational bands of luminescent zinc(II)-octaethylporphyrin using a polarization-sensitive 'microscopic' multiplex CARS technique," J. Raman Spectrosc. **32**, 495–501 (2001).

[66] M. Müller and J. M. Schins, "Imaging the Thermodynamic State of Lipid Membranes with Multiplex CARS Microscopy," J. Phys. Chem. B **106**, 3715–3723 (2002).

[67] H. Kano, "Molecular vibrational imaging of a human cell by multiplex coherent anti-Stokes Raman scattering microspectroscopy using a supercontinuum light source," J. Raman Spectrosc. **39**, 1649–1652 (2008).

[68] A. Volkmer, L. D. Book, and X. S. Xie, "Time-resolved coherent anti-Stokes Raman scattering microscopy: Imaging based on Raman free induction decay," Appl. Phys. Lett. **80**, 1505–1507 (2002).

[69] C. L. Evans, E. O. Potma, and X. S. Xie, "Coherent anti-Stokes Raman scattering spectral interferometry: determination of the real and imaginary components of nonlinear susceptibility $\chi^{(3)}$ for vibrational microscopy," Opt. Lett. **29**, 2923–2925 (2004).

[70] E. O. Potma, C. L. Evans, and X. S. Xie, "Heterodyne coherent anti-Stokes Raman scattering (CARS) imaging," Optics Letters **31**, 241 (2006).

[71] T. W. Kee, H. Zhao, and M. T. Cicerone, "One-laser interferometric broadband coherentanti-stokes raman scattering," Opt. Express **14**, 3631–3640 (2006).

[72] S. R. Keiding, E. R. Andresen, and E. O. Potma, "Picosecond anti-Stokes generation in a photonic-crystal fiber for interferometric CARS microscopy," Opt. Express **14**, 7246–7251 (2006).

[73] M. Cui, M. Joffre, J. Skodack, and J. P. Ogilvie, "Interferometric Fourier transform Coherent anti-Stokes Raman Scattering," Optics Express **14**, 8448 (2006).

[74] N. Dudovich, D. Oron, and Y. Silberberg, "Single-pulse coherently controlled nonlinear Raman spectroscopy and microscopy." Nature **418**, 512–514 (2002).

[75] B. von Vacano, J. Rehbinder, T. Buckup, and M. Motzkus, "Microanalytical nonlinear single-beam spectroscopy combining an unamplified femtosecond fibre laser, pulse shaping and interferometry," Applied Physics B **91**, 213 (2008).

[76] S.-H. Lim, A. G. Caster, O. Nicolet, and S. R. Leone, "Chemical imaging by single pulse interferometric coherent anti-stokes Raman scattering microscopy." J. Phys. Chem. B **110**, 5196–5204 (2006).

[77] C. H. Camp, A. A. Eftekhar, and A. Adibi, "Single-source interferometric multiplex coherent anti-Stokes Raman scattering with a photonic crystal fiber light source," in "Conference on Lasers and Electro-Optics/Quantum Electronics and Laser Science Conference and Photonic Applications Systems Technologies," (Optical Society of America, 2008), p. CThII3.

[78] E. M. Vartiainen, K. Peiponen, and T. Asakura, "Phase Retrieval in Optical Spectroscopy: Resolving Optical Constants from Power Spectra," Appl. Spectrosc. **50**, 1283–1289 (1996).

[79] E. M. Vartiainen, "Phase retrieval approach for coherent anti-Stokes Raman scattering spectrum analysis," Journal of the Optical Society of America B **9**, 1209 (1992).

[80] H. A. Rinia, M. Bonn, M. Müller, and E. M. Vartiainen, "Quantitative CARS spectroscopy using the maximum entropy method: the main lipid phase transition," ChemPhysChem **8**, 279–287 (2007).

[81] E. M. Vartiainen, H. A. Rinia, M. Mller, and M. Bonn, "Direct extraction of Raman line-shapes from congested CARS spectra," Optics Express **14**, 3622 (2006).

[82] Y. Liu, Y. J. Lee, and M. T. Cicerone, "Broadband CARS spectral phase retrieval using a time-domain Karmers-Kronig transform," Opt. Lett. **34**, 1363–1365 (2009).

[83] J. Herrmann, U. Griebner, N. Zhavoronkov, A. Husakou, D. Nickel, J. C. Knight, W. J. Wadsworth, P. S. J. Russell, and G. Korn, "Experimental Evidence for Supercontinuum Generation by Fission of Higher-Order Solitons in Photonic Fibers," Phys. Rev. Lett. **88**, 173901 (2002).

[84] A. V. Husakou and J. Herrmann, "Supercontinuum generation, four-wave mixing, and fission of higher-order solitons in photonic-crystal fibers," J. Opt. Soc. Am. B **19**, 2171–2182 (2002).

[85] C. H. Camp, S. Yegnanarayanan, A. A. Eftekhar, H. Sridhar, and A. Adibi, "Multiplex coherent anti-Stokes Raman scattering (MCARS) for chemically sensitive, label-free flow cytometry," Opt. Express **17**, 22879–22889 (2009).

[86] C. H. Camp, S. Yegnanarayanan, A. A. Eftekhar, H. Sridhar, and A. Adibi, "Multiplex coherent anti-Stokes Raman scattering flow cytometry for real-time classification of particles in a microfluidic channel," Proc. of SPIE **7569**, 75692F (2010).

[87] C. H. C. Jr., S. Yegnanarayanan, A. A. Eftekhar, and A. Adibi, "Label-free flow cytometry using multiplex coherent anti-Stokes Raman scattering (MCARS) for the analysis of biological specimens," Opt. Lett. **36** (2011).

[88] G.-B. Lee, C.-C. Chang, S.-B. Huang, and R.-J. Yang, "The hydrodynamic focusing effect inside rectangular microchannels," Journal of Micromechanics and Microengineering **16**, 1024 (2006).

[89] Andor Technology plc, "Newton EMCCD Spetcroscopy Detectors," `http://www.andor.com/scientific\_cameras/newton/` .

[90] Newport Corporation, "Oriel InstaSpecX CCD," `http://www.newport.com/store/genproduct.aspx?id=415018` .

[91] Princeton Instruments, "PIXIS - CCD (spectroscopy version)," `http://www.princetoninstruments.com/products/speccam/pixis/` .

[92] E. Batista, S. Monnerat, K. Kato, L. Stragevitch, and A. J. A. Meirelles, "LiquidLiquid Equilibrium for Systems of Canola Oil, Oleic Acid, and Short-Chain Alcohols," J. Chem. Eng. Data **44**, 1360 (1999).

[93] T. Czabany, K. Athenstaedt, and G. Daum, "Synthesis, storage and degradation of neutral lipids in yeast." Biochim. Biophys. Acta **1771**, 299–309 (2007).

[94] C. F. Kurat, K. Natter, J. Petschnigg, H. Wolinski, K. Scheuringer, H. Scholz, R. Zimmermann, R. Leber, R. Zechner, and S. D. Kohlwein, "Obese yeast: triglyceride lipolysis is functionally conserved from mammals to yeast." J. Biol. Chem. **281**, 491–500 (2006).

[95] C. Brackmann, J. Norbeck, M. keson, D. Bosch, C. Larsson, L. Gustafsson, and A. Enejder, "CARS microscopy of lipid stores in yeast: the impact of nutritional state and genetic background," J. Raman Spectrosc. **40**, 748–756 (2009).

[96] S. Martin and R. G. Parton, "Lipid droplets: a unified view of a dynamic organelle," Nat. Rev. Mol. Biol. **7**, 373–378 (2006).

[97] D. J. Murphy and J. Vance, "Mechanisms of lipid-body formation," Tech. Biol. Sci. **24**, 109–115 (1999).

[98] F. Ganikhanov, C. L. Evans, B. G. Saar, and X. S. Xie, "High-sensitivity vibrational imaging with frequency modulation coherent anti-Stokes Raman scattering (FM CARS) microscopy," Opt. Lett. **31**, 1872–1874 (2006).

[99] Fluorophores.org, "The database for fluorescent dyes and applications," `www.fluorophores.tugraz.at` .

[100] J. Jose and K. Burgess, "Benzophenoxazine-based fluorescent dyes for labeling biomolecules," Tetrahedron **62**, 11021 (2006).

[101] S. Adkins and M. Burmeister, "Visualization of DNA in agarose gels as migrating colored bands: applications for preparative gels and educational demonstrations." Anal. Biochem. **240**, 17–23 (1996).

[102] P. Greenspan, "Nile red: a selective fluorescent stain for intracellular lipid droplets," The Journal of Cell Biology **100**, 965 (1985).

[103] G. VAMOSI, C. GOHLKE, and R. CLEGG, "Fluorescence characteristics of 5-carboxytetramethylrhodamine linked covalently to the 5' end of oligonucleotides: multiple conformers of single-stranded and double-stranded dye-DNA complexes," Biophysical Journal **71**, 972 (1996).

[104] C. Eggeling, J. R. Fries, L. Brand, R. Günther, and C. A. M. Seidel, "Monitoring conformational dynamics of a single molecule by selective fluorescence spectroscopy," Proc. Natl. Acad. Sci. **95**, 1556–1561 (1998).

[105] W. G. Eisert, "High resolution optics combined with high spatial reproducibility in flow." Cytometry **1**, 254–9 (1981).

[106] T. K. Sharpless, M. Bartholdi, and M. R. Melamed, "Size and refractive index dependence of simple forward angle scattering measurements in a flow system using sharply-focused illumination." J. Histochem. Cytochem. **25**, 845 (1977).

[107] K. C. Neuman and S. M. Block, "Optical trapping." Rev Sci Instrum **75**, 2787–809 (2004).

[108] K. Pearson, "On lines and planes of closest fit to systems of points in space," Philisophical Magazine **2**, 559–572 (1901).

[109] Y. Chisti, "Biodiesel from microalgae," Biotechnol. Adv. **25**, 294–306 (2007).

[110] A. L. Mascarelli, "Gold rush for algae," Nature **461**, 460–461 (2009).

[111] D. L. Alonso, E.-H. Belarbi, J. M. Fernndez-Sevilla, J. Rodrguez-Ruiz, and E. M. Grima, "Acyl lipid composition variation related to culture age and nitrogen concentration in continuous culture of the microalga Phaeodactylum tricornutum," Phytochemistry **54**, 461–471 (2000).

[112] I. A. Guschina and J. L. Harwood, "Lipids and lipid metabolism in eukaryotic algae." Prog. Lipid Res. **45**, 160–186 (2006).

[113] C. Bowler, A. E. Allen, J. H. Badger, J. Grimwood, K. Jabbari, A. Kuo, U. Maheswari, C. Martens, F. Maumus, R. P. Otillar, E. Rayko, A. Salamov, K. Vandepoele, B. Beszteri, A. Gruber, M. Heijde, M. Katinka, T. Mock, K. Valentin, F. Verret, J. A. Berges, C. Brownlee, J.-P. Cadoret, A. Chiovitti, C. J. Choi, S. Coesel, A. De Martino, J. C. Detter, C. Durkin, A. Falciatore, J. Fournet, M. Haruta, M. J. J. Huysman, B. D. Jenkins, K. Jiroutova, R. E. Jorgensen, Y. Joubert, A. Kaplan, N. Krger, P. G. Kroth, J. La Roche, E. Lindquist, M. Lommer, V. Martin-Jzquel, P. J. Lopez, S. Lucas, M. Mangogna, K. McGinnis, L. K. Medlin, A. Montsant, M.-P. Oudot-Le Secq, C. Napoli, M. Obornik, M. S. Parker, J.-L. Petit, B. M. Porcel, N. Poulsen, M. Robison, L. Rychlewski, T. A. Rynearson, J. Schmutz, H. Shapiro, M. Siaut, M. Stanley, M. R. Sussman,

A. R. Taylor, A. Vardi, P. von Dassow, W. Vyverman, A. Willis, L. S. Wyrwicz, D. S. Rokhsar, J. Weissenbach, E. V. Armbrust, B. R. Green, Y. Van de Peer, and I. V. Grigoriev, "The Phaeodactylum genome reveals the evolutionary history of diatom genomes." Nature **456**, 239–44 (2008).

[114] L. A. Zaslavskaia, J. C. Lippmeier, P. G. Kroth, A. R. Grossman, and K. E. Apt, "Transformation of the diatom Phaeodactylum tricornutum (Bacillariophyceae) with a variety of selectable marker and reporter genes," Journal of Phycology **36**, 379 (2001).

[115] B. R. Wood, P. Heraud, S. Stojkovic, D. Morrison, J. Beardall, and D. McNaughton, "A Portable Raman Acoustic Levitation Spectroscopic System for the Identification and Environmental Monitoring of Algal Cells," Analytical Chemistry **77**, 4955 (2005).

[116] P. Heraud, J. Beardall, D. McNaughton, and B. R. Wood, "In vivo prediction of the nutrient status of individual microalgal cells using Raman microspectroscopy." FEMS Microbiol. Lett. **275**, 24–30 (2007).

[117] B. Hahn-Hgerdal, M. Galbe, M. F. Gorwa-Grauslund, G. Lidn, and G. Zacchi, "Bio-ethanol–the fuel of tomorrow from the residues of today." Trends Biotechnol. **24**, 549–556 (2006).

[118] A. Goffeau, B. G. B. andH. Bussey, R. W. Davis, B. Dujon, H. Feldmann, F. G. andJ. D. Hoheisel, C. Jacq, M. Johnston, E. J. Louis, H. W. Mewes, Y. Murakami, Philippsen, P. H. Tettelin, and S. G. Olive, "Life with 6000 genes," Science **274**, 546–567 (1996).

[119] P. G. Kopelman, "Obesity as a medical problem," Nature **404**, 635–643 (2006).

[120] L. J. Goldstein and S. M. Brown, "The low-density lipoprotein pathway and its relation to atherosclerosis," Ann. Rev. Biochem. **46**, 897–930 (1977).

[121] A. L. Koch, B. R. Robertson, and D. K. Button, "Deduction of the cell volume and mass from forward scatter intensity of bacteria analyzed by flow cytometry," Methods Microbiol. **27**, 49–61 (1996).

[122] H. Kano and H. Hamaguchi, "Vibrationally resonant imaging of a single living cell by supercontinuum-based multiplex coherent anti-Stokes Raman scattering microspectroscopy," Opt. Express **13**, 1322–1327 (2005).

[123] C. L. Evans, E. O. Potma, M. Puorishaag, D. Cote, C. P. Lin, and X. S. Xie, "Chemical imaging of tissue in vivo with video-rate coherent anti-Stokes Raman scattering microscopy," Proc. Natl. Acad. Sci. **102**, 16807–16812 (2005).

[124] E. R. Andresen, V. Birkedal, J. Thgersen, and S. R. Keiding, "Tunable light source for coherent anti-Stokes Raman scattering microspectroscopy based on the soliton self-frequency shift," Optics Letters **31**, 1328 (2006).

[125] H. Kano and H. Hamaguchi, "Near-infrared coherent anti-Stokes Raman scattering microscopy using supercontinuum generated from a photonic crystal fiber," Applied Physics B **80**, 243 (2005).

[126] B. von Vacano, L. Meyer, and M. Motzkus, "Rapid polymer blend imaging with quantitative broadband multiplex CARS microscopy," J. Raman Spectrosc. **38**, 916–926 (2007).

[127] D. AKIMOV, A. IVANOV, M. ALFIMOV, and A. ZHELTIKOV, "Photonic-crystal fiber sources for nonlinear spectroscopy," Vibrational Spectroscopy **42**, 33 (2006).

[128] J. M. Dudley and S. Coen, "Supercontinuum generation in photonic crystal fiber," Rev. Mod. Phys. **78**, 1135–1184 (2006).

[129] Y. Fu, H. Wang, R. Shi, and J.-X. Cheng, "Characterization of photodamage in coherent anti-Stokes Raman scattering microscopy," Optics Express **14**, 3942 (2006).

[130] N. G. Usechak, "Solving the Generalized NLSE in the frequency domain using RKF5," (2003). `http://www.optics.rochester.edu/users/noodles/work.html`.

[131] P. L. Franois, "Nonlinear propagation of ultrashort pulses in optical fibers: total field formulation in the frequency domain," Journal of the Optical Society of America B **8**, 276 (1991).

[132] B. Washburn, S. Ralph, and R. Windeler, "Ultrashort pulse propagation in air-silica microstructure fiber." Opt Express **10**, 575–80 (2002).

[133] K. M. Hilligsœ, T. Andersen, H. Paulsen, C. Nielsen, K. Mlmer, S. Keiding, R. Kristiansen, K. Hansen, and J. Larsen, "Supercontinuum generation in a photonic crystal fiber with two zero dispersion wavelengths." Opt Express **12**, 1045–54 (2004).

[134] C. W. Freudiger, W. Min, G. R. Holtom, B. Xu, M. Dantus, and X. Sunney Xie, "Highly specific label-free molecular imaging with spectrally tailored excitation-stimulated Raman scattering (STE-SRS) microscopy," Nature Photonics **5**, 103 (2011).

[135] G. J. Despotis, S. A. Santoro, E. Spitznagel, K. M. Kater, J. L. Cox, P. Barnes, and D. G. Lappas, "Prospective evaluation and clinical utility of on-site monitoring of coagulation in patients undergoing cardiac operation," J Thorac Cardiovasc Surg **107**, 271–279 (1994).

[136] L. T. Goodnough, G. J. Despotis, C. W. H. Jr, and T. B. F. Jr, "On the need for improved transfusion indicators in cardiac surgery," Ann Thorac Surg **60**, 473–480 (1995).

[137] V. Anttila, I. Hagino, D. Zurakowski, H. G. W. Lidov, and R. A. Jonas, "Higher bypass temperature correlates with increased white cell activation in the cerebral microcirculation," J Thorac Cardiovasc Surg **127**, 1781–1788 (2004).

[138] J. H. Nichols, T. S. Kickler, K. L. Dyer, S. K. Humbertson, P. C. Cooper, W. L. Maughan, and D. G. Oechsle, "Clinical outcomes of point-of-care testing in the interventional radiology and invasive cardiology setting ," **46**, 543–550 (2000).

[139] H. A. Rinia, M. Bonn, E. M. Vartiainen, C. B. Schaffer, and M. Müller, "Spectroscopic analysis of the oxygenation state of hemoglobin using coherent anti-Stokes Raman scattering," J. Biomed. Opt. **11**, 050502 (2006).

[140] Government of Wetern Australia Department of Health, "Standard drinking water assay," `http://www.public.health.wa.gov.au/cproot/2395/2/Standard\%20Drinking\%20Water\%20Assay.pdf` pp. 1–5 (2011).

[141] D. A. Veal, D. Deere, B. Ferrari, J. Piper, and P. V. Attfield, "Fluorescence staining and flow cytometry for monitoring microbial cells," J Immunol Methods **243**, 191–210 (2000).

[142] A. Rompr, "Detection and enumeration of coliforms in drinking water: current methods and emerging approaches," Journal of Microbiological Methods **49**, 31 (2002).

[143] E. F. Neufeld, "Lysosomal storage diseases," Ann. Rev. Biochem. **60**, 257–280 (1991).

[144] S. Michel, A. Courjaud, J. Dudley, C. Finot, E. Mottay, and H. Rigneault, "Broadband multiplex CARS microspectroscopy in the picosecond regime," in "Proc. of SPIE," (2010), p. 75692V.

VITA

Charles Camp was born in Lake Charles, Louisiana, but he was raised in the Washington, D.C. metropolitan area. He received his BS and MS from the University of Maryland in Electrical Engineering. His thesis work focused on all-optical thresholding via patterned active-region multimode switches (PARMS) under the tutelage of Professor Julius Goldhar and Dr. Christopher Richardson at the Laboratory for Physical Science in College Park, MD. His current research interests are the applications of nonlinear optics to biological, biomedical, and chemical analysis– especially, microscopy and flow cytometry. When he is not buried in the lab, Mr. Camp enjoys running, reading, and playing with furry sons Remy and Baron.